Title
Kinetic Consequences of Chemisorbed Oxygen Atoms during Methane Oxidation on Group VIII Metal Clusters

Author
Chin, Ya Huei

Publication Date
2011

Peer reviewed|Thesis/dissertation

Kinetic Consequences of Chemisorbed Oxygen Atoms during Methane Oxidation on Group VIII Metal Clusters

by

Ya-Huei Chin

A dissertation submitted in partial satisfaction of the
requirements for the degree of

Doctor of Philosophy

in

Chemical Engineering

in the

Graduate Division

of the

University of California, Berkeley

Committee in charge:

Professor Enrique Iglesia, Chair
Professor Alexis T. Bell
Professor Gabor Somorjai

Spring 2011

Kinetic Consequences of Chemisorbed Oxygen Atoms during Methane Oxidation on Group VIII Metal Clusters

by

Ya-Huei Chin

Abstract

Kinetic Consequences of Chemisorbed Oxygen Atoms during Methane Oxidation on Group VIII Metal Clusters

by

Ya-Huei Chin

Doctor of Philosophy in Chemical Engineering

University of California, Berkeley

Professor Enrique Iglesia, Chair

Molecular insights and the kinetic relevance of reaction elementary steps for methane activation on Group VIII metal and oxide clusters are established based on kinetic, isotopic, and theoretical assessments. These fundamental understandings enable accurate prediction of complex rate dependencies and cluster size effects during methane conversion reactions in catalytic partial oxidation, reforming, and combustion processes.

Kinetics of methane reactions with oxygen are described by several regimes, each with unique rate dependencies and kinetic requirements, as the identities of the kinetically-relevant step and the most abundant surface intermediates vary with the surface and bulk oxygen contents of Pt and Pd clusters. C-H bond activation is the kinetically-relevant step in all regimes except for one that occurs immediately before the complete O_2 depletion. C-H bond activation steps may, however, proceed via mechanistically distinct paths of oxidative insertion of metal atom, oxidative insertion coupled with H abstraction, or H abstraction routes, over metal-metal, oxygen-metal, or oxygen-oxygen site pairs, respectively, thus exhibiting different activation enthalpies and entropies. The predominant route for C-H bond activation is dictated by the coverages and reactivities of oxygen on cluster surfaces and accessibility of metal atom to CH_4 reactants. In a narrow regime before the complete O_2 consumption, C-H bond activation becomes kinetically inconsequential on oxygen-depleted surfaces and oxygen dissociative-adsorption steps limit methane conversion rates.

The relation among oxygen coverages, oxygen reactivities, and CH_4 reaction paths leads to a single-valued functional dependence of reactive CH_4 collision probabilities on oxygen chemical potentials at the cluster surfaces. The oxygen chemical potentials are given by kinetic coupling of the generation and removal of reactive oxygen atoms and thus are kinetic properties of CH_4 reactions; they become a thermodynamic property only in the limiting case of equilibrated oxygen dissociative-recombination steps.

The fate of oxygen during catalysis was rigorously defined as the reactive collision probabilities for CO oxidation relative to those for CH_4 and was measured at low oxygen coverages on Pt in which CO is most likely to desorb before encountering an oxygen atom and undergoing further oxidation to CO_2. The reactive collision probabilities are much larger for CO oxidation than for CH_4 oxidation; these results have

unequivocally confirmed that CO and H_2, if formed on and desorbed from catalytic surfaces, rapidly undergo sequential oxidation to form CO_2 and H_2O and that direct CO and H_2 formation via molecular coupling of CH_4 and O_2 is impractical at any residence time required for practical extents of CH_4 conversion.

Thermodynamics of oxygen dissolution from cluster surfaces into the bulk, cluster size and metal coordination effects on thermodynamic tendencies of bulk oxidation, and their catalytic consequences are established on Pd clusters. Oxidation of Pd clusters occurs via gradual dissolution of chemisorbed oxygen atoms into the bulk phase over a wide range of oxygen chemical potentials. The oxygen dissolution steps initiate and complete at lower oxygen chemical potentials in small than large clusters, indicating that small clusters exhibit a higher thermodynamic tendency for bulk oxidation. Oxygen dissolution leads to more weakly bound surface oxygen atoms and to exposed Pd atoms. These Pd atoms, together with vicinal lattice oxygen atoms, form Pd-oxygen site pairs that are more effective for C-H bond activation than O*-O* sites prevalent on metallic Pd cluster surfaces via concerted steps of an oxidative insertion of Pd atoms into the C-H bonds and oxygen assisted H abstraction. As oxygen binding strength decreases and Pd atoms become accessible with increasing oxygen contents in the clusters, C-H bond activation rate constants increase over the entire range of O-to-Pd atomic ratios throughout the Pd-to-PdO phase transition.

This fundamental study describes how oxygen thermochemical properties influence active site structures and, in turn, dictate the kinetics of methane oxidation reactions. The direct relation between the oxygen thermochemical properties and methane oxidation kinetics has not been previously interpreted at the atomic scale; this relation appears to be general for alkane oxidation reactions over transition metal and oxide clusters, as has been shown also in our recent work on ethane oxidation.

Dedication

for my Grandmother and Dad,
in loving memory,
and Mom,
without whose tireless efforts in instilling me the desire to make a difference
this work would not have been possible.

Kinetic Consequences of Chemisorbed Oxygen Atoms during Methane Oxidation on Group VIII Metal Clusters

Acknowledgements

This thesis reflects the culmination of my thinking in catalytic science which has matured under the guidance of Professor Enrique Iglesia. My perspective on catalytic chemistry has deepened under his relentless guidance and unconditional supports. I feel incredibly privileged to have been close to a remarkable scientist, dedicated teacher, and warm-hearted mentor on a daily basis. Professor Iglesia, you have taught me how to think critically, remain steadfast in various kinetic (and thermodynamic) situations, and to be persistent, calm, yet rigorous. Thank you for your patience in developing my perspectives and my ability of being coherent in words and colors. I will make sure that these trainings pay off.

I am indebted to Professor Matthew Neurock at the University of Virginia, who, in many ways, has acted as my second advisor. He has in countless times put my plea for help as a priority, and has dedicated an enormous amount of his time to catalyze my professional growth from across the country. His friendship and support have always been and will continue to remain close to my heart.

Special thanks to Dr. Mónica García-Diéguez, a talented individual who has showed me the meaning of dedication and at times kept me and our regimes under control. I owe a great deal to Dr. Corneliu Buda for his continuous support and patience in teaching me how to treat molecules and their reactions on the computer; he has offered me a place to seek shelter from experimental problems. I thank Dr. Huamin Wang and Dr. Aritomo Yamaguchi for their support, advice, and the countless hours they have spent on entertaining me. All of your friendships are important to me, both personally and professionally.

I also want to thank all past and present members of the Laboratory of Science and Application of Catalysis, in particular, Mike Zboray, Dr. Akio Ishikawa, Professor Aditya Bhan, Professor De Chen, Dr. Josef Macht, Dr. Brian Weiss, Raj Gounder, Brett Loveless, Alexander Buechner, Dr. Dante Simonetti, Professor Carlo Visconti, Dr. Beata Kilos, Dr. Xuebing Li, and Professor Raul Lobo, who have spent countless hours challenging and entertaining me. You have not only taught me the science, but also have brightened my daily laboratory life.

I am grateful to BP for providing the financial support through the BP-Methane Conversion Coorperative Research Program.

Last, but not the least, I would like to thank all my friends, especially those who have occasionally kidnapped me away from the laboratory, and in particular, George and Mary Cooke, who took times off for me, and Chin Seang Tan for his friendships and continuous support. I would like to thank my family for their inspiration and continuous patience in accommodation of my zest for the kinetic regimes. Specifically, my parents for their tireless effort in educating me and my brother and sister for continuously setting higher standards to challenge me.

Together, we have had a great time playing with these oxygen atoms!!

Chapter 1:
Introduction to Methane Oxidation Catalysis on Transition Metal and Oxide Clusters

Catalytic C-H bond cleavage has been a ubiquitous and important theme for chemical transformations of saturated hydrocarbons. This thesis advances our understanding of C-H bond activation in methane, which contains four equivalent C-H bonds (439.3 kJ mol^{-1})[1], over Group VIII transition metal and oxide clusters and specifically in the presence of reactive oxygen atoms. Methane oxidation occurs via several kinetic regimes; relations among oxygen thermochemical properties, active site structures, kinetically-relevant steps and the associated activation free energies for methane oxidation reactions in each of the regimes are established from a combined kinetic, isotopic, and ab initio density functional theory assessment.

Methane reacts with CO_2 or H_2O co-oxidants to form synthesis gas in highly endothermic reactions (ΔH^o_{298} =206 kJ mol^{-1} (H_2O), 247 kJ mol^{-1} (CO_2)). The use of O_2 as a co-oxidant instead of CO_2 or H_2O could form the same products, but with a significantly smaller and slightly negative reaction enthalpy (ΔH^o_{298} = -36 kJ mol^{-1}). This thermo-neutral reaction has been considered as an alternative path for CH_4 conversions because it avoids the energetically intensive reforming reactions.[2,3] Earlier reports[4,5] of high H_2 and CO selectivities (e.g. CO/CO_2 > 90 %) from CH_4-O_2 reactions in short monolith reactors have since spurred interest in the direct CH_4 oxidation reactions. O_2 co-reactants may, however, first combust with CH_4 (ΔH^o_{298} = -802 kJ mol^{-1}) to form CO_2 and H_2O, which are then converted to CO and H_2 in sequential reforming reactions. This indirect molecular coupling of methane and oxygen conversion steps gives the same overall enthalpy change as the direct CH_4-O_2 reaction path.

Many research groups have attempted to analyze the reaction path and oxygen selectivities by regression of the reactant and product pressures, either at the effluent streams[6,7,8] or along the reactor,[9,10,11] against proposed kinetic models and rate parameters; other groups have adapted combined kinetic and spectroscopic studies[12,13,14,15] to interrogate the surface species and/or chemical states of the catalysts during CH_4 catalytic turnovers. Despite exhaustive efforts spent over the past decades, the occurrence of direct catalytic partial oxidation of methane has, however, remained elusive with contradictory reports on whether CO and H_2 are formed before O_2 depletion.

The lack of an unequivocal conclusion on the reaction path and oxygen selectivity is caused, in large part, by the strong temperature and concentration gradients resulted from the rapid endothermic reforming and exothermic combustion reactions, which may occur concurrently or sequentially within the length scales of heat and mass transports, during the rate measurements. These gradients, together with the complex reactor hydrodynamics, have corrupted the measured rate and selectivity data intended to probe the coupling of chemical bonds at catalytic sites. In addition, surface structures and bulk chemical states of the metal clusters may change as O_2 is being consumed and oxygen chemical potential decreases,[16,17] either within catalyst pellets or along the packed reactor bed. The transitions of surface structures and bulk chemical states have further complicated the assessment of intrinsic surface chemistries. Questions about the identity

of reaction elementary steps and their kinetic relevance, roles of oxidants, oxidation tendencies of the clusters, and even the fate of oxygen within the catalytic cycle persist.

In this thesis, the prevalent temperature and concentration gradients are rigorously eliminated to gain insight into the interdependence among chemical reaction kinetics, active site structures, and catalyst chemical states during methane oxidation on Group VIII metal clusters. These efforts lead to rate and selectivity data solely reflecting surface chemistry at temperatures and concentrations equal to those in the contacting fluid phase. The rigorous kinetic studies are combined with ab initio density functional theory calculations to examine the various C-H bond activation paths, active site requirements, and their activation free energies on transition metal and oxide clusters for CH_4 oxidation reactions.

Complex kinetic dependencies and their relation to the coverages of chemisorbed oxygen during methane oxidation reactions on metallic Pt clusters are reported in Chapter 2. Four kinetic regimes, each of which exhibits a unique kinetic dependence on reactant pressures, a pre-exponential factor, and an effective activation barrier, are discovered. Identities of the kinetically-relevant step and the most abundant surface intermediates prevalent in each of the regimes are established using kinetic and isotopic measurements and density functional theory calculations of CH_4 and O_2 activation steps on model cubo-octahedral Pt clusters. The shifts among kinetic regimes and kinetically-relevant steps reflect changes in oxygen coverage and oxygen chemical potential on Pt clusters, both of which are set by the relative rates of surface oxygen atom removal by reactions with methane and their replacement via O_2 dissociative adsorption. As the oxygen coverage varies, different abundances of chemisorbed oxygen atoms (O*) and oxygen vacancies (*) provide a distribution of O*-O*, O*-*, and *-* site pairs on Pt cluster surfaces that activate the C-H bond in CH_4 via mechanistically different routes of H abstraction, concerted H abstraction and oxidative insertion, and oxidative insertion steps, respectively. In a narrow regime before O_2 depletion, C-H bond activation becomes kinetically-irrelevant on cluster surfaces essentially uncovered of reactive intermediates and oxygen dissociative adsorption limits rates.

The influences of average coordination number of surface metal atoms and oxygen binding strengths on CH_4 oxidation rates were examined by varying the cluster diameters and the relative abundances of atoms residing at the terraces and coordinatively less saturated corner and edge sites. Turnover rates increase with increasing cluster diameter when the kinetically-relevant C-H bond activation step is assisted by O*, decrease with increasing cluster diameter when the step uses only oxygen vacancies, and are independent of cluster diameter when C-H bond activation is kinetically-irrelevant and oxygen dissociation limits rates. These different structure-sensitivity trends reflect that metal and/or oxygen binding strengths affect the free energies of the transition states differently among the kinetically-relevant steps of C-H and O=O activation.

We show that oxygen virtual pressure, a fictitious oxygen pressure that is equilibrated with chemisorbed oxygen atoms, defines the oxygen coverages on metal cluster surfaces during catalysis. The oxygen virtual pressure is a rigorous surrogate of oxygen chemical potentials at cluster surfaces and is derived from the kinetic coupling of C-H and O=O activation steps. Thus, oxygen chemical potentials and oxygen virtual pressures at cluster surfaces depend on both the oxidant and reductant pressures, the identity of the kinetically-relevant step, the involvement of oxygen and oxygen vacancy

as active sites, and the rate constants for the kinetically-relevant CH_4 and O_2 activation steps. They become a thermodynamic property only in the limiting case of equilibrated O_2 adsorption-desorption steps. Oxygen virtual pressures are shown to prescribe the reactive methane collision probabilities (also the first-order CH_4 reaction rate constants) because of the direct relation between oxygen coverages and CH_4 reaction paths.

The fate of oxygen atoms during their reactions with methane and the yields of CO (and H_2) from direct chemical couplings of methane and oxygen on Pt and Rh clusters are rigorously interpreted in terms of the ratio of reactive collision probabilities for O* reactions with CO and CH_4 in Chapter 3. This ratio reflects the rates of CO, if formed, to undergo sequential oxidation during the timescale of methane turnovers and thus, is a measure of the maximum attainable CO yield from direct methane and oxygen reactions. The reactive collision probability ratios for CO and CH_4 were measured in ^{12}CO-$^{13}CH_4$-O_2 mixtures on Pt cluster surfaces at low oxygen coverages, because CO* are most likely to desorb from such surfaces before subsequent reactions with vicinal O* species to form CO_2. The reactive collision probability ratios for CO and CH_4 were also calculated from statistical averaging of the CO and CH_4 oxidation barriers derived from density functional theory (DFT) over all types of exposed Pt sites (terrace, edge, and corner sites) on cubo-octahedral Pt_{201} clusters (201 Pt atoms) using a transition state theory formalism. The reactive collision probability ratios are given by the rate constant ratios for O=O and C-H bond activation steps and are proportional to O* coverages because O* preferentially increases the CO oxidation rates but not the C-H bond activation rates. In spite of the low O* coverages at which CO is most likely to desorb unreacted, the CO to CH_4 reaction probability ratios are much larger than unity. These results unequivocally confirm that chemical coupling of methane and oxygen leads exclusively to combustion products and that CO and H_2 must form from the sequential reforming reactions.

The methane reactive collision probabilities and the fate of chemisorbed oxygen during CH_4-O_2 reactions on metallic Pd clusters are reported and compared with those on metallic Pt clusters in Chapter 4. Similar dependencies of reactive methane collision probabilities on oxygen coverages were found for Pd and Pt but their values were lower for Pd: reactive methane collision probabilities remain constant at high O* coverages and increase as O* coverages decrease below saturation. This trend reflects a transition from the use of O*-O* sites to O*-* sites, the latter are more effective, as the active structures in the kinetically-relevant C-H bond activation step as oxygen vacancies prevail below surface O* saturation. Unlike Pt, the kinetic regime corresponding to O_2 dissociation on uncovered cluster surfaces was not detected on Pd. The absence of oxygen-depleted surfaces at all measurable O_2 pressures and lower reactive methane collision probabilities on Pd than Pt clusters, when comparing at the same metal coordination and cluster size, are caused by the stronger oxygen bindings on Pd clusters. The stronger oxygen binding to Pd than Pt leads to more effective CO oxidation relative to CH_4, and thus to exclusive formation of combustion products. Dependencies of reactive methane collision probabilities on cluster size and oxygen binding strength are similar for Pt and Pd, as expected, because CH_4 oxidation reactions on these metals proceed via identical kinetically-relevant steps and thus exhibit similar kinetic requirements.

Chapter 5 addresses whether Pd metal or oxide surfaces are more effective for CH_4 conversions. Initial C-H bond activation remains as the kinetically-relevant step on

metal, O* saturated metal, and oxide cluster surfaces, but occurs via mechanistically different paths mediated by both the surface metal and/or oxygen atoms. Kinetic requirements for the various C-H bond activation paths are interpreted in terms of the changes in thermodynamic properties between the transition state complexes and gas phase reactants. Measured activation enthalpies and entropies, together with DFT derived barriers, suggest that the kinetically-relevant C-H bond activation step occurs via oxidative insertion, H abstraction, or oxidative insertion-H abstraction steps over metal, oxygen saturated metal, or oxide surfaces, respectively. The predominant C-H bond activation path is dictated by the availability of exposed Pd atoms to insert into the C-H bond and stabilize the CH_3 fragments and the presence of vicinal O atoms to assist with the H abstraction at the transition states. In the absence of exposed Pd atoms, C-H bond activation occurs over O*-O* sites via transition states with high activation enthalpies and low entropy losses that involve unbound CH_3 radical-like species and nearly formed OH groups. Bulk oxidation exposes Pd^{2+} sites and leads to Pd_{ox}-O_{ox} site pairs (Pd_{ox} and O_{ox} denote lattice Pd^{2+} and O^{2-} atoms, respectively) that activate C-H bond much more effectively than O*-O* sites because Pd_{ox} atoms interact strongly with the C and H atoms and thus stabilize the transition state energy and lower the activation enthalpies markedly from those on O*-O* site pairs. Similar oxidative insertion step was found also for C-H bond activation on Pd atom site pairs prevalent in CH_4-H_2O/CO_2 reactions but O* atoms are unavailable in assisting the H abstraction step.

The reactivities of oxygen on metal and oxide surfaces for H abstraction were assessed using DFT calculations. Lattice oxygen atoms in Pd_{ox}-O_{ox} sites on oxide surfaces were found to exhibit lower affinities towards H and thus are less reactive for OH bond formation than chemisorbed O* on metallic Pd surfaces. In spite of the lower H affinity and oxygen reactivities, C-H bond activation are much more effective on Pd_{ox}-O_{ox} than on O*-O* sites prevalent on metallic Pd clusters, as a result of the strong Pd_{ox} and CH_3 interactions that lower the transition state energy. The gain in enthalpy overcomes the larger entropy losses and leads to larger CH_4 oxidation rates on PdO than on O* saturated Pd cluster surfaces.

Interconversions of Pd clusters between the metal and oxide states, their catalytic consequences, and effects of cluster size on their thermodynamic tendencies for bulk oxidation are described in Chapter 6. The transient between Pd-PdO chemical states is probed at equal oxygen chemical potentials in the gas phase, in the bulk and at the surfaces of the clusters using a combined kinetic and oxygen uptake measurement. Pd to PdO phase transition occurs gradually over a wide range of oxygen chemical potentials via dissolution of surface oxygen atoms into the bulk. Oxygen dissolution depends strongly on cluster size and initiates at lower oxygen chemical potentials on smaller than larger clusters, indicating that the thermodynamic tendencies for bulk oxidation are stronger for smaller clusters. The oxygen dissolution increases the oxygen contents in the clusters and leads, in turn, to a decrease in oxygen binding strengths and to more effective H abstraction steps. It also exposes Pd atoms, making them accessible to CH_4 reactants and available for the oxidative insertion step during C-H bond activation. As a result of more effective H abstraction and stronger extent of CH_3 stabilization at the transition states, CH_4 activation are more effective on Pd clusters with higher oxygen contents than with lower oxygen contents.

In the following chapters, details on how to unravel the complex catalytic chemistry in CH_4 oxidation reactions using combined kinetic, isotopic, and theoretical methods are provided. The atomic-scale insights of the catalytic chemistry gained in this study enable a rigorous description of the kinetic dependencies and accurate predictions of cluster size and surface coordination effects on turnover rates. The relation among the thermochemical properties of oxygen, active site structures, and their catalytic functions for C-H bond activation appears to be general for alkane oxidation reactions on transition metal and oxide clusters, as has been shown also in our recent work on ethane oxidation over Pt clusters.

References

[1] Lide, D. R., Ed. CRC Handbook of Chemistry and Physics, 91st ed.[Online]; CRC Press: Boca Raton, FL, 2010; page. 9-71.
[2] Peña, M. A.; Gómez, J. P.; Fierro, J. L. G. *Appl. Catal. A: Gen.* **1996**, *144*, 7-57.
[3] Rostrup-Nielsen, J. R. *Catal. Today* **2002**, *71*, 243-247.
[4] Hickman, D. A.; Schmidt, L. D. *Science* **1993**, *259*, 343.
[5] Hickman, D. A.; Haupfear, E. A.; Schmidt, L. D. *Catal. Lett.* **1993**, *17*, 223.
[6] Tavazzi, I.; Beretta, A.; Groppi, G.; Forzatti, P. *J. Catal.* **2006**, *241*, 1-13.
[7] Mhadeshwar, A. B.; Vlachos, D. G. *Ind. & Engr. Chem. Res.* **2007**, *46*, 5310-5324.
[8] Schwiedernoch, R.; Tischer, S.; Correa, C.; Deutschmann, *Chem. Engr. Sci.* **2003**, *58*, 633-642.
[9] Michael, B. C.; Nare, D. N.; Schmidt, L. D. *Chem. Engr. Sci.* **2010**, *65*, 3893-3902.
[10] Dalle Nogare, D.; Degenstein, N. J.; Horn, R.; Canu, P.; Schmidt, L. D. *J. Catal.* **2011**, *277*, 134-148.
[11] Horn, R.; William, K. A.; Degenstein, N. J.; Bitsch-Larsen, A.; Nogare, D. D.; Tupy, S. A.; Schmidt, L. D. *J. Catal.* **2007**, *249*, 380-393.
[12] Hannemann, S.; Grunwaldt, J. D.; Kimmerle, B.; Baiker, A.; Boye, P.; Schroer, C. *Topics in Catal.* **2009**, *52*, 1360-1370.
[13] Kimmerle B.; Haider, P. Grunwaldt, J. D.; Baiker, A.; Boye, P.; Schroer, C. G. *Appl. Catal. A-Gen.* **2009**, *353*, 36-45.
[14] Weng, W. Z.; Chen, M. S.; Yan Q. G.; Qu, T. H.; Chao, Z. S.; Liao, Y. Y.; Wan, H. L. *Catal. Today* **2000**, *63*, 317-326.
[15] Weng, W. A.; Yan, Q. G.; Luo, C. R.; Liao, Y. Y.; Wan, H. L. *Catal. Lett.* **2001**, *74*, 37-43.
[16] Balint, I.; Miyazaki A.; Aika, K. *J. Catal.* **2003**, *220*, 74-83.
[17] Rabe, S.; Nachtegaal, M.; Vogel, F. *Phys. Chem. Chem. Phys.* **2007**, *9*, 1461-1468.

Chapter 2:
Reactivity of Chemisorbed Oxygen Atoms and their Catalytic Consequences during CH_4-O_2 Catalysis on Supported Pt Clusters

Abstract

Kinetic and isotopic data and density functional theory treatments provide evidence for the elementary steps and the active site requirements involved in the four distinct kinetic regimes observed during CH_4 oxidation reactions using O_2, H_2O, or CO_2 as oxidants on Pt clusters. These four regimes exhibit distinct rate equations because of the involvement of different kinetically-relevant steps, predominant adsorbed species, and rate and equilibrium constants for different elementary steps. Transitions among regimes occur as chemisorbed oxygen (O*) coverages change on Pt clusters with O_2/CH_4 reactant ratios. O* coverages are given, in turn, by a virtual O_2 pressure, which represents the pressure that would give the prevalent steady-state O* coverages if their adsorption-desorption equilibrium were maintained; it acts as a surrogate for oxygen chemical potentials at catalytic surfaces and reflects the kinetic coupling between C-H and O=O activation steps. O* coverages and virtual pressures depend on O_2 pressure when O_2 activation is equilibrated and on O_2/CH_4 ratios when this step becomes irreversible as a result of fast scavenging of O* by CH_4-derived intermediates. In three of these kinetic regimes, C-H bond activation is the sole kinetically-relevant step, but occurs on different active surface species, which evolve from oxygen-oxygen (O*-O*), to oxygen-oxygen vacancy (O*-*), and to vacancy-vacancy (*-*) site pairs as O* coverages decrease.

On O*-saturated clusters, O*-O* site pairs activate C-H bonds in CH_4 via homolytic hydrogen abstraction steps that form CH_3 groups with significant radical character and weak interactions with surfaces at the transition state. In this regime, rates depend linearly on CH_4 pressure but are independent of O_2 pressure; the observed normal CH_4/CD_4 kinetic isotope effects are consistent with the kinetic-relevance of C-H bond activation and $^{16}O_2$-$^{18}O_2$ isotopic exchange rates in the presence or absence of CH_4 show that O_2 activation steps are quasi-equilibrated and Pt surfaces are nearly saturated with O* during catalysis. Measured and DFT-derived activation barriers are large, because of the weak stabilization of the CH_3 fragments at transition states, but are compensated by the high entropy of these radical-like species. Turnover rates in this regime decrease with increasing Pt dispersion, because low-coordination exposed atoms on small clusters bind O* more strongly than low-index facets on large clusters, thus making O* less effective in H-abstraction. As vacancies (*, also exposed Pt atoms) become available on O*-covered surfaces, O*-* site pairs activate C-H bonds via concerted oxidative addition and H-abstraction in transition states effectively stabilized via CH_3 interactions with the vacancies, which lead to much higher turnover rates than on O*-O* pairs. In this regime, O_2 activation becomes irreversible, because fast C-H bond activation steps scavenge O* as it forms. Thus, O* coverages are set by the prevalent O_2/CH_4 ratios instead of the O_2 pressures; CH_4/CD_4 isotope effects are larger than for turnovers mediated by O*-O* site pairs, because C-H (and C-D) activation steps are also required to form the * sites involved in C-H bond activation. Turnover rates for CH_4-O_2 reactions mediated by O*-* pairs decrease with increasing Pt dispersion, as in the case of O*-O* active structures, because stronger O* binding on small clusters leads to less reactive O* atoms, but also to

lower concentrations of vacancies at cluster surfaces. As O_2/CH_4 ratios and O* coverages become smaller, O_2 activation becomes the sole kinetically-relevant step; turnover rates are proportional to O_2 pressures and independent of CH_4 pressure and no CH_4/CD_4 isotope effects are observed. In this regime, turnover rates become nearly independent of Pt dispersion, because O_2 activation is essentially barrierless on the bare Pt clusters prevalent during CH_4-O_2 reactions in this kinetic regime. In the absence of O_2, alternate weaker oxidants, such as H_2O or CO_2, lead to a final kinetic regime in which C-H bond dissociation on *-* pairs at bare cluster surfaces limit CH_4 conversion rates, rates become first-order in CH_4 and independent of co-reactant and normal kinetic isotope effects are observed. In this case, turnover rates increase with increasing dispersion, because low-coordination Pt atoms stabilize transition states more effective via stronger binding to CH_3 and H fragments.

These findings and their mechanistic interpretations are consistent with all rate and isotopic data and with theoretical estimates of activation barriers and of cluster size effects on transition states. They serve to demonstrate the essential role of the coverage and reactivity of chemisorbed oxygen in determining the type and effectiveness of surface structures in CH_4 oxidation reactions using O_2, H_2O, or CO_2 as oxidants, as well as the diversity of rate dependencies, activation energies and entropies, and cluster size effects that prevail in these reactions. These results also show how theory and experiments can unravel complex surface chemistries for practical reactions and realistic catalysts and conditions and provide through the resulting mechanistic insights specific predictions for the effects of cluster size and surface coordination on turnover rates, the trends and magnitude of which depend sensitively on the nature of the predominant adsorbed intermediates and the kinetically-relevant steps.

2.1. Introduction

The catalytic conversion of methane has been extensively studied because of its practical significance and apparent molecular simplicity.[1] Among chemical conversion routes, indirect conversion of CH_4 to H_2-CO mixtures using CO_2, H_2O, and/or O_2 oxidants remains the preferred route to fuels and chemicals from natural gas.[2,3] Reforming processes use H_2O or CO_2 as co-reactants and their endothermic nature (ΔH^o_{298} =206 kJ mol^{-1} (H_2O), 247 kJ mol^{-1} (CO_2))[3] and thermodynamic constraints lead to complex and costly infrastructure.[4] Reforming reactions with CO_2 and H_2O co-reactants proceed via the same catalytic sequence on all Group VIII metals (Ni,[5] Rh,[6] Pt,[7] Ir,[8,9] Ru,[10] and Pd[11]). The elementary steps involve activation of the first C-H bond in CH_4 as the sole kinetically-relevant step. This step is kinetically-coupled with sequential reactions of CH_x* species with oxygen atoms derived from CO_2 or H_2O in quasi-equilibrated steps, which lead to CO_2/CO and H_2O/H_2 product ratios controlled exclusively by the thermodynamics of water-gas-shift reactions.

Catalytic partial oxidation (CPOX) uses O_2 for the selective conversion of CH_4 to CO and H_2 on metals[12,13] (e.g. Pt, Ru, Ni) and oxides (e.g. La-Ru oxides) at moderate temperatures (1000-1200 K).[14,15] This reaction is nearly thermoneutral (ΔH^o_{298} = -38 kJ mol^{-1}) and avoids the extensive heat transfer and second-law inefficiencies inherent in reforming processes by coupling of exothermic and endothermic reactions at the molecular scale.[16] CPOX maintains the stoichiometry and overall enthalpy achieved in

practice through autothermal reforming,[19] a process in which a flame at the reactor inlet uses O_2 to form H_2O and CO_2 and the heat released is used to convert residual CH_4 via catalytic reforming reactions. The relative rates of CH_4-O_2 and CH_4-H_2O/CO_2 reactions, the role of chemisorbed oxygen and their catalytic consequences have remained inconclusive, even after considerable study. Short adiabatic catalytic reactors operate under extreme gradients in temperature and concentrations can form H_2 and CO with high selectivity, but claims for their direct formation from CH_4-O_2 reactants[17,18] are inconsistent with other studies.[19, 20, 21] These claims are also at odds with the exclusive formation of CO_2 and H_2O from CH_4-O_2 reactants before O_2 depletion[22] and with the reported effects of O_2 and CH_4 pressures on CO_2/CO and H_2O/H_2 ratios in products,[23] which, taken together, indicate that combustion precedes reforming reactions and that partial oxidation does not occur at the molecular scale on catalyst surfaces.

These controversies reflect, at least in part, the thermal coupling of rapid combustion (ΔH^{o}_{298} = -891 kJ mol^{-1}) and reforming reactions, which can occur within length scales of conducive and convective heat transports[24,25] and lead to severe gradients across undiluted catalyst pellets and the reactor. Mechanistic interpretations of rate data are ubiquitously impaired by abrupt changes in oxygen surface coverages and most abundant surface intermediates and by metal-oxide phase transitions caused by concomitant changes in temperature and reactant concentrations within catalyst pellets and along the catalyst bed. Reported rate data under conditions of strict kinetic control and without transport artifacts show that CO_2 and H_2O are the nearly exclusive products of CH_4-O_2 reactions on Pt and Rh clusters at relevant O_2 pressures and that a trace amount of CO is detected only at O_2/CH_4 ratios below 0.04 (873 K).[26] Competitive reactions of ^{12}CO and $^{13}CH_4$ with O_2 on Pt confirmed that any CO that desorbs would form CO_2 at rates much faster than the initial C-H bond activation step required for the formation of CO or CO_2,[26] as also found on Rh[26] and Pd[27] catalysts. CO and H_2 formed only via sequential reforming reactions after O_2 depletion and partial oxidation occurs in practice only by axial thermal coupling of combustion and reforming reactions on Pt, Rh, and Pd catalysts.

Here, we provide a rigorous mechanistic interpretation of CH_4-O_2 reactions on supported Pt clusters, based on kinetic and isotopic data obtained under conditions of strict kinetic control and results from density functional theory (DFT) calculations. We propose a sequence of elementary steps and describe how kinetically-relevant steps and surface intermediates evolve as O_2 and CH_4 concentrations change. The changes in the identities of the kinetically-relevant steps and surface intermediates lead to four distinct kinetic regimes, each with a distinct rate equation; the transitions between these regimes are delineated by the coverage of chemisorbed oxygen atoms (O*) on Pt surfaces. In three of these regimes, C-H bond activation is the kinetically-relevant step, but occurs on different active structures, which evolve from oxygen-oxygen (O*-O*), oxygen-vacancy (O*-*), or vacancy-vacancy (*-*) site pairs as the O* coverage decreases. At very low O_2/CH_4 ratios, C-H bond activation becomes kinetically-irrelevant and O_2 dissociation on bare Pt cluster surfaces becomes the sole kinetically-relevant step. These distinct kinetically-relevant steps lead in turn to different rate equations, effects of Pt cluster size on rate constants, and CH_4/CD_4 kinetic isotope effects. Transitions among the regimes are prescribed rigorously by oxygen chemical potentials at Pt surfaces, which are set by the kinetic coupling of C-H and O=O bond activation steps and shown here to depend on O_2

pressures when O_2 activation steps are equilibrated but on O_2/CH_4 ratios when the O_2 activation steps become irreversible.

2.2. Methods

2.1.1. Catalyst Synthesis. γ–Al_2O_3 (Sasol North America Inc., Lot number C1643, 193 m^2 g^{-1}, 0.57 cm^3 g^{-1} pore volume) and SiO_2 (Davison Chemical, Chromatographic Silica Media, CAS no. 112926-00-8, Lot number 995, 280 m^2 g^{-1}, 0.85 cm^3 g^{-1} pore volume) were treated in flowing dry air (Praxair, 99.99%, 0.8 cm^3 g^{-1} s^{-1}) to 923 K for 3 h (0.083 K s^{-1} ramp). Pt catalysts were prepared by incipient wetness impregnation of γ–Al_2O_3 or SiO_2 with aqueous hexachloroplatinic acid ($H_2PtCl_6 \cdot (H_2O)_6$, Aldrich, CAS #16941-12-1). Samples were treated in ambient air at 383 K for > 8 h and in flowing dry air (Praxair, 99.99%, 0.8 cm^3 $g^{-1}s^{-1}$) to 823 K (0.033 K s^{-1} ramp) for 3 h. Portions of the catalyst were then treated at temperatures between 900 K and 1023 K (0.033 K s^{-1} ramp) in flowing dry air (Praxair, 99.99%, 0.8 cm^3 $g^{-1}s^{-1}$) for 5 h to vary the size of Pt clusters between 1.8 to 8.5 nm and then cooled to ambient temperature. These catalysts were finally treated at 873-923 K in flowing 10% H_2/Ar (Praxair certified standard, 0.083 K s^{-1} ramp, 0.8 cm^3 $g^{-1}s^{-1}$) for 2 h, cooled to ambient temperature in flowing He (Praxair UHP grade), and then in flowing 1% O_2/He (Praxair certified standard, 0.8 cm^3 $g^{-1}s^{-1}$) at ambient temperature for at least 4 h before exposure to ambient air. The mean cluster size in these samples was calculated from volumetric uptakes of chemisorbed hydrogen at 313 K, which were measured using a Quantasorb Chemisorption Analyzer (Quantachrome Corp.), extrapolated to zero pressure by assuming a 1:1 H:Pt_s adsorption stoichiometry, hemispherical clusters, and density of the Pt clusters similar to that of bulk Pt metal (21.5 g cm^{-3}).[28]

2.2.2. Steady-State Catalytic Rate Measurements. CH_4 conversion turnover rates and selectivities were measured in a tubular flow reactor (quartz; 8.1 mm inner diameter) using catalyst particles diluted with silicon dioxide granules to prevent temperature gradients. Reaction temperatures (810-900 K) were measured with a K-type thermocouple held within a concentric quartz thermowell. The catalyst was mixed with SiO_2 (Davison Chemical, Chromatographic Silica Media, CAS no. 112926-00-8, 280 m^2 g^{-1}; treated in flowing dry air; Praxair, 99.99%, 0.8 cm^3 g^{-1} s^{-1}, 0.083 K s^{-1} ramp for 5 h at 1123 K), shown to be inert at all reaction conditions, to achieve a 200 intraparticle diluent-to-catalyst ratio (λ). The physical mixtures were pelleted and sieved to retain agglomerates with 0.1-0.25 mm diameter. These pellets were further diluted with silicon dioxide granules (Fluka, acid purified, product number 84880; 0.1-0.25 mm diameter) to give a bed diluent-to-catalyst (supported Pt on Al_2O_3 or SiO_2) weight ratio (χ) of 4700. These intra and interparticle dilution ratios were shown to avoid temperature and concentration gradients within catalyst pellets or bed and to ensure that rate and selectivity data reflect chemical reaction dynamics under conditions of strict kinetic control.[26]

Catalyst mixtures (0.15 mg Pt/Al_2O_3 or Pt/SiO_2 and diluents) were treated *in-situ* in flowing H_2 (Praxair UHP grade, 0.083 K s^{-1} ramp, 0.5 cm^3 s^{-1}) at reaction temperatures (813-898 K) for 1 h and then in He (Praxair UHP grade, 2.1 cm^3 s^{-1}) for 0.167 h before rate measurements. Mixed gases (Praxair certified standard, 25% CH_4/Ar, 5% O_2/He, 50% CO_2/N_2, and 1% CO/He) and O_2 (Praxair UHP grade) were used as reactants with

He (Praxair UHP grade) as an inert diluent. Flow rates were metered with electronic flow controllers (Porter, type 201). The effect of H_2O on the reaction rates was probed by introducing distilled and deionized water using a gas tight syringe (Hamilton # 1005, 5000 μL) and a syringe micropump (Cole Parmer, Model 60061) into the reactant stream in an evaporation volume held at 423 K. CO_2, CH_4, and CO concentrations were measured by gas chromatography (Agilent 3000A) equipped with Poraplot Q and Molecular Sieve 5A columns connected to thermal conductivity detectors. CH_4 conversion rates are reported based on CO and CO_2 concentrations in the effluent stream and confirmed from residual CH_4 concentrations for conversions above 20 %.

CD_4-O_2, CH_4-CD_4-O_2, CH_4-$^{16}O_2$-$^{18}O_2$, and $^{16}O_2$-$^{18}O_2$ reactant mixtures were prepared with CD_4, (Isotec, chemical purity > 99.0%) or 2% $^{18}O_2$/He mixture (Icon, 98% isotopic purity) in addition to the reactant gases. Kinetic isotope effects and exchange rate measurements were carried out using methods similar to those described above. The concentrations of methane, CO_2, and O_2 isotopomers (CH_xD_y (x+y=4), $^{13}C^{16}O_2$, $^{12}C^{16}O_2$, $^{12}C^{16}O^{18}O$, $^{12}C^{18}O_2$, $^{18}O_2$, $^{16}O_2$, $^{16}O^{18}O$) were measured with a mass selective detector (Agilent 5973). Catalysts were treated in CH_4-$^{16}O_2$-$^{18}O_2$ mixtures before the oxygen exchange rate measurements in $^{16}O_2$-$^{18}O_2$ and CH_4-$^{16}O_2$-$^{18}O_2$ mixtures. During the pre-treatment, oxygen atoms in $C^{16}O_2$, $C^{18}O_2$, and $C^{16}O^{18}O$ isotopomers formed from CH_4-$^{16}O_2$-$^{18}O_2$ reactions also exchanged with the lattice oxygen (O^*_L) in Al_2O_3 support. The rapid exchange between CO_2 isotopomers and O^*_L in Al_2O_3 causes the $^{18}O^*_L$ to $^{16}O^*_L$ ratio on the Al_2O_3 support to become identical to the ratios of $^{18}O_2(g)/^{16}O_2(g)$ and the $^{18}O^*/^{16}O^*$ on Pt surfaces. The oxygen exchange rate measurements were carried out after the isotopic contents of Al_2O_3 support and Pt clusters became identical, as confirmed by the distribution of CO_2 isotopomers in statistical ratios during the treatment in CH_4-$^{16}O_2$-$^{18}O_2$ mixture. H_2O, D_2O, and HDO molecules formed in CH_4-CD_4-O_2 reactions were removed from the effluent stream with anhydrous $CaSO_4$ (Drierite) before mass spectrometric analysis. Pt/SiO_2 was used instead of Pt/Al_2O_3 samples to determine the CH_4-CD_4 cross exchange rates on Pt because Al_2O_3 supports also catalyzed the CH_4-CD_4 cross exchange steps in CH_4-CD_4-O_2 mixtures.

2.2.3. Computational Methods. A number of studies previously reported in the literature have examined the adsorption and activation of methane over different single crystal surfaces at low coverage conditions.[29-42] The results from these studies indicate that the C-H bond of methane is activated via metal atom insertion into the C-H bond in an oxidative addition process that results in the formation of a three-centered transition state involving the metal, carbon and hydrogen atoms. While these studies offer important insights into the activation of the C-H bond, there are no published reports, however, that examine the influence of oxygen and the effects of cluster size. Herein we carry out non-local gradient-corrected periodic plane wave density functional theory (DFT) calculations as implemented in the Vienna Ab-initio Simulations Package (VASP)[43,44,45] to determine the adsorption energies for oxygen and methane as well as the activation barriers and reaction energies for CH_4 and oxygen over model 1.8 nm cubo-octahedral Pt clusters. All of the calculations discussed herein were carried out using the Perdew Wang 91 (PW91)[46] form of the generalized gradient approximation (GGA) to determine the corrections to the exchange and correlation energies. The wavefunctions used to describe the system were represented by a periodic expansion of plane-wave with a basis set cutoff energy of 38,214 kJ mol^{-1} (396 eV) where the interactions between core

and valence electrons were described by Vanderbilt ultra-soft pseudopotentials (US-PP)[47]. The electronic energies for all structures were converged to within 9.65 $\times 10^{-3}$ kJ mol^{-1} (1×10^{-4} eV). The geometric structures were all optimized until the forces on each atom were within 48.25 kJ $(mol\text{-}nm)^{-1}$ (0.5 eV nm^{-1}).

The model 1.8 nm Pt cluster used to carry out the simulations consisted of 201 Pt atoms arranged in a cubo-octohedral structure containing eight (111) and six (100) edge-sharing facets (Scheme 1), as described previously[48] and denoted herein as Pt_{201}. The cluster contains four types of Pt atoms (sites 1-4) depending on their coordination numbers and five distinct types of O* adsorption sites (sites I-V) on the (111) and (100) facets. The cluster was placed at the center of a $3\times3\times3$ nm^3 unit cell with a minimum distance of 0.8 nm from the edges of the cell, the details of which are provided elsewhere.[26] A (1×1×1) Monkhorst-Pack k-point mesh[49] grid was used to sample the first Brillouin zone and calculate the electronic energies of the Pt_{201} systems. These energies were used to approximate the enthalpies for all systems considered here. The rigorous calculation of enthalpies would require accurate second derivative calculations to determine energy changes with respect to all nuclear degrees of freedom to determine vibrational frequencies and zero-point energies for all reactant, transition, intermediate, and product states and accurate assessments of the rotational, and translational energies. Such calculations would require unrealistic supercomputing CPU resources and would only influence the calculated reaction energies by less than 15 kJ mol^{-1}.

The oxygen saturation coverage (1 ML O*) was defined based on an O^*/O^*_{max} stoichiometry of unity. The O* binding strength was defined as the absolute value of reaction energy required to remove an O* atom on O* covered Pt clusters:

$$n\ O^*/Pt_{201} \rightarrow (n-1)\ O^*/Pt_{201} + O \qquad (1)$$

where the n O^*/Pt_{201} and (n-1) O^*/Pt_{201} are in their optimized structures.

All activation barriers were calculated using the climbing image-nudged elastic band (CI-NEB) methods to locate transition states.[50,51,52] This method first minimizes the forces normal to the reaction trajectory on all of the atoms in evolving structures initially chosen at equally spaced points along the reaction coordinate to within 48.3 kJ $(mol\text{-}nm)^{-1}$ (0.5 eV nm^{-1}). The climbing algorithm is then used to maximize the energy of the climbing image along the reaction coordinate while minimizing the energy in all other directions. The transition states reported here were converged to structures for which the forces on all of the atoms were <10 kJ $(mol\ nm)^{-1}$ (0.1 eV nm^{-1}).

2.3. Results and Discussion

2.3.1. Kinetic Dependence and Selectivity of CH_4-O_2 Reactions. Rate data were measured at intraparticle (λ) and bed (χ) dilution ratios ($\lambda = 200$; $\chi = 4700$) larger than those required to avoid temperature and concentration gradients;[26] measured rates and selectivities remained unchanged upon further dilution.[26] Turnover rates were independent of the ratio of void volume to catalyst mass in reactors, consistent with the absence of homogeneous reactions. Thus, all reported reaction rates reflect the intrinsic dynamics of chemical events at catalytic surfaces unaffected by transport artifacts or gas phase reactions.

Figures 1 and 2 show CH_4 turnover rates (per surface Pt atom; 873 K, 0.2 % wt. Pt/Al_2O_3, 8.5 nm mean cluster diameter) as a function of CH_4 (0.4-4.9 kPa) and O_2 (0-

23.0 kPa) pressures, respectively. Four kinetic regimes (labeled 1-4 in the figures) are evident from these data; each regime exhibits different rate equations and CH_4/CD_4 kinetic isotope effects (Sections 3.2-3.4). CO was not detected in regimes 1 or 2 and formed only in trace amounts ($CO/CO_2 < 0.005$) at the lowest O_2 pressures ($O_2/CH_4 < 0.08$) in regime 3. These data show that CH_4 reacts predominantly via combustion reactions at all relevant O_2/CH_4 ratios and that CO selectivities become detectable only after O_2 depletion or when H_2O or CO_2 are used as co-reactants (regime 4);[26] in the latter case, the effluent CO/CO_2 ratios correspond to those expected from water-gas-shift equilibrium.[7]

CH_4 turnover rates at 873 K depend linearly on CH_4 pressure but are not influenced by O_2 pressure for O_2/CH_4 ratios between 2.0 and 4.6 (regime 1, labeled **1** in Fig. 1a), which are typical of catalytic combustion practice. At lower O_2/CH_4 ratios ($0.08 < O_2/CH_4 < 2$), turnover rates show a stronger than linear dependence on CH_4 pressure and increase with decreasing O_2 pressure (regime 2, labeled **2** in Fig. 1b) in a manner accurately described by the rate equation:

$$r_2 = k_{eff,2} \frac{(CH_4)^2}{(O_2)} \qquad (2)$$

where $k_{eff,2}$ denotes an apparent rate constant. For O_2/CH_4 ratios below 0.08 (regime 3, labeled **3** in Fig. 1b), turnover rates become independent of CH_4 pressure and proportional to O_2 pressure. These kinetic regimes are also evident from the effects of O_2 pressure on turnover rates at each CH_4 pressure (Fig. 2) and from the measured effects of increasing residence time,[26] which causes a concomitant decrease in O_2/CH_4 ratios along the catalyst bed.

H_2O (5 kPa) or CO_2 (5 kPa) in CH_4-O_2 (or $^{13}CH_4$-O_2) reactants did not influence turnover rates (Figs. 1a and 2) for any of these kinetic regimes, even when O_2 was excluded from the stream and H_2O or CO_2 were the only co-reactants (regime 4, labeled **4** in Fig. 1a).[7] Thus, we conclude that H_2O and CO_2 do not modify the surface coverages of any reactive intermediates during CH_4 reactions with O_2, H_2O, or CO_2 on supported Pt clusters. They also do not catalyze the reforming reactions at detectable rates when O_2 is present.

These effects of CH_4 and O_2 pressures on rates (Figs. 1 and 2) are presented as pseudo first-order rate constants ($r_{CH_4}(CH_4)^{-1}$) as a function of O_2/CH_4 ratios in Figure 3. O_2/CH_4 ratios above 2 (regime 1) lead to $r_{CH_4}(CH_4)^{-1}$ values that do not depend on O_2 pressure and rigorously represent first-order rate constants and reactive collision probabilities. For O_2/CH_4 ratios between 0.08 and 2 (regime 2), $r_{CH_4}(CH_4)^{-1}$ become inversely proportional to O_2/CH_4 ratios. At lower O_2/CH_4 ratios (< 0.08, regime 3), $r_{CH_4}(CH_4)^{-1}$ become proportional to O_2/CH_4 ratios, indicating that turnover rates depend linearly on O_2 pressures. These data show that $r_{CH_4}(CH_4)^{-1}$ values are a single-valued function of O_2/CH_4 ratios (Fig. 3) and that these ratios determine O* coverages, the involvement and reactivity of chemisorbed oxygen atoms, and the identity of kinetically-relevant steps.

The sequence of elementary steps shown in Scheme 2 is consistent with the rate equations measured in each of the four kinetic regimes (Table 1) and reflect most

abundant surface intermediates and kinetically-relevant steps that depend only on O* coverages, which are set, in turn, by either the O_2 pressures (regime 1) or the O_2/CH_4 reactant ratios (regimes 2 and 3) (to be discussed in Sections 3.2-3.4). This sequence includes elementary steps that form CO_2, H_2O, CO, and H_2; the latter two species form via desorption of their respective adsorbed precursors (CO* and H*) before subsequent oxidation by O*. C-H bonds in CH_4 are activated using chemisorbed oxygen-oxygen (O*-O*), oxygen-vacancy (O*-*), or vacancy-vacancy (*-*) site pairs (Step 1.1-1.3, Scheme 2) and O=O bonds are activated on *-* site pairs in kinetically-relevant steps that give rate equations and activation barriers and entropies consistent with rate data.

In what follows, we show that these mechanism-based rate equations and kinetic parameters accurately describe all rate data (Fig. 1-3) and that assumptions about the kinetic relevance and reversibility of C-H and O=O activation steps are consistent with CH_4/CD_4 kinetic isotope effects (KIE) and isotopic exchange reactions between CH_4 and CD_4 and between $^{16}O_2$ and $^{18}O_2$ during CH_4-O_2 catalysis. Measured activation barriers and reaction energies for kinetically-relevant steps are also in agreement with density functional theory estimates as O* coverages vary on Pt clusters containing 201 Pt atoms (Pt_{201}). We report these results and simulations for each kinetic regime in the order of decreasing O* coverages, starting with the kinetic, isotopic, and the theoretical results in regime 1 ($O_2/CH_2 > 2$), for which the C-H bond activation on O*-O* site pairs present on saturated Pt surfaces is the sole kinetically-relevant step.

2.3.2. Kinetically-Relevant C-H Bond Activation on Pt Surfaces Saturated with Chemisorbed Oxygen. CH_4 conversion turnover rates in regimes 1 ($O_2/CH_4 > 2$) are proportional to CH_4 pressure and independent of O_2 pressure (Fig. 1). These results, together with CH_4/CD_4 KIE values larger than unity and independent of O_2 pressure (KIE = 1.66; 873 K; $O_2/CH_4 > 2$), suggest that kinetically-relevant C-H bond activation steps occur on surfaces containing species at coverages and reactivities that do not depend on O_2 pressure. Rates for CH_4 reactions with H_2O or CO_2 (regime 4) also depend similarly on the CH_4 and co-reactant pressures.[7] CH_4/CD_4 kinetic isotope effects in CH_4-H_2O/CO_2 mixtures are also larger than unity and independent of co-reactant (KIE, 1.69 (H_2O) and 1.77(CO_2), 873 K, Table 1) on Pt,[7] as also found on other Group VIII metals (1.66 (Ni),[5] 1.54 (Rh),[6] 1.81 (Ir),[8] and 1.40 (Ru)[10] for H_2O reforming, 873 K). Our previous results have shown that the CH_4-H_2O/CO_2 reactions proceed via C-H bond cleavage assisted by metal atom site pairs (*-*) on essentially bare cluster surfaces (Step 1.3, Scheme 2). Activation energies and pre-exponential factors for CH_4-H_2O/CO_2 (regime 4) and CH_4-O_2 (regime 1) reactions, however, differ significantly, as shown in Figure 4 and Table 1. These differences led us to conclude that kinetically-relevant C-H bond activation steps in CH_4-O_2 mixtures (regime 1) occur on surfaces different from those in CH_4-H_2O/CO_2 mixtures (regime 4), where the surfaces of Pt clusters are saturated with chemisorbed oxygen atoms (O*). At O* saturation, kinetically-relevant C-H activation steps are assisted by O* atoms, the number of which is independent of O_2 pressure, to form CH_3O* and OH* (Step 1.1, Scheme 2). CH_4-CD_4 cross exchange rates measured during chemical reactions of CH_4-CD_4-O_2 mixtures on 0.2 % wt. Pt/SiO_2 at 920 K[53] gave CH_3O* and *OD (or CD_3O* and *OH) recombination rates (reverse of Step 1.1, Scheme 2) ~ 50 times smaller than CH_4 chemical conversion rates, consistent with irreversible C-H bond activation steps. The coverages of species derived from H_2O and CO_2 (OH* and CO*) are

small, as evident from the lack of kinetic effects of H_2O and CO_2 pressures (0-5 kPa H_2O or CO_2; Figs. 1a and 2).

These data and mechanistic inferences indicate that CH_4 conversion rates in regime 1 (r_1) are accurately described by a rate equation (derived in Supporting Information):

$$r_1 = k_{1[O^*\text{-}O^*]}(CH_4)^1(O_2)^0 \quad (3)$$

in which $k_{1[O^*\text{-}O^*]}$ represents the rate constant for C-H bond dissociation elementary steps on O*-O* site pairs (Step 1.1, Scheme 2). Equation 3 remains the same whether O_2 dissociation steps (Steps 2.1 and 2.2) are irreversible or quasi-equilibrated because Pt surfaces are saturated with O* (derived in Supporting Information). Oxygen vacancies (*) can participate in C-H bond dissociation, but they are minority species and do not contribute to measured CH_4-O_2 reaction rates in regime 1; the kinetically-relevant involvement of vacancies would cause turnover rates to increase with decreasing O_2 pressure, in contradiction with the lack of O_2 pressure effects in regime 1.

O* coverages during CH_4-O_2 reactions can be measured by comparing $^{18}O_2$-$^{16}O_2$ isotopic exchange rates in the presence and absence of CH_4 reactants. Without CH_4, chemisorbed O* atoms are in equilibrium with O_2(g) and O* coverages depend only on O_2 pressure. The (O*)/(*) ratio at chemical equilibrium, $[(O^*)/(*)]_{eq}$, is given by the Langmuir adsorption equation:

$$\left(\frac{(O^*)}{(*)}\right)_{eq} = \sqrt{K_{2a}K_{2b}(O_2)} \quad (4)$$

in which K_{2a} and K_{2b} are the equilibrium constants for the adsorption of O_2 molecules (k_{2af}/k_{2ar}; Step 2.1, Scheme 2) and the dissociation of O_2* (k_{2bf}/k_{2br}; Step 2.2, Scheme 2), respectively. O* coverages during steady-state CH_4-O_2 reactions may become lower than equilibrium, because O* atoms can be removed via reactions with CH_4 faster than O* recombination (reverse of Step 2.2, Scheme 2). Irreversible C-H bond dissociation on O*-O* pairs (Step 1.1, Scheme 2) and reversible O_2 dissociation (Steps 2.1 and 2.2, Scheme 2) in regime 1 lead to steady-state (O*)/(*) ratios given by:

$$\left(\frac{(O^*)}{(*)}\right)_{ss,1} = \sqrt{\frac{K_{2a}k_{2bf}(O_2)}{2k_{1[O^*-O^*]}(CH_4)+k_{2br}}} = \sqrt{K_{2a}K_{2b}(O_2)_v} \quad (5)$$

in which the subscripts "ss,1" denote steady-state and regime 1. This equation defines $(O_2)_v$ as a virtual O_2 pressure[54,55] that reflects, by analogy with Eq. 4, the O_2 pressure that would give the prevalent O* coverage ($(O^*)_{ss}$) if O_2 adsorption-desorption steps were equilibrated. This virtual pressure acts as a rigorous surrogate for the oxygen chemical potential at surfaces during the catalytic reaction.[56] The concept of virtual pressure and its role in surface reactions[54,55] have been demonstrated for many catalytic reactions; NH_3 decomposition[57] and alkane dehydrogenation[58] catalysis are specific examples. The values of $(O_2)_v$ and of $[(O^*)/(*)]_{ss}$ ratios depend on the rate constants for O_2* dissociation (k_{2bf}), O* recombination (k_{2br}), and C-H bond dissociation ($k_{1[O^*\text{-}O^*]}$), on the equilibrium constant for molecular O_2 adsorption (K_{2a}), and on the prevalent O_2 and CH_4 pressures during catalysis, as shown in Equation 5. Equations 4 and 5 become identical when $k_{2br} >> 2k_{1[O^*-O^*]}(CH_4)$, an inequality stating that O* recombination rates (Step 2.2, Scheme 2) are much larger than for C-H bond activation (Step 1.1, Scheme 2). In such

instances, O_2 adsorption-desorption steps are quasi-equilibrated during CH_4-O_2 reactions, $(O_2)_v$ and $O_2(g)$ become identical, and the oxygen chemical potential at surfaces equals that in the contacting O_2 gas phase. When O_2 dissociation steps are irreversible ($k_{2br} << 2\,k_{1[O^*-O^*]}(CH_4)$), O* is predominantly removed via reactions with CH_4 instead of recombination and $(O_2)_v$ values (Eq. 5) become smaller than the O_2 pressures and $[(O^*)/(^*)]_{ss}$ ratios become smaller than at conditions of adsorption-desorption equilibrium (Eq. 4).

These considerations indicate that the ratio of isotopic $^{18}O_2$-$^{16}O_2$ exchange rates with CH_4-$^{18}O_2$-$^{16}O_2$ and $^{18}O_2$-$^{16}O_2$ mixtures reflect the reversibility of O_2 dissociation steps and the $(O_2)_v$ values during catalysis. Steady-state $^{16}O_2$-$^{18}O_2$ isotopic exchange rates (at 0.15-1.85 kPa O_2; 873 K) were measured in $^{18}O_2$-$^{16}O_2$ and CH_4-$^{18}O_2$-$^{16}O_2$ mixtures on 0.2 % wt. Pt/Al_2O_3 samples with 1.8 or 8.5 nm Pt clusters. CH_4-O_2 chemical conversion rates (Fig. 1a) are independent of O_2 pressure at these O_2 pressures (regime 1), consistent with Pt surfaces saturated with O* during catalysis, as must also be the case at chemical equilibrium during $^{18}O_2$-$^{16}O_2$ reactions at the same O_2 pressure. $^{16}O_2$-$^{18}O_2$ exchange rates at chemical equilibrium ($r_{ex,eq}$) are proportional to $(O_2)^{0.5}$ (Fig. 5) on both Pt catalysts, a kinetic dependence consistent with $^{18}O_2$-$^{16}O_2$ exchange routes that form $^xO^yO$ (x and y are used herein to differentiate 16 and 18 labeled O) via concerted steps between adsorbed $^xO_2$* (x = 16 or 18) and vicinal ^yO* (y=18 or 16) (Step 11, Scheme 2). This mechanistic proposal also accounts for the molecular $^xO_2$ adsorption (as $^xO_2$*) followed by migration of one of the ^xO atoms on Pt surfaces nearly saturated with ^yO*, which may desorb as $^xO^yO$ before dissociation (to be discussed in Sec. 3.3). It also accounts for the preferential initial formation of $^{16}O^{18}O(g)$ isotopologues when Pt clusters with chemisorbed ^{16}O* monolayers are exposed to $^{18}O_2$ (g) ($^{18}O_2/^{16}O^{18}O < 0.22$),[59] in contrast with the expected initial formation of $^{16}O_2$ (g) via the recombinative desorption of two O* atoms. The rate of $^{16}O^{18}O$ formation from equimolar $^{16}O_2$-$^{18}O_2$ reactant mixtures (derived in Supporting Information) is given by:

$$r_{ex,eq} = \frac{2k_{11f}K_{2a}^{1.5}K_{2b}^{0.5}(O_2)^{1.5}}{\left(1+2\sqrt{K_{2a}K_{2b}(O_2)}+2K_{2a}(O_2)\right)^2} \qquad (6a)$$

$$\uparrow \quad * \qquad \uparrow \quad O* \qquad \uparrow \quad O_2*$$

Each denominator term represents the coverage of the denoted intermediate relative to unoccupied surface atoms. Equation 6a gives the $(O_2)^{0.5}$ effects on exchange rates (Fig. 5) when O* is the MASI:

$$r_{ex,eq,O^*} = \frac{k_{11f}}{2}\left(\frac{K_{2a}}{K_{2b}}\right)^{0.5}(O_2)^{0.5} \qquad (6b)$$

No other combination of elementary steps was found to describe the measured O_2 effects on exchange rates for O*-saturated clusters and the initial formation of $^{16}O^{18}O$ species from $^{18}O_2$ (g)-^{16}O* reactions.

$^{16}O_2$-$^{18}O_2$ exchange rates (Step 11, Scheme 2) are proportional to ^xO* (x = 16 or 18) and $^yO_2$* (y = 18 or 16) coverages, where $^yO_2$* species are in equilibrium with $O_2(g)$ (Step 2.1, Scheme 2). The ratio of isotopic exchange rates for CH_4-$^{18}O_2$-$^{16}O_2$ ($r_{ex,ss}$) and $^{18}O_2$-$^{16}O_2$ ($r_{ex,eq}$) mixtures (denoted as χ) can then be expressed in terms of O* and *; it

reflects the coverages of O* during steady-state catalysis $(O^*)_{ss}$ relative to those at chemical equilibrium $(O^*)_{eq}$:

$$\chi = \left(\frac{r_{ex,ss}}{r_{ex,eq}}\right) = \frac{k_{11f}\left(({}^aO_2{}^*)({}^bO^*)\right)_{ss}}{k_{11f}\left(({}^aO_2{}^*)({}^bO^*)\right)_{eq}} = \frac{O_2\left((O^*)(^*)\right)_{ss}}{O_2\left((O^*)(^*)\right)_{eq}} = \frac{(O^*)_{ss}\left(1-(O^*)_{ss}\right)}{(O^*)_{eq}\left(1-(O^*)_{eq}\right)} \quad (7)$$

where O* denotes the combined surface coverages of both oxygen isotopes ($^{16}O^*$ and $^{18}O^*$). Isotopic exchange rates during CH_4-O_2 reactions ($r_{ex,ss}$) are also given by Equation 6a, except that $(O_2)_v$ replaces the (O_2) terms. Taken together with Equation 5, Equation 7 (for χ in regime 1; χ_1) can be written in terms of CH_4 pressure and the relevant kinetic ($k_{1[O^*-O^*]}$, k_{2br}, k_{2bf}) and thermodynamic (K_{2b}) constants defined in Scheme 2:

$$\chi_1 = \left(\frac{r_{ex,ss,1}}{r_{ex,eq}}\right) = \frac{(O^*)_{ss,1}(1-(O^*)_{ss,1})}{(O^*)_{eq}(1-(O^*)_{eq})} = \sqrt{\frac{(O_2)_v}{(O_2)}} = \sqrt{\frac{k_{2bf}}{\left(2k_{1[O^*-O^*]}(CH_4)+k_{2br}\right)K_{2b}}} \quad (8)$$

$^{16}O^{18}O$ formation rates were measured during CH_4-$^{16}O_2$-$^{18}O_2$ reactions in regime 1 ($O_2/CH_4 > 0.3$; 1.8 nm Pt clusters; $O_2/CH_4 > 2$ for 8.5 nm clusters) at 873 K. These rates, shown as their corresponding rate constants ($0.5k_{11f}\left(K_{2a}K_{2b}\right)^{0.5}$; Eq. 6b) in Figure 5, are similar to those measured at chemical equilibrium with CH_4-free $^{18}O_2$-$^{16}O_2$ reactants. Thus, χ_1 (Eq. 8) is essentially unity throughout regime 1 and $(O_2)_v$ and O_2 pressures are therefore identical. These results confirm that O_2 dissociation steps are quasi-equilibrated during CH_4-O_2 reaction ($2k_{1[O^*-O^*]}(CH_4) << k_{2br}$ in Eqs. 5 and 8) and that CH_4 reactions with O* are too slow to perturb equilibrium O* coverages during CH_4-O_2 catalysis in regime 1.

$(O_2)_v$ (also the prevalent O_2 pressure in regime 1), acts as a rigorous surrogate for the oxygen chemical potential at Pt cluster surfaces and determines both O* coverages and the thermodynamic tendency of such clusters to form bulk oxides during CH_4-O_2 catalysis. Thermodynamic data for Pt, Pt_3O_4, and PtO_2 bulk structures[60] give the O_2 pressures required for Pt-Pt_3O_4 and Pt_3O_4-PtO_2 phase transitions. Assuming thermodynamic properties of the larger Pt clusters (8.5 nm) used here resemble those of large Pt crystallites, extrapolation of the Pt-Pt_3O_4 phase diagram[60] to 873 K indicates that these Pt clusters retain a metallic bulk at all O_2 pressures below ~800 kPa and at all conditions used in this study (< 23 kPa). The size of the Pt cluster may affect its thermodynamic tendency to oxidize. Surfaces of small clusters (< 3 nm) contain a larger fraction of atoms residing at the corner and edge sites. These atoms, because of their lower degrees of coordinative saturation, bind O* more strongly. The stronger binding of O* and larger O*-to-overall Pt atomic ratios inherent in these small clusters may cause them to exhibit oxide-like properties well below the required $(O_2)_v$ for the oxidation of bulk Pt metals. The bulk oxidation is expected to increase the CH_4 conversion rates markedly, as has been established on Pd,[61] because exposed Pd^{2+} atoms on PdO surfaces interact with CH_3 groups at the transition state and, in turn, lower the C-H bond activation barriers.[62] These catalytic consequences of phase transition were, however, not detected on Pt clusters (1.8 nm-8.5 nm) under the conditions of our study ($0 < O_2/CH_4 < 10$, 873 K). We conclude that the bulk of Pt clusters (1.8 to 8.5 nm average cluster size) remains in metallic state throughout our rate measurements.

These rate data and mechanistic interpretations indicate that CH_4 reaction rates in regime 1 are limited by C-H bond activation on O*-saturated surfaces, in a step that uses

O*-O* site pairs to form CH_3O* and OH* (Step 1.1, Scheme 2). The barriers and reaction energies for this step can be estimated for different O*-O* site pairs on (111) and (100) facets of 1.8 nm Pt_{201} clusters saturated with O* atoms (refers to Scheme 1 for the placements of O* atoms at sites I-V and the structure of the Pt_{201} cluster) using density functional theory. Chemisorbed O* atoms preferentially reside at five distinct adsorption sites on Pt_{201} clusters:[26] three-fold fcc sites (types II, IV, and V) on (111) facets and bridge sites (types I and III) on (100) facets. The three-fold fcc and bridge sites are also found to be the most stable O* adsorption sites on single crystal Pt(111) and Pt(100) surfaces,[63,64,65] respectively. O* binding energies at sites I-V on bare Pt_{201} clusters range from 372 kJ mol^{-1} to 410 kJ mol^{-1} (Table 2), depending on the location of the O* atoms (fcc or bridge) and the coordination of the Pt atoms to which the O* atom is bound.[26] O* saturation on Pt_{201} clusters is achieved by the occupation of every three-fold fcc site on (111) facets and every two-fold bridge site on (100) facets to give a 1:1 O*-to-Pt surface atomic stoichiometry (O^*/Pt_s). At saturation, binding energies for O* at each position are much smaller than on bare clusters because of lateral repulsion between coadsorbed oxygen as summarized in Table 2. One exception occurs at site II where Pt-Pt distances at these coordinatively unsaturated corner sites expand from 0.270 nm to 0.315 nm with increasing O* coverages. The neighboring oxygen atoms that bind to the same Pt site are located on the adjacent facets; such configurations remove through space repulsive interactions between the O* atoms. These combined effects lead to stronger Pt-O interactions at O* saturation (426 kJ mol^{-1} vs. 391 kJ mol^{-1} for O* saturated and uncovered Pt_{201} clusters, respectively). The 1:1 O^*/Pt_s stoichiometry for Pt_{201} clusters is much larger than at O* saturation on Pt(111) single crystals (0.5-0.73 O* ML[66,67] depending on oxidant). Larger O* coverages on Pt(111) lead to unfavorable adsorption of oxygen, where the differential heat of O* adsorption is $>$ 0 kJ mol^{-1} on 0.89 O* ML Pt(111) surfaces in contrast to the exothermic differential O* adsorption energies (-37 kJ mol^{-1}) found on the Pt_{201} clusters. The lower O* saturation coverages on the (111) surface reflect, at least in part, the lateral rigidity of extended surfaces, which preserves aligned structures that maximize lateral repulsion and prevent the attainments of higher coverages. In contrast, Pt clusters form surface structures with O^*/Pt_s ratios near unity as found experimentally even at low O_2 pressures,[68] because the small dimensions of exposed low-index planes allow lateral flexibility in O* monolayers and relieve to some extent repulsive interactions, while also providing more coordinatively unsaturated surface atoms that form stronger O*-Pt bonds. Cubo-octahedral clusters also expand radially as O* coverages increase, thus increasing O*-O* distances.

Next, we probe the details of C-H bond activation steps on O*-O* site pairs and the roles of O* binding strength on their reactivity for H-abstraction (Step 1.1, Scheme 2) on Pt_{201} clusters saturated with O* (O^*/Pt_s=1). Irrespective of the location and binding energy of O*, these species activate C-H bonds via hydrogen abstraction paths similar to that shown in Figure 6 for O* atoms at three-fold terrace sites (site V, Scheme 1) in (111) facet. This step has a reaction energy of -54 kJ (mol CH_4)$^{-1}$ and proceeds via H-abstraction from CH_4 by one of the O* atoms in the O*-O* site pair, in a step mediated by a late transition state in which the C-H bond is nearly cleaved (0.170 nm vs. 0.109 nm in CH_4(g)) and the O-H bond is almost formed (0.105 nm vs. 0.099 nm in OH* product). The O* atom involved in H-abstraction moves from its stable three-fold fcc site to a less stable and more reactive bridge site along the reaction coordinate in a step that is

significantly endothermic ($\Delta E_{O^*promotion}$ = 44 kJ mol^{-1}). The CH_3 formed in the H-abstraction step exhibits sp^2 hybridization and free radical character at the transition state and coordinates weakly to the H-atom in the O-H species that concurrently forms. The distance between the CH_3• fragment and the other O* in the O*-O* site pair (0.265 nm) indicates that CH_3• interacts very weakly with the O* and OH* species at the transition state.

C-H activation barriers on different O*-O* site pairs on Pt_{201} clusters range from 111 to 175 kJ mol^{-1} (Table 2) and depend on the average coordination numbers of the metal atoms to which the O* atoms are bound and the number of O* neighbors as well as the specific locations of the O* neighbors that surround this site. These sites can be grouped into three types: a) bridging O* sites (I and III) with barriers of 111-112 kJ mol^{-1}, b) corner and edge O* sites (II and IV) with barriers of 170-175 kJ mol^{-1}, and c) terrace sites (V) with barriers of 149 kJ mol^{-1}. The structural details of the reactant, transition, and product states for each of these site pairs are shown in Supplementary Information (Table S-1). O* atoms at bridge sites on 100 facets (I and III) gave the lowest C-H bond activation barriers because they lie closest to the active bridge-bound O* present at all H-abstraction transition states; as a result they require the smallest energies for promotion to their active locations ($\Delta E_{O^*promotion}$ = 9-13 kJ mol^{-1}). O* atoms at corner and edge sites on (111) facets (site II or IV) are least reactive because their binding to low-coordination Pt atoms at three-fold sites makes their promotion to active location very endothermic (66-99 kJ mol^{-1}). O* atoms at (111) terrace sites (V) are more weakly-held than those at corner and bridge sites (II and IV) because of the higher coordination of the Pt atoms (average coordination number <CN> = 9) than at three-fold edge (<CN>=8.33) and corner (<CN>=7.33) sites. These O* atoms (V) are also less strongly bound than at (100) sites with lower coordination number (<CN> of 6.5 for site I and 7.33 for site III). The more weakly held O* at (111) terrace sites (V) are more basic and show greater proton affinity, but the energy required to promote them to the active bridge location ($\Delta E_{O^*promotion}$ = 44 kJ mol^{-1}) is 31-35 kJ mol^{-1} larger than for O* at bridge sites on (100) facets, but 23-55 kJ mol^{-1} smaller than at corner and edge sites. As a result, C-H activation barriers on these O* atoms (V; 149 kJ mol^{-1}) lie between the barriers on edge and corner sites (170-175 kJ mol^{-1}) and on (100) facets (111-112 kJ mol^{-1}). These C-H activation barriers can be rigorously interpreted using Born-Haber thermochemical cycles that account for the properties of O* and Pt atoms and also for the local O* interactions, as will be discussed in detail in later studies.

O* at (111) facets of Pt_{201} clusters (site V) are the most abundant species on O*-saturated surfaces of Pt clusters with diameters larger than 5 nm (> 70 % assuming cubo-octahedral geometries[48]). Indeed, C-H activation barriers at such sites (149 kJ mol^{-1}) are very similar to the barriers measured on 8.5 nm Pt clusters (155 kJ mol^{-1}; Table 1). The low coordinate Pt atoms associated with the more closed-packed corner and edge sites (sites II and IV) become more abundant with decreasing cluster size (70 % of exposed atoms in a 1.5 nm cubo-octahedral cluster reside at corner and edge sites[48]) and activation barriers will increase with decreasing cluster size as observed experimentally and shown in Section 3.6.

Activation barriers for C-H bond dissociation on O*-O* site pairs (149 kJ mol^{-1} for O* atoms at the terrace sites (V) on the (111) facet (theory) and 155 kJ mol^{-1}

(experiment)) are much larger than on *-* site pairs (79 kJ mol^{-1} (theory);[26] 75 kJ mol^{-1} (CH_4-H_2O) and 83 kJ mol^{-1} (CH_4-CO_2) (experiment)[7]). These large differences, however, do not cause commensurate differences in measured C-H bond activation rate constants, which were 1.1 kPa^{-1} s^{-1} ($k_{1[O*-O*]}$, measured in CH_4-O_2 mixtures, regime 1) and 0.6 kPa^{-1} s^{-1} ($k_{1[*-*]}$, measured in CH_4-H_2O mixtures, regime 4)[7] at 873 K. Large barriers on O*-O* site pairs are compensated by a large pre-exponential factor, which reflects a small negative activation entropy (ΔS = -12.2 J mol^{-1} K^{-1}, experimental, Table 1), because the weakly-bound CH_3 at the transition state retains most of the translational entropy of CH_4(g) reactants. Measured pre-exponential factors are indeed much larger in regime 1 (2.1×10^9 kPa^{-1} s^{-1}) than on the *-* site pairs prevalent in regime 4 (Step 1.3, Scheme 2; 2.0×10^4 kPa^{-1} s^{-1} and 5.9×10^4 kPa^{-1} s^{-1} for H_2O and CO_2 co-reactants, respectively, Table 1) and also larger than estimates from the transition state theory[69] by assuming the loss of one translational mode at the transition state (2.2×10^4 kPa^{-1} s^{-1}). This entropy-enthalpy compensation accounts for the similar rate constant values measured for CH_4-O_2 and CH_4-H_2O reactions in the temperature range of catalytic relevance (Fig. 4). We have also observed small entropic losses, high barriers (130-150 kJ mol^{-1}), and radical-like transition states for C-H activation at O*-O* site pairs on Pd metal clusters and on α–PtO_2 (0001), RhO_2 (110), and Rh_2O_3 (001) surfaces when oxygen vacancies (*) are unavailable to stabilize CH_3 groups at transition states.[70] Such radical-like transition states are also found for C-H bond activation in larger alkanes on oxide structures[71] and detected during oxidative coupling of methane on non-reducible Li-MgO catalysts, in which methyl radicals actually desorb onto the gas phase and react via homogeneous coupling and oxidation reactions.[72]

2.3.3. Kinetically-Relevant C-H Bond Activation on Pt Surfaces at Intermediate O* Coverages (Kinetic Regime 2). We consider next the catalytic consequences of oxygen vacancies (*), which form within O* monolayers as the O_2/CH_4 reactant ratio decreases and the reverse rates of the O_2 dissociation steps become lower than the CH_4 activation rates. Specifically, we address the kinetic and mechanistic evidence for the involvement of vacancy sites (*), which can stabilize the CH_3 fragment in C-H activation transition states and lead to >100-fold increases in rates as O_2/CH_4 ratios decrease from 9.5 to 0.08 (Fig. 3) and for the role of these vacancy sites in the binding of CH_3. Vacancies with vicinal O* species form O*-* site pairs that combine the role of O* in H-abstraction and the binding of CH_3 in a manner that stabilizes the energies of the transition states $(*\text{--}CH_3\text{--}H\text{--}O*)^{\ddagger}$. Such concerted O--H and *--CH_3 interactions lead to more effective C-H bond activation on O*-* than on O*-O* site pairs (Steps 1.2 and 1.1, respectively, Scheme 2), as also proposed for the kinetically-relevant C-H bond activation step in CH_4-O_2 reactions on PdO_x[73] and CH_3OCH_3-O_2 reactions on Pt.[74]

The effects of CH_4 and O_2 pressures on CH_4 turnover rates in regime 2 (Figs. 1b and 2) are consistent with the rate equation derived from pseudo steady-state treatments of all intermediates and the assumptions of irreversible steps for C-H bond dissociation on O*-* site pairs (Step 1.2, Scheme 2), quasi-equilibrated molecular O_2 adsorption and O* migration, and irreversible O_2* dissociation on vacancy site pairs (Steps 2.2, 11, and 2.2, Scheme 2):

$$r_{O^*-*} = \frac{0.5k_{2bf}K_{2a}(O_2)}{\left(1+\frac{k_{2bf}K_{2a}(O_2)}{2k_{1[O^*-*]}(CH_4)}\right)^2} \quad (9)$$

This rate equation contains the rate constants for O_2 and CH_4 dissociation ($k_{1[O^*-*]}$, k_{2bf}) and the equilibrium constant for non-dissociative O_2 adsorption (K_{2a}) (Scheme 2). K_{11} is omitted in this equation because it equals unity and does not modify the form of the rate equation (to be discussed later in this section). In contrast, assumptions of irreversible C-H bond dissociation and quasi-equilibrated O_2 dissociation steps (as in regime 1) lead to rates proportional to CH_4 pressure (derivation in Supporting Information):

$$r_{O^*-*} = \frac{k_{1[O^*-*]}(CH_4)(K_{2a}K_{2b}(O_2))^{0.5}}{\left(1+(K_{2a}K_{2b}(O_2))^{0.5}\right)^2} \quad (10)$$

in contradiction with rates that depend more sensitively on CH_4 pressure (Fig. 1b). The strong dependence on CH_4 pressures (Fig. 1b) suggest that the second denominator term in Equation 9 is much larger than one and that cluster surfaces are nearly saturated with O* ((O*)/(*)>>1), in which case rates are given by:

$$r_2 = k_{1[O^*-*]}(CH_4)\left(\frac{2k_{1[O^*-*]}}{(k_{2bf}K_{2a})}\frac{(CH_4)}{(O_2)}\right) \quad (11)$$

The second parenthesis term in this equation represents the fraction of Pt atoms that are uncovered (*), which is set by the kinetic coupling of irreversible CH_4 and O_2 activation steps. The emergence of vacancy sites with decreasing O_2/CH_4 ratio leads to the preferential activation of C-H bonds by O*-* site pairs, on which transition states benefit from the O* role in H-abstraction and the * role in CH_3 stabilization. The strong CH_4 pressure effects on rates in this regime 2 (Eq. 11) arise from the dual role of CH_4 in determining collision rates with surfaces and the likelihood that surfaces contain vacancy sites.

The irreversible nature of C-H bond dissociation steps on O*-* site pairs was confirmed from the absence of isotopic scrambling in CH_4-CD_4-O_2 mixtures at all O_2/CH_4 ratios and conversions in regime 2. The ratios of $CH_{4-x}D_x$ isotopomer formation rates, which reflect the rates of $CH_{3-x}D_x$*-OD* and $CD_{3-x}H_x$*-OH* recombination (reverse of Step 1.2, Scheme 2) to those of CH_4 chemical conversion rates (r_{CH_4}), were much less than one (~0.01 at 918 K), consistent with net C-H dissociation rates (Step 1.2) that are much larger than for its reverse reaction. We conclude from these data that C-H bond dissociation steps on O*-* pairs are irreversible during CH_4-O_2 reactions in regime 2, as also found in the case of CH_4 reactions in regimes 1 and 4.

The kinetic and thermodynamic parameters (k_{2bf}, $k_{1[O^*-*]}$, and K_{2a}) in Equation 11 remain essentially unchanged over the broad range of O_2/CH_4 ratios that defines regime 2 ($0.17 < O_2/CH_4 < 2$ for 8.5 nm Pt clusters) because (*) sites remain isolated and similar in reactive properties at the near saturation O* coverages prevalent throughout this regime. Cluster surfaces behave as uniform structures in this dilute vacancy regime and can be rigorously treated by Langmuir formalisms of adsorption and surface reactions. Measured pseudo first-order rate constants ($r_2(CH_4)^{-1}$) in regime 2 are proportional to CH_4/O_2 ratios (Fig. 7), consistent with Equation 11, which is derived based on uniform Langmuirian

surfaces, C-H bond activation on O*-* site pairs, irreversible O_2* dissociation steps (Step 2.2, Scheme 2), and O* as the most abundant surface species. At higher CH_4/O_2 ratios (> 6), O* coverages may cause vacancies to also become abundant species, causing the assumptions of O* as MASI and of uniform surfaces to become inaccurate and interactions among vicinal vacancies to influence the reactivity of the neighboring oxygen and the ensemble size of the sites available for CH_3 stabilization, as shown by DFT calculations described below.

The kinetic and isotopic studies reported next were carried out at CH_4/O_2 ratios between 0.5 and 6, for which O* coverages are near saturation, vacancies are dilute, and surfaces behave uniformly. The apparent rate constant in regime 2 ($k_{app,2} = 2k_{1[O^*-*]}^2 \left(k_{2bf}K_{2a}\right)^{-1}$; Eq. 11) estimated from the slope of the rate data in Figure 7 (873 K, 0.2 % wt. Pt/Al_2O_3 catalyst, 8.5 nm average Pt cluster size), is 22.0 ± 0.5 mol CH_4 $[(\text{g-atom Pt}_{surface})\text{-s-kPa}]^{-1}$. The ratio of these effective rate constants for reactions of CH_4 ($(k_{app\text{-}H})_2$) and CD_4 ($(k_{app\text{-}D})_2$) with O_2 in regime 2 is given by the ratio of the slopes of the respective rate data in Figure 7 for these two methane isotopologues. This ratio gives the CH_4/CD_4 kinetic isotope effect (KIE) and reflects the effects of isotopic substitution on the rate and equilibrium constants that determined these effective rate constants:

$$\left(\frac{k_{app\text{-}H}}{k_{app\text{-}D}}\right)_2 = \left(\frac{k_{1[O^*\text{-}*]\text{-}H}}{k_{1[O^*\text{-}*]\text{-}D}}\right)^2 \left(\frac{\left(k_{2bf}K_{2a}\right)_D}{\left(k_{2bf}K_{2a}\right)_H}\right)^1 \qquad (12)$$

The KIE value was found to be 4.2 ± 0.3 at 873 K. These large isotope effects confirm the kinetic relevance of C-H bond activation in this regime. The O_2 adsorption equilibrium constant (K_{2a}) and the O_2 dissociation rate constant (k_{2bf}) do not depend on the identity of the reductant (CH_4 or CD_4); thus K_{2a-H}/K_{2a-D} and k_{2bf-H}/k_{2bf-D} in Equation 12 are unity and the first term in this equation $\left(k_{1[O^*-*]-H}/k_{1[O^*-*]-D}\right)$ is responsible for the observed H/D effects on reaction rates. The measured isotope effects are significantly larger than for C-H bond activation steps on O*-saturated surfaces (1.66, regime 1) or on uncovered surfaces (1.69 (CH_4-H_2O) and 1.77 (CH_4-CO_2), regime 4)[7] because the ratio of rate constants appears as a square term (Eq. 12) in regime 2, but as a linear term in regimes 1 and 4 ($k_{1[O^*-O^*]-H}/k_{1[O^*-O^*]-D}$ and $k_{1[*-*]-H}/k_{1[*-*]-D}$, respectively). The KIE value in regime 2, however, is slightly larger than expected from the square of the KIE values in regimes 1 and 4 ($(k_{1[O^*-O^*]-H}/k_{1[O^*-O^*]-D})^2$ or $(k_{1[*-*]-H}/k_{1[*-*]-D})^2 \sim$ 2.9-3.3)). These stronger isotope effects may reflect a larger difference between the energies for $(H_3C^*\text{--}^*OH)^‡$ and $(D_3C^*\text{--}^*OD)^‡$ activated complexes than those for $(H_3CO^*\text{--}^*OH)^‡$ and $(D_3CO^*\text{--}^*OD)^‡$ and for $(H_3C^*\text{--}^*H)^‡$ and $(D_3C^*\text{--}^*D)^‡$, which are formed during the C-H bond activation steps on O*-O* and *-* site pairs in regimes 1 and 4, respectively. We surmise that the strong KIE effects are caused in part by the formation of an earlier transition state structure than those occur on O*-O* and *-* site pairs, as suggested by the shorter C-H bond length (0.129 nm (O*-* site pairs) vs. 0.170 nm (O*-O* site pairs) and 0.152 nm (*-* site pairs)[26]) in the $(H_3C^*\text{--}^*OH)^‡$ transition state derived from DFT calculations on Pt_{201} clusters.

The apparent activation energy ($E_{app,2}$; regime 2) measured from temperature effects on the effective rate constants in Equation 11, $2k_{1[O^*-*]}^2(k_{2bf}K_{2a})^{-1}$, is 89±20 kJ mol^{-1}. Its value reflects the combined effects of the C-H activation barrier on O*-* site pairs ($E_{1[O^*-*]}$), the O_2* dissociation barrier (E_{2bf}) on *-* site pairs, and the heat of adsorption of molecular O_2 species (Q_{O_2}):

$$E_{app,2} = 2E_{1[O^*-*]} - (E_{2bf} - Q_{O_2}) \quad (13)$$

The individual contributions cannot be discerned from experiments, but DFT calculations on the various types of sites at Pt_{201} clusters provide significant insights into this matter and into the effects O* and CH_3* binding strengths on individual barriers, as well as theoretical support for the mechanistic conclusions based on experiments, as shown later in this section.

Next, we examine the reversibility of O_2 dissociation steps and the O* coverages prevalent during CH_4-O_2 reactions in regime 2. We first derive a general expression for the oxygen virtual pressure, $(O_2)_v$, which relates O* coverages during catalysis to CH_4 and O_2 pressures in this kinetic regime. A pseudo steady-state balance on reactive O* intermediates with kinetically-relevant C-H bond activation occurring via parallel routes on O*-O*, O*-*, and *-* site pairs (Steps 1.1-1.3, Scheme 2) gives:

$$2k_{1[O^*-*]}(O^*)(*) + 2k_{1[O^*-O^*]}(O^*)^2 + 2k_{1[*-*]}(*)^2 = K_{2a}k_{2bf}\frac{(O_2)}{(CH_4)}(*)^2 - k_{2br}\frac{(O^*)^2}{(CH_4)} \quad (14)$$

which depends on the CH_4 and O_2 pressures, the equilibrium constant for molecular O_2 adsorption (K_{2a}), and the rate constants for the three C-H activation routes ($k_{1[O^*-O^*]}, k_{1[O^*-*]}, k_{1[*-*]}$) and for O_2* dissociation (k_{2bf}) and recombination (k_{2br}) (as defined by the steps in Scheme 2). This quadratic equation can be solved to give a general expression for the O*/(*) ratio during steady-state catalysis and the defining equation for the virtual O_2 pressure ($(O_2)_v$), as a rigorous measure of the oxygen chemical potential on catalytic surfaces:

$$\left(\frac{(O^*)}{(*)}\right)_{ss} = \frac{-2k_{1[O^*-*]}(CH_4) \pm \sqrt{(2k_{1[O^*-*]}(CH_4))^2 - 4(2k_{1[O^*-O^*]}(CH_4) + k_{2br})(2k_{1[*-*]}(CH_4) - K_{2a}k_{2bf}(O_2))}}{2(2k_{1[O^*-O^*]}(CH_4) + k_{2br})}$$

$$\left(\frac{(O^*)}{(*)}\right)_{ss} = \sqrt{K_{2a}K_{2b}(O_2)_v} \quad (15)$$

When the O* recombination is fast relative to the C-H bond activation:

$$k_{2br}(O^*)^2 >> k_{1[O^*-O^*]}(CH_4)(O^*)^2, k_{1[O^*-*]}(CH_4)(O^*)(*), k_{1[*-*]}(CH_4)(*)^2 \quad (16)$$

Equation 15 simplifies to Equation 4, in which case $(O_2)_v$ becomes equal to the prevalent O_2 pressure. This inequality thus defines the conditions required for quasi-equilibrated O_2 dissociation steps when C-H bond activation can occur in parallel by any of the postulated site pairs in the various kinetic regimes. The effects of O_2 and CH_4 pressures on rates suggest that C-H bonds predominantly dissociate on O*-* site pairs in regime 2, at rates much higher (up to 160 times) than on the O*-O* (regime 1, Fig. 2) and *-* site pairs (regime 4, Fig. 1):

$$k_{1[O^*-*]}(O^*)(*) >> k_{1[O^*-O^*]}(O^*)^2, k_{1[*-*]}(*)^2 \quad (17)$$

The inequalities in Equations 16 and 17 simplify Equation 15 to:

$$\left(\frac{(O^*)}{(*)}\right)_{ss} = \sqrt{K_{2a}K_{2b}(O_2)_v} = \frac{K_{2a}k_{2bf}}{2k_{1[O^*-*]}}\left(\frac{O_2}{CH_4}\right) \quad (18a)$$

$$(O_2)_v = \frac{K_{2a}k_{2bf}k_{2br}}{4k^2_{1[O^*-*]}}\left(\frac{O_2}{CH_4}\right)^2 \quad (18b)$$

These (O*)/(*) and $(O_2)_v$ values in regime 2 are single-valued functions of the O_2/CH_4 ratio and not just of O_2 pressure as in regime 1 (Section 3.2). At any given O_2 pressure, (O*)/(*) values in regime 2 are smaller than those at chemical equilibrium and, by inference, $(O_2)_v$ are smaller than the prevalent O_2 pressures, because of more effective O* scavenging by CH_4 reactions in this regime. These lower $(O_2)_v$ and oxygen chemical potentials reduce the oxidation tendencies of Pt clusters from those given by the actual O_2 pressures. Additionally, the lower oxygen chemical potentials in this regime than regime 1 lead the bulk of the Pt clusters to remain in the metallic phase.

The ratio of $^{16}O_2$-$^{18}O_2$ exchange rate constants during steady-state catalysis (in CH_4-$^{18}O_2$-$^{16}O_2$ mixtures) to those at chemical equilibrium (in $^{18}O_2$-$^{16}O_2$ mixtures) (χ_2) provides otherwise inaccessible estimates of O* coverages and $(O_2)_v$ values (Eqs. 18a-b) during steady-state CH_4-O_2 reactions relative to those at chemical equilibrium with the prevalent O_2 pressures. Figure 5 shows the effective rate constants for O_2 isotopic exchange ($r_{ex,2}(O_2)^{-0.5}$; Eq. 6) for CH_4-$^{16}O_2$-$^{18}O_2$ reactions in regime 2 ($0.08 < O_2/CH_4 < 2$; 8.5 nm Pt clusters) together with their measured values in regime 1 ($O_2/CH_4 > 2$; 8.5 nm Pt clusters) and also with the values measured in $^{18}O_2$-$^{16}O_2$ mixtures without CH_4. O_2 exchange rate constants in regime 2 decreased with decreasing O_2/CH_4 ratio and become smaller than those in regime 1 (16.5 mol (g-atom $Pt_{surface}$-s)$^{-1}$ $kPa^{-0.5}$) and than those at chemical equilibrium (Section 3.2). The ratios of these rate constants to those at equilibrium (χ_2) are near unity in regime 1, but decrease as CH_4-O_2 reactions undergo a transition from regime 1 to 2 and as the faster C-H activation steps on O*-* site pairs deplete the O* and prevent oxygen equilibration. The O_2 exchange rate equation (Eq. 6b), derived by assuming equilibrated O_2 dissociation steps (Steps 2.1 and 2.2, Scheme 2), becomes inadequate to describe the $^{16}O_2$-$^{18}O_2$ rate dependence in this regime. This is shown in Figure 5 where the O_2 exchange "rate constants" ($r_{ex}(O_2)^{-0.5}$) are no longer constant, but instead decrease with decreasing O_2/CH_4 ratio. The exchange rates remain proportional to O* and O_2* concentrations, the latter of which are proportional to the O_2 pressures and the number of binding sites (*). The pseudo first-order O_2 exchange rate constants ($r_{ex,SS}(O_2)^{-1}$) are proportional to the O* and * concentrations, similar to the case for CH_4 conversion in this regime ($r_2(CH_4)^{-1}$), and therefore also a strict function of O_2/CH_4 ratios and the related O* coverages and $(O_2)_v$, as shown in Figure 8.

The elementary steps involved in O_2 adsorption (Step 2.1) and C-H and O=O bond dissociation steps (Steps 1.2 and 2.2 in Scheme 2) control reactivity in regime 2. DFT calculations were carried out over different O*-* site pairs on O*-covered Pt_{201} clusters. More specifically we analyze here the lowest energy and most likely O*-* pair on the (111) terrace which is comprised of a central terrace oxygen vacancy site (*) (type 4 in scheme 1) and a reactive next nearest neighbor O* site. O* chemisorbed at site IV is the only active site in scheme 1 as the nearest neighbor O* sites (site II) are too close to the adsorbed methane and thus result in very high repulsive interactions and barriers that exceed 170 kJ mol^{-1} (to be discussed later in this section). First, we examine the high

O_2/CH_4 region in regime 2 (> 0.25) to probe the properties of O*-* site pairs and then extend our study to lower O_2/CH_4 ratios (< 0.25) where vicinal (*) species may influence C-H bond activation barriers.

Calculations were carried out on isolated O* vacancies (also exposed Pt atoms) at (111) facets (type 4) of O* covered Pt_{201} clusters (O* occupies all of the (111) fcc and (100) bridge sites). O* coverages (O^*/O^*_{max}) are > 0.99, consistent with the mechanistic proposal of O* as MASI required to describe rate data and with the presence of isolated vacancies. The structures of the reactants, transition states, and products of C-H bond activation on O*-* site pairs are shown in Figure 9. C-H bond activation occurs via concerted oxidative addition[75] of the exposed Pt atom to C-H bonds and H-abstraction by O* with a barrier of 144 kJ mol^{-1}. The transition state is stabilized by C-H bond interactions with the exposed Pt atom which is evident from the elongation of the C-H bond. This elongation lowers the C-H antibonding (σ^*_{C-H}) orbital, thus allowing for the back donation of electron density from the metal into this state and dissociation of the C-H bond (Pt-C and Pt-H bonds at the transition state are 0.234 nm and 0.208 nm, respectively). The O* atom, initially adsorbed at the three-fold fcc site, migrates to the bridge position to interact with the H in CH_4 (O-H bond is 0.149 nm at the transition state) and assist in the C-H bond activation. This step occurs together with the metal insertion into the C-H bond to form a four-centered $(M\text{--}C\text{--}H\text{--}O)^{\ddagger}$ transition state (Fig. 9b), in a process reminiscent of σ-bond metathesis and 1,2 addition on organometallic complexes, which form $(M\text{--}C\text{--}H\text{--}X)^{\ddagger}$ transition states (X= amido, alkoxo, imido, etc).[76,77,78] These findings confirm the synergistic roles of * and O* in the activation of C-H bonds, in which vacancies weaken C-H bonds and stabilize the CH_3 fragment and O* abstract and stabilize the H-atom. These conclusions suggest that O*-* site pairs in which * can form strong *-CH_3 bonds but O* are weakly bound would give the most stable transition states and the lowest C-H bond activation barriers.

The specific influence of the properties of O* and * sites on C-H bond activation barriers was probed by varying O* and *-CH_3 binding energies. O* binding energy effects were explored by varying O* coverages and binding energies on extended Pt(111) surfaces with surface Pt atoms of identical coordination and similar in structure to (111) facets in large Pt clusters. As O* coverage increases (from 0.11 ML to 0.67 ML), the O* binding energy (expressed here as heat of atomic oxygen adsorption, Q_{O^*}) decreases (from 256 to 365 kJ mol^{-1})[79] and C-H bond activation barriers also decrease linearly with both the O* coverage and O* binding energy from 122 to 94 kJ mol^{-1} (see Figures S-3 and S-4) consistent with Brønsted-Evans-Polanyi relations and with similar trends reported for C-H activation in CH_3OCH_3 on O*-* site pairs on Pt[74] and also in accordance with proposed basis for the high reactivity of weakly-bound O* on Ag.[80] The effects of M-CH_3 binding energies on C-H bond activation rates were examined by varying the coordination number of the * site in O*-* site pair on Pt_{201} clusters. These effects of Pt coordination number on C-H bond activation barriers were recently reported for O*-* site pairs on bare Pt_{201} clusters and reported elsewhere.[26] C-H bond activation barriers on O*-* site pairs were found to decrease from 119 kJ mol^{-1} to 88 kJ mol^{-1} as the coordination number of * site in the O*-* site pair decreases from 9 to 6 and the M-CH_3 bond strength concomitantly increases.[26] On coordinatively unsaturated sites such as corner and edge sites (sites 1 and 2 in Scheme 1, respectively), the barriers were lower because these sites afford stronger Pt-C interactions and concomitantly higher reaction

exothermicity, consistent with the predicted trend between barriers and heats of reaction from the Brønsted-Evans-Polanyi relation. Similar trends between barriers and heats of reaction and the related metal-carbon binding energies were also reported for C-H bond activation on *-* site pairs on Pt_{201} clusters[26] and on closed-packed metal surfaces[81] because C-H bond activation steps on both the O*-* and *-* site pairs occur via oxidative addition of the metal atom to the C-H bond.[26] These trends were also found for *-* site pairs on different closed-packed metal surfaces, in which the barriers decrease from 200 kJ mol^{-1} to 71 kJ mol^{-1} as the M-CH_3 bond strength increases from 115 kJ mol^{-1} (Au(111)) to 253 kJ mol^{-1} (Rh(111)), respectively.[82]

The effective barrier for methane activation in regime 2 (Eq. 13) includes contributions from CH_4 ($E_{1[O^*-*]}$) and oxygen activation barriers (E_{2bf}-Q_{O2}), each of which is given by the difference in energy between the transition state ((*--CH_3--H--O*)‡ or (O*=*O)‡) and its gas phase reactants (CH_4 or O_2) as their adsorption from the gas phase is quasi-equilibrated. The CH_4 activation barrier on a single isolated vacancy with a vicinal O* is 144 kJ mol^{-1}. O_2, however, can not directly dissociate to form 2O* on an isolated vacancy (*). Instead, it adsorbs as O_2* in equilibrated steps (Step 2.1, Scheme 2) and then dissociates onto a vicinal O* site resulting in the formation of a new O_2* ($^xO_2$*+^yO*→ ^xO*+$^x O^y$O*), x and y are used to differentiate the O*, Step 11, Scheme 2). This process of O_2* activation by vicinal O* allows for the rapid migration of O* along the top of the O*-covered surface which continues until O_2* dissociates via the reaction O_2* + * → 2O* (Step 2.2, Scheme 2) to complete the O_2 dissociation process. Such mobile O* species and elementary steps have also been proposed to account for O_2 activation during isotopic exchange and NO-O_2 reactions on Pt and Pd surfaces.[59,83]

The reaction energy diagram for O_2 activation at isolated vacancies on Pt clusters (Figure 10) includes the initial formation of weakly-coordinated η_1-superoxo O_2^- intermediate with a barrier of 58 kJ mol^{-1}, which contrasts the barrierless adsorption of O_2 at low O* coverages (O^*/O^*_{max}= 0.01) on Pt_{201} clusters involving the exothermic formation of η_2-peroxo species (Sec. 3.4). O_2 adsorption cannot occur in a η_2 configuration on O*-covered Pt_{201} clusters because of the lack of *-* site pairs to bind the two O-atoms. O-atoms migrate on top of the O* covered surface via the formation of three-centered transition states in which the O-atom in O_2* that is not in contact with the surface ($O_{migrating}$) is shared between the bound oxygen of O_2* (O_{bound}*) and the vicinal O* ($O_{vicinal}$*), as shown in transition state in Figure 10. The barrier for this O-atom transfer step is 75 kJ mol^{-1}. O* migration continues until newly formed O_2* reside next to a vacancy site (*), a situation that causes dissociation via a late transition state in which the migrating oxygen ($O_{migrating}$) binds with the exposed metal atom. This step exhibits the largest barrier in this overall reaction coordinate (207 kJ mol^{-1}); the barriers for adsorption of molecular O_2 (58 kJ mol^{-1}), O* migration (75 kJ mol^{-1}), and O_2 desorption (10 kJ mol^{-1}) are considerably smaller. Thus, we conclude that the elementary O_2* dissociation step is irreversible and kinetically-relevant while O_2 adsorption and O migration steps are quasi-equilibrated. The effective O_2 dissociation rate constant (k_{eff,O_2}) is then given by:

$$k_{eff,O_2} = k_{2bf} K_{2a} K_{11} = k_{2bf} K_{2a} \quad (19)$$

in terms of the O_2 dissociation rate constant (k_{2bf}) and the O_2* adsorption (K_{2a}) and O atom migration (K_{11}) equilibrium constants (Scheme 2, Figure 10 for the definition of these constants). The O* migration equilibrium constant (K_{11}) equals unity because the

free energy change for this step is zero. Thus, the effective O_2 dissociation rate constant (Eq. 19) is equal to the product of O_2* adsorption equilibrium constant and O_2 dissociation rate constant, $k_{2bf}K_{2a}$, used in Equations 9 and 11. The expression is identical to the rate constant derived by assuming direct O_2 dissociation steps occur over two vacancy sites but reflects different O_2 activation paths.

DFT-derived barriers for C-H bond (144 kJ mol^{-1}) and O_2 (207 kJ mol^{-1}) activation can be used together with Equation 11 to estimate an effective barrier of 81 kJ mol^{-1} for kinetic regime 2, in excellent agreement with measured activation energies (79 kJ mol^{-1}; Table 1). These barriers are much smaller than for CH_4 activation on O*-O* site pair in regime 1 (155 kJ mol^{-1} (experiment) and 149 kJ mol^{-1} (theory)), consistent with CH_4-O_2 reactions that are much faster in regime 2 than regime 1. Although the calculated effective barrier in regimes 2 is in very good agreement with measured barriers, the intrinsic C-H (144 kJ mol^{-1}) activation barrier in this regime is higher than expected as the C-H activation barrier is rather similar to that in regime 1 (149 kJ mol^{-1}) especially considering the significant differences in the turnover rates between these two regimes. It is likely that the intrinsic barrier for O_2 dissociation (207 kJ mol^{-1}) is also higher than expected. The high barriers are likely due to the fact that the Pt sites are not fully exposed and therefore can not take fully advantage of the formation of a strong M-CH_3 bond in the transition state. O* in the surface appear to block access to the vacancy site. This may be the result of the constraints imposed by not considering the changes that occur in the adlayer structure prevalent at the high temperatures and O_2 pressures of this reaction. Including these effects would likely increase oxygen saturation coverages and expand the lattice which will help to push the metal atoms out of the surface and thus better expose the vacancy sites. We have seen similar effects on Pt(111) surfaces where saturation surface coverages result in a bulking of the surface structure which exposes metal sites (see Figure S-4) and lowers the barrier from 122 kJ mol^{-1} at 0.25 O* ML to 94 kJ mol^{-1} at 0.67 O* ML. This is consistent with the results found by Weaver et al.,[67] who suggest the formation of subsurface oxides on O*-covered Pd(111) surfaces. We will report these details in surface reconstruction and their influence on both the C-H and O=O activation barriers in a follow up manuscript. The over prediction of the C-H and O_2 dissociation barriers appear to cancel one another out in determining the effective activation energy barrier (Eq. 11) as both are limited by the exposure and access to metal vacancy sites in the fully covered O*-adlayer. Similar cancelations are also likely to occur in the low O_2/CH_4 region of regime 2.

As O_2/CH_4 ratios decrease, O* coverages decrease and the number of vacancies increase (Eq. 18a) and ultimately lead to vicinal *-* sites; these trends cause also an increase in the O* binding strength near such sites and a concomitant decrease in the reactivity of O* in H-abstraction. Yet, C-H bond activation barriers decreased from 149 kJ mol^{-1}, to 125 kJ mol^{-1}, and to 70 kJ mol^{-1} as the number of oxygen vacancies increased from one to three. Larger ensembles of vacancies reflect a decrease in the number of O* bound to each exposed Pt atom and, in turn, stronger interactions between CH_4 and exposed Pt atoms. These interactions stabilize the C-H bond activation transition states and compensates for the lower O* reactivity caused by an increase in the O* binding strength.

2.3.4. Kinetically-Relevant O=O Activation on Pt Surfaces Uncovered of Oxygen Atoms (Kinetic Regime 3). Turnover rates for CH_4-O_2 ultimately decrease as

the size of the oxygen vacancy ensemble increases with decreasing O_2/CH_4 ratios beyond those that define kinetic regime 2 ($O_2/CH_4 < 0.08$, 873 K, 8.5 nm clusters, Figs. 2 and 3). This transition in kinetic response reflects a decrease in oxygen chemical potential and O* coverage, which causes O*-mediated C-H bond activation to become less frequent and rates ultimately to become limited by O_2 activation. In this regime (denoted as regime **3** in Figs. 2 and 3), rates become proportional to O_2 pressure and independent of CH_4 pressure. We rule out mass transport across boundary layers around catalyst pellets (which would give such a rate dependence) as the controlling step by varying intrapellet dilution ratios from 100 to 300 without consequences on measured rates, as reported elsewhere.[26] The measured first-order dependence on O_2 indicates that rates are limited solely by the reactive collisions of O_2 on essentially bare Pt cluster surfaces. CH_4 turnover rates in this regime are given by:

$$r_3 = 0.5K_{2a}k_{2bf}(O_2) \quad (20)$$

In this regime, C-H bond activation becomes kinetically-irrelevant, consistent with the absence of CH_4/CD_4 kinetic isotope effects (KIE, 1.0±0.15, regime 3, Table 1, Fig. 11). The sole kinetic relevance of the O_2 dissociation step (Step 2.2, Scheme 2) is also consistent with turnover rates that do not depend on reductant pressures for both $CO\text{-}O_2$ and $CH_4\text{-}O_2$ reactions at the conditions required for this kinetic regime (0.05-0.35 kPa O_2, 873 K, Fig. 11). The O_2 consumption rates in $CO\text{-}O_2$ and $CH_4\text{-}O_2$ mixtures, which are related to the CO or CH_4 turnover rates via the respective reaction stoichoimetries, are essentially identical at each O_2 pressure, because these reactions are limited by the same O_2 dissociation step on surfaces essentially free of adsorbed species.

Turnover rates at all O_2 pressures in regime 3 are much larger than for C-H bond activation steps in $CH_4\text{-}H_2O/CO_2$ mixtures (regime 4) at a given CH_4 pressure (< 5 kPa). Thus, it appears that C-H bond activation occurs much faster with $CH_4\text{-}O_2$ than $CH_4\text{-}H_2O$ reactants, because otherwise $CH_4\text{-}O_2$ reactions would be limited by C-H bond activation instead of O_2 dissociations steps. C-H bond activation rate constants measured at low O* coverages in $^{13}CH_4\text{-}^{12}CO\text{-}O_2$ mixtures remain insensitive to O* content, thus this step must also occur predominantly on *-* site pairs that are prevalent in this regime.[26] Although CH_4 activation proceeds via the same kinetically-relevant step on *-* site pairs in $CH_4\text{-}O_2$ (regime 3) and $CH_4\text{-}H_2O/CO_2$ (regime 4) mixtures, turnover rates were much larger in the $CH_4\text{-}O_2$ mixtures. We surmise that a portion of the coordinatively unsaturated sites that are highly effective for C-H bond activation[7] are occupied by CH_x* in $CH_4\text{-}H_2O/CO_2$ reactions and remain kinetically invisible at all H_2O/CH_4 or CO_2/CH_4 ratios. These undercoodinated sites become available for catalytic turnovers in $CH_4\text{-}O_2$ mixtures because the CH_x* were removed by reactions with O*, as reported elsewhere.[26]

Rate constants for CH_4 conversion in regime 3 (Eq. 20) are related to O_2 dissociation rate constant ($K_{2a}k_{2bf}$, 5.6×10^3 ± 195 kPa^{-1} s^{-1}, 873 K, Table 1) by the stoichoimetry of the combustion reaction. O_2 dissociation rate constants reflect the rate of O_2 collisions with Pt cluster surfaces and a sticking coefficient, which is found to be ~ 3.5×10^{-3}, similar to values reported on Pt(111) (0.016; extrapolated to 873 K from sticking coefficients measured at 320 K-620 K).[84] The measured barrier for O_2 dissociation ($E_{2bf}\text{-}Q_{O_2}$) reflects the difference between the O_2* dissociation activation barrier (E_{2bf}) and the heat of molecular O_2 adsorption (Q_{O_2}); their values are typically small, as confirmed by DFT-derived values reported below. Measured $CH_4\text{-}O_2$ turnover

rates depend weakly on temperature (810-900 K, Fig. 12) and measured activation energies were near zero (~3 kJ mol^{-1}) and much smaller than in regimes 1, 2, and 4 (155 kJ mol^{-1}, 79 kJ mol^{-1}, and 75(H_2O)-83(CO_2) kJ mol^{-1}, respectively), where barriers reflect those for C-H bond activation steps ($E_{1[O^*-O^*]}$, $E_{1[O^*-*]}$, or $E_{1[*-*]}$; Table 1). The measured pre-exponential factor ($5.6\times10^3 \pm 195$ kPa^{-1} s^{-1}, 873 K, Table 1) in regime 3 is larger than estimates derived from a transition state formalism by assuming an immobile activated structure (5.5×10^1 kPa^{-1} s^{-1})[85] and reflects an entropy loss between the reactant and transition state of -118.8 J mol^{-1} K^{-1}.

DFT treatments were used to describe the molecular details of kinetically-relevant O_2 dissociation steps on bare Pt_{201} clusters. Molecular adsorption of O_2(g) (Step 2.1, Scheme 2) requires a triplet-to-singlet transition upon adsorption, as also found for O_2 adsorption on CO-covered Pt(111) and Pt_{201} cluster surfaces.[86,87] O_2* prefers to adsorb in a di-σ configuration (Fig. 13), as a molecular precursor to O_2* dissociation (Step 2.2, Scheme 2), as shown previously.[88] O_2* dissociation (Step 2.2, Scheme 2) occurs over a Pt atom that connects the two neighboring three-fold fcc sites that ultimately bind the O* products via a late transition state (Fig. 13) at which the O=O bond lengthens from 0.124 nm in O_2(g) to 0.176 nm. There is a charge transfer from the metal into the antibonding $2\pi^*$ state in O_2 that occurs upon the adsorption of O_2 to the surface. The two O* atoms formed bind to vicinal three-fold fcc sites with O-Pt bonds about 0.210 nm in length and share a Pt surface atom. The effective barrier (E_{2bf}- Q_{O_2}) for O_2 dissociation, measured as the difference in energy between the $(*O\text{--}O^*)^{\ddagger}$ transition state and O_2(g), is < 20 kJ (mol O_2)$^{-1}$, a value much smaller than on O*-saturated Pt_{201} clusters (207 kJ mol^{-1}, Fig. 10), because O* repulsive interaction are absent on bare surfaces. These DFT-derived barriers are consistent with measured barriers (< 3 kJ mol^{-1}). The nearly cleaved O=O bonds and the nearly formed O-Pt bonds (0.199 nm and 0.201 nm) at the late transition states are consistent with the large entropic losses (Table 1) detected in the rate measurements.

2.3.5. Effects of Temperature on O* Coverage and Consequences for the O_2/CH_4 Ratios Required for Transitions among Kinetic Regimes. Reaction temperatures influence rate and equilibrium constants and, in turn, O* coverages, according to Equations 5 or 18 depending on the regimes. A change in operating O_2 pressures or O_2/CH_4 ratios is required to compensate for the changes in rate and equilibrium constants to attain the same O* coverages that would result in transitions among kinetic regimes. Figure 12 shows CH_4 turnover rates increased and then decreased with increasing O_2/CH_4 ratio at all temperatures (813-898 K), consistent with the general nature of the mechanistic conclusions reached based on kinetic and isotopic studies at 873 K and discussed above. Specifically, the transition between bare Pt clusters (regime 3) and O*-covered clusters (regime 2) occurs near the O_2/CH_4 ratio required for maximum rates; these ratios increased with increasing temperature (from 0.045 at 813 K to 0.06 at 853 K). Simplifying Equation 15 with the assumptions that C-H bonds are predominantly activated on O*-* and *-* site pairs and the rates of O* removal via recombination are much smaller than their reactions with CH_4 (Sec. 3.3) leads to steady-state $[(O^*)/(*)]_{ss}$ ratios in regimes 2 and 3:

$$\left(\frac{(O^*)}{(*)}\right)_{ss,\,2\,\&\,3} = \frac{k_{2bf}K_{2a}}{2k_{1[O^*-*]}}\frac{(O_2)}{(CH_4)} - \frac{k_{1[*-*]}}{k_{1[O^*-*]}} \qquad (21)$$

which depends on O_2/CH_4 ratios and on rate (k_{2bf}, $k_{1[O^*-*]}$, $k_{1[*-*]}$) and thermodynamic (K_{2a}) constants and, in turn, on the effective barriers for O_2^* (E_{2bf}) and CH_4 ($E_{1[O^*-*]}$, $E_{1[*-*]}$) dissociation, the heat of molecular O_2 adsorption (Q_{O_2}), and the pre-exponential factors (A_i) for the elementary step i in Scheme 2:

$$\left(\frac{(O^*)}{(*)}\right)_{ss,2\&3} = \frac{A_{2bf}A_{2af}}{2A_{1[O^*-*]}A_{2ar}}\exp\left(\frac{-\left(E_{2bf} - Q_{O_2} - E_{1[O^*-*]}\right)}{k_BT}\right)\left(\frac{O_2}{CH_4}\right) - \frac{A_{1[*-*]}}{A_{1[O^*-*]}}\exp\left(\frac{-\left(E_{1[*-*]} - E_{1[O^*-*]}\right)}{k_BT}\right) \quad (22)$$

The pre-exponential factors for molecular O_2 adsorption (A_{2af}, Step 2.1) and desorption (A_{2ar}, reversed of Step 2.1), O_2^* dissociation (A_{2bf}, Step 2.2), and C-H bond dissociation ($A_{1[O^*-*]}$, Step 1.2; $A_{1[*-*]}$, Step 1.3) steps, as defined in Scheme 2, vary weakly with temperature (e.g. ~ $T^{-0.5}$ for an immobile transition state complex[85]). Both of the exponential terms in Equation 22 decrease dramatically as the temperature increases, because the calculated barriers for C-H bond dissociation on O*-* site pairs at low O* coverages ($E_{1[O^*-*]}$, 91-121 kJ mol^{-1} for 0.01 ML on Pt_{201} clusters[26]) are much larger than on *-* site pairs ($E_{1[*-*]}$, 89 kJ mol^{-1} on Pt(111) and 50-82 kJ mol^{-1} on Pt_{201} clusters[26]) and those for O_2 dissociation (E_{2bf}- Q_{O_2}, < 3 kJ mol^{-1} (experimental) and ~20 kJ mol^{-1} (theory)). The exponential terms in Equation 22 decrease dramatically as the temperature increases, leading to lower (O*)/(*) ratios for any given O_2/CH_4 value at higher temperatures. These effects of temperature on rate and equilibrium constants lead to wider operating O_2/CH_4 windows for reactions to occur on uncovered surfaces (regime 3) at higher temperatures.

2.3.6. Effects of Pt Cluster Size and Oxygen Binding Strength on CH_4 Conversion Rates. The specific effects of the size of Pt clusters on measured turnover rates for CH_4-O_2 reactions differ among the kinetic regimes discussed here, because each regime reflects rate and equilibrium constants with potentially different sensitivity to the coordination of exposed metal atoms, which vary with cluster size. We examine next the consequences of Pt cluster size and of the coordination and binding properties of exposed Pt atoms on turnover rates at each kinetic regime. The effects of cluster size were measured on a series of 0.2% wt. Pt/Al_2O_3 catalysts at 873 K and the data are shown in Figure 14 and Table 3.

The *-* site pairs on small clusters predominantly consist of coordinatively unsaturated atoms, which bind CH_3^* and H* strongly in stabilizing the transition state involved in C-H bond activation during reactions of CH_4-H_2O/CO_2 mixtures (regime 4). Strong binding of CH_3^* and H* leads to more exothermic C-H bond activation steps and stabilizes transition states to give smaller activation barriers, consistent with thermodynamic guidance from Brønsted-Evans-Polanyi relations.[26] This decrease in C-H bond activation barriers caused the larger turnover rates widely reported on small clusters for reforming reactions on smaller Pt clusters (Table 1) and other Group VIII metals.[6,8,9,10,11]

C-H bond dissociation rates on O*-O* site pairs (regime 1) exhibit instead an opposite effect of cluster size. Measured rate constants ($k_{1[O^*-O^*]}$, Step 1.1) increased by a factor of ~2.5 as Pt cluster size increased from 1.8 nm to 8.5 nm. The barrier for this step depends on the energy required to promote O* to the active bridge sites and on the H-abstraction reactivity of vicinal O* species (Section 3.2). O* binding energies increase as exposed atoms become less coordinated with decreasing cluster size (Table 2), as

expected from bond-order conservation principles, which preserve the total bond order (O-Pt and Pt-Pt bonds) and bond energy for each Pt atom.[89] Weakly chemisorbed O* atoms predominantly present on larger Pt clusters form stronger bonds with the H atoms at the transition state, thus decreasing activation barriers ($E_{1[O^*\text{-}O^*]}$) and increasing C-H bond activation rate constants ($k_{1[O^*\text{-}O^*]}$).

In regime 2, both the C-H and O=O bond activation steps are kinetically-relevant. The weakly bound O* atoms on larger Pt clusters are more effective for the H abstraction during C-H bond activation on O*-* site pairs (regime 2), as shown from the linear decrease in the C-H bond activation barriers with O* binding energies calculated from DFT (Sec. 3.3; Figure S-3 in the Supplementary Information). These effects of weaker O* binding strength are, however, partly compensated by an increase in C-H bond barriers caused by weaker interactions between the oxygen vacancy sites (*) and the CH_3 in the $(H_3C^*\text{--}^*OH)^{\ddagger}$ transition state on larger clusters (Sec. 3.3). The weaker O* binding strengths also infer less effective O_2 dissociation steps, as predicted from the Brønsted-Evans-Polanyi relationship between the O_2 dissociation barriers and the exothermicity of the reactions (also related to the heats of O* adsorption). These effects of O* binding strengths lead to higher C-H bond activation and lower O=O bond dissociation rate constants and, in turn, to larger effective rate constants ($k_{app,2} = 2k_{1[O^*\text{-}^*]}^2 \left(k_{2bf} K_{2a}\right)^{-1}$) on the larger Pt clusters. Such effects are, however, compensated by an increase in C-H bond barriers resulted from weaker *-CH_3 binding strengths. These combined effects lead to a weak dependence of rate constants on cluster size, where the effective rate constants vary only by a factor of < 4 for the 1.8 nm and 8.5 nm Pt clusters, despite that these rate constants contain a square term of the C-H bond activation rate constants ($k_{1[O^*\text{-}^*]}^2$).

Isotopic $^{16}O_2$-$^{18}O_2$ exchange rates confirm that O* binding strength increases and reactivity decreases with decreasing Pt cluster size. $^{16}O_2$-$^{18}O_2$ exchange rate constants (873 K) on 8.5 nm Pt clusters are ~2.5 times larger than on 1.8 nm clusters (Fig. 5). These rate constants (Eq. 6b) depend on the ratio of O_2* and O* equilibrium adsorption constants (K_{2a} and K_{2b}, respectively) and the $^{16}O^*$ and $^{18}O_2^*$ (or $^{18}O^*$ and $^{16}O_2^*$) reaction rate constants (k_{11}; Step 11, Scheme 2). Thus, the effective barrier for the $^{16}O_2$-$^{18}O_2$ reactions ($E_{ex,app}$) depends on the heats of molecular (Q_{2a}) and atomic (Q_{2b}) oxygen adsorption[90] and on the activation barrier (E_{11f}) for the $^{16}O^*$ and $^{18}O_2^*$ (or $^{18}O^*$ and $^{16}O_2^*$) exchange step (Step 11, Scheme 2):

$$E_{ex,app} = E_{11f} + 0.5\left(Q_{2b} - Q_{2a}\right) \quad (23)$$

The $\left(Q_{2b} - Q_{2a}\right)$ term is positive because heats of O* adsorption (Q_{2b}, 171.5 kJ mol^{-1}) is much larger than the heat of molecular O_2 adsorption (Q_{2a}, 15.9 kJ mol^{-1}), as established previously from thermal desorption experiments on Pt(111) surface.[84,91] The larger O_2 exchange rate constants on the 8.5 nm clusters could reflect lower apparent activation barriers, as a result of the weaker O_2* binding (Q_{2b}) and/or smaller differences between the heats of atomic and molecular oxygen adsorption $\left(Q_{2b} - Q_{2a}\right)$. It is expected that the barriers of the $^{16}O^*$ and $^{18}O_2^*$ exchange may also be affected by the cluster size but to a lesser extent because the reactions (Step 11, Scheme 2) involve similar extent of energy stabilization and destabilizing of reactant, transition and product states with O* binding strength.

Finally, the slope of the $r_{CH_4}(CH_4)^{-1}$ versus O_2/CH_4 data in regime 3 (Fig. 14, $O_2/CH_4 < 0.02$ for 1.8 nm to 8.5 nm Pt clusters, Table 3) reflects the rate constants of O_2 activation on uncovered Pt surfaces ($0.5K_{2a}k_{2bf}$; Eq. 20). The effective rate constants, unlike those for other regimes, depend strictly on the sticking coefficients of O_2 and remain insensitive to cluster size (1.8 nm-8.5 nm) because O_2 dissociation is a non-activated step (~ 3 kJ mol^{-1}; Table 1).

Effects of Pt cluster size on reactive collision probabilities of CH_4 ($r_{CH_4}(CH_4)^{-1}$) are shown here to be different for CH_4-O_2 reactions in each kinetic regime, as expected because the reactive collision probabilities in each regime reflect different elementary rate constants depending on the identity of the kinetically-relevant step and the involvement of Pt atoms and oxygen vacancies. The effective rate constants were found to either increase (regimes 1 and 2), decrease (regime 4), or remain insensitive (regime 3) with Pt cluster sizes, delineating by the O* coverages on Pt clusters.

2.3.7. Fundamental Relations between First-Order Rate Constants, O_2/CH_4 Ratios, and Oxygen Coverages and the Limits of Langmuirian Treatments of Surface Reactions. The seemingly complex kinetic behavior of catalytic CH_4-O_2 reactions on Pt clusters and the observed transitions among kinetic regimes depend on either the O_2 pressures (regime 1) or prevalent O_2/CH_4 (regimes 2 and 3) ratios, because these parameters set the oxygen chemical potentials (also the (oxygen virtual pressures) at surfaces and, in turn, the O* coverages during steady-state catalysis. CH_4 molecules colliding with clusters encounter a distribution of O*-O*, O*-* and *-* site pairs that is set by such O* coverages. Thus, the reactivity and rate equations in each kinetic regime (shown as the first-order rate constant $r_{CH_4}(CH_4)^{-1}$ in Figs. 3 and 14) reflect the predominance of a specific activating site and the identity of the respective kinetically-relevant step through the defining role of O* coverages (set by the O_2 pressures or O_2/CH_4 ratios).

At O_2/CH_4 ratios above 2 (regime 1, 873 K, 8.5 nm Pt clusters), O*-O* pairs prevalent on O*-saturated clusters activate C-H bonds in CH_4 reactants; O* coverages are unaffected by O_2 pressures at saturation and $r_{CH_4}(CH_4)^{-1}$ become true rate constants that reflect the reactive probability upon collisions with cluster surfaces. Oxygen vacancies (exposed Pt atoms) emerge at O_2/CH_4 ratios lower than 2 (regime 2, 873 K, 8.5 nm Pt clusters) and O*-* site pairs provide a more effective parallel C-H bond activation route. The number of * sites is set by the kinetic coupling between the steps that form them (C-H activation) and consume them (O_2 activation) and therefore by O_2/CH_4 ratios (Eq. 18). The $r_{CH_4}(CH_4)^{-1}$ values are no longer constant but inversely proportional to O_2/CH_4 ratios. At O_2/CH_4 ratios near the point of O_2 depletion (<0.08, regime 3, 873 K, 8.5 nm Pt clusters), rates become limited by O_2 activation and proportional to O_2 pressure, causing rate constants ($r_{CH_4}(CH_4)^{-1}$) to increase linearly with O_2/CH_4 ratios.

These rate equations are based on non-interacting O* and * species and elementary steps with rate and equilibrium constants that do not depend on coverages, an assumption that becomes rigorous at the extremes of bare (regimes 3 and 4) and O*-saturated (regime 1) clusters. Such assumptions also seem appropriate near the transition between regimes 1 and 2, for which vacancies are isolated minority species on nearly

saturated surfaces. As the system approaches the transition between regimes 2 and 3, rate and equilibrium constants and the binding energy and reactivity of O* species are expected to vary with O* coverage, causing deviations from the kinetic behavior expected of uniform surfaces. These considerations are borne out by the deviations between the predictions from Equation 11 for regime 2 and the data shown in Figure 7 near the transition between regimes 2 and 3 ($CH_4/O_2 > 8$). These effects reflect the formation of diverse structures in which the number of vicinal vacancies differ, leading to concomitant changes in the binding energy of CH_3 fragments on exposed metals and in the reactivity and binding energy of neighboring O* species. These subtle transitions between surfaces that cannot be rigorously treated as Langmuirian ensembles require the adoption of more realistic DFT-based theoretical descriptions combined with kinetic Monte Carlo simulations. We have carried out these simulations using DFT-derived rate and equilibrium parameters on model Pt(111) surfaces, as will be described in detail elsewhere.

2.4. Conclusions

A simple sequence of elementary reaction steps is proposed based on kinetic dependencies, kinetic isotope effects, isotopic exchange evidence, and density functional theory results to describe the seemingly complex reaction kinetics observed during CH_4 reactions with O_2, H_2O, or CO_2 oxidants on supported Pt clusters. Four kinetic regimes, each with a unique rate equation and kinetic dependence, are detected. These regimes are resulted from changes in the identity of kinetically-relevant steps and active site structures in response to a transition in surface O* coverages on Pt from saturation to uncovered. C-H bond activation steps are kinetically-relevant in three of the four regimes but proceed via mechanistically different paths on O*-O*, O*-*, or *-* site pairs, where their relative distribution depend on O* coverages. In a narrow regime before the complete O_2 depletion, C-H bond activation steps become kinetically-irrelevant and O_2 activation on uncovered Pt clusters limits the CH_4 conversion rates.

C-H bond activation on O*-O* site pairs proceeds via an O* assisted hydrogen abstraction route and involves the formation of a radical-like transition state complex with low entropy losses and high activation barriers. In contrast, C-H bond activation on *-* site pairs proceeds via an oxidative addition of one of the Pt atoms in *-* pairs into the C-H bond, forming a three-centered Pt-C-H transition state. C-H bond activation on O*-* site pairs occurs via similar oxidative Pt atom addition steps but with O* assisting the H abstraction step. The barriers for C-H bond dissociation on O*-O* and O*-* site pairs are related to the reactivity of the O* in carrying out the H abstraction step and thus, are correlated to the oxygen binding strengths. C-H bond activation barriers on O*-* site pairs are also related to the binding strength of CH_3 on exposed Pt atoms, as also found for similar steps on *-* site pairs, because both of these steps involve the oxidative addition of Pt atoms in the C-H bond.

Reactive collision probabilities of CH_4 (also the pseudo first-order rate constants, $r_{CH_4}(CH_4)^{-1}$) are a single-value function of O_2/CH_4 ratios because they are either i) insensitive to O_2/CH_4 ratios on O* saturated or uncovered surfaces or ii) depend strictly on O_2/CH_4 ratios that set the O* coverages on Pt surfaces. The Pt cluster size and specifically, Pt coordination numbers and O* binding strengths, influence rates differently

in each of these regimes depending on the associated kinetically-relevant steps. When O* atoms are involved in assisting the C-H bond activation steps (i.e. on O*-O* and O*-* site pairs), the first-order rate constants are higher for larger Pt clusters because weakly adsorbed O* atoms prevalent on larger clusters are more effective than the strongly adsorbed O* for the hydrogen abstraction steps. C-H bond activation on *-* site pairs, however, exhibits the exact opposite trend because coordinatively less saturated Pt atoms prevalent on small clusters form stronger metal-carbon bond with CH_3 in the transition state, thus stabilizing the transition state energy and lowering the barriers. In the regime that O_2 dissociation controls rates, CH_4 turnover rates are insensitive to cluster sizes because kinetically-relevant O_2 dissociation steps are non-activated and determined strictly by the O_2 collision rates.

We show that the diversity of rate dependencies, activation enthalpies and entropies, cluster size effects in CH_4-O_2 reactions on Pt surfaces are rigorously described by a shift in the identity of kinetically-relevant steps and active site structures in response to changes in oxygen coverages and their reactivities and, in turn, the oxygen chemical potentials on catalytic surfaces.

2.5. References

[1] Twigg, M.V. *Catalyst Handbook*, 2nd ed.; Manson: London, 1994.
[2] Rostrup-Nielsen, J. R. *Catal. Today* **1993**, *18*, 305.
[3] Rostrup-Nielsen, J. R.; Sehested, *J. Adv. Catal.* **2002**, *47*, 65.
[4] Rostrup-Nielsen, J. R. Catalytic Steam Reforming. In *Catalysis Science and Technology;* Andersen, J. R., and Boudart, M., Eds.; Springer, Berlin, **1984**, *5*, 1.
[5] Wei, J. M.; Iglesia, E. *J. Catal.* **2004**, *224*, 370.
[6] Wei, J. M.; Iglesia, E. *J. Catal.* **2004**, *225*, 116.
[7] Wei, J. M.; Iglesia, E. *J. Phys. Chem. B* **2004**, *108*, 4094-4103.
[8] Wei, J. M.; Iglesia, E. *Angew. Chem., Int. Ed.* **2004**, *43*, 3685.
[9] Wei, J. M.; Iglesia, E. *Phys. Chem. Chem. Phys.* **2004**, *6*, 3754.
[10] Wei J. M.; Iglesia, E. *J. of Phys. Chem. B* **2004**, *108*, 7253.
[11] Yamaguchi, A.; Iglesia, E. *J of Catal.*, **2010**, *274*, 52.
[12] Ashcroft, A. T.; Cheetham, A. K.; Green, M. L. H.; Vernon, P. D. F. *Nature* **1991**, *352*, 225.
[13] Prettre, M.; Eichner, C.; Perrin, M. *Transactions of the Faraday Society* **1946**, *42*, 335.
[14] Vernon, P. D. F.; Green, M. L. H.; Cheetham, A. K.; Ashcroft, A. T. *Catal. Lett.* **1990**, *6*, 181.
[15] Ashcroft, A. T.; Cheetham, A. K.; Foord, J. S.; Green, M. L. H.; Grey, C. P.; Murrell, A. J.; Vernon, P. D. F. *Nature* **1990**, *344*, 319.
[16] Aasberg-Petersen, K.; Hansen J. H. B.; Christensen, T. S.; Dybkjaer, I.; Christensen, P. S.; Nielsen, C. S.; Madsen, S.; Rostrup-Nielsen, J. R. *Appl. Catal. A* **2001**, *221*, 379.
[17] Hickman, D. A.; Schmidt, L. D. *Science* **1993**, *259*, 343.
[18] Hickman, D. A.; Haupfear, E. A.; Schmidt, L. D. *Catal. Lett.* **1993**, *17*, 223.
[19] Mhadeshwar A. B.; Vlachos, D. G. *Ind. & Engr. Chem. Res.* **2007**, *46*, 5310.
[20] O'Connor A. M.; Ross J. R. H. *Catal. Today* **1998**, *46*, 203.
[21] Heitnes, K.; Lindberg, S.; Rokstad, O. A.; Holmen, A. *Catal. Today* **1995**, *24*, 211.
[22] van Looij, F; Stobbe, E. R.; Geus, J. W. *Catal. Lett.* **1998**, *50*, 59.
[23] Dissanayake, D.; Rosynek, M. P.; Kharas, K. C. C.; Lunsford, J. H. *J. Catal.* **1991**, *132*, 117.
[24] Beretta, A.; Gianpiero, G.; Lualdi M.; Tavazzi, I.; Forzatti, P. *Ind. Eng. Chem. Res.* **2009**, *48*, 3825.
[25] Enger, B. C.; Lødeng, R.; Holmen, A. *Appl. Catal.* **2008**, *346*, 1.
[26] Chin, Y-H.; Buda, C.; Neurock, M.; Iglesia, E. *J. Catal.* submitted.
[27] Chin, Y-H.; Buda, C.; Neurock, M.; Iglesia, E. in preparation.
[28] David, R. L. *Handbook of Chemistry and Physics*, 87th ed.; CRC Press: Boca Raton, FL, 2006; 4-81.
[29] Abild-Pedersen, F.; Lytken, O.; Engbaek, J.; Nielsen, G.; Chorkendorff, I.; Norskov, J. K. *Surf. Sci.* **2005**, *590(2-3)*, 127.
[30] Anghel, A. T.; Wales, D. J.; Jenkins, S. J.; King, D. A. *Phys. Rev. B.* **2005**, *71*, 11.
[31] Bunnik, B. S.; Kramer, G. J. *J. Catal.* **2006**, *242(2)*, 309.
[32] Burghgraef, H.; Jansen, A. P. J.; van Santen, R. A. *Surf. Sci.* **1995**, *324(2-3),* 345.

[33] Ciobica, I. M.; Frechard, F.; van Santen, R. A.; Kleyn, A. W.; Hafner, J. A. *J. Phys. Chem. B.* **2000**, *104(14)*, 3364.
[34] Henkelman, G.; Jonsson, H. *Phys. Rev. Lett.* **2001**, *86(4)*, 664.
[35] Jones, G.; Jakobsen, J. G.; Shim, S. S.; Kleis, J.; Andersson, M. P.; Rossmeisl, J.; Abild-Pedersen, F.; Bligaard, T.; Helveg, S.; Hinnemann, B.; Rostrup-Nielsen, J. R.; Chorkendorff, I.; Sehested, J.; Norskov, J. K. *J. Catal.* **2008**, *259(1)*, 147.
[36] Kokalj, A.; Bonini, N.; Sbraccia, C.; de Gironcoli, S.; Baroni, S. *J. Am. Chem. Soc.* **2004**, *126(51)*, 16732.
[37] Kokalj, A.; Bonini, N.; de Gironcoli, S.; Sbraccia, C.; Fratesi, G.; Baroni, S. *J. Am. Chem. Soc.* **2006**, *128(38)*, 12448.
[38] Pallassana, V.; Neurock, M. *J. Catal.* **2000**, *191(2)*, 301.
[39] Petersen, M. A.; Jenkins, S. J.; King, D. A. *J. Phys. Chem. B.* **2004**, *108(19)*, 5909.
[40] Vines, F.; Lykhach, Y.; Staudt, T.; Lorenz, M. P. A.; Papp, C.; Steinruck, H. P.; Libuda, J.; Neyman, K. M.; Gorling, A. *Chem.--Eur. J.* **2010**, *16(22)*, 6530.
[41] Weaver, J. F.; Hakanoglu, C.; Hawkins, J. M.; Asthagiri, A. *J. Chem. Phys.* **2010**, *132(2)*, 024709.
[42] Zhang, C. J.; Hu, P. *J. Chem. Phys.* **2002**, *116(1)*, 322.
[43] Kresse, G.; Hafner, J. *Phys. Rev. B* **1994**, *49*, 14251.
[44] Kresse, G.; Furthmuller, *J. Comput. Mater. Sci.* **1996**, *6*, 15.
[45] Kresse, G.; Furthmuller, *J. Phys. Rev. B* **1996**, *54*, 11169.
[46] Perdew, J. P.; Chevary, J. A.; Vosko, S. H.; Jackson, K. A.; Pederson, M. R.; Singh, D. J.; Fiolhais, C. *Phys. Rev. B* **1992**, *46*, 6671.
[47] Vanderbilt, D. *Phys. Rev. B* **1990**, *41*, 7892.
[48] Van Hardeveld, R.; Hartog, F. *Surf. Sci*, **1969**, *15*, 189.
[49] Monkhorst, H. J.; Pack, J. D. *Phys. Rev. B* **1976**, *13*, 5188.
[50] Henkelman, G.; Uberuaga, B. P.; Jonsson, H. *J. Chem. Phys.* **2000**, *113*, 9901.
[51] Henkelman, G.; Jonsson, H. *J. Chem. Phys.* **2000**, *113*, 9978.
[52] Sheppard, D.; Terrell, R.; Henkelman G. *J. Chem. Phys.* **2008**, *128*, 134106.
[53] The CH_4-CD_4 cross exchange rates were calculated from the sum of CH_3D, CHD_3, and two times the CH_2D_2 concentrations. The CH_4-CD_4 exchange rates from Al_2O_3 supports were comparable to those on Pt clusters for the 0.2 % wt. Pt/Al_2O_3 catalyst. SiO_2 support, however, gives negligible CH_4-CD_4 exchange rates. CH_4-CD_4 exchange rates during CH_4-CD_4–O_2 were measured on a 0.2 % wt. Pt/SiO_2 catalyst to eliminate the contribution from support.
[54] Boudart, M. *J. Phys. Chem.* **1983**, *87*, 2786.
[55] Kemball, C. *Discuss. Faraday Soc.* **1966**, *41*, 190.
[56] Boudart, M. *Catal. Lett.* **1989**, *3*, 111.
[57] Temkin, M.; Pyzhez, *V. Zhur. Fiz. Xhim.* ***1939***, *13*, 851.
[58] Yu, S. Y.; Biscardi, J. A.; Iglesia, E. *J. Phys. Chem. B* **2002**, *106*, 9642.
[59] Weiss, B. M.; Iglesia E. *J. Phys. Chem. C*, *113*, **2009**, 13331.
[60] Muller, O.; Roy, R. *J. of Less-Common Metals* **1968**, *16*, 129.
[61] McCarty, J. G. *Catal. Today* **1995**, *26*, 283.
[62] Chin Y-H.; Buda C.; Neurock, M.; Iglesia, E., in preparation.
[63] Eichler, A.; Mittendorfer F.; Hafner, J. *Phys. Rev. B*, **2000**, *62*, 4755.

[64] Tang, H. R.; Van der Ven, A.; Trout, B. L. *Phys. Rev. B*, **2004**, *70*, 045420.
[65] Legare, P. *Surf. Sci.* **2005**, *580*, 137.
[66] Getman, R. B.; Xu, Y.; Schneider, W. F. *J. Phys. Chem. C* **2008**, *112*, 9559.
[67] Weaver, J. F.; Chen, J. J.; Gerrard, A. L. *Surf. Sci.* **2005**, *592*, 83.
[68] Benson, J. E.; Boudart, M. *J. Catal.* **1965**, *4*, 704.
[69] Pre-exponential factor is estimated using transition state theory treatment on the C-H bond activation step by assuming that the CH_4(g) reactant formed a mobile transition state complex, which retained two translational degree of freedom. The contributions from the rotational and vibrational partition functions on the pre-exponential factors are unimportant compared to that of translational partition functions.
[70] Buda C.; Neurock, M. 2009 Unpublished results.
[71] Rozanska, X.; Kondratenko, E. V.; Sauer, J. *J. of Catal.* **2008**, *256*, 84.
[72] Lunsford, J. H. *Angew. Chem., Int. Ed.* **1995**, *34,* 970.
[73] Fujimoto K.; Ribeiro, F. H.; Avalos-Borja, M.; Iglesia, E. *J. Catal.* **1998**, *179,* 431.
[74] Ishikawa, A.; Neurock, M.; Iglesia, E. *J. Am. Chem.* Soc. **2007**, *129*, 13201.
[75] Crabtree, R. H. *The Organometallic Chemistry of Transition Metals*; J. Wiley and Sons, 1994.
[76] Cundari, T. R.; Grimes, T. V.; Gunnoe, T. B. *J. Am. Chem.* Soc. **2007**, *129*, 13172.
[77] Cummins, C. C.; Baxter, S. M.; Wolczanski, P. T. *J. Am. Chem.* Soc. **1988**, *110*, 8731.
[78] Cummins, C. C.; Schaller, C. P.; Van Duyne, G. D.; Wolczanski, P. T.; Chan, A. W. E.; Hoffmann, R. *J. Am. Chem.* Soc. **1991**, *113*, 2985.
[79] The O* binding strengths were defined as the energies required to remove an O* from the O* covered Pt(111) surfaces, also the absolute values of the reaction energies for the nO*/Pt(111)→ (n-1)O*/Pt(111)+O reactions.
[80] Madix, R. J.; Roberts, J. T. The Problem of Heterogeneously Catalyzed Partial Oxidation: Model Studies on Single Crystal Srufaces. In *Surface Reactions*, Madix, R. J., Ed.; Springer-Verlag, **1994**; 5-53.
[81] van Santen, R. A.; Neurock, M.; Shetty, S. G. *Chem. Rev.* **2010**, *110*, 2005.
[82] Wasileski, S.A.; Janik, M.J.; Plaisance, C.P.; Van Santen, R. A.; Neurock, M. A First Principles Analysis of Periodic Trends in the C-H and O-H Activation over Closed Packed Transition Metal Surfaces. *J. Phys. Chem. C*, to be submitted.
[83] Weiss, B. M.; Iglesia, E. *J. Catal*., **2010**, *272*, 74.
[84] Campbell, C. T.; Ertl, G.; Kuipers, H.; Segner, J. *Surf. Sci.* **1981**, *107*, 220.
[85] Dumesic, J. A.; Rudd, D. R.; Aparicio, L. M.; Rekoske, J. E.; Trevino, A. A. *The Microkinetics of Heterogeneous Catalysis*; ACS Professional Reference Book: Washington, D. C., 1993; 40.
[86] Allian A. D.; Takanabe K.; Fujdala, K. L.; Hao, X.; Truex, T. J.; Cai, J.; Buda, C.; Neurock, M.; Iglesia, E. *J. Am. Chem.* Soc., March 2, 2011, ASAP.
[87] Shan, B.; Zhao, Y.; Hyun, J.; Kapur, N.; Nicholas, J. B.; Cho, K. *J. Phys. Chem. C*, **2009**, *113*, 6088.
[88] Eichler, A.; Hafner, J. *Phys. Rev. Lett*., **1997**, *79*, 4481.
[89] Benziger, J. Thermochemical Methods for Reaction Energetics on Metal Surfaces. In *Metal-Surface Reaction Energetics: Theory and Applications to Heterogeneous*

Catalysis, Chemisorption, and Surface Diffusion, Shustorovich, E., Ed.; VCH, 1991; 53-107.

[90] Q_{2a} and Q_{2b} is equal to $-\Delta H_{2a}$ and $-\Delta H_{2b}$, the reaction enthalpies for Steps 2.1 and 2.2 in Scheme 2, respectively.

[91] Gland, J.L. *Surf. Sci.* **1980**, *93*, 487.

2.6. Figures

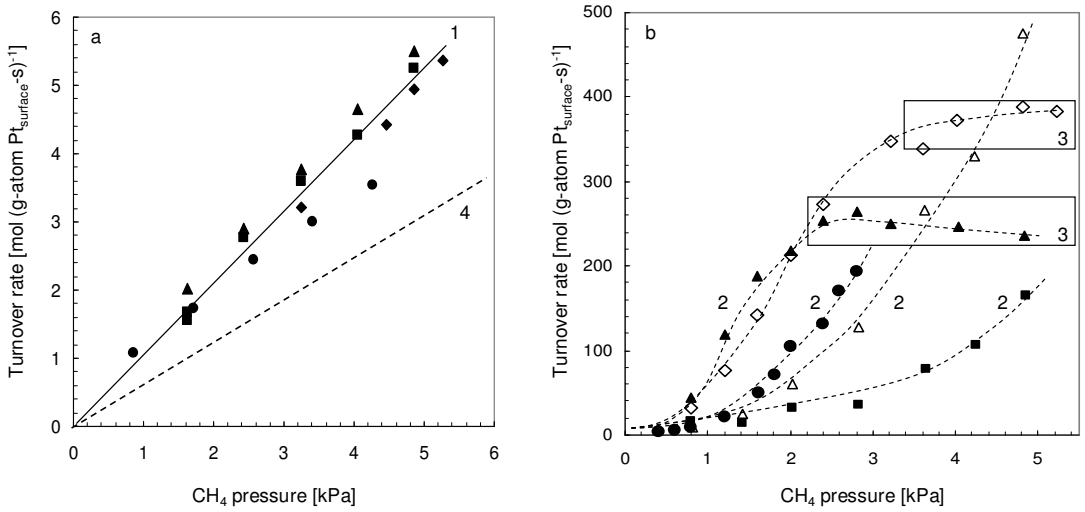

Figure 1a. CH_4 turnover rates (873 K) during CH_4-O_2 reactions at 8.1 kPa (■) and 22.7 kPa (▲) O_2 and during $^{13}CH_4$-O_2-CO_2 (♦) and CH_4-O_2-H_2O (●) reactions (22.7 kPa O_2, 5kPa CO_2 or H_2O) in regime 1 (labeled as **1**, $O_2/CH_4 > 2$) on Pt clusters (8.5 nm average cluster size) plotted against the CH_4 pressure. CH_4 reforming rates (regime 4, labeled as **4**, without O_2) are extrapolated using the rate constant reported in ref. [1] and shown here for comparison (**1:** regime 1, $O_2/CH_4 > 2$; **4:** regime 4, $O_2/CH_4 = 0$).

Figure 1b. CH_4 turnover rates (873 K) during CH_4-O_2 reactions on Pt clusters (8.5 nm average cluster size) for O_2 pressures of 0.17 kPa (▲), 0.27 kPa (◊), 0.39 kPa (●), 0.70 kPa (Δ), 1.6 kPa (■), as a function of CH_4 pressure for O_2/CH_4 ratios between 0.035 and 2. These rate data measured in regimes 2 and 3 (as defined by the O_2/CH_4 ratio) are labeled as **2** and **3**, respectively. (**2:** regime 2, $0.08 < O_2/CH_4 < 2$; **3:** regime 3, $0 < O_2/CH_4 < 0.08$).

(0.15 mg 0.2 % wt. Pt/Al_2O_3, 200 SiO_2/catalyst intraparticle (λ) and 4700 quartz/catalyst interparticle dilution (χ) ratios, 2.08 cm^3 (STP) s^{-1})

[1] Wei, J. M.; Iglesia, E. *J. Phys. Chem. B* **2004**, *108*, 4094-4103.

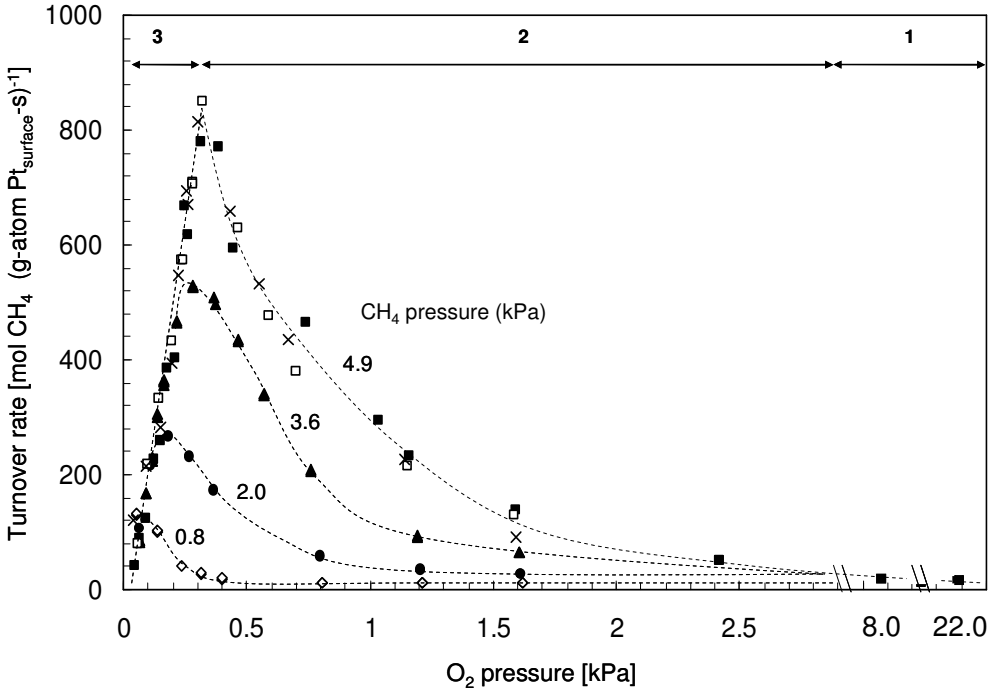

Figure 2. CH_4 turnover rates (873 K) during CH_4-O_2 reactions with 0.8 kPa (◊), 2.0 kPa (●), 3.6 kPa (▲), or 4.9 kPa (■) CH_4 and during $^{13}CH_4$-O_2-CO_2 (×) and CH_4-O_2-H_2O (□) reactions with either 5 kPa CO_2 or 5 kPa H_2O on Pt clusters (8.5 nm average cluster size) as a function of O_2 pressure. Kinetic regimes 1-3 are labeled as **1**-**3**, respectively.

(0.15 mg 0.2 % wt. Pt/Al_2O_3, 200 SiO_2/catalyst intraparticle (λ) and 4700 quartz/catalyst interparticle (χ) dilution ratios, 2.08 cm^3 (STP) s^{-1}; **1**, $O_2/CH_4 > 2$; **2**, $0.08 < O_2/CH_4 < 2$; **3**, $0 < O_2/CH_4 < 0.08$)

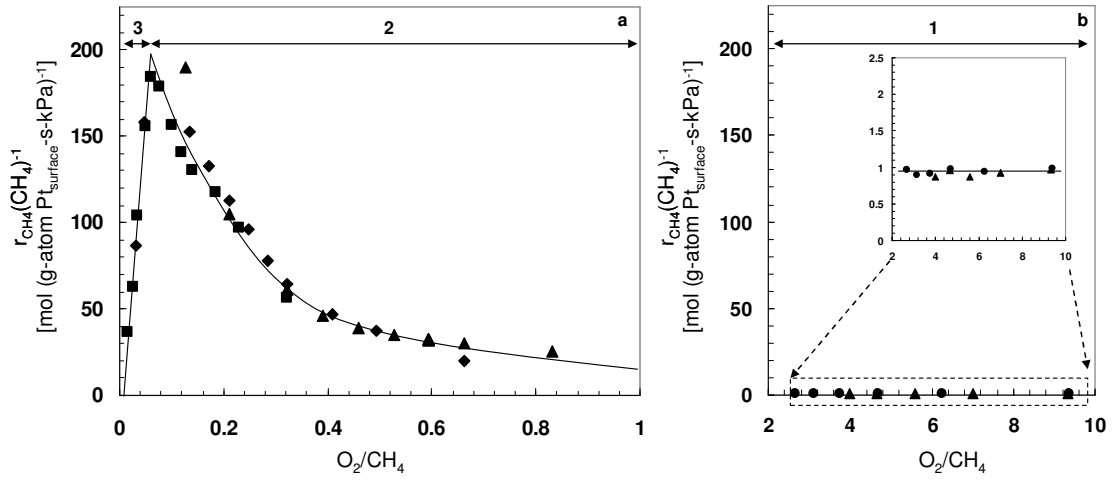

Figure 3a. Pseudo first-order rate constant ($r_{CH_4}(CH_4)^{-1}$) for CH_4-O_2 reactions as a single-valued function of O_2/CH_4 ratio on Pt clusters (8.5 nm average cluster size) with 1.2 kPa (●), 2.4 kPa (▲), and 4.8 kPa (■) CH_4 in kinetic regimes 2 (labeled as **2**, $0.08 < O_2/CH_4 < 2$) and 3 (labeled as **3**, $0 < O_2/CH_4 < 0.08$).

Figure 3b. Pseudo first-order rate constant ($r_{CH_4}(CH_4)^{-1}$) for CH_4-O_2 reactions as a single-valued function of O_2/CH_4 molar ratio on Pt clusters (8.5 nm average cluster size) with 8 kPa (♦), 15 kPa (●), 22 kPa (▲) O_2 in kinetic regime 1 (labeled as **1**, $O_2/CH_4 > 2$).

(0.15 mg 0.2 % wt. Pt/Al_2O_3, 873 K, 200 SiO_2/catalyst intraparticle (λ) and 4700 quartz/catalyst interparticle (χ) dilution ratios, 2.08 cm^3 (STP) s^{-1})

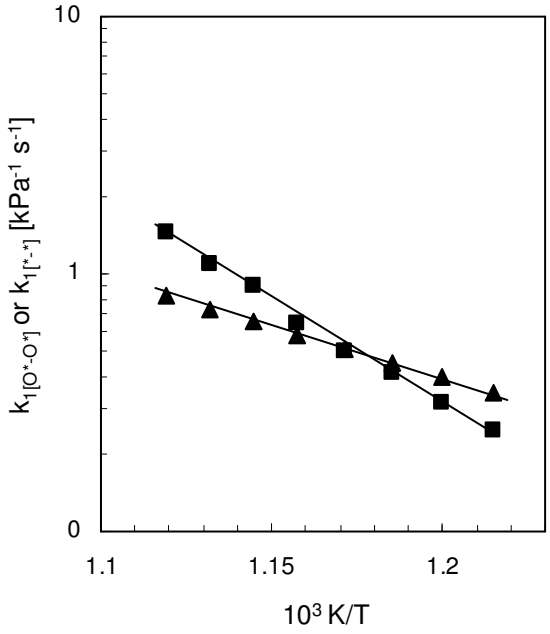

Figure 4. Arrhenius plots for CH_4 combustion (■, $k_{1[O^*-O^*]}$)[a] and steam reforming (▲, $k_{1[^*-^*]}$)[b] first-order rate constants on supported Pt clusters.

([a]8.5 nm Pt clusters, 0.15 mg 0.2 % wt. Pt/Al_2O_3, 2.08 cm^3 (STP) s^{-1}; [b]1.6 % wt. Pt/ZrO_2, calculated from kinetic parameters reported in ref. [2])

[2] Wei, J. M.; Iglesia, E. *J. Phys. Chem. B* **2004**, *108*, 4094-4103.

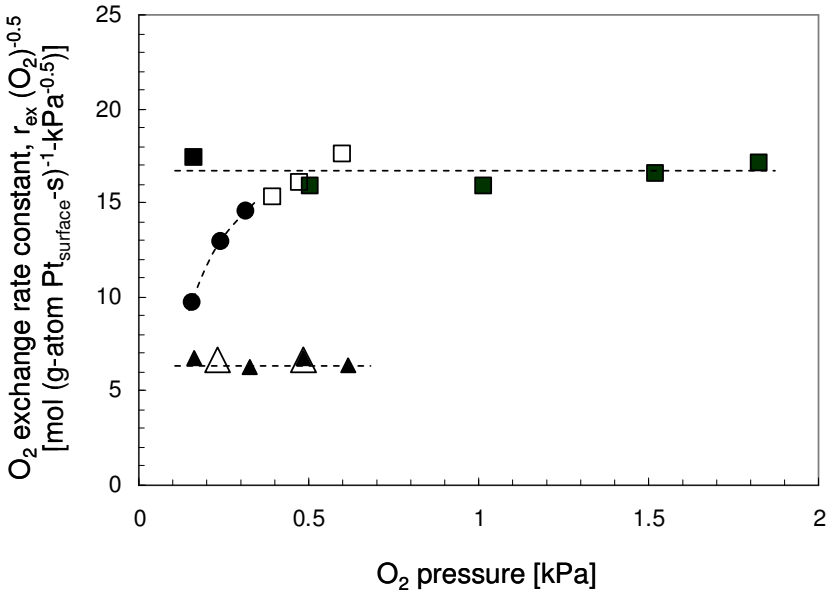

Figure 5. Isotopic oxygen-exchange rate constants ($r_{ex}(O_2)^{-0.5}$) of 0.2 % wt. Pt/Al_2O_3 (1.8 nm (▲, Δ) and 8.5 nm (■,□,●) Pt clusters) during $^{16}O_2$-$^{18}O_2$ (▲,■) and CH_4-$^{16}O_2$-$^{18}O_2$ (Δ, □, ●) reactions in kinetic regimes 1 (Δ, □) and 2 (●) at 873 K.

(200 SiO_2/catalyst intraparticle (λ) and 4700 quartz/catalyst interparticle (χ) dilution ratios, 2.08 cm^3 (STP) s^{-1}, 0.25-1.6 kPa CH_4 for CH_4-$^{16}O_2$-$^{18}O_2$ (Δ, □) reactions, $^{16}O_2/^{18}O_2$ = 1. Regime 1: O_2/CH_4 ratios > 0.3 and > 2 for 1.8 nm and 8.5 nm Pt clusters, respectively; regime 2: $O_2/CH_4 < 2$ for 8.5 nm Pt clusters)

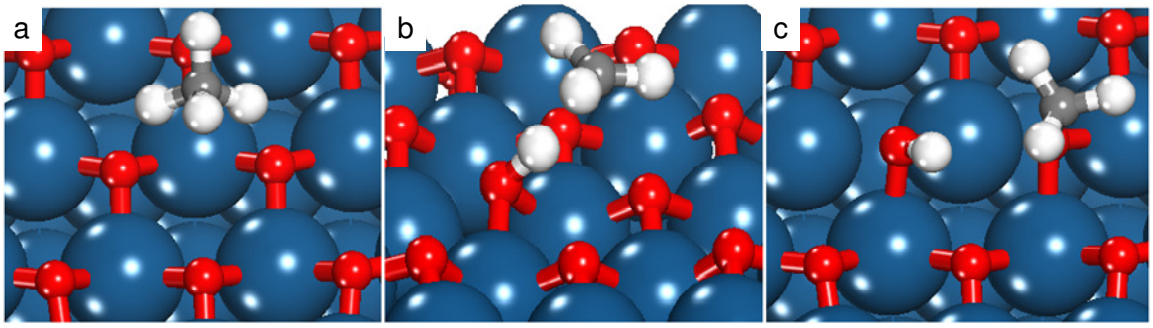

Figure 6. Structures of reactant (a, CH_4(g), O*-O*), transition state (b, O*--H_3C•--*$OH^{‡}$), and product (c, CH_3O*, OH*) for the initial C-H bond dissociation of CH_4 on O*-O* site-pairs formed from two O* atoms chemisorbed at terrace sites (sites V, Scheme 1) of the (111) facet of a Pt_{201} cluster saturated with chemisorbed oxygen atoms (O^*/O_{max}=1). O-H, C-H, and O-C bond lengths of the O*--CH_3•--$OH^{*‡}$ transition state complex are 0.104 nm, 0.170 nm, and 0.265 nm, respectively. (See Supporting Information Figure S-1 for the view of the entire Pt cluster.)

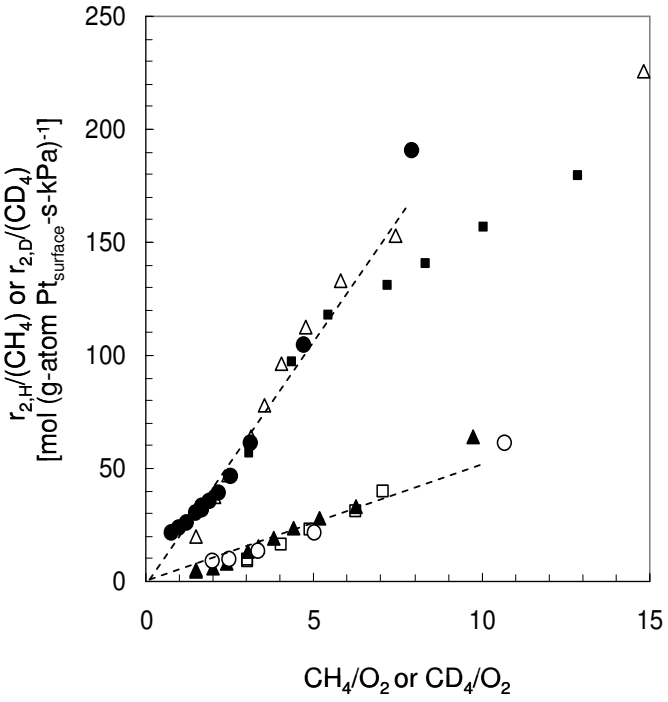

Figure 7. Pseudo first-order rate constants ($r_{2,H}(CH_4)^{-1}$ or $r_{2,D}(CD_4)^{-1}$) during CH_4 (or CD_4) reactions with O_2 on Pt clusters (8.5 nm average cluster size) in kinetic regime 2 as a function of CH_4/O_2 (or CD_4/O_2) ratios. (1.2 kPa (●), 2.4 kPa (Δ), 4.8 kPa (■) CH_4; 0.8 kPa (○), 2.4 kPa (▲), 4.8 kPa (□) CD_4).

(0.15 mg 0.2 % wt. Pt/Al_2O_3, 873 K, 200 SiO_2/catalyst intraparticle (λ) and 4700 quartz/catalyst interparticle (χ) dilution ratios, 2.08 cm^3 (STP) s^{-1})

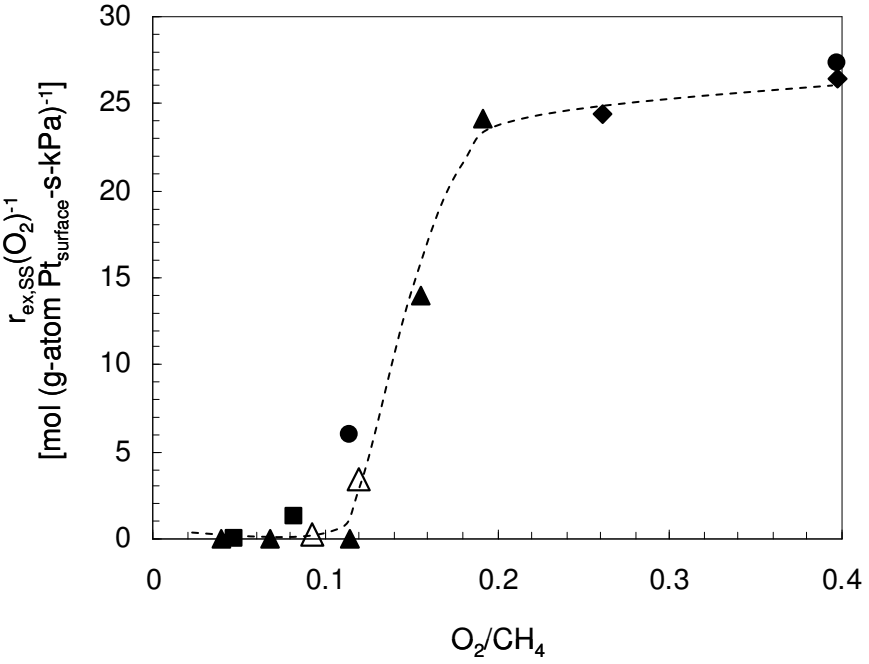

Figure 8. Pseudo first-order oxygen-exchange rate constants ($r_{ex,SS}(O_2)^{-1}$, 873 K) during CH_4-$^{16}O_2$-$^{18}O_2$ reactions on Pt clusters (8.5 nm average cluster size) for 0.6 kPa (♦), 1.2 kPa (●), 2.4 kPa (▲), 3.6 kPa (Δ), and 4.8 kPa (■) CH_4 plotted against the O_4/CH_4 reactant ratio.

(0.15 mg 0.2 % wt. Pt/Al_2O_3, 200 SiO_2/catalyst intraparticle (λ) and 4700 quartz/catalyst interparticle (χ) dilution ratios, 2.08 cm^3 (STP) s^{-1}, $^{16}O_2/^{18}O_2 = 1$)

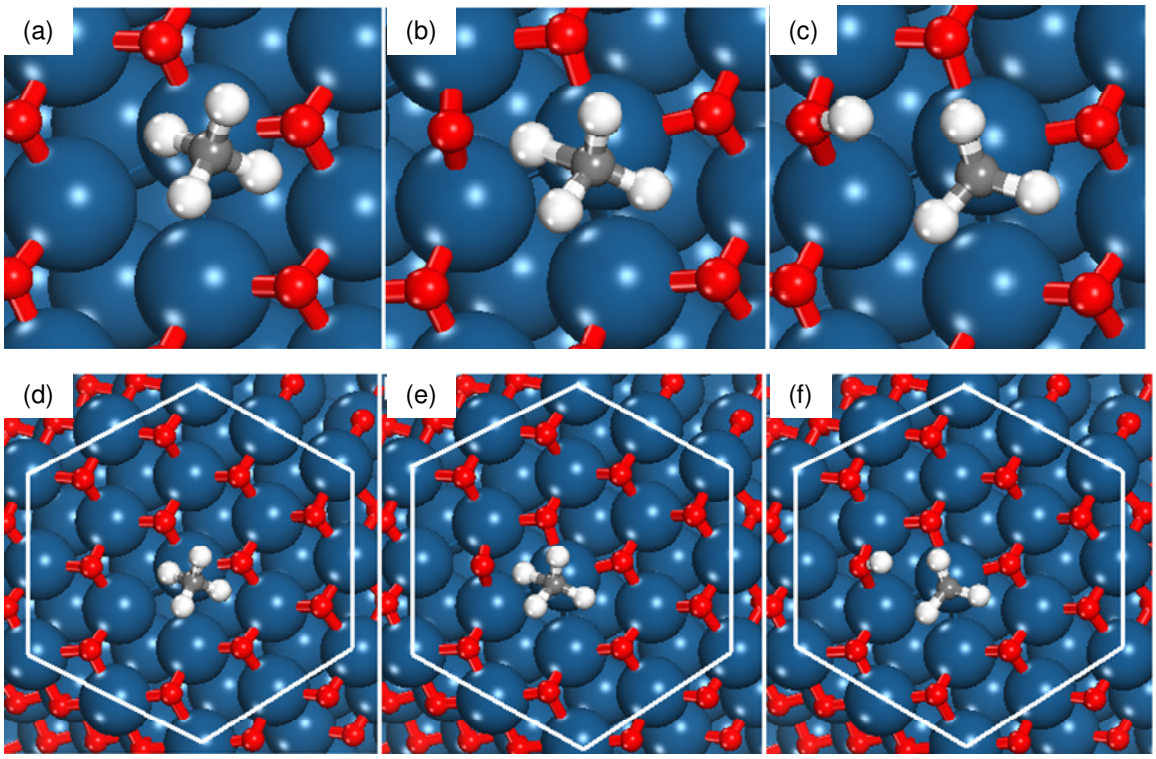

Figure 9. Structures of reactant (a, d CH_4(g), O*-*), transition (b, e $(H_3C$*--*$OH)^{‡}$), and product (c, f CH_3*, OH*) states for the initial C-H bond dissociation in CH_4 on O*-* site-pairs formed from an O* atom (site IV, Scheme 1) and a Pt atom (site 4, Scheme 1) on the (111) facet of a Pt_{201} cluster nearly saturated with chemisorbed oxygen atoms (O^*/O_{max}=0.99). O-H, C-H, and Pt-C bond lengths of the *--CH_3--*$OH^{‡}$ transition state complex are 0.149 nm, 0.128 nm, and 0.234 nm, respectively. (See Supporting Information Figure S-2 for the view of the entire Pt cluster.)

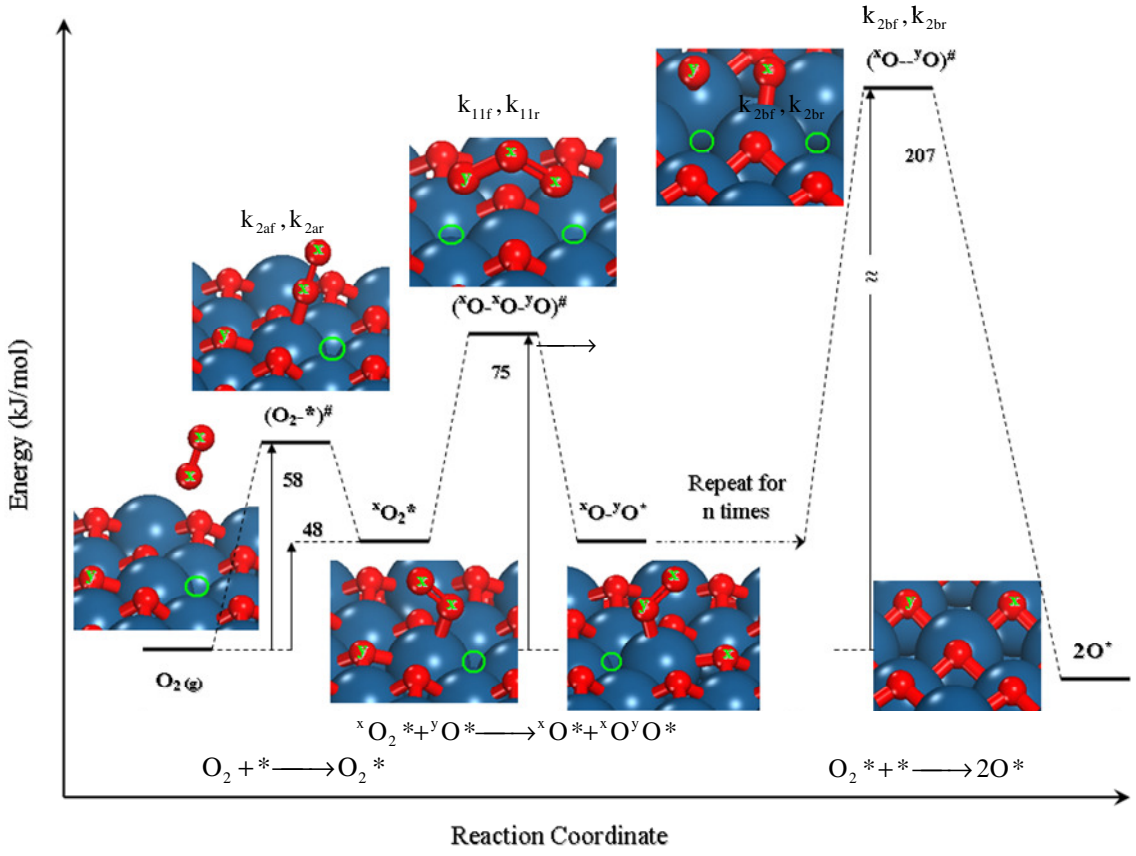

Figure 10. Reaction coordinate and structures of reactant, transition state, intermediate, and product for O_2 dissociation on the (111) facet of a Pt_{201} cluster nearly saturated with chemisorbed oxygen atoms where oxygen vacancies present as isolated species (O^*/O_{max}=0.99) (Green circle denotes oxygen vacancy; x and y are used to differentiate the O atoms involved in the steps; refer to Scheme 2 for the elementary reaction steps and rate constants).

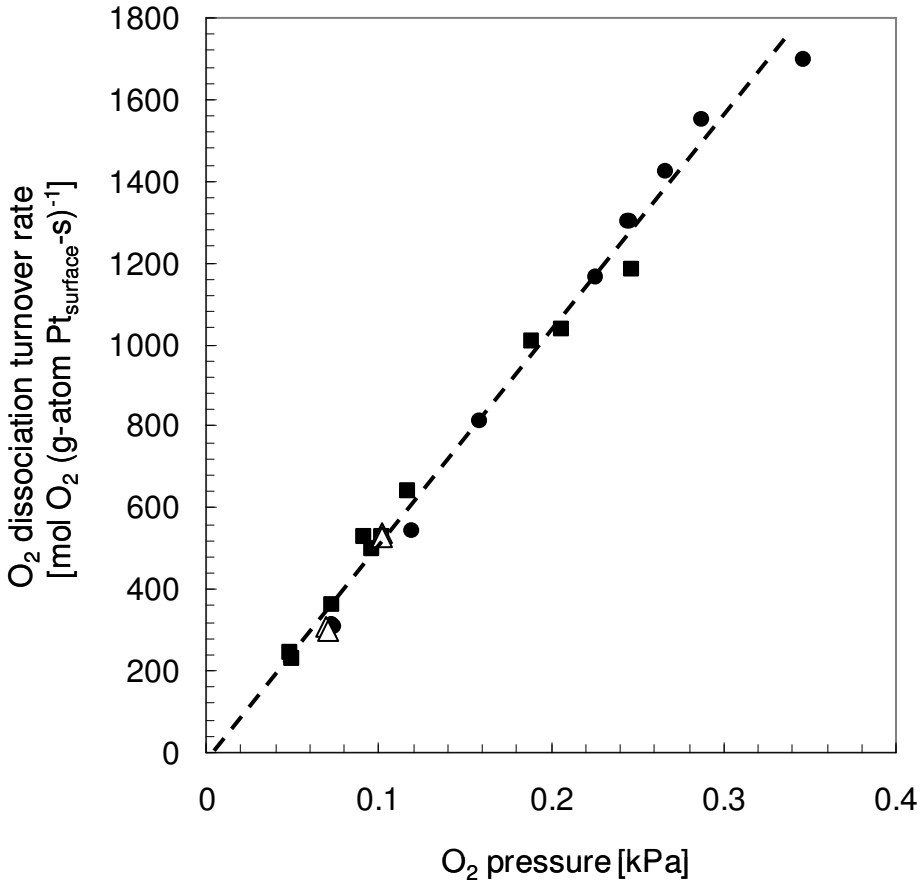

Figure 11. O_2 dissociation turnover rates (873K) during CH_4-O_2 (●), CD_4-O_2 (Δ), and CO-O_2 (■) reactions on Pt clusters (8.5 nm average cluster size) measured in kinetic regime 3 ($0 < O_2/CH_4 < 0.08$), in which O_2 dissociation is the sole kinetically-relevant step (Step 2.2, Scheme 2).

(0.15 mg 0.2 % wt. Pt/Al_2O_3, 4.9 kPa CH_4, 4.9 kPa CD_4, or 0.5-0.65 kPa CO, 200 SiO_2/catalyst intraparticle (λ) and 4700 quartz/catalyst interparticle (χ) dilution ratios, 2.08 cm^3 (STP) s^{-1})

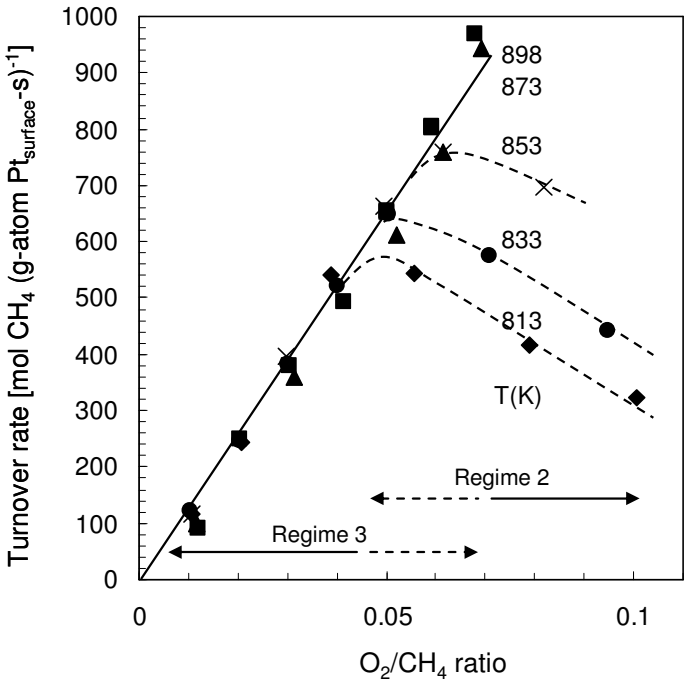

Figure 12. Effects of O_2/CH_4 ratio on CH_4 turnover rates during CH_4-O_2 reactions at 813 K (♦), 833 K (●), 853 K (×), 873 K (▲), and 898 K (■) in regimes 2 (- - -, dash line) and 3 (—, solid line) on Pt clusters (8.5 nm average cluster size).

(0.15 mg 0.2 % wt. Pt/Al_2O_3, 4.9 kPa CH_4, 200 SiO_2/catalyst intraparticle (λ) and 4700 quartz/catalyst interparticle (χ) dilution ratios, 2.08 cm^3 (STP) s^{-1})

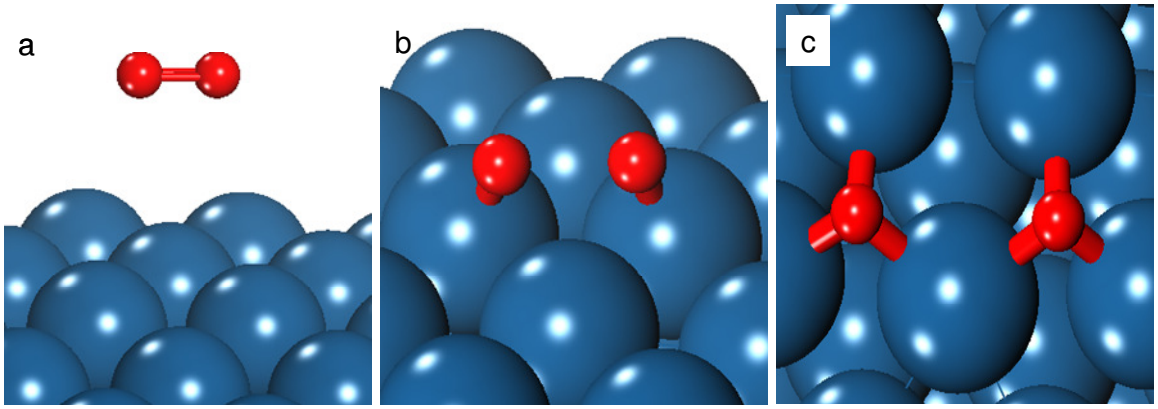

Figure 13. Structures of reactant (a, O_2(g)), transition state (b, $(*O\text{--}O*)^{\ddagger}$), and product (c, 2O*) during O_2* dissociation (Step 2.2, Scheme 2) on a Pt_{201} cluster uncovered of reactive intermediates. The $(O\text{--}O)^{\ddagger}$ bond length at the transition state is 0.184 nm.

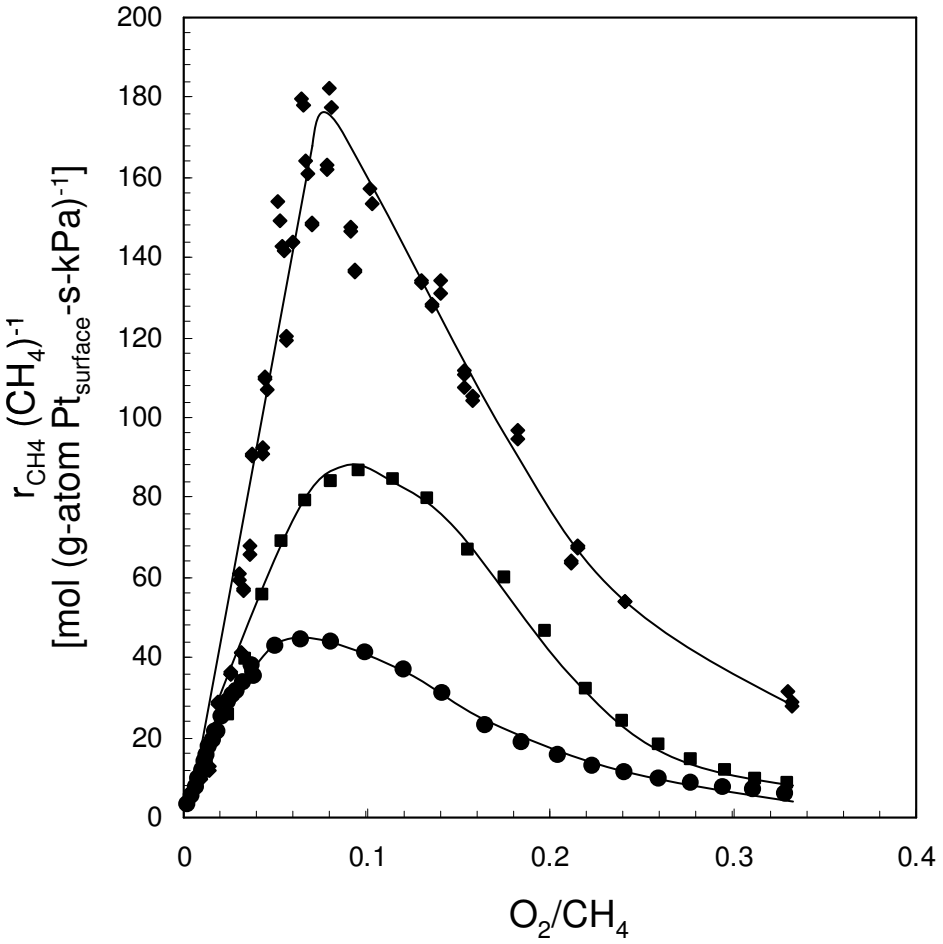

Figure 14. Generalized correlation of pseudo first-order rate constants, r $(CH_4)^{-1}$, and O_2/CH_4 ratio during CH_4-O_2 reactions on supported Pt clusters of different sizes (1.8 nm (●), 3.3 nm (■) , and 8.5 nm (♦) average cluster size) in kinetic regimes 2 and 3.

(0.15 mg 0.2 % wt. Pt/Al_2O_3, 200 SiO_2/catalyst intraparticle (λ) and 4700 quartz/catalyst interparticle (χ) dilution ratios, 2.08 cm^3 (STP) s^{-1})

2.7. Schemes

Scheme 1a and 1b. A 201 atom cubo-octahedral Pt cluster (1.8 nm cluster diameter) consists of eight (111) and six (100) facets and saturated with O* atoms. There are five distinct types of O* atoms (labeled I-V) and four types of Pt atoms (labeled 1-4) on the facets. O* atoms chemisorb on three-fold fcc sites on the (111) (types II, IV, and V) and two-fold bridge sites on the (100) (types I and III) facets. Saturation occurs at full coverage in which all of the sites I-V on the cluster are occupied by O* atoms.

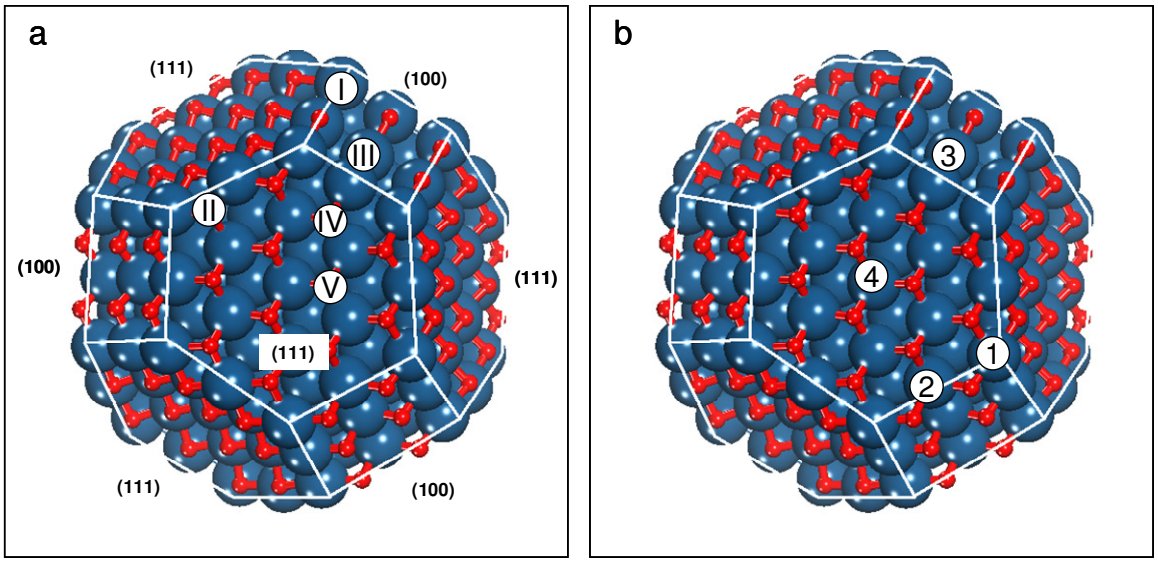

Scheme 2. Elementary steps for CH_4–O_2, CH_4–CO_2, CH_4–H_2O, and $^{16}O_2$-$^{18}O_2$ isotopic oxygen exchange reactions.

Step	Elementary reaction step	Rate and equilibrium constant
1.1	$CH_4 + O* + O* \longrightarrow CH_3O* + OH*$	$k_{1[O*-O*]}$
1.2	$CH_4 + O* + * \longrightarrow CH_3* + OH*$	$k_{1[O*-*]}$
1.3	$CH_4 + * + * \longrightarrow CH_3* + H*$	$k_{1[*-*]}$
2.1	$O_2 + * \rightleftharpoons O_2*$	k_{2af}, k_{2ar}
2.2	$O_2* + * \rightleftharpoons 2O*$	k_{2bf}, k_{2br}
3	$C* + O* \rightleftharpoons CO* + *$	k_3
4	$CO* + O* \leftrightarrows CO_2* + *$	k_{4f}, k_{4r}
5	$2\,H* \leftrightarrows H_2 + 2*$	K_{H_2}
6	$H* + O* \leftrightarrows OH* + *$	$K_{O*,H*}$
7	$CO_2* \leftrightarrows CO_2 + *$	K_{CO_2}
8	$2\,OH* \leftrightarrows H_2O* + O*$	K_{OH*}
9	$H_2O* \leftrightarrows H_2O + *$	K_{H_2O}
10	$CO* \leftrightarrows CO + *$	K_{CO}
11	$^{x}O_2* + {}^{y}O* \longrightarrow {}^{x}O* + {}^{x}O^{y}O*$ [a]	k_{11f}, k_{11r}

[a] x and y are used to differentiate the oxygen atoms. $\longrightarrow$ denotes an irreversible step and $\leftrightarrows$ a quasi-equilibrated step; k_{if} and k_{ir} are the forward and reverse rate coefficients of step i, respectively, and K_i is the equilibrium constant for step i.

2.8. Tables

Table 1. Rate equations, kinetically-relevant steps, kinetic parameters, and kinetic isotope effects for the various kinetic regimes during CH_4-O_2 reactions on 0.2 % wt. Pt/Al_2O_3 catalyst (8.5 nm average Pt cluster size).

Kinetic regime and MASI[a]	Rate equation	Kinetically-relevant step	Effective rate constant[b] (k_{eff})	Kinetic isotope effect[c] (873 K)	Apparent activation energy (kJ mol^{-1})	Pre-exponential factor (kPa^{-1} s^{-1})	Entropy loss (J mol^{-1} K^{-1})
Regime 1 (O*-O*)	$k_{eff1}(CH_4)$	$CH_4 + O* + O* \xrightarrow{k_{1[O*-O*]}} CH_3O* + OH*$	$k_{1[O*-O*]}$	1.66	155±9	2.1 x 10^{9}	12.2
Regime 2 (O*-*)	$k_{eff2}\frac{(CH_4)^2}{(O_2)}$	$CH_4 + O* + * \xrightarrow{k_{1[O*-*]}} CH_3* + OH*$	$\frac{2k_{1[O*-*]}^2}{(K_{2a}k_{2bf})}$	4.2± 0.3[d]	79	1.2 x 10^{6} [e] 5.8 x 10^{4} [f]	99.0 [g]
Regime 3 (*-*)	$k_{eff3}(O_2)$	$O_2 + 2* \xrightarrow{K_{2a}k_{2bf}} 2O*$	$0.5\,K_{2a}k_{2bf}$	1.0± 0.15[h]	<3±16	2800 [i]	118.8[j]
Regime 4 (*-*)	$k_{eff4}(CH_4)$	$CH_4 + * + * \xrightarrow{k_{1[*-*]}} CH_3* + H*$	$k_{1[*-*]}$	1.69[k] 1.77[l]	75[k] 83[l]	2.0 x 10^{4} [k] 5.9 x 10^{4} [l]	108.1[k] 99.2[l]

[a]Most abundant surface intermediates. [b]Rate and equilibrium constants are defined in Scheme 2. [c] $r_{CH_4}(r_{CD_4})^{-1}$. [d]Effective rate constants ($k_{eff2,H}$, $k_{eff2,D}$) in $r_{CH_4}(r_{CD_4})^{-1}$ term were determined by least-squares regression of $r_{CH_4}(CH_4)^{-1}$ versus CH_4/O_2 (or $r_{CD_4}(CD_4)^{-1}$ versus CD_4/O_2) data. [e]Apparent pre-exponential factor. [f]C-H bond dissociation pre-exponential factor, calculated from the apparent pre-exponential factor by assuming the pre-exponential factors for O_2 activation steps are the same for regimes 2 and 3. [g]Entropy loss for CH_4(g) upon the formation of $(H_3C*\text{--}*OH)^{\ddagger}$ transition state structures, calculated by assuming the pre-exponential factors for O_2 activation steps are the same for regimes 2 and 3. [h]Effective rate constants in $r_{CH_4}(r_{CD_4})^{-1}$ term determined by least-squares regression of r_{CH_4} versus O_2 pressure (or r_{CD_4} versus O_2 pressure). [i]Estimated based on non-activation O_2 dissociation steps (±195 kPa^{-1} s^{-1}). [j]Entropy loss for O_2 dissociation steps. [k]CH_4-H_2O (ref.3). [l] CH_4-CO_2 (ref. 1).

[3] Wei, J. M.; Iglesia, E. *J. Phys. Chem. B* **2004**, *108*, 4094-4103

Table 2. Average Pt coordination numbers, oxygen binding strengths on uncovered and O* saturated Pt clusters (201 atom, 1.8 nm diameter), C-H bond activation barriers on O*-O* site-pairs (regime 1), and the energies required to promote O* to reactive bridge sites ($\Delta E_{O^*promotion}$) for the various types of O* atoms on Pt_{201} clusters.

O*[a]	Average Pt coordination number for Pt atoms interact with the O*	O* binding strength on uncovered clusters (kJ mol^{-1})	O* binding strength at O* saturation[b] (kJ mol^{-1})	$\Delta E_{O^*promotion}$ [c] (kJ mol^{-1})	C-H bond activation barrier on O*-O* site-pair (kJ mol^{-1})
I	6.50	410	368	13	112
II	7.33	391	426	67	175
III	7.33	383	353	9	111
IV	8.33	375	352	99	170
V	9.00	372	271	44	149

[a]refer to Scheme 1 for the placement of O* atom. [b]defined by the O^*/O^*_{max} atomic ratio equals 1 where O^*_{max} is the total number of O* adsorption sites (sites I-V) on the Pt_{201} cluster. [c]energies required to promote the O* atom from the stable adsorption site to interact with the H.

Table 3. Effects of average Pt cluster sizes on rate constants for the various kinetic regimes during CH_4-O_2 reactions on 0.2 % wt. Pt/Al_2O_3 catalysts at 873 K.

	Kinetic regimes and effective rate constants (kPa^{-1} s^{-1})			
Average Pt cluster size (nm)	1 $k_{1[O^*-O^*]}$	2 $2k^2_{1[O^*-*]}(K_{2a}k_{2bf})^{-1}$	3 $0.5K_{2a}k_{2bf}$	4 (reforming)[a] $k_{1[*-*]}$
1.8 nm cluster[b]	0.44	5.7	2164	1.2
3.3 nm cluster[b]	0.58	9.7	2520	0.88
8.5 nm cluster	1.1	22	2800	0.53

(0.15 mg cat., 200 SiO_2/catalyst intraparticle (λ) and 4700 quartz/catalyst interparticle (χ) dilution ratios, 2.08 cm^3 (STP) s^{-1}, [a] from ref. [4], [b] initial rate constants[5])

[4] Wei, J. M.; Iglesia, E. *J. Phys. Chem. B* **2004**, *108*, 4094-4103.

[5] For the smaller Pt clusters (1.8 nm and 3.3 nm average diameters), the rate constants for regimes 1-3 decreased with the reaction time-on-stream. We rule out metal sintering as the cause of the activity decrease because these samples have been treated to higher temperatures (> 898 K). The decrease in rate constants with time are attributed to the gradual formation of a more stable chemisorbed O* layer on Pt surfaces upon the initial exposure to CH_4-O_2 feed mixtures, since the initial rate constants can be recovered after treating in H_2 (5 kPa, 873 K, > 600 s). Similar trends were also detected for supported Pd clusters, as will be reported in a separate contribution.

2.9. Supporting Information

2.9.1. Derivation of CH_4 reaction rates limited by C-H bond activation on O*-O* site-pairs on Pt surfaces. Pseudo steady-state assumptions on the surface species, together with the irreversible C-H bond activation on O*-O* site-pairs and quasi-equilibrated O_2 activation steps (Scheme 2), give the rate equation for CH_4 conversion on Pt surfaces covered with chemisorbed oxygen (O*), hydroxyl (OH*), and carbon dioxide (CO_2*) intermediates:

$$r_1 = \frac{k_{1[O^*\text{-}O^*]} K_{2a} K_{2b} (CH_4)(O_2)}{\left(1 + \sqrt{K_{2a} K_{2b} (O_2)} + \sqrt{\frac{K_{2a} K_{2b}}{K_{H_2O} K_{OH^*}} (O_2)(H_2O)} + \frac{(CO_2)}{K_{CO_2}}\right)^2} \quad \text{(S1)}$$

$$\downarrow \quad \downarrow \quad \downarrow \quad \downarrow$$

$$* \quad O^* \quad OH^* \quad CO_2$$

Similar assumptions, except that the O_2 activation steps are irreversible, lead to

$$r_1 = \frac{0.5\, K_{2a} k_{2bf} (O_2)}{\left(1 + \sqrt{\frac{K_{2a} k_{2bf} (O_2)}{2k_{1[O^*\text{-}O^*]} (CH_4)}} + \sqrt{\frac{(H_2O)}{K_{H_2O} K_{OH^*}} \left(\frac{K_{2a} k_{2bf} (O_2)}{2k_{1[O^*\text{-}O^*]} (CH_4)}\right)^{0.5}} + \frac{(CO_2)}{K_{CO_2}}\right)^2} \quad \text{(S2)}$$

$$\downarrow \quad \downarrow \quad \downarrow \quad \downarrow$$

$$* \quad O^* \quad OH^* \quad CO_2$$

where rate and equilibrium constants in these equations are defined in Scheme 2.
Both of the rate equations S1 and S2 can be simplified to

$$r_1 = k_{1[O^*\text{-}O^*]} (CH_4) \quad \text{(S3)}$$

when O* is the most abundant surface intermediate (MASI), as given by Eq. 3.

2.9.2. Derivation of isotopic $^{16}O_2$-$^{18}O_2$ exchange rate expression. We examine here plausible sequence of elementary steps during $^{16}O_2$-$^{18}O_2$ exchange reactions on Pt surfaces leading to $^{16}O^{18}O$ isotopologues. O_2 exchange proceeds via initial O_2 adsorption on a Pt atom (*) to form a bound O_2* species (Step 2.1, Scheme 2). Chemisorbed $^{16}O^{18}O$ isotopologues could form in the sequential steps via one of the two routes: (i) a step-wise mechanism involves dissociation of $^{x}O_2$* to ^{y}O* (herein and after x and y are used to differentiate the oxygen atoms of mass 16 and 18) followed by surface O* recombination (Step 2.2, Scheme 2), or (ii) concerted exchange of $^{x}O_2$* with a neighboring ^{y}O* atom (Step 11, Scheme 2). Desorption of $^{16}O^{18}O$* isotopologues from Pt surfaces leads to detection of $^{16}O^{18}O$ isotopologues in the reactor effluent. The surface O* concentrations are in chemical equilibrium with O_2 (g) during the $^{16}O_2$-$^{18}O_2$ exchange, which required that

$$r_{2af} = r_{2ar}\ ;\ r_{2bf} = r_{2br};\ r_{11f} = r_{11r} \quad \text{(S4a)}$$

$$k_{2af}(O_2)(*) = k_{2ar}(O_2*);\ k_{2bf}(O_2*)(*) = k_{2br}(O*)^2;\ k_{11f}(O_2*)(O*) = k_{11r}(O_2*)(O*) \quad \text{(S4b)}$$

The rates of $^{16}O^{18}O$ isotopologues formation acquired the following form depending on the relative rates of r_{2a}, r_{2b}, and r_{11}. We derived the O_2 exchange rate equation based on an equimolar $^{18}O_2$-$^{16}O_2$ reactant mixture. If the O_2 recombination rate is slower than both the rates of O_2 dissociation (Step 2.2, Scheme 2) and of $^xO_2*$ and $^yO*$ concerted exchange reaction (Step 11, Scheme 2), O_2 exchange rate is

$$r_{ex,eq} = k_{2ar}(^xO^yO*) = \frac{k_{2ar}(O_2)}{2\left(1 + K_{2a}(O_2) + \sqrt{K_{2a}K_{2b}(O_2)}\right)} \quad \text{(S5)}$$

This expression can be simplified to

$$r_{ex,eq,O*} = k_{2ar}(^xO^yO*) = \frac{k_{2ar}}{2}\left(\frac{K_{2a}}{K_{2b}}\right)^{0.5}(O_2)^{0.5} \quad \text{(S6)}$$

when O* is the MASI.

When the rates for O_2* dissociation are slow relative to that of O_2* desorption ($r_{2b} < r_{2a}$) and the rates of molecular exchange (Step 11, Scheme 2) is negligible ($r_{11} << r_{2b}$ and r_{2a}), then

$$r_{ex,eq} = k_{2br}(^xO*)\frac{(^yO*)}{L} = \frac{k_{2br}K_{2a}K_{2b}(O_2)}{2\left(1 + K_{2a}(O_2) + \sqrt{K_{2a}K_{2b}(O_2)}\right)^2}, \quad \text{(S7)}$$

which reduces to an apparent zero-order O_2 dependence if O* is the MASI. Similarly, if the concerted O_2* and O* exchange reaction is slow relative to the O_2* desorption rate ($r_{11} < r_{2a}$) and the rate of the recombinative desorption step is negligible ($r_{2b} << r_{2a}$ and r_{11}), then

$$r_{ex,eq} = k_{11f}(^xO_2*)\frac{(^yO*)}{L} = \frac{2k_{11f}K_{2a}^{1.5}K_{2b}^{0.5}(O_2)^{1.5}}{\left(1 + 2\sqrt{K_{2a}K_{2b}(O_2)} + 2K_{2a}(O_2)\right)^2} \quad \text{(S8)}$$

This equation is also Eq. 6a. When O* is the MASI, this equation simplifies to the equation below, which is also Eq. 6b:

$$r_{ex,eq,O*} = k_{11f}(^xO_2*)\frac{(^yO*)}{L} = \frac{k_{11f}}{2}\left(\frac{K_{2a}}{K_{2b}}\right)^{0.5}(O_2)^{0.5} \quad \text{(S9)}$$

An O_2 dependence remains unchanged at 0.5 throughout the range of O_2 pressure studied may indicate that the rates of $^{16}O^{18}O$ isotopologue formation can be described by Eq. S9. The O_2 pressure dependence is consistent with that observed on platinum film[6] and the detection of only predominantly $^{16}O^{18}O$ during temperature-programmed isotopic exchange of $^{16}O_2$ on Pt clusters chemisorbed with ^{18}O*.[7]

---

[6] G.K. Boreskov, *Discussions of the Faraday Society* **1966**, *41*, 263.

[7] Weiss, B. M.; Iglesia E. *J. Phys. Chem. C*, *113*, **2009**, 13331.

2.9.3. Structures of reactant, transition state, and product for the initial C-H bond dissociation in CH_4 on O*-O* site-pairs on Pt_{201} clusters saturated with chemisorbed oxygen atoms.

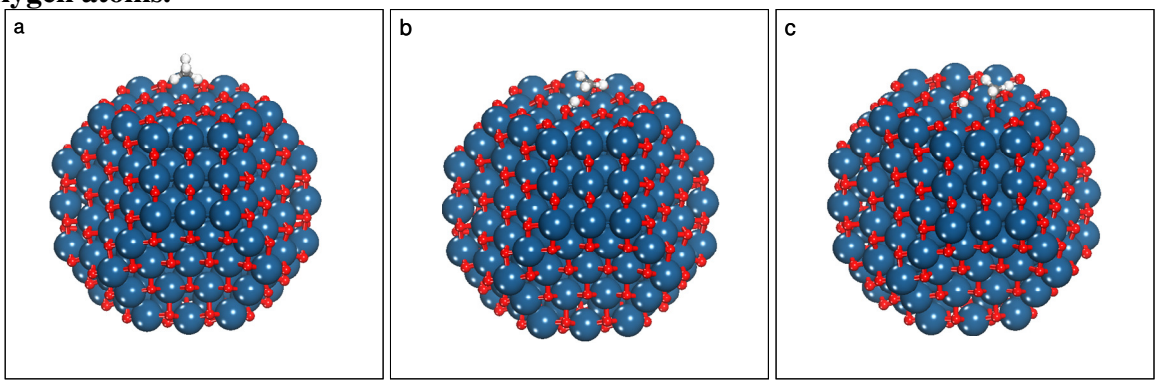

Figure S-1. Structures of reactant (a, CH_4(g), O*-O*), transition state (b, (O*--H_3C--HO*)‡), and product (c, CH_3O*, HO*) for the initial C-H bond dissociation in CH_4 on O*-O* site-pairs on Pt_{201} clusters saturated with chemisorbed oxygen atoms (O*/Pt_s=1.08 ML).

Table S-1. Geometries of transition and product states for C-H bond activation on O*-O* site-pairs (regime 1) for the various types of O* atoms (I-V, Scheme 1) on Pt_{201} cluster.

O*[1]	Transition state			Product state		
	C-H bond distance (nm)	O-H bond distance (nm)	C-O bond distance (nm)	C-H bond distance (nm)	O-H bond distance (nm)	C-O bond distance (nm)
I	0.152	0.111	0.270	0.253	0.100	0.145
II	0.169	0.104	0.280	0.332	0.099	0.142
III	0.144	0.116	0.259	0.275	0.100	0.145
IV	0.155	0.104	0.303	0.312	0.098	0.144
V	0.170	0.105	0.265	0.262	0.099	0.144

[1] refer to Scheme 1 for the placement of O* atom.

2.9.4. Derivation of the CH_4 turnover rate equation with the assumptions that irreversible C-H bond activation on O*-* site-pairs is the kinetically-relevant step. Kinetically-relevant C-H bond activation step on O*-* site-pairs, irreversible O_2 activation steps on *-* sites (Scheme 2), together with the assumption of pseudo steady-state balances of all reactive intermediates lead to the following rate equation:

$$r_2 = k_{1[O^*-^*]}(CH_4)(O^*)\frac{(^*)}{L}$$

$$r_2 == \frac{0.5K_{2a}k_{2bf}(O_2)}{\left(1+\frac{K_{2a}k_{2bf}(O_2)}{2k_{1[O^*-^*]}(CH_4)}+\left(\frac{(H_2O)}{K_{H_2O}K_{OH^*}}\right)^{0.5}\left(\frac{K_{2a}k_{2bf}(O_2)}{2k_{1[O^*-^*]}(CH_4)}\right)^{0.5}+\frac{1}{K_{CO_2}}(CO_2)\right)^2}$$

$$\downarrow \quad \downarrow \qquad \downarrow \qquad \downarrow$$

$$^* \quad O^* \qquad OH^* \qquad CO_2^*$$

(S10)

Rate and equilibrium constants are given in Scheme 2. Eq. S10 simplifies to Eq. S11 (also Eq. 9) when * and O* are the MASI:

$$r_{O^*-^*} = \frac{0.5K_{2a}k_{2bf}(O_2)}{\left(1+\frac{K_{2a}k_{2bf}(O_2)}{2k_{1[O^*-^*]}(CH_4)}\right)^2} \tag{S11}$$

In contrast, quasi-equilibrated O_2 activation steps on *-* would lead to the rate equation below:

$$r_2 = k_{1[O^*-^*]}(CH_4)(O^*)\frac{(^*)}{L}$$

$$r_2 = \frac{k_{1[O^*-^*]}(CH_4)\sqrt{K_{2a}K_{2b}(O_2)}}{\left(1+(K_{2a}K_{2b}(O_2))^{0.5}+\left(\frac{(H_2O)}{K_{H_2O}K_{OH^*}}\right)^{0.5}(K_{2a}K_{2b}(O_2))^{0.25}+\frac{1}{K_{CO_2}}(CO_2)\right)^2} \tag{S12}$$

which simplifies to S13 (also Eq. 10) when O* and * are the MASI.

$$r_{O^*-^*} = \frac{k_{1[O^*-^*]}(CH_4)(K_{2a}K_{2b}(O_2))^{0.5}}{\left(1+(K_{2a}K_{2b}(O_2))^{0.5}\right)^2} \tag{S13}$$

2.9.5. Structures of $(H_3C^*\text{--}^*OH)^{\ddagger}$ transition state complexes during C-H bond dissociation on O*-* site-pairs.

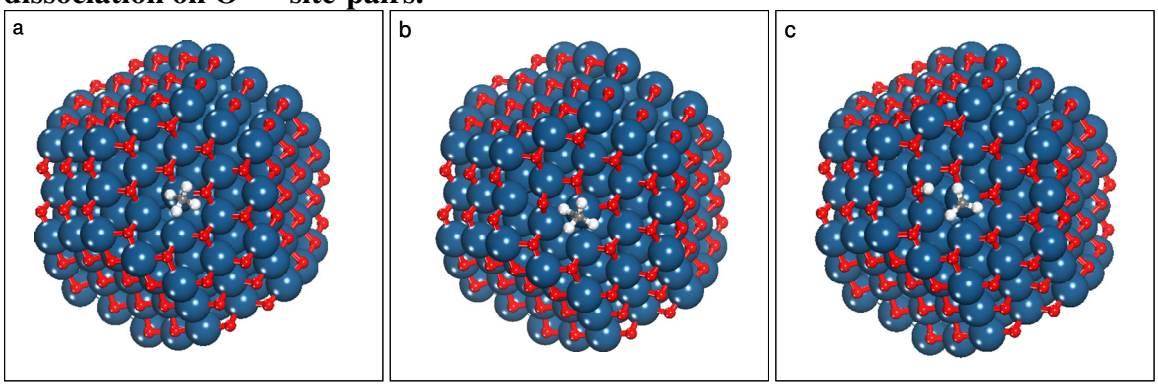

Figure S-2. Structures of reactant (a, CH_4(g), O*-*), transition state (b, $(H_3C^*\text{--}^*OH)^{\ddagger}$), and product (c, CH_3*, OH*) for the initial C-H bond dissociation in CH_4 on O*-* site-pairs formed from an O* atom (site IV, Scheme 1) and a Pt atom (site 4, Scheme 1) on the (111) facet of a Pt_{201} cluster nearly saturated with chemisorbed oxygen atoms (O^*/O_{max}=0.99). O-H, C-H, and Pt-C bond lengths of the $(H_3C^*\text{--}^*OH)^{\ddagger}$ transition state complex are 0.149 nm, 0.128 nm, and 0.234 nm, respectively.

2.9.6. Effects of O* binding strength on the barriers of C-H bond activation on O*-* site pairs. Figure S-3 shows the linear correlation between the DFT-calculated activation barrier for the initial C-H bond dissociation in CH_4 on oxygen-oxygen vacancy (O*-*) site pairs and O* binding energies (expressed here as heat of atomic oxygen adsorption, Q_{O*}) over Pt(111) surfaces.

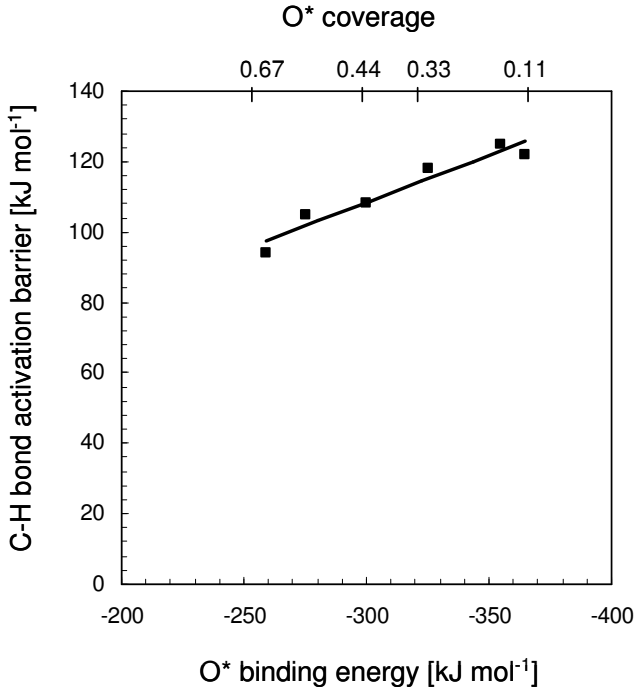

Figure S-3. Linear correlation between the DFT-calculated activation barriers for the initial C-H bond dissociation in CH_4 on oxygen-oxygen vacancy (O*-*) site pairs and O* binding energies (expressed here as heats of atomic oxygen adsorption, Q_{O*}) over Pt(111) surfaces covered with 0.11-0.67 ML of chemisorbed O*.

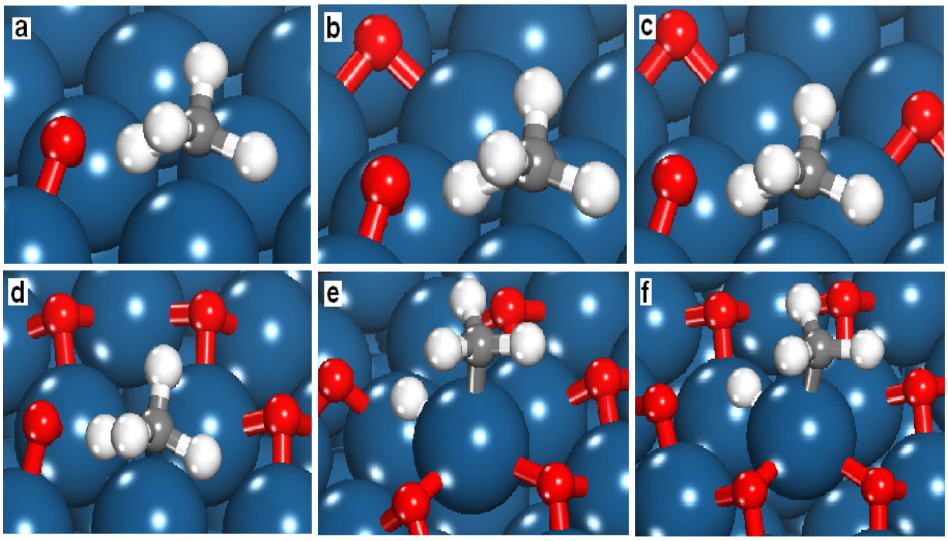

Figure S-4. Periodic DFT derived transition states for the initial C-H bond activation of methane assisted by the O*-* site-pairs on Pt(111) surfaces (Step 1.2, Scheme 1) covered with (a) 0.11 ML, (b) 0.22 ML, (c) 0.33 ML, (d) 0.44 ML, (e) 0.55 ML, and (f) 0.67 ML of oxygen atoms.

Chapter 3:
Selectivity of Chemisorbed Oxygen in C-H Bond Activation and CO Oxidation and Kinetic Consequences for CH_4-O_2 Catalysis on Pt and Rh Clusters

Abstract

Rate measurements, density functional theory (DFT) within the framework of transition state theory, and ensemble averaging methods are used to probe oxygen selectivity, defined as the reaction probability ratios for O* reactions with CO and CH_4, during CH_4-O_2 catalysis on Pt and Rh clusters. CO_2 and H_2O are the predominant products, but small amounts of CO form as chemisorbed oxygen atoms (O*) are depleted from cluster surfaces. Oxygen selectivities, measured using ^{12}CO-$^{13}CH_4$-O_2 reactants, increase with O_2/CO ratio and are much larger than unity at all conditions on Pt clusters. These results suggest that O* reacts much faster with CO than with CH_4, causing any CO that forms and desorbs to react along the bed with other O* to form CO_2 at any residence time required for detectable extents of CH_4 conversion. O* selectivities were also calculated by averaging DFT-derived activation barriers for CO and CH_4 oxidation reactions over all distinct surface sites on cubo-octahedral Pt_{201} clusters (1.8 nm diameter) at the low O* coverages prevalent at low O_2 pressures during catalysis. Oxidation of CO involves kinetically-relevant molecular CO adsorption on exposed Pt atoms with vicinal chemisorbed O* atoms (*-O* site-pairs) via non-activated steps. CH_4 reacts via kinetically-relevant C-H bond activation on *-* site-pairs involving oxidative insertion of a Pt-atom into one of the C-H bonds in CH_4. Barriers for C-H bond activation reflect the strength of the Pt-C bonds at the transition state, which correlate, in turn, with the coordination of exposed metal atoms and with CH_3* binding energies. Ensemble-averaged O* selectivities depend linearly on O_2/CO ratios because the latter determines O* coverages during catalysis. The proportionality constants is determined by the ratio of rate constants for O_2 dissociation and C-H activation elementary steps; they are much larger than unity and higher on larger Pt clusters (1.8-33 nm) at all temperatures (573-1273 K) relevant for CH_4-O_2 reactions. The barriers for the kinetically-relevant C-H bond dissociation step increase while those for CO oxidation remain unchanged as the Pt coordination number and cluster size increase, and lead, in turn, to higher O* selectivities on larger Pt clusters. The oxygen selectivities were much larger on Rh than Pt, because the limiting reactants for CO oxidation were completely consumed in ^{12}CO-$^{13}CH_4$-O_2 mixtures, also consistent with the lower CO/CO_2 ratios measured by varying the residence time and O_2/CH_4 ratio independently in CH_4-O_2 reactions. The rigorous mechanistic assessment and theoretical treatments of O* selectivity lead to low intrinsic limits of the maximum CO yields and provide rigorous evidence that direct catalytic partial oxidation of CH_4 to CO (and H_2) does not occur at the molecular scale on Pt and Rh. CO (and H_2) are predominantly formed upon complete O_2 depletion from the sequential reforming steps.

3.1. Introduction

The direct catalytic partial oxidation (CPOX) of methane is mildly exothermic ($\Delta H^{o}_{reaction}$= -36 kJ mol^{-1}) and provides an attractive thermoneutral route to H_2-CO mixtures suitable as reactants in methanol and Fischer-Tropsch syntheses.[1,2] H_2 and CO may form via direct CH_4-O_2 reactions, as proposed based on high CO selectivities ($CO/CO_2 > 90$ %) in short monolith reactors.[3,4] These direct paths seem inconsistent with the fast reactions of H_2 and CO with chemisorbed oxygen atoms (O*) at the conditions required for CH_4 activation. H_2-CO mixtures with direct partial oxidation stoichiometries ($H_2/CO=2$) can also form (with the same overall enthalpy) via initial CH_4 combustion to CO_2 and H_2O and their subsequent reactions with CH_4.[5] These sequential combustion and reforming reactions can proceed within axial conduction distances in a reactor, thus enabling the thermal coupling of sequential exothermic and endothermic reactions without the direct molecular coupling implied by catalytic partial oxidation. The discrimination between direct and indirect routes to H_2 and CO from CH_4-O_2 reactants is made difficult by the ubiquitous presence of temperature and concentration gradients within both packed-beds, monoliths, or catalyst pellets, caused by fast endothermic and exothermic reactions[6,7,8] and by thermodynamic constraints that corrupt the intended chemical origins and the mechanistic interpretations of measured rates and selectivities.[9,10]

Here, we address persistent controversies regarding the occurrence of direct catalytic partial oxidation on Pt and Rh catalysts by measuring rates and selectivities for CH_4-O_2 reactions under conditions of strict kinetic control. Only trace amounts of CO were detected at any conditions that retained measurable O_2 concentrations in the reactor effluent. The yields of CO reflect the ratios of rate constant for CO and CH_4 reactions with O_2, described here in terms of the relevant elementary steps and their rate and equilibrium constants. These ratios were measured using $^{13}CH_4$-^{12}CO-O_2 mixtures and showed that rate constants for ^{12}CO oxidation are much higher than for $^{13}CH_4$ oxidation at all O_2 pressures and oxygen surface coverages.

These conclusions are consistent with density functional theory (DFT) estimates of the respective reactivity of CO and CH_4 with chemisorbed oxygen (O*) and with ensemble-averaged rate constants on Pt clusters derived in the framework of transition state theory using DFT-calculated activation barriers. These experimental and theoretical data indicate that H_2 and CO do not form directly from CH_4-O_2 mixtures because any CO that desorbs from catalyst surfaces would form CO_2 via subsequent oxidation along the catalyst bed at all residence times required for measurable CH_4 conversions. Partial oxidation products (CO and H_2) are exclusively formed via subsequent reactions of CO_2 and H_2O with CH_4, after depletion of the limiting O_2 co-reactant on Pt and Rh catalysts at CH_4 conversions of practical interest.

3.2. Experimental and Theoretical Methods

3.2.1. Synthesis and Characterization of Pt and Rh Catalysts. Pt and Rh clusters on γ–Al_2O_3 or SiO_2 were prepared by incipient wetness impregnation with aqueous solutions of hexachloroplatinic acid (H_2PtCl_6, Aldrich, CAS #16941-12-1, 8 % wt. solution) or rhodium(III) nitrate ($Rh(NO_3)_3$, Aldrich, CAS #13139-58-9, 10 wt. %

solution), respectively. γ–Al_2O_3 (Sasol, Lot#C1643, 193 m^2 g^{-1}, 0.57 cm^3 g^{-1} pore volume) was treated in flowing dry air (Praxair, zero grade, 0.8 cm^3 g^{-1} s^{-1}) by heating (at 0.083 K s^{-1}) to 998 K or 1123 K (for Pt and Rh, respectively) and holding for 3 h. X-ray diffractograms of treated Al_2O_3 samples showed the exclusive presence of γ–phase Al_2O_3. SiO_2 (Grace Davison, Grade 62, Lot# 995, 280 m^2 g^{-1}) was treated in flowing dry air (Praxair, zero grade, 0.8 cm^3 g^{-1} s^{-1}) by heating to 923 K at 0.083 K s^{-1} and holding for 3 h. These supports were impregnated to incipient wetness with the respective metal precursors and treated in ambient air at 383 K for 8 h and in flowing dry air (Praxair, zero grade, 0.8 cm^3 g^{-1} s^{-1}) by heating to 998 K (for Pt) or 1123 K (for Rh) at 0.083 K s^{-1} and holding for 3 h. Samples were cooled to ambient temperature and then treated in a flowing H_2/Ar mixture (9 % H_2/Ar, Praxair, Certified Standard) by heating to 923 K (0.083 K s^{-1}, 0.8 cm^3 g^{-1} s^{-1}) and holding for 2 h and then cooling to 573 K. A He stream (Praxair, UHP grade, 0.8 cm^3 g^{-1} s^{-1}) was introduced to the sample at 573 K before cooling to ambient temperature when this stream was then replaced by an O_2/He mixture (0.5 % O_2/He, Praxair, Certified Standard, 0.8 cm^3 g^{-1} s^{-1}) for 2 h to prevent extensive oxidation of metal clusters upon contact with ambient air.

Pt and Rh dispersions, defined as the ratios of the number of exposed atoms to total metal atoms, were measured from volumetric H_2 uptakes (2-14 kPa, 313 K) (Quantasorb chemisorption analyzer) and determined by extrapolation of strong H_2 adsorption isotherms to zero pressures using a 1:1 $H:M_{surface}$ adsorption stoichoimetry.[11] Mean metal cluster diameters were calculated from these dispersion values by assuming hemispherical particles and the bulk densities of Pt (21.45 g cm^{-3})[12] and Rh (12.41 g cm^{-3}) metals.[12]

3.2.2. Catalytic Rate and Selectivity Measurements. CH_4 conversion turnover rates (per exposed metal atom) and selectivities (on a carbon basis) were measured on a packed-bed of catalyst particles held within a quartz tube (8.1 mm ID) fitted with an axial concentric thermowell that contains a K-type thermocouple. Inert SiO_2 granules (Davison Chemical, Chromatographic Silica Media, CAS no. 112926-00-8, 280 m^2 g^{-1}, < 100 μm) were used as intrapellet diluents for Pt/SiO_2, Pt/Al_2O_3, and Rh/Al_2O_3 catalysts (100-300 SiO_2/catalyst ratios) by mixing, pelletizing, and sieving to retain 100-180 μm agglomerates. These pellets were then mixed loosely with quartz granules (Fluka, #84880, 1000-4700 quartz/catalyst ratios) of similar size. These mixtures (containing 0.15-0.25 mg of Pt/Al_2O_3 or Rh/Al_2O_3) were heated in flowing He (Praxair, UHP grade, 1.67 cm^3 s^{-1}) at 0.083 K s^{-1} to reaction temperatures. Reactant mixtures were prepared using 25 % CH_4/He (Matheson Certified Plus Grade), 5 % O_2/He (Praxair, Certified Standard), and He (Praxair, UHP grade). Individual flow rates were metered using electronic mass flow controllers (Porter, type 201).

$^{13}CH_4$ (Isotec, 99 % ^{13}C purity), 1 % ^{12}CO/He (Praxair, Certified Standard), and 5 % O_2/He (Praxair, Certified Standard) were used in $^{13}CH_4$-^{12}CO-O_2 isotopic experiments. CH_4, CO, H_2, O_2, and CO_2 molecules were measured by thermal conductivity detectors after chromatographic separation (Agilent 3000A Micro GC with channels equipped with 5A and Porapak Q columns). $^{13}CO_2$, $^{12}CO_2$, ^{13}CO, and ^{12}CO concentrations were measured using mass selective detection after similar chromatographic separation (Agilent 5973N MSD and 6890 GC).

3.2.3. Density Functional Theory Methods. Gradient-corrected plane-wave density functional theory calculations were carried out to determine the optimized structures and energies of reactants, transition states, and products for reactions of adsorbed CH_4 and CO with isolated chemisorbed oxygen atoms (O*) on Pt (111) surfaces and on different sites on cubo-octahedral Pt clusters with 201 atoms (Pt_{201}, N_{total} = 201, 1.8 nm diameter, Scheme 1). The Pt(111) surface was described using periodic 3×3 unit cells comprised of 4 layers of Pt atoms (9 Pt atoms in each layer) and a 1.5 nm vacuum region to separate the metal surfaces. Pt_{201} cubo-octahedral clusters are low-energy optimized structures and expose eight (111) (Scheme 1b) and six (100) (Scheme 1c) edge-shared surfaces.[13] The (111) and (100) terraces on Pt_{201} cluster contain 19 and 9 Pt atoms, respectively; the number of these exposed atoms (N_S), together with the total number of Pt atoms (N_{total}=201), results in a fractional dispersion (N_S/N_{total}) of 0.61. These surface Pt atoms are denoted as sites 1-4 based on their coordination numbers and oxygen adsorption sites are denoted as sites I-V, as shown in Schemes 1b and 1c.

Simulations were carried out by placing the Pt_{201} cluster at the center of a 3×3×3 nm cubic unit cell and at least 0.8 nm from all cell edges to prevent electronic interactions among clusters. Subsequent simulations with larger 4×4×4 nm unit cells gave adsorption energies that differ by <2 kJ mol^{-1} from those in the 3×3×3 nm cell, consistent with the absence of inter-cluster interactions. All calculations were carried out using the Perdew Wang 91 (PW91)[14] form of the generalized gradient approximation (GGA) in the Vienna *Ab-initio* Simulation Package (VASP).[15-17] The wavefunctions were generated using a periodic expansion of plane waves up to a 396 eV kinetic energy cutoff. The interactions between valence and core electrons were described by Vanderbilt ultrasoft pseudopotentials (US-PP).[18] The electronic state energy of the system was converged to within 9.65 $\times 10^{-3}$ kJ mol^{-1} (10^{-4} eV) whereas the forces on each of the atoms were converged to within 48.2 kJ $(mol\text{-}nm)^{-1}$ (0.5 eV nm^{-1}). The first Brillouin zone was sampled using (1×1×1) and (3×3×1) Monkhorst-Pack k-point meshes for the Pt_{201} clusters and Pt(111) surfaces, respectively.[19]

The heat of adsorption of atomic oxygen (O*; with respect to O_2(g)), Q_O, is defined here as the negative of the energy for:

$$0.5\,O_2(g) + Pt \longrightarrow O^*\text{-}Pt \qquad (1)$$

in which Pt atoms are present on either Pt_{201} clusters or Pt(111) surfaces. Q_O is therefore given by the total DFT-optimized energies for a chemisorbed oxygen atom (O*) on Pt_{201} clusters (or Pt(111) surfaces) and bare Pt_{201} clusters (or bare Pt(111) surfaces) and for the O_2(g), denoted here as $E_{Pt\text{-}O}$, E_{Pt}, and $E_{O_2(g)}$, respectively:

$$Q_O = -\left(E_{Pt\text{-}O} - E_{Pt} - 0.5E_{O_2(g)}\right) \qquad (2)$$

We assume here that the zero-point energy contributions and any changes in heat capacity between 0 K and 298 K are small compared with overall reaction energies. The heats of non-dissociative adsorption for CO (Q_{CO}) and CH_4 (Q_{CH_4}) are taken as the negative value of the calculated reaction energies for molecular adsorption of CO ($\Delta E_{CO,ads}$) and CH_4 ($\Delta E_{CH_4,ads}$) on Pt_{201} clusters (or Pt(111) surfaces):

$$Q_{CO} = -\Delta E_{CO,ads} = -\left(E_{Pt\text{-}CO} - E_{Pt} - E_{CO(g)}\right) \qquad (3)$$

$$Q_{CH_4} = -\Delta E_{CH_4,ads} = -\left(E_{Pt\text{-}CH_4} - E_{Pt} - E_{CH_4(g)}\right) \qquad (4)$$

where $E_{Pt\text{-}CO}$ and $E_{Pt\text{-}CH_4}$ are the energies for chemisorbed CO and CH_4 on Pt_{201} clusters (or Pt(111) surfaces), E_{Pt} is the energy of the bare Pt_{201} cluster (or the bare Pt(111) surface), and $E_{CO(g)}$ and $E_{CH_4(g)}$ are the energies for the respective optimized gas phase molecules.

Transition state complexes and reaction barriers for C-H dissociation, CO adsorption, and their reactions were calculated by using the climbing-image nudged elastic band (CI-NEB) method.[20] Four equally-spaced images were chosen between the reactant and product states to represent the reaction coordinate. The forces perpendicular to the reaction coordinate for each of these images were optimized using 50 structural optimizations to establish the highest energy state along the reaction trajectory. The climbing algorithm was then turned on and used to drive the highest image up along the reaction coordinate by maximizing the energy along the tangent to the potential energy surface to within a force of 48.2 kJ (mol-nm)$^{-1}$ (0.5 eV nm^{-1}) to isolate the transition state and establish the activation energy.

3.2.4. Ensemble-Averaged Rate Constants. The relative rates of CO and CH_4 oxidation reactions were calculated on Pt_{201} clusters (Scheme 1) using statistical and transition state theory methods, DFT estimates of activation barriers on sites with different Pt coordinations on Pt_{201} clusters, and measured activation entropies. These reactions can proceed on metal-metal (*-*) and metal-oxygen (*-O*) site-pairs with different barriers depending on the coordination of available (*) sites or the heat of adsorption of O* (Eq. 2); therefore, their barriers were averaged over all possible site-pairs on Pt_{201} clusters and taken together with the activation entropies to obtain the ensemble-averaged CO and CH_4 oxidation rate constants. We have examined in detail the reactivity of five distinct oxygen adsorption sites (sites I-V) and four types of Pt sites (sites 1-4), including corner, edge, and terrace locations on (111) and (100) surfaces (Schemes 1b and 1c). We considered clusters with one O* atom, because such low O* coverages prevail during CH_4-O_2 reactions at the near complete O_2 consumption would favor CO* desorption before subsequent oxidation to CO_2. Both (111) and (100) facets were treated as Langmuirian surfaces, on which site-pairs involved in CO and CH_4 reactions were treated as non-interacting ensembles.

We consider two limiting cases for the distribution of O* on Pt_{201} clusters: (i) random occupation of all Pt sites irrespective of coordination and (ii) site occupancy prescribed by oxygen adsorption thermodynamics (Q_O; Eq. 2). In the first case, the occupation probability ($P_{j,\,random}$) is given by the fraction of O* atoms of type j among all O* atoms, where j is a roman numeral from I to V, as shown in Scheme 1. In the second case, $P_{j,\,weighted}$ is determined by the heats of oxygen adsorption ($Q_{O,j}$, $Q_{O,k}$) on sites I-V and the number of each type of site (m_j or m_k), where j and k refer to the specific sites for O* in Scheme 1 (j, k = 1-5; 1=I, 2=II, 3=III, 4=IV, 5=V):

$$P_{j,weighted} = \frac{m_j \exp(\frac{Q_{O,j}}{RT})}{\sum_{k=1}^{5} m_k \exp(\frac{Q_{O,k}}{RT})} \qquad (5)$$

3.3. Results and Discussion

3.3.1. Detection and Removal of Transport Corruptions in Measured Rates. Rigorous kinetic measurements require the absence of transport restrictions within catalyst pellets and reactors in order to ensure that local temperatures and reactant and product concentrations at active sites reflect those measured in the fluid phase. Measured rates and selectivities that do not depend on the extent of dilution of active catalysts provide the sole unequivocal evidence for strict kinetic control and for the rigorous absence of transport corruptions of measured chemical reaction rates.[21,22]

Figure 1 shows CH_4 turnover rates (873 K) at various dilution ratios within the pellets (λ) (100-300 diluent-to-catalyst ratio) or the catalyst bed (χ) (1000-4700 diluent-to-catalyst ratio) at 0.02-0.33 O_2/CH_4 reactant ratios on Pt/Al_2O_3 (0.2 % wt. Pt; 8.5 nm mean Pt cluster diameter). For these O_2/CH_4 values, the O_2/CH_4 ratios determine O* coverages on cluster surfaces because of the kinetic coupling between irreversible C-H bond and O_2 dissociation steps that form and remove the O* atoms.[23] Turnover rates reached their highest values (> 900 mol CH_4 (g-atom $Pt_{surface}$-s)$^{-1}$, hereinforth denoted as s^{-1}) on Pt surfaces covered partially with chemisorbed oxygen atoms (O*), which prevail at intermediate O_2/CH_4 ratios (0.07-0.12). These O* species form O*-* site-pairs with vicinal Pt atoms (*, also denoted as oxygen vacancies on O* covered surfaces), which activate C-H bonds more effectively than O*-O* or *-* site-pairs prevalent at larger or smaller O_2/CH_4 ratios, respectively; these O*-* site-pairs lead to the sharp maximum observed in turnover rates at intermediate O_2/CH_4 ratios (Fig. 1).[23] CO was only detected ($CO/CO_2 < 0.02$) at O_2/CH_4 ratios below 0.04, indicating that CH_4 combustion, instead of partial oxidation, is the predominant catalytic reaction, even at very low O_2/CH_4 ratios (Sec. 3.2).

Any effects of gradients in temperature and concentration within catalyst pellets on CH_4 turnover rates (873 K) were ruled out by varying intrapellet dilution ratios (λ; 100-300) at constant bed dilution ratios (χ; 4700). The smallest intrapellet dilution ratios (100) gave higher turnover rates than larger ratios (>200), because of small residual temperature gradients even after such significant dilutions (Fig. 1a). Turnover rates did not depend on intrapellet dilution for λ values above 200, which rendered intrapellet temperature gradients kinetically undetectable and led to CH_4-O_2 reaction rates strictly proportional to the number of surface Pt atoms within such pellets and therefore to turnover rates that are independent of intrapellet site densities (Fig. 1a).

Bed temperature gradients were probed using physical mixtures of diluent and catalyst particles at bed dilution ratios (χ) of 1000-4700 and constant intraparticle dilution ratios (λ; 200). Bed dilution ratios of 1000 gave higher turnover rates than at higher values ($\chi \geq 2000$) at the intermediate O_2/CH_4 ratios (0.06-0.18) that give the highest reaction and heat generation rates (Fig. 1b). Turnover rates became insensitive to bed dilution for χ values above 2000, for which turnover rates no longer depended on the number of sites within the catalyst bed. These extensive dilution levels ($\lambda \geq 200$ and $\chi \geq 2000$) were required for strict kinetic control and for identical temperatures and concentrations at active sites and in the contacting fluid phase; these dilution requirements, which have been seldom (if at all) met in previously reported rate data and correspond to reactor heat loads smaller than 0.35 W cm^{-3} for the dimensions of the reactor and pellets (8.1 mm and 0.180 mm, respectively) used here, are required to

eliminate transport artifacts to obtain the rate data and associated mechanistic interpretations.

CH_4-O_2 turnover rates were also measured on Rh/Al_2O_3 (0.2 % wt. Rh; 3.3 nm mean cluster diameter) at similar bed and intrapellet dilutions (λ=100-300; χ=1900-2800; Table 1). Turnover rates on Rh were smaller than on Pt at all O_2/CH_4 ratios (maximum rates were ~70 s^{-1} for Rh (Table 1, Fig. 2b) vs. ~900 s^{-1} for Pt (Fig. 1) for 0.02-0.33 O_2/CH_4 ratios; Sec. 3.2); these reaction rates led to a maximum volumetric heat generation rate of 5.4×10^{-2} W cm^{-3}, which was much smaller than that on the Pt catalysts (0.35 W cm^{-3}). Therefore, CH_4-O_2 reactions on Rh are less likely to cause temperature gradients, as confirmed from turnover rates that are independent of the values of λ and χ (Table 1).

These data show that extensive dilutions at the scales of pellets ($\lambda \geq 200$; 0.180 mm pellet diameter) and reactor beds ($\chi \geq 2000$; 8.1 mm reactor diameter) are required to measure CH_4-O_2 rate data under conditions of strict kinetic control and to eliminate transport artifacts ubiquitous in these highly exothermic catalytic reactions. All rates and selectivities reported herein were measured using these dilution ratios and volumetric heat generation rates much smaller than those causing transport corruptions of chemical rates ($\leq$ 0.35 W cm^{-3}).

3.3.2. Residence Time Effects on Turnover Rates and CO/CO_2 Selectivities. Figures 2a and 2b show CH_4 turnover rates, CO/CO_2 selectivity ratios, and outlet O_2 pressures as a function of residence time on Pt/Al_2O_3 (0.2 % wt.; 8.5 nm mean cluster diameter) and Rh/Al_2O_3 (0.2 % wt.; 3.3 nm mean cluster diameter) for inlet O_2/CH_4 ratios of 0.125 and 0.13, respectively, which make O_2 the limiting reactant.

On Pt, turnover rates initially increased (from 270 to 370 s^{-1}) as the residence time increased (from 0.4×10^{-4} to 1.2×10^{-4} (g-atom $Pt_{surface}$-s)(mol CH_4)$^{-1}$), but ultimately decreased as O_2 co-reactants were depleted and O_2/CH_4 ratios concurrently decreased. Similar effects were observed when inlet O_2/CH_4 ratios (instead of residence time) were changed while keeping residence times constant (Fig. 1). These trends were also observed on 0.2 % wt. Rh/Al_2O_3 (Fig. 2b). These kinetic effects of O_2/CH_4 ratios reflect changes in the identities of the most abundant surface species and of the kinetically-relevant steps.[23] As the O* coverage on Pt clusters decreases with decreasing O_2/CH_4 ratio, the kinetically-relevant step shifts from C-H bond activation on oxygen-oxygen (O*-O*) site-pairs, to metal-oxygen (*-O*) site-pairs, and ultimately to O_2 activation on metal-metal (*-*) site-pairs;[23] when O_2 is no longer present, CH_4 reforming becomes the prevalent reaction and C-H bond activation occurs on metal-metal (*-*) site-pairs, with the chemisorbed carbon formed by C-H activation removed by O* species derived from H_2O or CO_2.[24]

H_2 was not detected before O_2 depletion on any of the catalysts used, apparently because if formed, it reacted very rapidly with O* to form H_2O before the reactor exit at all residence times required for practical CH_4 conversions. CO_2 and H_2O were the only products detected even at residence times that led to nearly complete O_2 conversion (1.2×10^{-4} (g-atom $Pt_{surface}$-s)(mol CH_4)$^{-1}$ and 1.4×10^{-3} (g-atom $Rh_{surface}$-s)(mol CH_4)$^{-1}$)). Even at the smallest O_2/CH_4 ratios (< 0.04 for Pt; <0.03 for Rh), CO/CO_2 ratios were near CO detection limits (<0.013 for Pt; <<0.005 for Rh) at all residence times that led to detectable O_2 effluent concentrations. These data are consistent with those measured by varying the O_2/CH_4 ratios at a constant residence time (Fig. 1), for which CO was

detected ($CO/CO_2 < 0.02$) only at O_2/CH_4 ratios below 0.04. These effects of residence time and O_2/CH_4 ratio on outlet CO/CO_2 ratios indicate that CH_4-O_2 reactions form only CO_2 and H_2O at all practical O_2/CH_4 ratios and CH_4 conversion levels.

These results were carried out at shorter residence times than previous studies[3,4] (~ 3.6×10^{-5} (cm^3 catalyst)-s-(std cm^3 total flow)$^{-1}$ in Fig. 1 vs. ~10^{-2} (cm^3 monolith volume)-s-(std cm^3 total flow)$^{-1}$ reported in ref. [3,4]). At the shorter residence times, our results contradict the previous findings[3,4] that CO selectively forms at short residence times. These previous conclusions[3,4] were based on data acquired on catalysts wash-coated on monoliths, for which the metal site densities and the operating heat load (per unit volume) were estimated to be much larger than our samples (~135 W cm^{-3} [25] vs. $\leq$ 0.35 W cm^{-3} used herein). Rate and selectivity data on those samples were influenced strongly by very severe temperature and concentration gradients with a reported temperature difference between the inlet feed and catalyst surfaces exceeding 350 K.[3,4] The very small and typically undetectable CO/CO_2 ratios observed here before O_2 depletion under conditions of strict kinetic control at all residence times and inlet O_2/CH_4 ratios rigorously show that CO and H_2 do not form via direct reactions of CH_4-O_2 mixtures on Pt or Rh catalysts. Even if CO* desorbed unreacted, it would readsorb and react via subsequent reaction with O* along the catalyst bed at all residence times required for detectable levels of CH_4 conversion. CO (and H_2) molecules form only via secondary reactions of CH_4 with CO_2 and H_2O products only after O_2 depletion.

The direct formation of CO (or H_2) from CH_4-O_2 reactants requires that CO* (or H*) desorb from catalyst surfaces before subsequent reactions with O* and that desorbed CO (or H_2) does not re-adsorb and react with O* at reactor residence times required for practical CH_4 conversion. The overall CO yields attainable in CH_4-O_2 reactions depend on the selectivity of O* reactions with CO and CH_4. In what follows, we first address the mechanism for CH_4 and CO reactions with O* and then describe O* selectivities in terms of kinetic and thermodynamic constants for the elementary steps that we propose to account for the kinetic dependence, kinetic isotope effect, and ensemble-averaged rates obtained from transition state and density functional theory. These quantitative and molecular scale interpretations of O* selectivities provide a rigorous assessment on the maximum CO yield attainable from direct CH_4-O_2 reactions (Sec. 3.7).

3.3.3. Oxygen Selectivities from Competitive Reactions of ^{12}CO and $^{13}CH_4$ with O_2 on Pt Clusters. Here, we consider O* selectivities on Pt clusters essentially uncovered by reactive intermediates, because such surfaces are most likely to desorb CO* (or H*) before subsequent reactions with vicinal O* species to form CO_2 (or H_2O). O* selectivities (S_{O^*}) on such surfaces reflect the ratio of reactive collision probabilities of desorbed CO and CH_4 reactant with O* given by the first-order CO (k_{O_2-CO}) to CH_4 ($k_{O_2-CH_4}$) rate constants:

$$S_{O^*} = \frac{k_{O_2-CO}}{k_{O_2-CH_4}} \qquad (6)$$

These O* selectivities can be rigorously measured by introducing ^{12}CO into a $^{13}CH_4$-O_2 mixture. The evidence for the low coverage of intermediates on Pt clusters at these low O_2/CH_4 ratios (< 0.08 for 8.5 nm Pt clusters) and for the sequence of elementary steps (Scheme 2) involved in CH_4 and CO reactions with O_2 via O* species are consistent with the rate dependencies and kinetic isotope effects reported elsewhere.[23]

At these O_2/CH_4 ratios, CH_4 conversion rates are limited by O_2 dissociation steps on uncovered Pt surfaces, as confirmed from rates that are proportional to O_2 pressure and unaffected by either the CH_4 pressure or isotope identity (CH_4/CD_4 kinetic isotope effects=1.01) and from the small measured activation barriers (< 3 kJ mol^{-1}).[23]

In Scheme 2, O_2 chemisorbs molecularly as O_2* on unoccupied Pt sites (*, Step 1, refer to Scheme 2 herein for the identity of elementary steps)[26] and subsequently dissociates on vicinal * sites (Step 2) to form O*. CH_4 adsorbs weakly on vacant sites (*, Step 3) and then reacts with vicinal * species to form CH_3* and H* (Step 4). CH_4* can also react with vicinal O* species to form CH_3* and OH* (Step 5). In either case, the CH_3* formed subsequently decomposes via successive H-abstractions and O* insertions (Step 6) to form CO*. CO* can desorb (Step 7) or react with another O* to form CO_2 (Steps 8 and 9). Similarly, H* can recombine with another H* to form H_2 (Step 10) or react with O* and then H* (or OH*) to form H_2O (Steps 11-13). These steps also include the possible readsorption of CO and H_2 (reverse of Steps 7 and 10) to re-form CO* and H*, which can react with O* to form CO_2 and complete a combustion turnover.

CO oxidation turnover rates are proportional to O_2 pressure and unaffected by CO pressure,[23] consistent with kinetically-relevant O_2 dissociation steps on bare Pt clusters. In fact, CH_4,[23] C_2H_6,[27] and CO[23] oxidation rates on uncovered Pt clusters were all independent of the identity, concentration, or reactivity of the reductant and limited solely by O_2 activation steps. These rates are related to the O_2 consumption rates (r_{O_2}) by their respective reaction stoichiometries. O_2 consumption rates are limited by O_2 dissociation and thus are proportional to O_2 pressures with an effective rate constant given by the product of equilibrium constant for O_2 molecular adsorption (K_{O_2}) and rate constant for O_2* dissociation (k_{O*}), as defined in Steps 1 and 2 of Scheme 2, respectively, and derived elsewhere.[23, 27] O_2 consumption rates were identical for $CO-O_2$ and CH_4-O_2 reactants (Table 2; Entries 1-2, 0.2 % wt. Pt/SiO_2, 33 nm mean cluster diameter). CO (r_{CO}) and CH_4 (r_{CH_4}) turnover rates for $CO-O_2$ and CH_4-O_2 reactants are related to each other and to the O_2 consumption rates by reaction stoichiometry:

$$r_{O_2} = 2\, r_{CH_4} = 0.5\, r_{CO} = K_{O_2} k_{O*} (O_2) \qquad (7)$$

O_2 consumption rates are also limited by O_2 activation for CH_4-CO-O_2 mixtures and are given by the combined rates of O_2 reactions with CH_4 and CO (and H_2) weighed by their respective conversion stoichoimetries. O_2 consumption rates in CH_4-CO-O_2 mixtures (Table 2, Entry 3) are similar to those measured with $CO-O_2$ or CH_4-O_2 mixtures (Entries 1-2) for a given O_2 pressure, because CH_4 and CO oxidation share a common kinetically-relevant O_2 dissociation step. O_2 consumption rates in CH_4-CO-O_2 mixtures are given by:

$$r_{O_2} = 2\nu_1 r_{CH_4,1} + 0.5\nu_2 r_{CH_4,2} + 0.5\, r_{CO} + 0.5\, r_{H_2} \qquad (8)$$

in which $r_{CH_4,1}$ and $r_{CH_4,2}$ are the rates of CH_4 conversion to CO_2 and H_2O and to CO and H_2, respectively, r_{H_2} is the rate of sequential H_2 reactions with O_2, and ν_1 and ν_2 are the selectivity ratios. Although CO forms only in trace concentrations from CH_4-O_2 reactants before O_2 depletion (Sec. 3.2), CO may form more readily from CH_4 when additional CO is added to the CH_4-O_2 reactants, because CO effectively scavenges O* (as shown later in this section) and decreases the O* coverages. At the low O* coverages prevalent in CH_4-CO-O_2 mixtures, rates of initial C-H bond activation are unaffected by O* concentrations

and thus remain the same with those in CH_4-O_2 mixtures, because O* atoms are not involved in the kinetically-relevant C-H activation step (Sections 3.3, 3.5, and 3.6). The sequential oxidation of the CO* intermediates formed from CH_4, however, becomes much less effective at the low O* coverages, because this step requires an O* atom vicinal to the CO* (Sec. 3.6). This decrease in CO* oxidation rates leads to incomplete CH_4 oxidation and thus to CO formation from CH_4 in CH_4-CO-O_2 mixtures. The first-order rate constants for O_2 reactions with CH_4 ($k_{O_2-CH_4}$) and CO (k_{O_2-CO}) on bare Pt surfaces are given by their turnover rates divided by the respective reactant pressure:

$$k_{O_2-CH_4} = \frac{2\nu_1 r_{CH_4,1} + 0.5\nu_2 r_{CH_4,2} + 0.5 r_{H_2}}{(CH_4)} \quad (9)$$

$$k_{O_2-CO} = \frac{0.5 r_{CO}}{(CO)} \quad (10)$$

Their ratios give the O* selectivities (S_{O^*}) upon substitution into Eq. 6.

O* selectivities were measured from $^{12}CO_2$, $^{13}CO_2$, and ^{13}CO formation rates using $^{13}CH_4$-^{12}CO-O_2 mixtures (O_2/CO=0.02-0.23; O_2/CH_4=0.0027-0.017) on Pt clusters (1.8 nm and 33 nm mean diameter, 0.2 % wt. Pt) at 873 K. O_2 turnover rates (also the total CO and CH_4 rates) were proportional to O_2 pressure, consistent with O_2 dissociation on essentially uncovered Pt cluster surfaces as the kinetically-relevant step during catalysis. O* selectivities are shown in Figure 3 as a function of O_2/CO inlet ratios. These selectivities (Eq. 6) were much greater than unity (10-60), indicating that O* atoms react preferentially with CO* instead of CH_4 on Pt clusters. O* selectivities increased with O_2/CO ratios on both large and small Pt clusters, but were higher on larger Pt clusters. The mechanistic origins of these size effects are discussed in Section 3.4.

O* coverages reflect the kinetic coupling between the steps that scavenge O* using CO and CH_4 and the step that forms O* via O_2 dissociation. The fractional O* coverages during steady-state $^{13}CH_4$-^{12}CO-O_2 reactions, denoted as $((O^*)/(L))_{CO-CH_4-O_2}$ where L is the total number of exposed Pt sites, are given by a pseudo-steady-state treatment of O* intermediates with unoccupied sites (*) as the most abundant surface intermediates (MASI). This treatment, together with the assumption that the concentration of * equals L, leads the O* coverages to become proportional to O_2/CO ratios with a coefficient that contains the equilibrium constant for O_2 adsorption (K_{O_2}) and the rate constants for O_2* dissociation (k_{O^*}) and molecular CO adsorption ($k_{CO\ ads}$) (defined in Scheme 2), as derived in the Appendix:

$$\left(\frac{(O^*)}{(L)}\right)_{CO-CH_4-O_2} = \frac{2K_{O_2}k_{O^*}}{k_{CO\,ads}}\left(\frac{O_2}{CO}\right) \quad (11)$$

The kinetic relevance of molecular CO adsorption steps in CO oxidation reactions and the presence of its rate constant ($k_{CO\ ads}$) in Eq. 11 are shown in Section 3.6. The linear relations between O* coverage on O_2/CO ratios (Eq. 11) and between O* selectivity and O_2/CO ratios (for ratios below 0.06 on 33 nm Pt clusters, Fig. 3) provide evidence for a concomitant relation between the O* coverage and selectivity; this relation indicates, in turn, that reactive collision probabilities for CO oxidation (the numerator term in Eq. 6) relative to those of CH_4 increase with increasing O* coverage.

A Langmuir treatment of CO oxidation reactions requires immobile O* atoms adjacent to CO* for CO* reactions with O*. The observed linear increase in O*

selectivity with increasing O_2/CO ratio and the related O* coverage (Eq. 11) for O_2/CO ratios below 0.06 (on 33 nm Pt clusters, Fig. 3) indicates that the reactive collision of CH_4, which appears in the denominator of the O* selectivity expression (Eq. 6), is insensitive to O* coverages. The reactive collision of CH_4, which reflects the kinetically-relevant C-H bond activation, occurs on exposed metal atom site-pairs (*-*) with O* atoms involved only in latter steps that remove C* and H* products of C-H bond activation. These kinetic treatments, together with the assumption that the selectivity ratios for CH_4 to form CO_2 and CO in CH_4-CO-O_2 mixtures (ν_1 and ν_2) are equal,[28] lead to the selectivity expression:

$$S_{O^*} = \frac{k_{CO\ ads}}{7k_{[*-*]}K_{CH_4}}\left(\frac{[O^*]}{[L]}\right) = \frac{k_{O^*}K_{O_2}}{3.5k_{[*-*]}K_{CH_4}}\left(\frac{O_2}{CO}\right) \quad (12)$$

which depends on the CH_4 adsorption equilibrium constant (K_{CH_4}), the C-H bond activation ($k_{[*-*]}$) and CO adsorption ($k_{CO\ ads}$) rate constants (defined in Steps 3, 4, and 7 of Scheme 2, respectively), and O_2/CO ratios. This expression was derived by substituting Eq. 11 into Eqs. 6, 9, and 10 and the details are shown in the Appendix. The linear increase in S_{O^*} with O_2/CO ratio (Eq. 12) was confirmed from the selectivity data measured on 33 nm Pt clusters for O_2/CO ratios below 0.06 (Fig. 3). In contrast, the alternate route in which kinetically-relevant C-H bond activation occurs on O*-* site-pairs (Step 5, Scheme 2) would cause the S_{O^*} values to be unaffected by O_2/CO ratios because these ratios determine the O* concentrations required for both the CO and CH_4 oxidation steps and affect both rates to the same extent (derivation in Appendix):

$$S_{O^*} = \frac{k_{CO\ ads}}{7k_{[O^*-*]}K_{CH_4}} \quad (13)$$

The coordination of exposed Pt atoms influences O* selectivities because of its consequences for O_2 dissociation and C-H bond activation rate constants. O_2 dissociation is non-activated and its rate constant ($k_{O^*}K_{O_2}$, Eq. 7) is insensitive to Pt coordination.[23] Rate constants for C-H bond activation on *-* site-pairs ($k_{[*-*]}K_{CH_4}$), however, depend strongly on Pt coordination.[24] The rate constant for C-H bond activation increases as surface atoms become more coordinatively unsaturated with decreasing cluster size (Pt,[24] Rh,[29] Ru,[30] Pd[31]), consistent with the lower barriers for this step resulting from more effective stabilization of reaction products (CH_3* and H*) on the corner and edge sites prevalent on small clusters (as described in Sec. 3.5). These effects of surface Pt coordination on C-H bond activation rate constants are responsible for the lower O* selectivities observed on smaller clusters at all O_2/CO ratios (0.02-0.05; Fig. 3).

S_{O^*} values become smaller than expected from the predicted linear trend with O_2/CO ratios based on Eq. 12 at higher O_2/CO ratios (> 0.06) on the 33 nm Pt clusters and for the entire range of O_2/CO ratios (0.02-0.05) on the 1.8 nm clusters. The deviation in S_{O^*} is a result of an apparent increase in its denominator, the reactive collision probabilities of CH_4 with O* ($k_{O_2-CH_4}$, Eq. 9), with increasing O_2/CO ratio and O* coverage. In the next section, we show this increase in $k_{O_2-CH_4}$ resulting from the removal of CH_x* species chemisorbed on coordinatively unsaturated corner and edge sites of Pt clusters as CO or CO_2 via reactions with O* as the O* coverage increases, making such surface atoms accessible for C-H bond activation and catalytic turnovers

(Step 4, Scheme 2). These edge and corner sites are more reactive than terrace sites[24] and their availability for catalytic turnovers increases the overall reactive collision probabilities of CH_4 with O* ($k_{O_2-CH_4}$, Eq. 9) and thus decreases the O* selectivities.

3.3.4. Site Occupation by Carbonaceous Intermediates Produced from the Initial C-H Bond Activation Steps and their Effects on Oxygen Selectivities. Next, we examine the dependence of reactive collision probabilities for $^{13}CH_4$ reactions (also the effective rate constants, $k_{O_2-CH_4}$, Eq. 9) on $^{13}CH_4$ pressure and show that the CH_x* species, produced from the C-H bond activation steps, bind reversibly on a portion of the Pt sites at the low O* coverages prevalent in $^{13}CH_4$-^{12}CO-O_2 mixtures. We propose that the binding of CH_x* on these sites at low O_2/CO ratios and their gradual removal as the O_2/CO ratio increases cause the deviation in O* selectivity from the predicted linear trend with the O_2/CO ratio (Eq. 12) in Figure 3. We consider Pt atoms with high coordination (denoted as $*_W$) to remain accessible for the kinetically-relevant initial C-H bond activation in CH_4 (Step 4, Scheme 2). On these sites, elementary steps for the sequential C-H bond dissociation and CH_x* oxidation are kinetically-irrelevant. In contrast, coordinatively unsaturated Pt atoms (denoted as $*_S$) bind the carbonaceous intermediates produced from the initial C-H bond activation steps (CH_x*_S) strongly. On these coordinatively unsaturated $*_S$ sites, the initial C-H bond activation becomes kinetically-irrelevant and the removal of the CH_x*_S species via oxidation by vicinal reactive oxygen intermediates (Step 14, elementary rate constant k_{CH*}, Scheme 2) limits the CH_4 turnover rates. As O* coverages (set by O_2/CO ratio) increase, the rates of CH_x*_S reactions with O* increase. Assuming that the $*_S$ sites are surrounded predominantly by the $*_W$ sites, CH_4 turnover rates ($r_{CH_4,S}$) on the $*_S$ sites are given by:

$$r_{CH_4,S} = k_{CH*}(CH_x*_S)\frac{(O*_W)}{L} \qquad (14)$$

where $O*_W$ refers to the chemisorbed oxygen atom binds on the vicinal $*_W$ site. A pseudo steady-state approximation of the carbonaceous intermediates (CH_x*_S) and the assumption of $O*_S$ as minority surface species (relative to $*_S$ and CH_x*_S) give the first-order CH_4 reaction rate constant for the $*_S$ sites ($k_{CH_4,S}$), as derived in the Appendix:

$$k_{CH_4,S} = \frac{r_{CH_4,S}}{(CH_4)} = \frac{k_{[*-*],S}}{\left(1+\frac{k_{[*-*],S}(CH_4)}{k_{CH*}}\frac{k_{COads}}{2K_{O_2}k_{O*}}\left(\frac{CO}{O_2}\right)\right)} \qquad (15)$$

where $k_{[*-*],S}$ is the elementary rate constant for the initial C-H bond activation on the $*_S$-$*_W$ site-pairs (Step 4, Scheme 2). The overall first-order CH_4 reaction rate constant (k_{CH_4}, related to $k_{O_2-CH_4}$ via the reaction stoichoimetry) is simply the sum of the respective rate constants for $*_S$ ($k_{CH_4,S}$) and $*_W$ ($k_{CH_4,W}$) sites, weighted by the relative abundance of the sites, which is given here in terms of the fraction of surface atoms acting as $*_W$ sites (Γ):

$$k_{CH_4} = \Gamma k_{[*-*],W} + (1-\Gamma)\frac{k_{[*-*],S}}{\left(1+\frac{k_{[*-*],S}}{k_{CH^*}}(CH_4)\frac{k_{CO\,ads}}{2K_{O_2}k_{O^*}}\left(\frac{CO}{O_2}\right)\right)} \quad (16)$$

This equation is used to described the rate data in Figure 4, which shows the effective rate constants for $^{13}CH_4$ reactions ($k_{O_2-CH_4}$, Eq. 9) on a Pt/Al_2O_3 catalyst (1.8 nm mean cluster diameter, 0.2 % wt. Pt) as a function of O_2/CO ratio and different $^{13}CH_4$ pressures (1.2-2.8 kPa) in $^{13}CH_4$-^{12}CO-O_2 mixtures at 873 K. The effective rate constants for $^{13}CH_4$ reactions increased slightly with increasing O_2/CO ratio (which determines the O* coverage; Eq. 11) and were larger at 1.2 kPa $^{13}CH_4$ than at 2.0 kPa and 2.8 kPa $^{13}CH_4$ pressures for each O_2/CO ratio. A regression analysis of these data using Eq. 16 gives the predicted reactive collision probabilities for $^{13}CH_4$, which are plotted together with the measured values in Figure 4, and the derived kinetic parameters ($\Gamma k_{[*-*],W}$, $(1-\Gamma)k_{[*-*]S}$, $k_{[*-*]S}k_{COads}(2k_{CH^*}K_{O_2}k_{O^*})^{-1}$) in Table A.1 in the Appendix. Eq. 16 accurately describes the effects of CH_4 pressure, as well as the sublinear increase in O* selectivity with O_2/CO ratio for O_2/CO values above 0.06 and 0.02 on the 33 nm and 1.8 nm Pt clusters, respectively (Fig. 3). As the oxygen coverage (O^*_W, set by O_2/CO ratio) increases, the CH_x*_S coverage decreases and $*_S$ sites become available for the initial C-H bond activation. The $*_S$ sites are more reactive than the $*_W$ sites for the initial C-H bond activation because of their lower coordinations and concomitantly stronger binding to CH_3* (Sec. 3.5). As these sites participate in the initial C-H bond activation, the overall first-order CH_4 reaction rate constant (k_{CH_4}, Eq. 16) increases, causing the O* selectivities to become lower than the predicted linear trend according to Eq. 12 (Fig. 3).

The total number of unoccupied sites during $^{13}CH_4$-^{12}CO-O_2 reactions is smaller than for CO-O_2 reactions, because CH_x* species are not present during CO-O_2 reactions. O_2 consumption turnover rates in $^{13}CH_4$-^{12}CO-O_2 ($r_{^{13}CH_4-^{12}CO-O_2}$) and CO-$O_2$ (r_{CO-O_2}) mixtures are both limited by O_2 dissociation. Their ratio (β) reflects the fraction of exposed Pt atoms that are not covered by CH_x* during $^{13}CH_4$-^{12}CO-O_2 reactions on which the O_2 predominantly reacts with CO:

$$\beta = \frac{r_{O_2,^{13}CH_4-^{12}CO-O_2}}{r_{O_2,CO-O_2}} \approx \frac{K_{O_2}k_{O^*}(O_2)[(*)-(CH_x*)]^2}{K_{O_2}k_{O^*}(O_2)(*)^2} \approx \frac{[(*)-(CH_x*)]^2}{(*)^2} \quad (17)$$

The β values were 0.83 and 0.79 for CH_4 pressures of 1.13 and 2.73 kPa (O_2/CH_4 = 0.008 and 0.0033), respectively, at an O_2/CO ratio of 0.024 on the smaller Pt clusters (1.8 nm mean diameter; Table 2, Entries 5-6). In contrast, the β values are identical within experimental accuracy on the larger Pt clusters (33 nm; $\beta > 0.99$, O_2/CO = 0.022, Table 2, Entry 3), suggesting that almost all exposed Pt atoms are uncovered by CH_x* species produced from the C-H bond activation steps in $^{13}CH_4$-^{12}CO-O_2 mixtures under those conditions.

3.3.5. Theoretical Assessment of the Initial C-H Bond Dissociation in CH_4 on Metal Site-Pairs of Pt_{201} Clusters. Density functional theory calculations were carried out to determine reaction and activation energies for the initial C-H bond activation of CH_4 on the different Pt sites of the model Pt_{201} cubo-octahedral cluster (1.8 nm diameter,

refers to Scheme 1 herein), previously examined on single crystal surfaces. [32, 33,34] The structure of the bare Pt_{201} cluster was fully optimized, resulting in an average Pt-Pt distance within the inner core of the cluster (0.282 nm) similar to that for bulk Pt (0.277 nm[35]). The Pt-Pt bond lengths at the corner and edge sites were slightly shorter (0.272 nm) as a result of the lower coordination numbers of these sites (CN_{corner}=6 and CN_{edge}=7 for sites 1 and 2, respectively) verses the terrace sites ($CN_{100,terrace}$=8 and $CN_{111,terrace}$ =9 for sites 3 and 4, respectively), which leads to stronger Pt-Pt bonds and to a slight reconstruction at these sites, as also observed experimentally.[36] This bond contraction becomes even more evident on smaller clusters (55 atoms), as observed for Pt, Rh, and Pd clusters, because of larger fractions of coordinatively unsaturated metal atoms residing on the corner and edge sites of these clusters than on the larger clusters.[37] The bond contraction at these sites partially compensates for their lower degrees of coordinative saturation and lowers the overall surface free energy. These effects and their catalytic consequences cannot be appropriately captured in periodic calculations on extended, ordered single crystal surfaces because relaxation and reconstruction on such surfaces are constrained by actual structural differences between planar and curved surfaces as well as the computational limitations imposed by periodic cell boundaries. Clusters that are large enough (> 100 atoms) capture the various sites (e.g. terrace, corner, edge) of working catalytic particles and therefore provide a more reliable theoretical representation than extended flat or stepped surfaces, thus allowing for the systematic studies of the coordination and cluster size effects on catalytic rates.

CH_4 activation on the Pt_{201} cluster proceeds by the initial adsorption of CH_4 (Step 3, hereinafter referred to Scheme 2 for the identities of elementary steps) on a Pt site, which can be one of the four different Pt sites identified in Scheme 1. The weakly-adsorbed CH_4* precursor (Q_{i,CH_4} ~ 3 kJ mol^{-1}) is stabilized by weak van der Waal interactions between the hydrogen atoms and the Pt surface, the strength of which is under-predicted as gradient-corrected exchange-correlation functionals used in DFT such as PW91 (used herein) do not appropriately treat dispersion forces.[38,39] The dissociation of one of the C-H bonds in CH_4* (Step 4) occurs via an oxidative insertion of the Pt atom into the C-H bond (Fig. A.1b), followed by the transfer of the resulting H to a vicinal Pt-Pt bridge site (Fig. A.1c). The metal site-pair (*-*) discussed herein refers to the specific sites where the CH_3* and H* products reside rather than the total number of Pt atoms involved in the C-H bond dissociation step. Alternatively, the C-H bond dissociation step can proceed on a metal-oxygen site-pair via a concerted step involving the oxidative insertion of a Pt atom into the C-H bond and a hydrogen abstraction by a vicinal O* (Step 5, Fig. A.2), which will be discussed in Section 3.6. The structures of reactant, transition, and product states for the CH_4 activation at each of the different *-* and *-O* site-pairs (Steps 4 and 5, respectively) on the Pt_{201} cluster are given in Figures A.1-A.2 and Tables A.2 and A.3 in the Appendix. The reaction energy diagrams and the structures of the intermediates and transition states for the two distinct CH_4 activation paths on *-* and *-O* site-pairs, respectively, are summarized in Figure 5a.

The specific details for the activation of the C-H bond on the various *-* site-pairs are discussed by using a representative case in which the site-pairs consist of two terrace Pt atoms on the (111) facet (site 4, Scheme 1b) of the Pt_{201} clusters. The oxidative insertion of Pt into the C-H bond proceeds by the direct interaction of an exposed Pt atom with the C-H bond. This interaction weakens the C-H bond thus resulting in its

elongation from 0.109 nm (in the reactant state) to 0.152 nm (in the transition state). In the transition state, the Pt atom (labeled Pt1 in Fig. A.1b) interacts with both the C (0.222 nm) and H (0.162 nm) atoms to form a three-centered carbon-metal-hydrogen (H_3C^*--$H^*)^‡$ activated complex, similar to that involved in C-H bond activation by organometallic complexes.[40] The H-Pt distances between the H atom and the two vicinal Pt sites (labeled Pt2 and Pt3 in Fig. A.1b) in the transition state are 0.245 nm and 0.261 nm, respectively. These distances are much longer than the Pt-H bond lengths in the product state of 0.174 nm and 0.178 nm (Fig. A.1c), indicating that the vicinal Pt sites do not assist the C-H bond activation steps, but instead promote the H transfer later along the reaction coordinate. The calculated transition state for the C-H bond activation is rather late along the reaction coordinate as there is a significant stretch in the C-H bond (> 0.4 nm) and direct occupation of the σ* C-H bonding state with electron density as was suggested previously for alkane activation over transition metal surfaces.[41, 42] The transition state structure suggests strong interactions between the Pt atom that carries out the oxidative addition step and both the C and H atoms. These interactions indicate the formation of an immobilized $(H_3C^*$--$H^*)^‡$ transition state complex from a gas phase CH_4 molecule with a significant loss in entropy. The C-H bond activation step is completed by transferring the H-atom in the C-H bond to a vicinal Pt-Pt bridge site to form the CH_3^* and H* products.

The barriers for the C-H bond activation on *-* site-pairs are correlated directly with the coordination number of the Pt atom that carries out the oxidative insertion, as shown in Figure 6a. The barriers for reactions carried out at the Pt terrace sites (79 kJ mol^{-1} for site 4, Scheme 1) are significantly higher than the more coordinatively unsaturated corner, edge, and (100) sites (sites 1, 2 and 3, respectively, in Scheme 1), as the terrace sites bind the CH_3^* in the product state much more weakly than the coordinatively unsaturated sites. As the Pt coordination number decreases from 9 to 6, the C-H bond activation barriers decrease (from 79 to 47 kJ mol^{-1}, Fig. 6a) and the overall reaction becomes more exothermic as a result of the stronger CH_3^* binding to the Pt site. Taken together with the nearly fully formed Pt-CH_3 bonds in the transition states (Pt-CH_3 = 0.222 nm at the transition state vs. Pt-CH_3 = 0.207 nm at the product state, Table A.2), the correlation between the Pt coordination numbers and the C-H bond activation barriers and the reaction energies suggests a direct relation between the C-H bond activation barriers and the CH_3^* binding energies (given by the heats of CH_3^* adsorption in Table 4), as plotted in Figure 6b.

3.3.6. Theoretical Assessment of the Initial C-H Bond Dissociation in CH_4 and CO Oxidation Assisted by Metal-Oxygen Site-Pairs on Pt_{201} Clusters with a Single Chemisorbed Oxygen Atom. Next, we examine the C-H bond activation steps on the various *-O* site-pairs (Step 5, Scheme 2), each of which is formed from a single chemisorbed O* atom on the Pt_{201} cluster and a vicinal * site. The model Pt_{201} cluster with a single O* atom resembles Pt clusters encountered at low O_2/CH_4 ratios during CH_4-O_2 catalysis for which CO* intermediates are most likely to desorb and catalytic partial oxidation might become feasible. We first consider the O* binding energies at the various sites j (j=I-V, Scheme 1) of the Pt_{201} cluster and then analyze the effects of these binding strengths on the C-H bond activation barriers before extending the analysis to CO oxidation reactions.

The O* atoms preferentially reside at three-fold fcc sites (labeled II, IV, V in Scheme 1b) on (111) surfaces and at bridge sites (labeled I and III in Scheme 1c) on (100) surfaces. The binding energies of isolated O* at these sites are reported as their respective heats of oxygen adsorption (Q_O, Eq. 2) in Table 3. The heat of oxygen adsorption decreased from 133 to 96 kJ (mol O*)$^{-1}$ as the average coordination of the Pt atoms covalently bound to the O* increased from 6.5 to 9. As the average Pt coordination number approaches the value of 9 at the fcc terrace sites on the (111) surfaces (site V, Scheme 1b), the heats of oxygen adsorption (96 kJ mol^{-1}) become similar to those on the extended Pt(111) surfaces (89 kJ mol^{-1}), where their average coordination number is also 9.

The presence of O* atoms near CH_4* species may assist C-H bond activation (Step 5, Scheme 2) via concerted interactions reminiscent of the three- and four-centered transition states involved in oxidative addition,[43] σ-bond metathesis,[44] and oxidative hydrogen migration,[45] implicated in ligand-assisted C-H bond activation that can occur in organometallic complexes.[46] Such O*-assisted C-H activation routes have also been proposed for CH_3OCH_3[47] and CH_4[23] oxidation on O*-covered Pt clusters. In the O* assisted C-H bond activation step, a Pt atom inserts and elongates the C-H bond as the CH_4 evolves into the $(H_3C^*\text{--}OH^*)^{\ddagger}$ transition state complex (Fig. A.2, see Table A.3 for detailed bond length information), similar to the oxidative addition step described previously on *-* site-pairs (Sec. 3.5). The O* atom that is chemisorbed on the three-fold fcc site (site II, IV, or V, Scheme 1) shifts to the bridge site directly across from the Pt atom that carries out the oxidative insertion as the reaction proceeds in order to interact with the H-atom in the C-H bond. The O* atom chemisorbed on the (100) surface (site I or III, Scheme 1) already resides at the bridge site vicinal to the CH_4* and is thus appropriately positioned to abstract the targeted H atom. The O* and H interaction results in O--H bond lengths of 0.139-0.146 nm in the transition state (Table A.3). The C-H bond distance in the transition state was calculated to be 0.130-0.134 nm which is 0.021-0.025 nm shorter than those found without the assistance of O* on *-* site-pairs (C-H bond distance = 0.152 nm, Sec. 3.5).

The C-H bond activation barriers on the various *-O* site-pairs, $(E_i)_{*\text{-}O^*}$, are estimated by the energy difference between the $(CH_3^*\text{--}OH^*)^{\ddagger}$ transition state and the CH_4 in the gas phase. The barrier is reported for each type of Pt atom (i=1-4, Scheme 1) in the *-O* site-pairs, calculated by averaging the barriers ($E_{C\text{-}H,\ i,j}$) of all plausible reaction paths at that site resulting from using the different vicinal O* atoms (j=I-V, Scheme 1) to abstract the H, according to the following equation:

$$\left(E_i\right)_{*-O^*} = \ln\left(\frac{\sum_{j=1}^{5} n_j e^{\left(E_{C\text{-}H,\,i,j}\right)}}{\sum_{j=1}^{5}\left(n_j\right)}\right)_i \qquad (18)$$

where n_j is the number of vicinal O* atoms of type j in Scheme 1. The C-H bond activation barrier increased monotonically from 81 kJ mol^{-1} to 115 kJ mol^{-1} as the coordination number of the Pt atom (*) in the *-O* site-pairs increased from 6 to 9 on the Pt_{201} clusters (Fig. 6a), approaching the calculated value for the similar step on extended Pt(111) surfaces (122 kJ mol^{-1}, Pt coordination number of 9). This trend reflects a direct relation of the barriers with the extents of Pt-CH_3 interaction at the transition state and

with the CH_3* binding strengths. Such a relation is similar to those found for C-H bond activation on *-* site-pairs (Sec. 3.5; Fig. 6a) because both of the C-H bond activation steps (on *-O* and *-* site-pairs, Steps 4 and 5 of Scheme 2) proceed via an oxidative addition mechanism. The barriers for C-H bond activation on *-O* site-pairs are also influenced by the extent of O--H interactions at the transition state, which is related to the Pt-O bond strength. The correlation of the C-H bond activation barriers with the Pt-O bond strength, however, is much weaker than with the Pt-CH_3 bond strength,[23] as expected from the weak interactions between the O and H at the transition state (O-H bond length is 0.139-0.146 nm vs. 0.098 nm at the product state).

The calculated C-H bond activation barriers on *-O* site-pairs are, however, significantly larger (81-115 kJ mol^{-1}, Step 5, Scheme 2) than the barriers of similar steps on *-* site-pairs (47-79 kJ mol^{-1}, Step 4, Scheme 2) for each of the Pt sites (the specific * in the *-O* or *-* site-pair that inserts into the C-H bond), as also found on Pt(111) surfaces (122 kJ mol^{-1} vs. 89 kJ mol^{-1}) and included in Figure 6a. These larger barriers are the result of repulsive interactions between the O* and H atom in the C-H bond that increase the transition state energies. Both of the C-H bond activation routes are expected to exhibit similar entropy losses for the formation of the respective transition states ($(H_3C^*--H^*)^{\ddagger}$ or $(H_3C^*--OH^*)^{\ddagger}$) from CH_4(g) reactants because of the similar extent of interactions between the methyl groups and the Pt sites in these transition states (the Pt-CH_3 bond lengths for a type 4 Pt site are 0.222-0.230 nm; Tables A.2 and A.3). Thus, the pre-exponential factors for these steps are expected to be similar. Taken together with the much lower barriers for C-H bond activation on the *-* verses the *-O* sites for all Pt sites (Fig. 6a), we conclude that the C-H bond activation of CH_4 occurs predominantly on the *-* site-pairs at the low O* coverages prevalent at the conditions used for rate measurements in Sections 3.3 and 3.4. O* insertion steps (into CH_x* or C*) are kinetically-irrelevant because they occur later along the reaction path, except on a small fraction of coordinatively unsaturated Pt atoms that bind the CH_x* strongly and are occupied by CH_x* (Sec. 3.4). The kinetic irrelevance of O* insertion for the majority of the Pt sites is consistent with the increase in measured O* selectivity (S_{O^*}) with O_2/CO ratio (Eq. 12, Fig. 3).

We consider next the reactions of CO with a single O* atom chemisorbed at the various sites on Pt_{201} clusters. At such low O* coverages, CO* intermediates that form are most likely to desorb before encountering a second O* atom and undergoing further oxidation to CO_2, thus partial oxidation may become feasible. The resulting CO, however, can re-adsorb and sequentially oxidize to CO_2. An O* atom at site j can react with a CO* adsorbed at any of the vicinal atop sites (i=1-4, Scheme 1; see Fig. A.3 in the Appendix for examples on plausible O* and CO* reaction paths). The reaction energy diagram, which shows the energies of the transition, intermediate, and product states with respect to the gas phase reactant state, is given in Figure 5b. The structural details for each of these states are provided in Figure A.4 and Table A.4 in the Appendix. The calculated heats of CO* adsorption, $Q_{i,CO}$ (Eq. 3), at the different Pt sites increased from 161 to 198 kJ mol^{-1} as the Pt surface atom coordination decreased from 9 to 6 (Table 4). The activation barrier for the CO* and O* reaction (Step 8, Scheme 2), $(E_{,j})_{CO^*-O^*}$, was calculated and reported for each type of O* atom (j=I-V, Scheme 1) by averaging the individual barriers for the various reaction paths, which depend on the identity of the neighboring CO* adsorption sites (type i=1-4, Scheme 1):

$$\left(E_j\right)_{CO^*-O^*} = \ln\left(\frac{\sum_{i=1}^{4} n_i e^{\left(E_{CO\text{-}O,j,i}\right)}}{\sum_{i=1}^{4}\left(n_i\right)}\right)_j \tag{19}$$

where $E_{CO\text{-}O,j,i}$ is the energy difference between the $(CO^*\text{--}O^*)^{\ddagger}$ transition state and the chemisorbed CO* at the reactant state and n_i is the number of vicinal Pt atoms of type i (i=1-4, Scheme 1). These barriers, as shown in Table 3, were calculated to be between 69-123 kJ mol^{-1} depending on the specific O* atom used to oxidize CO*. The site-specific heats of CO adsorption were subsequently subtracted from the intrinsic CO oxidation barriers to determine the effective barriers for the CO*-O* reactions, $(E_j)_{CO^*\text{-}O^*,eff}$. The effective barriers were evaluated for each type of O* atom (type j=I-V, Scheme 1) by averaging over the different barriers resulting from the reactions of the O* with vicinal CO* bound on different types of Pt sites (type i=1-4, Scheme 1):

$$\left(E_j\right)_{CO^*-O^*,eff} = \ln\left(\frac{\sum_{i=1}^{4} n_i e^{\left(E_{CO\text{-}O,j,i} - Q_{CO,i}\right)}}{\sum_{i=1}^{4}\left(n_i\right)}\right)_j \tag{20}$$

where $Q_{CO,i}$ is the heat of CO adsorption for the CO chemisorbed at the vicinal * site i and $E_{CO\text{-}O,j,i}$ and n_i are defined above. The effective barriers for the CO*-O* reactions are much less than zero (< -65 kJ mol^{-1}, Table 3) for all of the O* atoms on the Pt_{201} cluster because the heats of CO adsorption (Table 4) are much larger than the intrinsic barriers for CO*-O* reactions (Fig. 5b, Table 3). The heats of CO adsorption are approximately equal to the CO* desorption barriers because the CO adsorption steps are non-activated with barriers that are less than 5 kJ $(mol\ CO)^{-1}$ for all O* atoms. The difference in barriers between the CO* desorption and the CO*-O* reaction provides an estimate of the rate ratio for the CO* desorption and sequential CO* oxidation steps. This rate ratio, derived by assuming similar activation entropy values for these steps, exceeds 2×10^4 for each type of O* atom. The much larger rates for the CO*-O* reactions than the CO* desorption indicate that the initial CO adsorption step is essentially irreversible. CO oxidation, as a result, is limited by the irreversible CO adsorption (reverse of Step 7, Scheme 2) where CO binds on a Pt site vicinal to an O* atom via the formation of a $(CO(g)\text{--}*)^{\ddagger}$ complex (structures in Appendix Fig. A.6). In the $(CO(g)\text{--}*)^{\ddagger}$ complex, the C=O bond is slightly elongated (from 0.116 nm to 0.117 nm) and the Pt--CO bond (0.185 nm) is formed. The ensemble-averaged barrier for CO oxidation, calculated by averaging the CO adsorption barriers over all the *-O* site-pairs on the Pt_{201} cluster, is less than 5 kJ $(mol\ CO)^{-1}$, which is within the errors associated with DFT calculations (< 15 kJ $(mol\ CO)^{-1}$). Thus, the CO oxidation is considered as a non-activated step.

3.3.7. Comparison of Experimentally Measured and Calculated Ensemble-Averaged Oxygen Selectivities in CH_4-O_2 Mixtures. Figure 7 shows the effects of temperature (885-935 K) on the ratio of rate constants for O_2 and C-H bond activation $(k_{O^*}K_{O_2}(3.5k_{[*\text{-}*]}K_{CH_4})^{-1})$ measured from $^{13}CH_4$-^{12}CO-O_2 reactions on Pt/SiO_2 (0.2 % wt.; 33 nm mean cluster diameter). The rate constant ratios $(k_{O^*}K_{O_2}(3.5k_{[*\text{-}*]}K_{CH_4})^{-1})$, together with the O_2/CO ratios, determine O* selectivities (Eq. 12) and, in turn, the intrinsic limits

of the maximum CO yields for the direct reactions of CH_4 and O_2. The rate constant ratios for O_2 to C-H bond activation were larger than 200 in the 885-930 K range and decreased with increasing temperature.

These rate constant ratios are interpreted using a transition state theory formalism and the thermodynamic properties of reactants and transition states for O_2 and C-H bond activation steps:

$$\frac{k_{O^*}K_{O_2}}{3.5k_{[*-*]}K_{CH_4}} = \frac{1}{3.5}\exp\left(\frac{\Delta S^*_{O_2} - \Delta S^*_{CH_4}}{k_B}\right)\exp\left(-\frac{\left(\Delta H^*_{O_2} - \Delta H^*_{CH_4}\right)}{k_B T}\right) \qquad (21)$$

$\Delta S^*_{O_2}$ (or $\Delta S^*_{CH_4}$) and $\Delta H^*_{O_2}$ (or $\Delta H^*_{CH_4}$) are the changes in entropy and enthalpy, respectively, required to form $(O^*\text{--}O^*)^{\ddagger}$ (or $(H_3C^*\text{--}H^*)^{\ddagger}$) transition states from gaseous O_2 (or CH_4) reactants. Linear regression analyses on the data in Figure 7 using Eq. 21 led to estimates for the ($\Delta S^*_{O_2} - \Delta S^*_{CH_4}$) and ($\Delta H^*_{O_2} - \Delta H^*_{CH_4}$) terms in Eq. 21. The ($\Delta S^*_{O_2} - \Delta S^*_{CH_4}$) term was -31 J (mol-K)$^{-1}$; $\Delta S^*_{CH_4}$ reflects the entropy loss of CH_4(g) upon formation of the $(H_3C^*\text{--}H^*)^{\ddagger}$ transition state in the C-H bond activation step on *-* site-pairs and was previously reported to be -99 J (mol-K)$^{-1}$ and -108 J (mol-K)$^{-1}$ for CH_4-CO_2 and CH_4-H_2O mixtures, respectively.[24] Substituting these values into the ($\Delta S^*_{O_2} - \Delta S^*_{CH_4}$) term of -31 J (mol-K)$^{-1}$ give, in turn, an O_2 activation entropy ($\Delta S^*_{O_2}$) of ~ -130 J (mol-K)$^{-1}$, which is less negative than that predicted for an immobile $(O^*\text{--}O^*)^{\ddagger}$ transition state (-175 J (mol-K)$^{-1}$). The measured enthalpy difference for the O_2 and CH_4 reactants to form their respective transition states from the gas phase, ($\Delta H^*_{O_2} - \Delta H^*_{CH_4}$), is -81 kJ mol^{-1}. This value, taken together with non-activated O_2 dissociation steps,[23] gives a $\Delta H^*_{CH_4}$ value of 81 kJ mol^{-1}, corresponding to the C-H bond dissociation barrier on *-* site-pairs. This value is similar to activation energies for CH_4 decomposition (78 kJ mol^{-1}), CH_4-CO_2 (83 kJ mol^{-1}), and CH_4-H_2O (75 kJ mol^{-1}) reactions,[24] all of which are limited by the initial activation of C-H bonds in CH_4 on *-* site-pairs (Step 4, Scheme 2). The measured C-H bond activation barrier (approximated by $\Delta H^*_{CH_4}$) is compared with the ensemble-averaged barrier, E_{CH_4}, which is related to the ensemble-averaged CH_4 reaction rate constant (k_{CH_4}) according to:

$$k_{CH_4} = A\exp\left(\frac{-E_{CH_4}}{k_B T}\right) = \sum_{i=1-4}\left(A_{i,CH_4}\exp\frac{\left(-E_{C\text{-}H,i}\right)}{k_B T}\right)P_i \qquad (22)$$

This rate constant was derived from DFT estimates of C-H bond activation barriers at various Pt sites i ($E_{C\text{-}H,i}$, i=1-4, Scheme 1, Fig. 6a) weighed by their relative abundances on Pt_{201} clusters (P_i). A is the ensemble-averaged pre-exponential factor and $\left(A_i\right)_{CH_4}$ is the pre-exponential factor for each Pt site (i). Assuming that $\left(A_i\right)_{CH_4}$ values for all Pt sites remain the same, Eq. 22 can be rearranged to give the ensemble-averaged barrier for C-H bond activation on *-* site-pairs (E_{CH_4}):

$$E_{CH_4} = -k_B T \ln\left(\sum_{i=1-4} P_i \exp\frac{\left(-E_{C\text{-}H,i}\right)}{k_B T} \right) \quad (23)$$

E_{CH_4} was calculated to be 76 kJ mol^{-1} for 33 nm Pt clusters, consistent with measured values (81 kJ mol^{-1}).

The ensemble-averaged rate constant ratios for 1.8 nm and 33 nm cubo-octahedral Pt clusters were obtained from measured differences in O_2 and C-H activation entropies ($\Delta S^*_{O_2} - \Delta S^*_{CH_4}$ = -31 J (mol-K)$^{-1}$), DFT-derived C-H bond activation barriers on the various Pt sites ($E_{C\text{-}H,i}$, Fig. 6, Table 3) and their relative abundances (P_i), assuming that O_2 dissociation is barrierless (E_{O_2} < 3 kJ mol^{-1} [23]) and that activation entropies are independent of the specific activation site ($\Delta S^*_{O_2} - \Delta S^*_{CH_4}$):

$$\frac{k_{O^*}K_{O_2}}{3.5k_{[*\text{-}*]}K_{CH_4}} = \frac{1}{3.5}\exp\left(\frac{\Delta S^*_{O_2} - \Delta S^*_{CH_4}}{k_B}\right)\frac{\exp\frac{\left(-E_{O_2}\right)}{k_B T}}{\sum_{i=1-4}\left(\exp\frac{\left(-E_{C\text{-}H,i}\right)}{k_B T}\right)P_i} \quad (24)$$

The specific location of O* (random or energy-weighted, Eq. 5) did not influence ensemble-averaged rate constant ratios, because rate constants for O_2 dissociation ($k_{O^*}K_{O_2}$) and C-H bond activation ($k_{[*\text{-}*]}K_{CH_4}$) were, in turn, insensitive to O* binding energies. O_2 dissociation rate constants depend only on entropy losses and are therefore insensitive to O* location and surface coordination. C-H bond dissociation rate constants depend on the entropy and enthalpy of formation of the $(H_3C^*\text{--}H^*)^{\ddagger}$ transition states from CH_4(g). The $(H_3C^*\text{--}H^*)^{\ddagger}$ species do not involve O* (Sec. 3.4-3.6) and, as a result, C-H activation rate constants also do not depend on the location or binding energy of O*. The ensemble-averaged rate constant ratios for O_2 and C-H bond activation ($k_{O^*}K_{O_2}(3.5k_{[*\text{-}*]}K_{CH_4})^{-1}$) were much larger than unity at all temperatures relevant to the practice of catalytic CH_4-O_2 reactions (873 K-1273 K, Fig. 7) for the large Pt clusters (33 nm mean cluster size). The ratios were smaller and approached unity at higher temperatures (> 1300 K) for the small Pt clusters (1.8 nm mean cluster size), indicating that desorbed CO may become detectable in effluent streams only at temperatures unlikely to preserve their small size.

Pt surface coordination and cluster size influence ensemble-averaged rate constant ratios [$k_{O^*}K_{O_2}(3.5k_{[*\text{-}*]}K_{CH_4})^{-1}$], predominantly because of their concomitant effects on the C-H bond activation rate constants ($k_{[*\text{-}*]}K_{CH_4}$), since they do not affect the O_2 dissociation rate constants ($k_{O^*}K_{O_2}$).[23] The ensemble-averaged C-H bond dissociation barriers calculated using Eq. 23 decreased from 76 kJ mol^{-1} to 64 kJ mol^{-1} (Fig. 8) as Pt clusters became smaller (33 nm to 1.8 nm) and as the surface fraction of coordinatively unsaturated metal atoms concomitantly increased. This decrease in barriers with cluster size leads to an increase in the ensemble-averaged CH_4 reaction rate constants (Eq. 22) and, in turn, to a decrease in the calculated ensemble-averaged rate constant ratios (Fig. 7) and smaller measured O* selectivities (Fig. 3) on the smaller clusters.

O* selectivities (Eq. 12), determined from ensemble-averaged rate constant ratios [$k_{O^*}K_{O_2}(3.5k_{[*-*]}K_{CH_4})^{-1}$] and O_2/CO ratios, were used in a kinetic model that captures the CH_4 oxidation to CO (and H_2) and their sequential oxidation to estimate the intrinsic limits of the maximum CO yields. Solving the mole balances for CH_4, CO, and O_2 in an isothermal-isobaric plug-flow reactor give the maximum CO yields (Figure A. 7 in the Appendix) as a single-valued function of the O* selectivities. These results suggest that a small amount of CO, initially formed in the reactor, would undergo rapid sequential oxidation because of the high $k_{O^*}K_{O_2}(3.5k_{[*-*]}K_{CH_4})^{-1}$ values and low O_2/CO ratios.

CO/CO_2 ratios were much lower on Rh than on Pt clusters at all conditions before the complete consumption of limiting O_2 reactants (Fig. 2), suggesting that CO oxidation reactions are more effective on Rh clusters. We were unable to measure the O* selectivities in $^{13}CH_4$-CO-O_2 mixtures on Rh clusters at all O_2/CO ratios without completely depleting the limiting reactants, which could be CO or O_2 depending on the O_2/CO ratio, because of the high CO oxidation rates. These results suggest more reactive surfaces for CO oxidation and, in turn, higher O* selectivities on Rh than Pt clusters, apparently caused by the stronger binding of O* on Rh than Pt (DFT calculated O* binding strengths are 469 kJ mol^{-1} and 354 kJ mol^{-1} for a single O* chemisorbed on Rh(111) and Pt(111), respectively[48]) and the concomitantly larger O* contents on Rh surfaces. Catalytic effects of oxygen vacancies were not detected at any amount of measurable O_2 and O_2/CH_4 ratio, as confirmed from the same kinetic dependence, where C-H bond activation rate constants on Rh clusters increase solely with oxygen chemical potential, throughout the entire O_2/CH_4 range (0.02-200; 873 K).[49] The bulk of the Rh clusters, as predicted from the phase equilibrium thermodynamics of Rh and their oxides (Rh_2O_3, RhO_2), remain in the oxide phase even at an equilibrium O_2 pressure of 0.01 kPa at 873 K.[50] In CH_4-O_2 mixtures, the Rh clusters are likely in their oxide phases in the presence of O_2 and surface oxygen atoms in the oxide structures appear to selectively promote the CO oxidation, leading to the lower CO/CO_2 ratios on Rh than on Pt. The low maximum CO yields on Pt and the expected even lower yields on Rh led us to conclude that direct CO (and H_2) formation from CH_4 and O_2 reactions is unlikely on Pt and Rh clusters at CH_4 conversions of practical interest because these products are much more reactive than CH_4. These partial oxidation products are formed from sequential reactions of CO_2 and H_2O combustion products with residual CH_4 at all practical temperatures and O_2/CH_4 ratios.

3.4. Conclusion

CO/CO_2 ratios resulting from CH_4 and O_2 reactions on supported Pt and Rh clusters were measured by varying the residence time and O_2/CH_4 feed ratio independently in a regime of strict kinetic control, achieved by extensive dilutions of catalyst pellets and the reactor bed. A small amount of CO was detected ($CO/CO_2 < 0.02$) only at very low O_2/CH_4 ratios ($O_2/CH_4 < 0.004$) as catalyst surfaces were depleted of reactive oxygen intermediates.

Oxygen selectivities, defined by the ratios of reactive collision probabilities (also the effective rate constants) of desorbed CO and CH_4 reactant with O*, determine the CO/CO_2 ratios in CH_4-O_2 reactions. We have interpreted the oxygen selectivities rigorously in terms of elementary rate and equilibrium constants and measured their

values by carrying out $^{13}CH_4$ and ^{12}CO oxidation in $^{13}CH_4$-^{12}CO-O_2 mixtures. Reactive collision probabilities for CO reactions with O* on uncovered Pt clusters are much larger than those for CH_4. The higher reactivity for CO than CH_4 towards the O* limits the maximum attainable CO yield from the direct reactions of CH_4 and O_2.

Density functional theory (DFT) results are used within the framework of transition state theory and ensemble averaging methods to probe the calculated oxygen selectivities. DFT calculations were carried out on the corner, edge, and terrace sites of a model cubo-octahedral Pt cluster (1.8 nm diameter) to probe the kinetically-relevant steps and the identity of active sites involved in CH_4 and CO oxidation. CH_4 oxidation proceeds via kinetically-relevant C-H bond dissociation on Pt atom site-pairs (*-*) in which one of the Pt sites undergoes an oxidative addition step into the C-H bond. The C-H bond activation barriers on *-* site-pairs are correlated to the Pt-CH_3 bond strength and the coordination number of the Pt atom. CO oxidation proceeds via a non-activated molecular CO adsorption step; this step is irreversible because its reverse step (CO* desorption) exhibits a much larger barrier than the sequential CO* and O* recombination reaction. The barriers for CO and CH_4 oxidation were calculated from ensemble-averaging the individual barriers for the various types of surface sites on the model Pt cluster. These barriers, together with the measured activation entropies, were used within the framework of transition state theory to calculate ensemble-averaged O* selectivities. O* selectivities are proportional to O_2/CO ratios and are estimated to be much larger than unity, especially when a small amount of CO is formed initially, over the entire temperature range typical of CH_4-O_2 catalysis. These results unequivocally show that oxidation of CO intermediates is much more rapid than the activation of CH_4 reactants. The marked reactivity differences lead to low intrinsic limits of the CO yields from direct reactions between the CH_4 and O_2 at any practical extent of CH_4 reactions.

3.5. References

[1] Rostrup-Nielsen, J.R. *Catal. Today* **2002**, *71*, 243.
[2] Dave, N.; Foulds, G.A. *Ind. Eng. Chem. Res.* **1995**, *34*, 1037.
[3] Hickman, D.A.; Schmidt, L.D. *Science* **1993**, *259*, 243.
[4] Hickman, D.A.; Haupfear, E.A.; Schmidt, L.D. *Catal. Lett.* **1993***, 17*, 223.
[5] Dissanayake, D.; Rosynek, M.P.; Kharas, K.C.C.; Lunsford, J.H. *J. Catal.* **1991**, *132*, 117.
[6] Vermeiren, W.J.M.; Blomsma, E.; Jacobs, P.A. *Catal. Today* **1992**, *13*, 427.
[7] Tavazzi, I.; Maestri, M.; Beretta, A.; Groppi, G.; Tronconi, E.; Forzatti, P. *AIChE J.* **2006***, 52*, 3234.
[8] Beretta, A.; Groppi, G.; Lualdi, M.; Tavazzi, I.; Forzatti, P. *Ind. & Engr. Chem. Res.* **2009**, *48*, 3825.
[9] Horn, R.; Williams, K.A.; Degenstein, N.J.; Bitsch-Larsen, A.; Dalle Nogare, D.; Tupy, S.A.; Schmidt, L.D. *J. Catal.* **2007**, *249*, 380.
[10] Enger, B.C.; Lødeng, R.; Holmen, A. *Appl. Catal. A* **2009**, *364*, 15.
[11] Vannice, M.A.; Benson, J.E.; Boudart, M. *J. Catal.* **1970**, *16*, 348.
[12] R.L. David, Handbook of Chemistry and Physics, 87th ed., CRC Press, Boca Raton, FL, 2006, p. 4-26 and p. 4-30.
[13] Van Hardeveld, R.; Hartog, F. *Surf. Sci.* **1969**, *15*, 189.

[14] Perdew, J.P.; Chevary, J.A.; Vosko, S.H.; Jackson, K.A.; Pederson, M.R.; Singh, D.J.; Fiolhais, C. *Phys. Rev. B* **1992**, *46*, 6671.
[15] Kresse, G.; Hafner, J. *Phys. Rev. B* **1994**, *49*, 14251.
[16] Kresse, G.; Furthmuller, J. *Comput. Mater. Sci.* **1996**, *6*, 15.
[17] Kresse, G.; Furthmuller, J. *Phys. Rev. B* **1996**, *54*, 11169.
[18] Vanderbilt, D. *Phys. Rev. B* **1990**, *41*, 7892.
[19] Monkhorst, H.J.; Pack, J.D. *Phys. Rev. B* **1976**, *13*, 5188.
[20] Henkelman, G.; Jonsson, H. *J. Chem. Phys.* **2000**, *113*, 9978.
[21] Koros, R.M.; Nowak, E.J. *Chem. Engr. Sci.* **1967**, *22*, 470.
[22] Madon, R.; Boudart, M. *Ind. Eng. Chem. Fundam.* **1982**, *21*, 438.
[23] Chin, Y-H.; Buda, C.; Neurock, M.; Iglesia, E. *J. Am. Chem. Soc.*, submitted.
[24] Wei, J.; Iglesia, E. *J. Phys. Chem. B* **2004**, *108*, 4094.
[25] Estimated based on monolith volume of 2.5 cm^3, 66.7 cm^3 s^{-1} CH_4/air feed mixtures with an O_2/CH_4 ratio of 2, and 50% CH_4 conversion.
[26] Eichler, A.; Hafner, J. *Phys. Rev. Lett.* **1997**, *79*, 4481.
[27] García-Diéguez M.; Chin, Y-H.; Iglesia, E. in preparation.
[28] The exact ν_1 and ν_2 values affect only the stoichoimetry that appears in the S_{O^*} expression but not the functional dependence of S_{O^*} on O_2/CO ratios.
[29] Wei, J.; Iglesia, E. *J. Catal.* **2004**, *225*, 116.
[30] Wei, J.; Iglesia, E. *J. Phys. Chem. B* **2004**, *108*, 7253.
[31] Yamaguchi A.; Iglesia, E. *J. Catal.* **2010**, *274*, 52.
[32] Burghgraef, H.; Jansen, A.P.J.; van Santen, R.A. *Surf. Sci.* **1995**, *324*, 345.
[33] Ciobica, I.M.; Frechard, F.; van Santen, R.A.; Kleyn, A.W.; Hafner, J.A. *J. Phys. Chem. B.* **2000**, *104*, 3364.
[34] Jones, G.; Jakobsen, J.G.; Shim, S.S.; Kleis, J.; Andersson, M.P.; Rossmeisl, J.; Abild-Pedersen, F.; Bligaard, T.; Helveg, S.; Hinnemann, B.; Rostrup-Nielsen, J.R.; Chorkendorff, I.; Sehested, J.; Norskov, J.K. *J. Catal.* **2008**, *249*, 147.
[35] Greenwood, N.N.; Earnshaw, A. Chemistry of the Elements, 2nd ed, Butterworth-Heinemann, 1997, p. 1148.
[36] Sanchez, S.I.; Menard, L.D.; Bram, A.; Kang, J.H.; Small, M.W.; Nuzzo, R.G.; Frenkel, A.I. *J. Am. Chem. Soc.* **2009**, *131*, 7040.
[37] Buda, C.; Neurock, M. unpublished results.
[38] Zhao, Y.; Truhlar, D.G. *Theor. Chem. Acc.* **2008**, *120*, 215.
[39] Scuseria, G.; Staroverov, V.N. in: Dykstra, C.E.; Frenking, G.; Kim, K.S.; Scuseria, G.E. (Eds.), Theory and Applications of Computational Chemistry: The First 40 Years, Elsevier, Amsterdam, The Netherlands, 2005, p. 669.
[40] Sakaki, S.; Ieki, M. *J. Am. Chem. Soc.* **1993**, *115*, 2373.
[41] Venkataraman, P.S.; Neurock, M.; Lusvardi, V.S.; Lerou, J.J.; Kragten, D.D.; van Santen, R.A. *J. Phys. Chem. B*, **2002**, *106*, 1656.
[42] Neurock, M. *Appl. Catal.* **1996**, *160*, 169.
[43] Jones, W.D. *Acc. Chem. Res.* **2003**, *36*, 140.
[44] Cundari, T.R. *J. Am. Chem. Soc.* **1994**, *116*, 340.
[45] Oxgaard, J.; Muller, R.P.; Goddard III, W.A.; Periana, R.A. *J. Am. Chem. Soc.* **2004**, *126*, 352.
[46] Cundari, T. R.; Grimes, T. V.; Gunnoe, T. B. *J. Am. Chem. Soc.* **2007**, *129*, 13172.

[47] Ishikawa, A.; Neurock, M.; Iglesia, E. *J. Am. Chem. Soc.* **2007**, *129*, 13201.
[48] van Santen, R.A. and Neurock, M. Molecular Heterogeneous Catalysis: a Conceptual and Computational Approach, Weinheim, Cambridge: Wiley-VCH, 2006, p. 107.
[49] Chin, Y-H.; Iglesia, E. unpublished results.
[50] Muller, O.; Roy, R. *J. of Less-Common Metals* **1968**, *16*, 129.

3.6. Figures

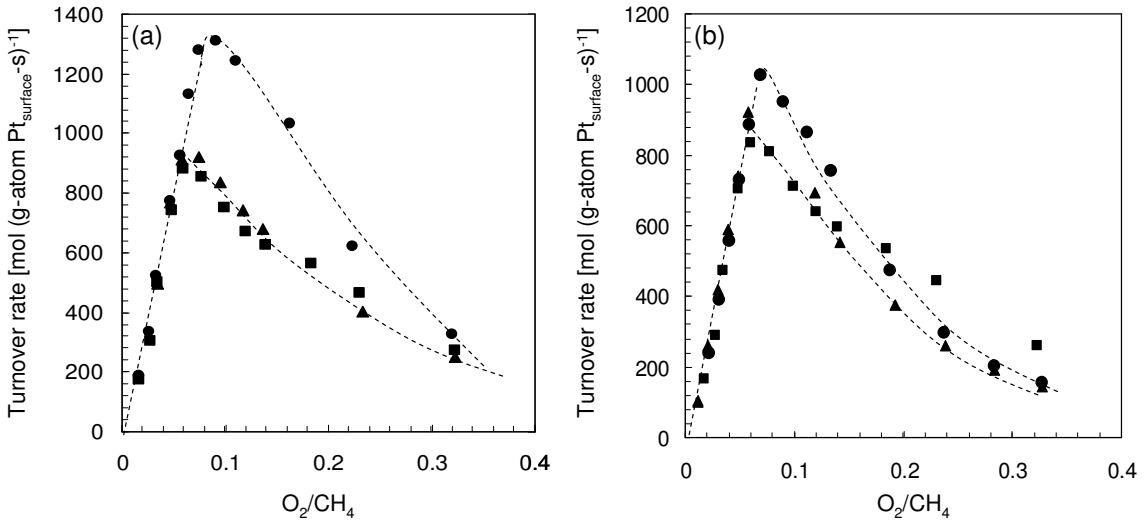

Figure 1a. Effects of intrapellet diluent-to-catalyst ratio (λ) {100 (●), 200 (▲), 300 (■)} on CH_4 turnover rates (per exposed Pt atom; 873 K) on 0.2 % wt. Pt/Al_2O_3 (8.5 nm mean cluster diameter), plotted here as a function of O_2/CH_4 ratio (4700 diluent/catalyst interpellet dilution ratio (χ), 0.15 mg cat., 2.08 cm^3 (STP) s^{-1}, 4.9 kPa CH_4).

Figure 1b. Effects of interpellet diluent-to-catalyst ratio (χ) {1000 (●), 2000 (▲), 4700 (■)} on CH_4 turnover rates (per exposed Pt atom; 873 K) on 0.2 % wt. Pt/Al_2O_3 (8.5 nm mean cluster diameter), plotted here as a function of O_2/CH_4 ratio (200 diluent/catalyst intrapellet dilution ratio (λ), 0.15 mg cat., 2.08 cm^3 (STP) s^{-1}, 4.9 kPa CH_4).

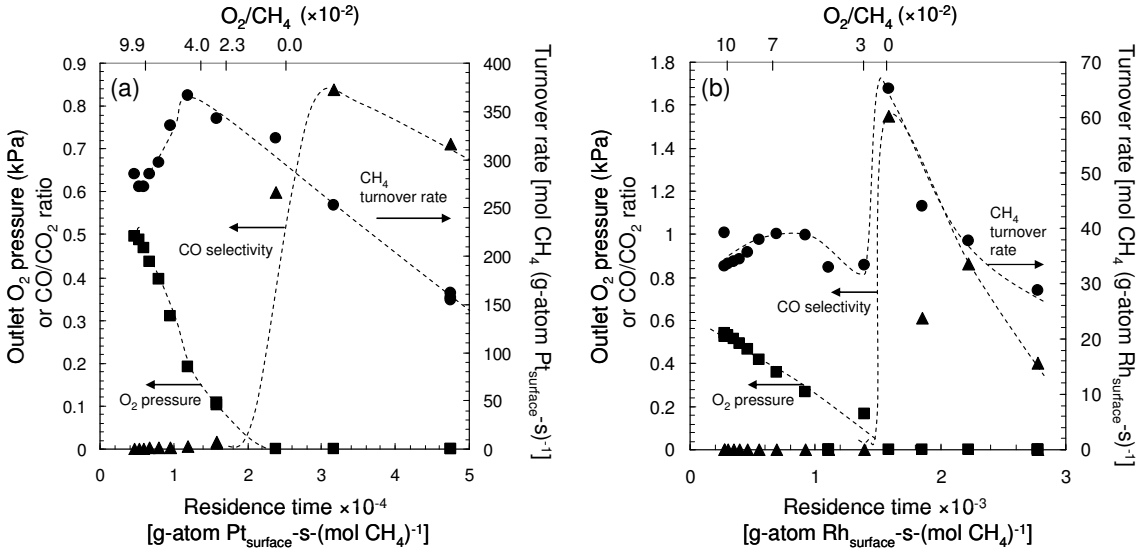

Figure 2a. CH_4 turnover rate (●), outlet O_2 pressure (■), and CO selectivity (▲) during CH_4-O_2 reactions on 0.2 % wt. Pt/Al_2O_3 (8.5 nm mean cluster diameter) as a function of residence time for an inlet O_2/CH_4 feed ratio of 0.13 (873 K, 4.9 kPa CH_4, λ=200, χ =4700). O_2/CH_4 ratios at the effluent stream are indicated in the secondary x-axis.

Figure 2b. CH_4 turnover rate (●), outlet O_2 pressure (■), and CO selectivity (▲) during CH_4-O_2 reactions on 0.2 % wt. Rh/Al_2O_3 (3.3 nm average cluster diameter) as a function of residence time for an inlet O_2/CH_4 feed ratio of 0.125 (873 K, 5.0 kPa CH_4, λ=200, χ =4700). O_2/CH_4 ratios at the effluent stream are indicated in the secondary x-axis.

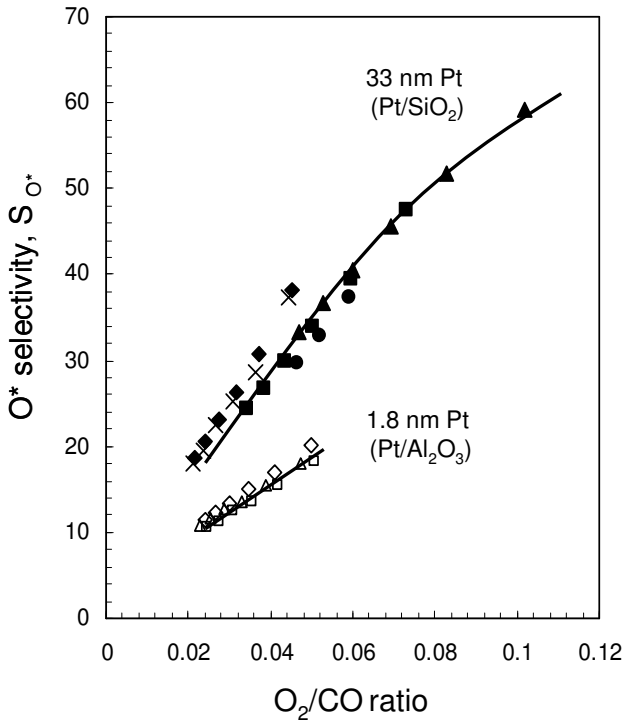

Figure 3. O* selectivity (S_{O^*}, 873 K) during competitive $^{13}CH_4$-^{12}CO oxidation reactions on 1.8 nm and 33 nm Pt clusters as a function of O_2/CO ratio (0.3 mg 0.2 % wt. Pt/Al_2O_3 or Pt/SiO_2, respectively; 1.2 kPa (Δ), 2.0 kPa (□,×), 2.8 kPa (◊, ♦, ▲, ■), and 4.2 kPa (●) CH_4; 0.008 kPa (♦,×), 0.009 kPa (□,◊,Δ), 0.013 kPa (■), and 0.017 kPa (▲,●) O_2, 2.08 $cm^3\ s^{-1}$, λ=200, χ =4700).

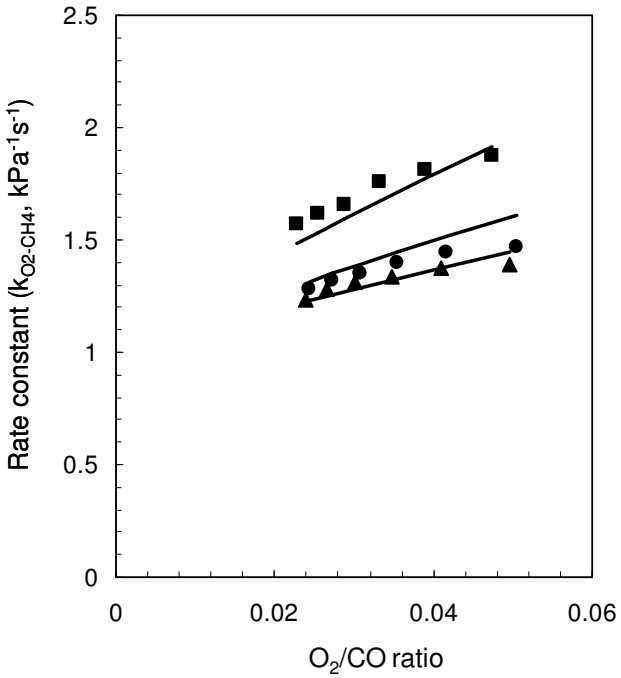

Figure 4. Effective rate constants (also the reactive collision probabilities) for $^{13}CH_4$ oxidation reactions ($k_{O_2-CH_4}$, Eq. 9, 873 K) in $^{13}CH_4$-^{12}CO-O_2 mixtures as a function of O_2/CO ratio on surfaces of 0.2 % wt. Pt/Al_2O_3 (1.8 nm mean cluster diameter); the lines are derived from regression of rate data with Eq. 16 (0.3 mg cat.; 1.2 kPa (■), 2.0 kPa (●), and 2.8 kPa (▲) CH_4, 0.0093 kPa (■,●,▲) O_2; 2.08 cm^3 s^{-1}, λ=200, χ =4700).

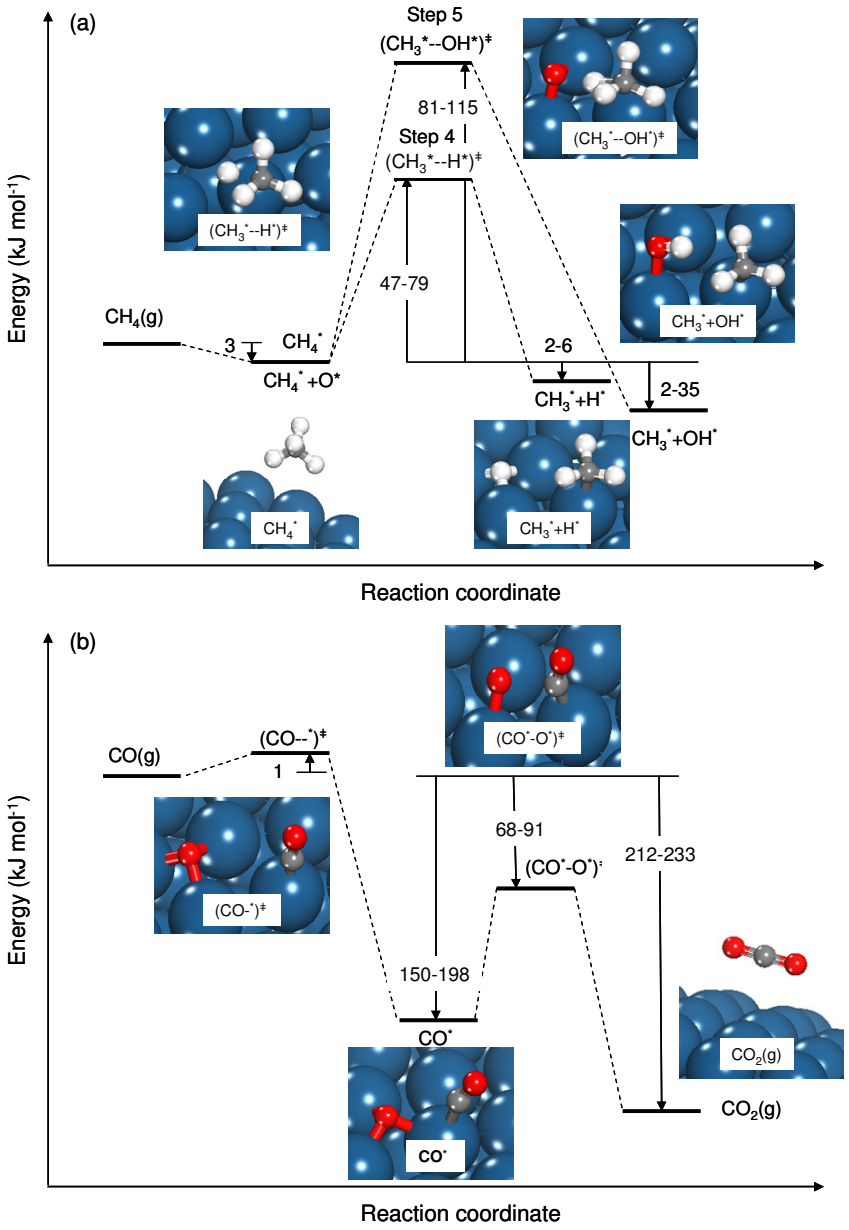

Figure 5a. Reaction energy diagram for initial C-H bond dissociation of CH_4 on the various Pt metal-metal (*-*) (Step 4, Scheme 2) and metal-oxygen (*-O*) site pairs (Step 5, Scheme 2) on Pt_{201} clusters. The energy ranges of intermediates, transition states, and products are given with respect to the reactant energy.

Figure 5b. Reaction energy diagram for CO oxidation reaction on the various Pt metal-oxygen (*-O*) site pairs on Pt_{201} clusters. The energy ranges of intermediates, transition states, and products are given with respect to the reactant energy.
See Appendix for the structural details of these steps.

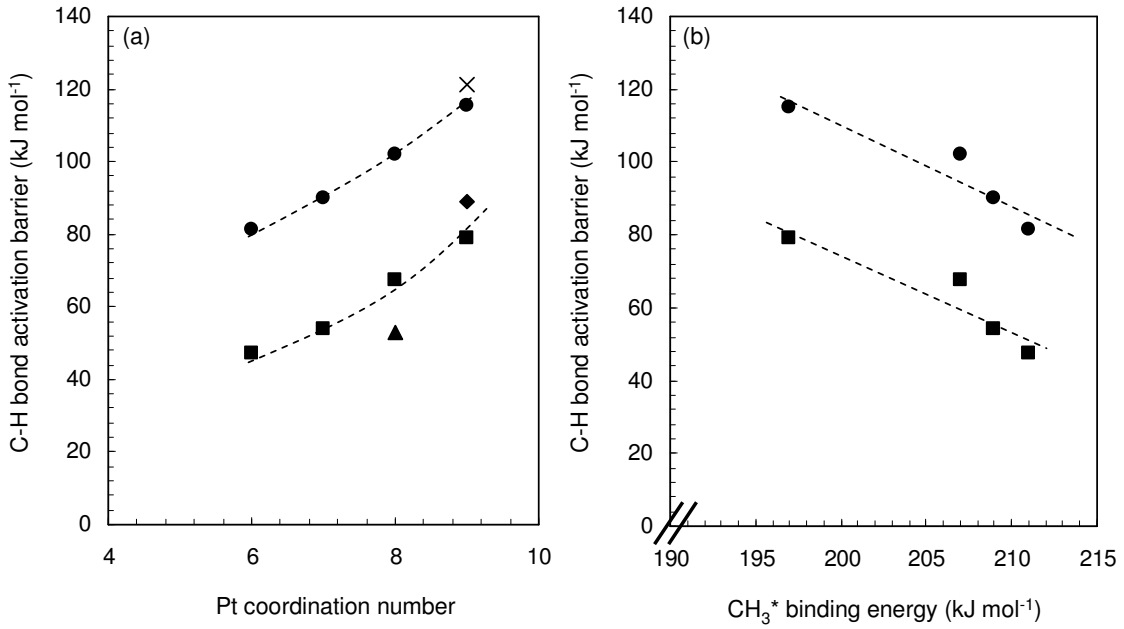

Figure 6a. Effects of the Pt coordination number on the DFT calculated C-H bond activation barriers of CH_4 on Pt metal-metal (*-*) site pairs (■) and on Pt metal-oxygen atom (*-O*) site pairs (●) on the various Pt sites (type i=1-4, Scheme 1) of a Pt_{201} cluster. C-H bond activation barriers on Pt metal-metal (*-*) site-pairs at Pt(111) (♦) and Pt(100) (▲) surfaces and on Pt metal-oxygen atom (*-O*) site-pairs at Pt(111) (×) surfaces are included for comparison.

Figure 6b. Effects of CH_3* binding energy at the various Pt sites (type i=1-4, Scheme 1) on the C-H bond activation barriers of CH_4 on Pt metal-metal (*-*) (■) and Pt metal-oxygen atom (*-O*) (●) site-pairs on the surfaces of a Pt_{201} cluster.

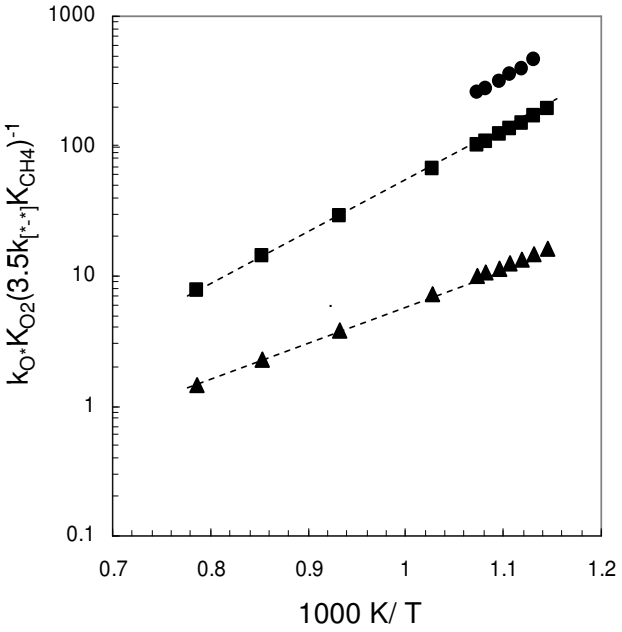

Figure 7. Comparison of experimentally measured (●) and calculated (■, ▲) ratio of rate constants for O_2 and C-H bond activation ($k_{O^*}K_{O_2}(3.5k_{[*-*]}K_{CH_4})^{-1}$) on 1.8 nm (▲) and 33 nm (●, ■) Pt clusters. The experimental data (●) were measured in $^{13}CH_4$-^{12}CO-O_2 mixtures on 0.2 % wt. Pt/SiO_2 catalyst (0.3 mg cat., 33 nm average Pt cluster diameter, 0.022 kPa O_2, 0.16 kPa CO, 1.3 kPa $^{13}CH_4$; 2.08 cm^3 s^{-1}, λ=200, χ =4700). The calculated ensemble-averaged rate constant ratios (■: 33 nm Pt cluster; ▲: 1.8 nm Pt cluster) were the same for the cases of random and energy-weighted O* placements at each temperature.

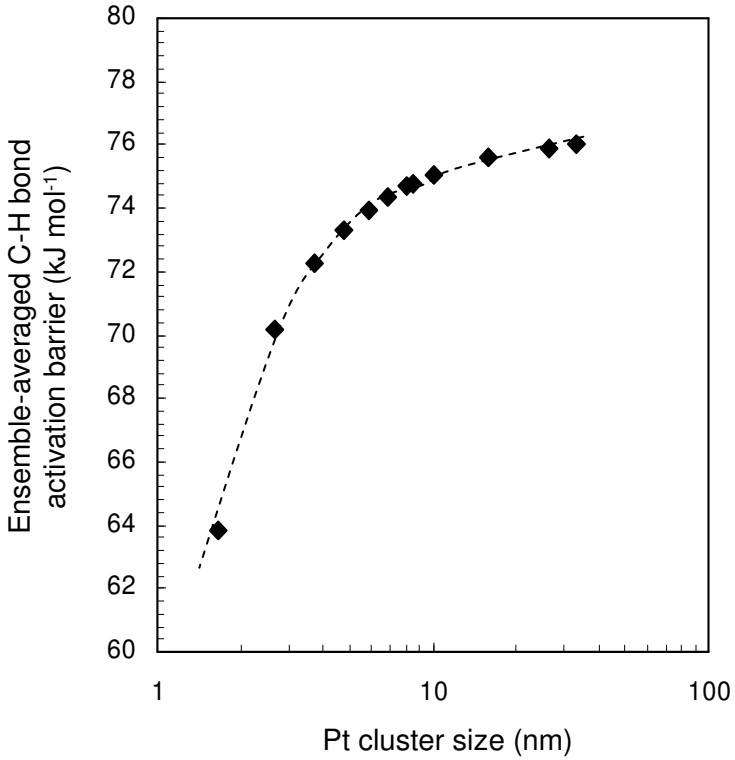

Figure 8. Effects of Pt cluster size on the calculated ensemble-averaged C-H bond activation barriers of CH_4 on Pt metal atom (*-*) site-pairs using Eq. 23.

3.7. Schemes

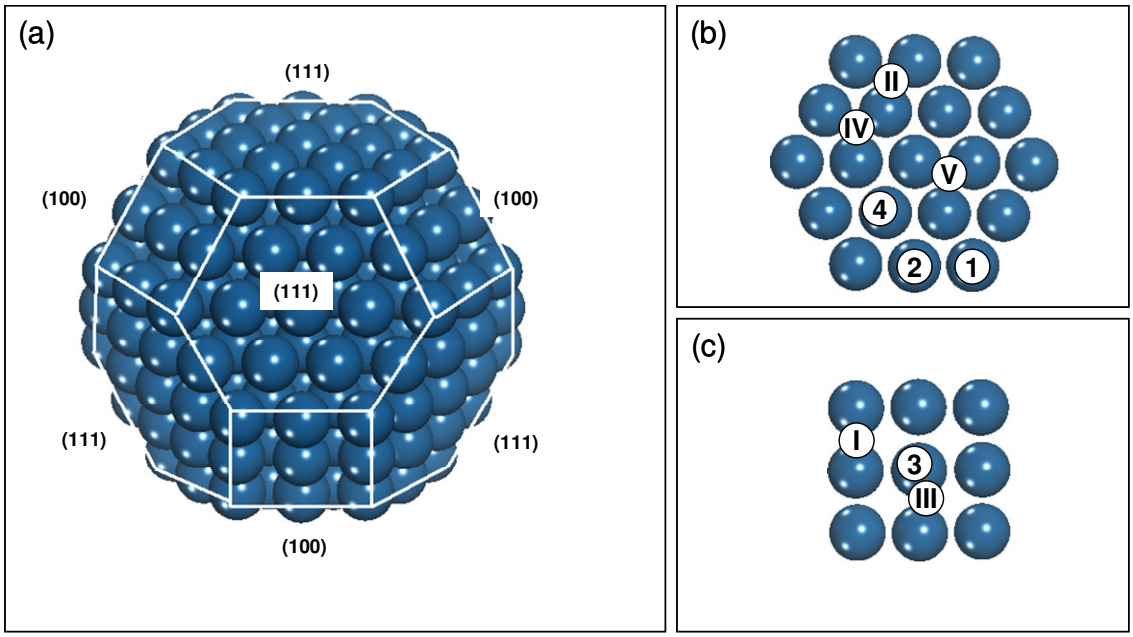

Scheme 1 a-c. (a) Model of a cubo-octahedral Pt cluster (1.8 nm cluster size) consists of 201 Pt atoms with: (b) eight (111) and (c) six (100) planes. There are 4 distinct types of surface Pt atom (labeled sites 1-4) depending on their coordination numbers. Oxygen adatoms bind on three-fold fcc sites (location II, IV, and V) on the (111) surfaces (b) and on the bridge sites (location I and III) on the (100) surfaces (c).

$$O_2 + * \xleftrightarrow{K_{O_2}} O_2 * \quad (1)$$

$$O_2 * + * \xrightarrow{k_{O*}} 2O * \quad (2)$$

$$CH_4 + * \xleftrightarrow{K_{CH_4}} CH_4 * \quad (3)$$

$$CH_4 * + * \xrightarrow[\Longrightarrow]{k_{[*-*]}} CH_3 * + H * \quad (4)$$

$$CH_4 * + O * \xrightarrow[\Longrightarrow]{k_{[O*-*]}} CH_3 * + OH * \quad (5)$$

$$C * + O * \xrightarrow{k_{C*+O*}} CO * + * \quad (6)$$

$$* CO \xrightarrow[\longleftarrow]{k_{CO\,des}, k_{CO\,ads}} CO + * \quad (7)$$

$$CO * + O * \xrightarrow{k_{CO\,oxi}} CO_2 * + * \quad (8)$$

$$CO_2 * \xleftrightarrow{K_{CO_2}} CO_2 + * \quad (9)$$

$$2H * \xleftrightarrow{K_{H_2}} H_2 + 2 * \quad (10)$$

$$H * + O * \xleftrightarrow{K_{H*+O*}} OH * + * \quad (11)$$

$$H * + OH * \xleftrightarrow{K_{H*+OH*}} H_2O * + * \quad (12)$$

$$H_2O * \xleftrightarrow{K_{H_2O}} H_2O + * \quad (13)$$

$$CH_x *_S + O *_W \xrightarrow{k_{CH*}} \quad (14)$$

Scheme 2. A proposed sequence of elementary steps for CH_4-O_2 reactions on Pt clusters uncovered of chemisorbed oxygen atoms. $\longrightarrow$ and $\longleftrightarrow$ denote irreversible and quasi-equilibrated steps, respectively. k is the rate coefficient and K the equilibrium constant for the respective elementary step.

3.8. Tables

Table 1. Effects of intra-particle (λ) and inter-particle (χ) diluent-to-catalyst ratios on CH_4 turnover rates on 0.2 % wt. Rh/Al_2O_3 (3.3 nm mean cluster diameter) catalyst at 873 K (0.37 mg cat., 0.583 cm^3 (STP) s^{-1}, 0.13 inlet O_2/CH_4 ratio).

Turnover rate (mol CH_4(g-atom $Rh_{surface}$-s)$^{-1}$)	Heat load × 10^{-2} (W cm^{-3})	Intraparticle (λ) diluent-to-catalyst ratio	Interparticle (χ) diluent-to-catalyst ratio
65.3	5.4	300	1900
68.1	3.8	300	2800
62.0	3.5	200	2800
71.9	4.1	100	2800

Table 2. O_2 turnover rates during $^{13}CH_4$-^{12}CO-O_2, $^{12}CH_4$-O_2, and ^{12}CO-O_2 reactions and ratios of O_2 turnover rates in $^{13}CH_4$-^{12}CO-O_2 and CO-O_2 mixtures (β, Eq. 17) on supported Pt clusters of 1.8 nm and 33 nm mean cluster diameters (0.2 % wt. Pt supported on Al_2O_3 and SiO_2, respectively) at 873 K.

Entry	Pt cluster size (nm)	Reactant mixture	O_2 pressure (kPa)	$\frac{(O_2)}{(CO)}$	$\frac{(O_2)}{(CH_4)}$	O_2 turnover rates (mol O_2(g-atom $Pt_{surface}$-s)$^{-1}$)	β
1	33	$^{12}CH_4$-O_2	0.036	-	0.022[1]	500.1	-
2	33	^{12}CO-O_2	0.036	0.23	-	512.4	-
3	33	$^{13}CH_4$-^{12}CO-O_2	0.036	0.23	0.022	496.0	0.99
4	1.8	^{12}CO-O_2	0.009	0.024	-	9.0	-
5	1.8	$^{13}CH_4$-^{12}CO-O_2	0.009	0.024	0.008	7.5	0.83
6	1.8	$^{13}CH_4$-^{12}CO-O_2	0.009	0.024	0.0033	7.1	0.79

(λ =200, χ =4700, 0.15 mg cat., 2.08 cm^3 (STP) s^{-1})

[1] The O* coverages during steady-state catalysis depends on the operating O_2/CH_4 ratios, the rate and thermodynamic constants for the O_2 and C-H bond activation elementary steps, which vary with Pt cluster size. For the 33 nm Pt clusters, the surfaces are depleted of O* for O_2/CH_4 ratios below 0.08 at 873 K.

Table 3. Average Pt coordination numbers, heats of oxygen adsorption, intrinsic and effective barriers for CO* and O* reactions on a cubo-octahedral Pt cluster (1.8 nm) consisting of 201 Pt atoms and on Pt(111) extended surface.

Oxygen adsorption sites[a]	Average Pt coordination	Heat of O* adsorption, Q_O (kJ mol^{-1})	Intrinsic barrier for CO*-O* reactions, $(E_j)_{CO^*-O^*}$ (kJ mol^{-1})[c]	Effective barrier for CO*-O* reactions, $(E_i)_{CO^*-O^*,\,eff}$ (kJ mol^{-1})[d]
I	6.5	133	112	-72
II	7.3	114	88	-82
III	7.5	106	123	-69
IV	8.3	98	69	-92
V	9	96	82	-87
Pt(111) surface[b]	9	89	-	-

[a] Refer to Scheme 1 for the location of these sites. [b] Single crystal Pt(111) surface. [c] Calculated using Eq. 19. [d] Calculated using Eq. 20, averaging over all plausible reaction paths by considering the various types of Pt sites vicinal of the O* atom.

Table 4. Pt coordination numbers, heats of CH_3* and molecular CO* adsorption on a cubo-octahedral Pt cluster (1.8 nm) consisting of 201 Pt atoms and on the Pt(111) extended surface.

Pt sites[a]		Heat of CH_3* adsorption, Q_{CH3*} (kJ mol^{-1})	Heat of molecular CO* adsorption, Q_{CO} (kJ mol^{-1})
1	6	211	198
2	7	209	189
3	8	207	166
4	9	197	161
Pt(111) surface[b]		-	150

[a] Refer to Scheme 1 for the location of these sites. [b] Single crystal Pt(111) surface.

3.9. Supporting Information

3.9.1. Derivation of O*-to-* ratio in $^{13}CH_4$-^{12}CO-O_2 mixtures on bare Pt clusters. A pseudo steady-state assumption of O* species on the elementary steps in Scheme 2 gives the expression below that relates the turnover rates of O_2 (r_{O_2}) to the rates of CO oxidation (r_{CO}), CH_4 conversion to CO_2 and H_2O ($r_{CH_4,1}$), CH_4 conversion to CO and H_2 ($r_{CH_4,2}$), and sequential H_2 oxidation to H_2O (r_{H_2}):

$$2\,r_{O_2} = r_{CO} + 4r_{CH_4,1} + r_{CH_4,2} + r_{H_2} \quad (A.1)$$

We note that the maximum rate of sequential H_2 oxidation is obtained when the H_2 intermediates produced from CH_4 are completely consumed by reactions with O_2. This rate is equal to the rate of CH_4 conversion to CO and H_2:

$$\left(r_{H_2}\right)_{max} = 2\left(r_{CH_4,2}\right)_{max} \quad (A.2)$$

For CO oxidation rates much larger than those of CH_4

$$r_{CO} >> (4r_{CH_4,1} + r_{CH_4,2} + r_{H_2}) \quad (A.3)$$

Eq. (A.1) is simplified to

$$2\,r_{O_2} = r_{CO} \quad (A.4)$$

Eq. (A.4) is expressed in terms of O_2 and CO pressures and O* and * surface intermediates according to the elementary steps in Scheme 2:

$$2k_{O*}K_{O_2}(O_2)(*)^2 = k_{CO\,ads}(CO)(O*)(*) \quad (A.5)$$

We note that $k_{CO\,ads}$ (step 7, Scheme 2) instead of $k_{CO\,oxi}$ (Step 8, Scheme 2) appears in this equation because CO oxidation proceeds via molecular CO* adsorption on a * site vicinal of O*, the details of which are provided by DFT studies in Section 3.6. On bare Pt clusters, the concentration of * sites, (*), is approximately equal to the overall Pt sites, (L). This assumption, together with Eq. (A.5), leads to Eq. (A.6) and Eq. 11 in Section 3.3:

$$\left(\frac{(O*)}{(*)}\right)_{CO-CH_4-O_2} \approx \left(\frac{(O*)}{(L)}\right)_{CO-CH_4-O_2} \approx \frac{2k_{O*}K_{O_2}}{k_{CO\,ads}}\left(\frac{O_2}{CO}\right) \quad (A.6)$$

3.9.2. Derivation of O* selectivity in terms of elementary rate and equilibrium constants and gas phase pressures on bare Pt clusters. The O* selectivity (S_{O*}) is defined as the ratio of reactive collision probabilities of CO and CH_4 with O*, also the ratio of first-order rate constants for O_2 reaction with CH_4 ($k_{O_2-CH_4}$) and CO (k_{O_2-CO}). The O* selectivity is derived from substituting Eqs. 9 and 10 into Eq. 6:

$$S_{O*} = \frac{k_{O_2-CO}}{k_{O_2-CH_4}} = \frac{0.5r_{CO}}{(CO)}\frac{(CH_4)}{2r_{CH_4,1} + 0.5r_{CH_4,2} + 0.5r_{H_2}} \quad (A.7)$$

where r_{CO}, $r_{CH_4,1}$, $r_{CH_4,2}$, and r_{H_2} are the rates of CO oxidation, CH_4 conversion to CO_2 and H_2O, CH_4 conversion to CO and H_2, and sequential H_2 oxidation, respectively. All the H_2 produced from CH_4 were oxidized sequentially to H_2O, as such the rate of oxygen consumption in the H_2 oxidation is related to that of CH_4 conversion to CO and H_2 by the reaction stoichoimetry given in Eq. (A.2).

The rate of CO oxidation is:

$$r_{CO} = k_{CO\,ads}(CO)(O^*)(*) \quad \text{(A.8)}$$

For CH_4 oxidation proceeds via activation of the first C-H bond on *-* site-pairs (Step 4, Scheme 2) as the kinetically-relevant step, the rates of CH_4 conversion ($r_{CH_4,1}$ and $r_{CH_4,2}$) are:

$$r_{CH_4,1} = r_{CH_4,2} = k_{[*-*]}K_{CH_4}(CH_4)(*)(*) \quad \text{(A.9)}$$

Substituting Eqs. (A.2), (A.6), (A.8), and (A.9) into Eq. (A.7) gives the O* selectivity proportional to O_2/CO ratio:

$$S_{O^*} = \frac{k_{CO\ ads}}{7k_{[*-*]}K_{CH_4}}\left(\frac{[O^*]}{[L]}\right) = \frac{k_{O^*}K_{O_2}}{3.5k_{[*-*]}K_{CH_4}}\left(\frac{O_2}{CO}\right) \quad \text{(A.10)}$$

as shown in Eq. 12.

For CH_4 oxidation proceeds via kinetically-relevant C-H bond activation step on O*-* site-pairs (Step 5, Scheme 2), the rate is:

$$r_{CH_4,1} = r_{CH_4,2} = k_{[O^*-*]}K_{CH_4}(CH_4)(O^*)(*) \quad \text{(A.11)}$$

Substituting Eqs. (A.2), (A.8), and (A.11) into Eq. (A.7) leads to O* selectivity independent of O_2/CO ratio:

$$S_{O^*} = \frac{k_{CO\ ads}}{7k_{[O^*-*]}K_{CH_4}} \quad \text{(A.12)}$$

as shown in Eq. 13.

3.9.3. Derivation of ensemble-averaged first-order rate constants for CH_4 reactions in $^{13}CH_4$-^{12}CO-O_2 mixtures at low O* coverages. The CH_4 turnover rates on coordinatively unsaturated Pt atoms ($*_S$), $r_{CH_4,S}$, are given by Eq. 14:

$$r_{CH_4,S} = k_{CH^*}(CH_x{*_S})\frac{(O{*_W})}{L} \quad \text{(A. 13)}$$

where $O*_W$ refers to a chemisorbed oxygen atom binds on the high coordination Pt site ($*_W$) vicinal of $*_S$, CH_x*_S is a product of the initial C-H bond activation step on the $*_S$ site, and k_{CH^*} is the rate constant for the removal of CH_x*_S species from $*_S$ sites via reactions with vicinal reactive $O*_W$ intermediates (Step 14, elementary rate constant k_{CH^*}, Scheme 2). A pseudo steady-state approximation of the CH_x*_S intermediates is used to equate the rates of CH_x*_S formation from CH_4 to those of CH_x*_S removal by reaction with vicinal O* to solve for the (CH_x*_S) in terms of ($*_S$), ($*_W$), and ($O*_W$):

$$(CH_x{*_S}) = \frac{k_{[*-*],S}(CH_4)}{k_{CH^*}}\frac{(*_W)(*_S)}{(O{*_W})} \quad \text{(A. 14)}$$

Substituting Eq. (A.14) into Eq. (A.13) and assuming that the fraction of $*_W$ on the surface is near unity gives

$$r_{CH_4,S} = k_{CH^*}(CH_x{*_S})\frac{(O{*_W})}{L} = k_{[*-*]S}(CH_4)\frac{(*_W)(*_S)}{L} \quad \text{(A.15)}$$

$$r_{CH_4,S} = \frac{k_{[*-*]S}(CH_4)}{\left(1+\frac{2k_{O^*}K_{O_2}}{k_{COads}}\left(\frac{O_2}{CO}\right)+\frac{k_{[*-*]S}(CH_4)}{k_{CH^*}}\frac{k_{COads}}{2k_{O^*}K_{O_2}}\left(\frac{CO}{O_2}\right)\right)} \qquad (A.16)$$

$$\downarrow \quad \downarrow \qquad\qquad \downarrow$$

$$*_S \qquad O*_S \qquad\qquad CH_x*_S$$

When the fractional coverages of $O*_S$ are smaller than $*_S$ and CH_x*_S, Eq. (A.16) is simplified to Eq. (A.17), as also shown in Eq. 15.

$$k_{CH_4,S} = \frac{r_{CH_4,S}}{(CH_4)} = \frac{k_{[*-*],S}}{\left(1+\frac{k_{[*-*],S}(CH_4)}{k_{CH^*}}\frac{k_{COads}}{2K_{O_2}k_{O^*}}\left(\frac{CO}{O_2}\right)\right)} \qquad (A.17)$$

Table A.1 summarizes the estimated values for the kinetic parameters in Eq. 16, derived from a regression analysis of the rate data in Figure 4.

Table A.1. Kinetic parameters for $^{13}CH_4$ reactions in $^{13}CH_4$-^{12}CO-O_2 mixtures on 0.2 % wt. Pt/Al_2O_3 (1.8 nm mean cluster diameter), derived from regression of the rate data in Figure 4 with Eq. 16.

Kinetic parameter	Estimated value
$\Gamma k_{[*-*],W}$	0.402 kPa^{-1} s^{-1}
$(1-\Gamma)k_{[*-*]S}$	2.26 kPa^{-1} s^{-1}
$\frac{k_{[*-*]S}}{k_{CH^*}}\frac{k_{COads}}{2K_{O_2}k_{O^*}}$	0.2085

3.9.4. Geometries of reactant, transition state, and product for initial C-H bond activation in CH_4 on *-* and *-O* site-pairs on Pt_{201} clusters. Figure A.1 shows the calculated structures of reactant, transition, and product state for initial C-H bond activation of CH_4 on a *-* site-pair (Step 4, Scheme 2), which is formed over two Pt sites of type 4 (Scheme 1b, atop Pt atom and a Pt-Pt bridge) located on the (111) facet of the Pt_{201} cluster. The bond distances for these structures are given in Table A.2.

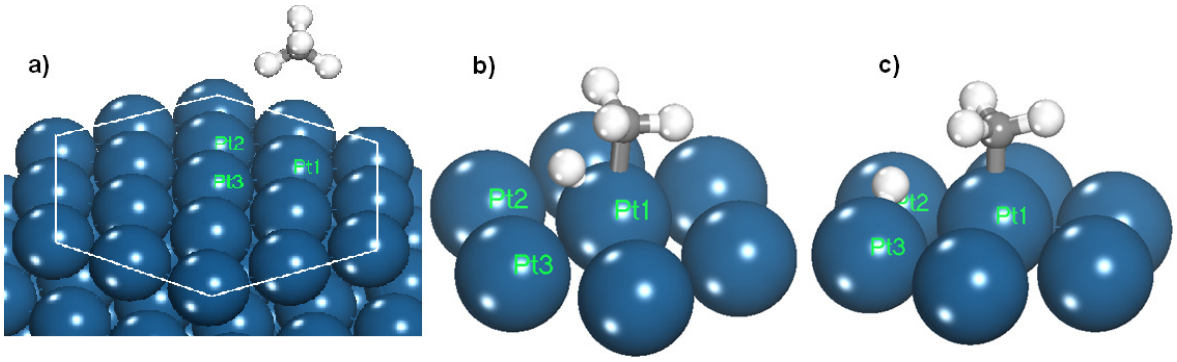

Figure A.1a, A.1b, and A.1c. DFT-calculated reactant (a), transition (b), and product (c) state structures for the activation of the first C-H bond in CH_4 over *-* site-pairs (Step 4, Scheme 2) (three Pt atoms, all are type 4, in Scheme 1b) on Pt_{201} cluster.

Table A.2. Bond lengths of the reactant, transition state, and product structures for the activation of the first C-H bond in CH_4 on *-* site-pairs (Step 4, Scheme 2). Geometries for these structures and the Pt atoms involved (Pt_{1-3}) are labeled in Figure A.1a-A.1c.

	Reactant (nm)	Transition State (nm)	Product (nm)
Pt_1-C	0.447	0.222	0.207
Pt_1-H	0.394	0.162	0.234
C-H	0.109	0.152	0.264
Pt_2-H	0.431	0.245	0.174
Pt_3-H	0.428	0.261	0.178

Figure A.2 shows the calculated structures of reactant, transition, and product state for the initial C-H bond activation of CH_4 on various *-O* site-pairs (Step 5, Scheme 2), which are formed from a Pt and an O* atom on the (111) facet of the Pt_{201} cluster (Scheme 1). The site-pairs presented here consist of Pt and O* located at sites 4 and V, 2 and V, and 1 and IV (see Scheme 1 for the location of Pt and O*), respectively. The bond distances for these structures are given in Table A.3.

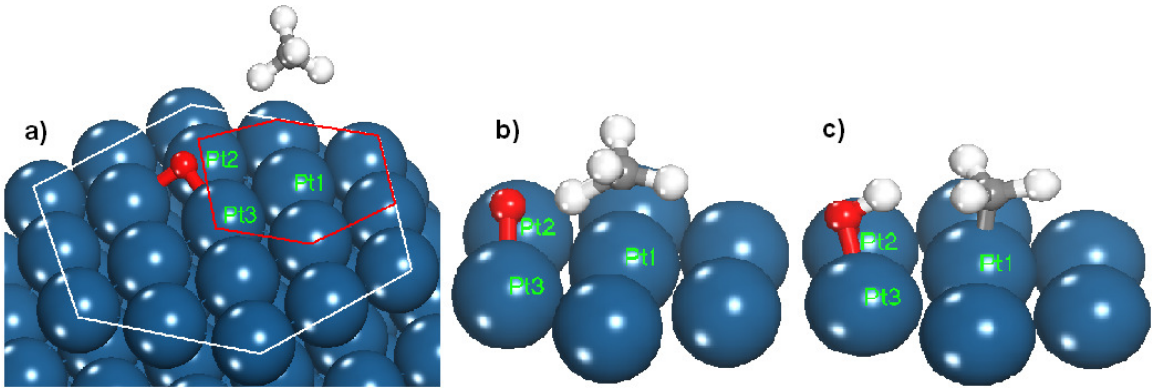

Figure A.2a, A.2b, and A.2c. DFT-calculated reactant (a), transition (b), and product (c) state geometries for the activation of the first C-H bond in CH_4 over a *-O* site-pair (Step 5, Scheme 2), which is formed from a Pt site of type 4 and an O* atom of type V (as illustrated in Scheme 1b) on the (111) facets of Pt_{201} cluster.

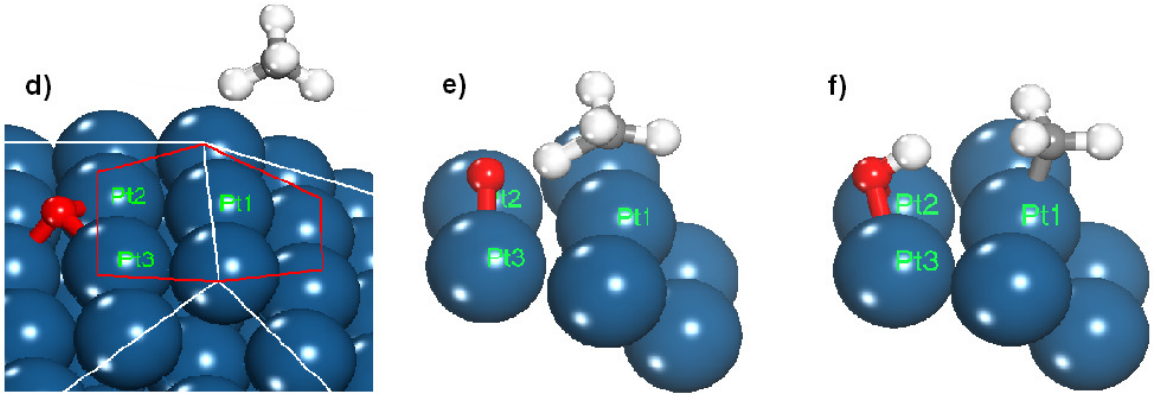

Figure A.2d, A.2e, and A.2f. DFT-calculated reactant (d), transition (e), and product (f) state geometries for the activation of the first C-H bond in CH_4 over a *-O* site-pair (Step 5, Scheme 2), which is formed from a Pt site of type 2 and O* atom of type V (as illustrated in Scheme 1b) on the edge of (111) facets of Pt_{201} cluster.

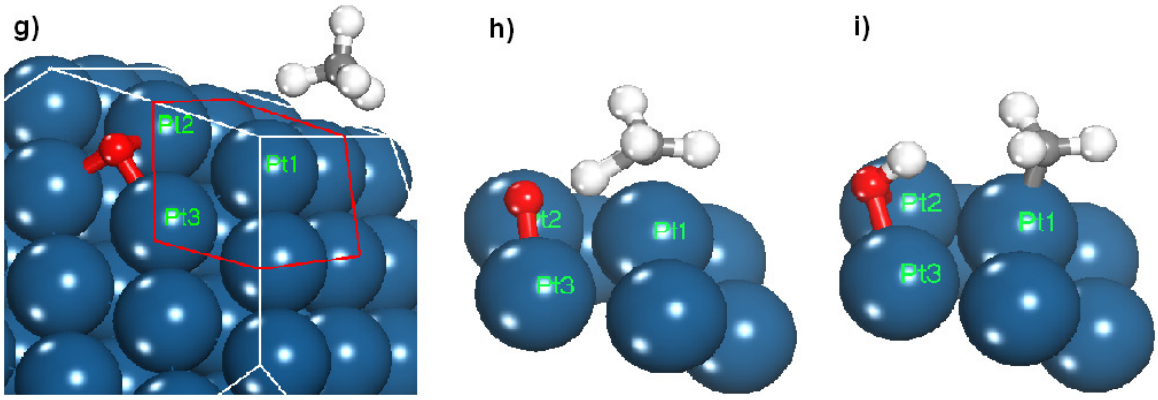

Figure A.2g, A.2h, and A.2i. DFT-calculated reactant (g), transition (h), and product (i) state structures for the activation of the first C-H bond in CH_4 over a *-O* site-pair (Step 5, Scheme 2), which is formed over Pt site of type 1 and O* atom of type IV (as illustrated in Scheme 1b) on the corner of (111) facets of Pt_{201} cluster.

Table A.3. Bond lengths of reactant, transition state, and product structures for the activation of the first C-H bond in CH_4 over *-O* site-pairs (Step 5, Scheme 2) that are shown in Figure A.2a-A.2i. Geometries of the structures are given and the Pt atoms involved (Pt_{1-3}) are labeled in Figure A.2.

CH_4 on *-O* site-pairs	*-O* (4-V)			*-O* (2-V)			*-O* (1-IV)		
Bond Distances (nm)	Reactant	TS	Product	Reactant	TS	Product	Reactant	TS	Product
Pt_1-C	0.449	0.230	0.207	0.418	0.227	0.207	0.376	0.227	0.206
Pt_1-H	0.397	0.200	0.285	0.341	0.204	0.279	0.314	0.202	0.287
C-H	0.109	0.130	0.225	0.110	0.133	0.276	0.110	0.134	0.275
O-H	0.350	0.146	0.098	0.514	0.140	0.098	0.453	0.139	0.098
Pt_2-O	0.203	0.204	0.216	0.203	0.203	0.217	0.212	0.205	0.220
Pt_3-O	0.205	0.205	0.217	0.203	0.203	0.215	0.204	0.206	0.218
Pt_2-H	0.424	0.261	0.261	0.500	0.268	0.259	0.467	0.266	0.266
Pt_3-H	0.426	0.261	0.261	0.510	0.268	0.258	0.459	0.271	0.262

3.9.5. Examples of O*-CO* reaction paths for CO oxidation reactions between an O* atom and CO* chemisorbed at the vicinal Pt sites on a (111) facet of the Pt_{201} cluster. Chemisorbed oxygen adatoms on three-fold fcc sites (IV and V in Fig. A.3) can react with CO* molecules chemisorbed atop at the vicinal Pt sites. An O* atom chemisorbed at site V can react with CO* at sites 3a, 3c, and 2b while an O* at site IV can react with CO* at sites 1a, 1b, and 3b.

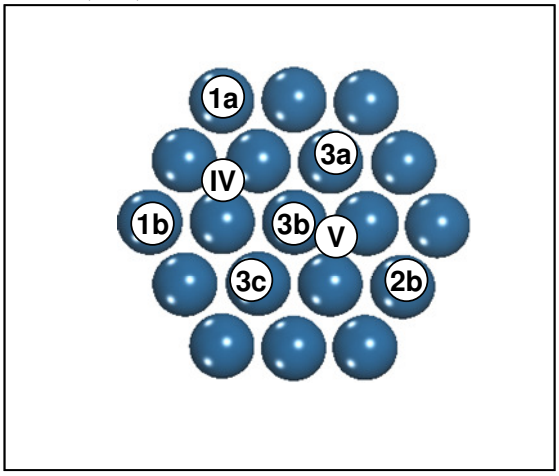

Figure A.3. Plausible O*-CO* reaction paths for reactions between chemisorbed O* at site IV or site V on a (111) surface of a cubo-octahedral Pt_{201} cluster (1.8 nm average diameter). The O* at site IV can react with CO* at sites 1a, 1b, and 3b whereas the O* at site V can react with CO* at sites 3a, 3c, and 2b.

3.9.6. Geometries of reactant, transition state, and product for CO* and O* recombination reactions on Pt_{201} clusters (Step 8, Scheme 2). Figure A.4 shows the calculated structures of reactant, transition, and product state of CO* and O* reactions, where CO* chemisorbs atop of a Pt atom reacts with a vicinal O* atom on the (111) facet of Pt_{201} cluster. The location of CO* and O* are sites 4 and V, 4 and IV, and 4 and II (see

Scheme 1 for the location of Pt and O*), respectively. The bond distances for these structures are given in Table A.4.

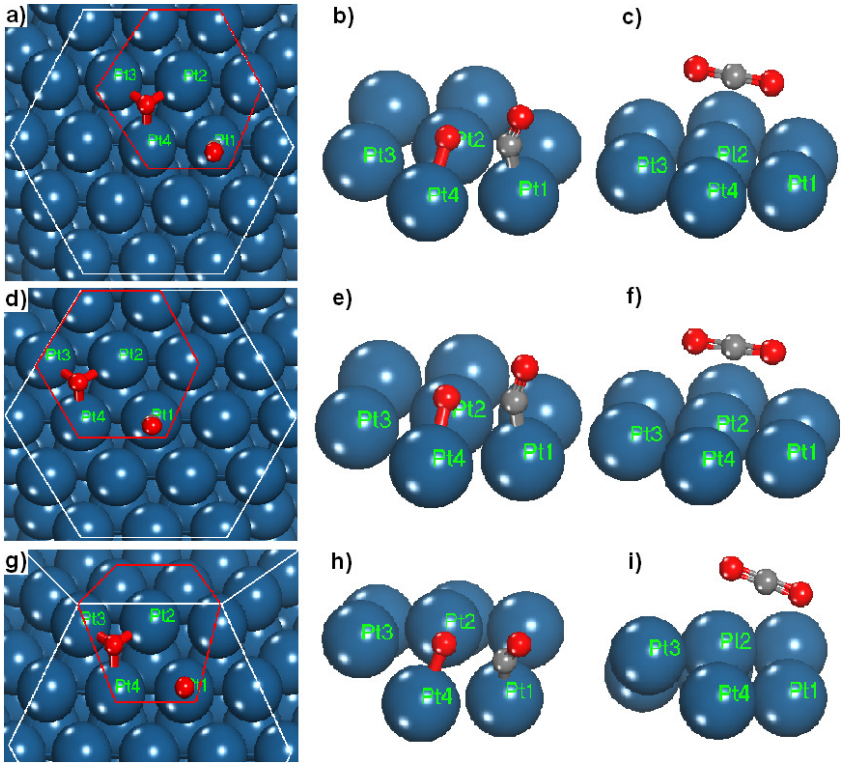

Figure A.4a-A.4i. Geometries of reactant (a, d, g), transition state (b, e, h), and product (c, f, i) for CO oxidation reactions where the CO* and O* atoms are located at sites 4 and V, 4 and IV, and 4 and II (refer to Scheme 1 for site identities) for the structures in a-c, d-f, and g-i, respectively, on the (111) facet of the Pt_{201} cluster.

Table A.4. Bond lengths of reactant, transition state, and product structures for the CO oxidation reactions (Step 8, Scheme 2) shown in Figure A.4. Geometries for the structures are given and the Pt atoms involved (Pt_{1-3}) are labeled in Figure A.4.

CO* on (*-O*)	*-O* (sites 4-V)			*-O* (sites 4-IV)			*-O* (sites 4-II)		
Bond distances (nm)	Reactant	TS	Product	Reactant	TS	Product	Reactant	TS	Product
Pt_1-C	0.185	0.192	0.395	0.185	0.192	0.391	0.185	0.192	0.398
Pt_2-C	0.348	0.307	0.360	0.349	0.302	0.361	0.354	0.309	0.498
Pt_4-C	0.348	0.307	0.373	0.354	0.306	0.379	0.345	0.303	0.513
C-O	0.116	0.117	0.117	0.116	0.116	0.117	0.116	0.117	0.117
Pt_2-O	0.204	0.206	0.370	0.204	0.206	0.363	0.208	0.208	0.447
Pt_3-O	0.202	0.307	0.386	0.212	0.296	0.389	0.208	0.289	0.576
Pt_4-O	0.206	0.207	0.387	0.205	0.206	0.385	0.208	0.207	0.470
O-C	0.347	0.194	0.117	0.351	0.201	0.117	0.341	0.197	0.117

Figure A.5 shows the calculated geometries of reactant, transition, and product states of CO* and O* reactions where CO* chemisorbs atop on a Pt atom and then reacts with a vicinal O* atom on the (100) facet of the Pt_{201} cluster. The CO* and O* are located at sites 1 and I and sites 2 and III (see Scheme 1 for the location of Pt and O*), respectively. The bond distances for these structures are given in Table A.5.

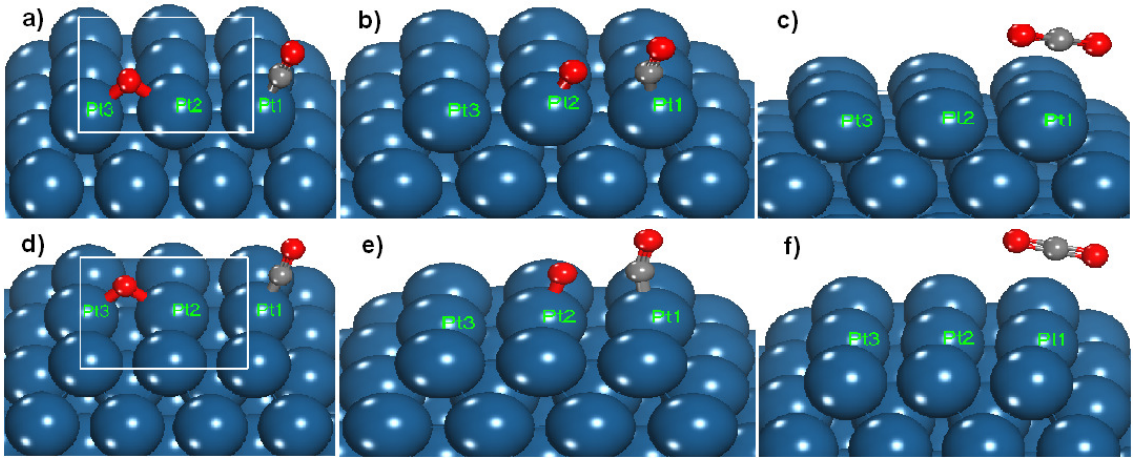

Figure A.5a-A.5f. Geometries of reactant (a, d), transition state (b, e), and product (c, f) for CO oxidation reactions, where the CO* and O* chemisorb on sites 1 and I and sites 2 and III, respectively (refer to Scheme 1 for the location of CO* and O*), for the structures of a-c and d-f, respectively, on the (100) facets of Pt_{201} clusters.

Table A.5. Bond lengths of reactant, transition state, and product structures for the CO oxidation reactions shown in Figure A.5. Geometries for the structures are given and the Pt atoms involved (Pt_{1-3}) are labeled in Figure A.5.

CO* on (*-O*)	*-O* (sites 1-I)			*-O* (sites 2-III)		
Bond distances (nm)	Reactant	TS	Product	Reactant	TS	Product
Pt_1-C	0.186	0.192	0.352	0.186	0.191	0.353
Pt_2-C	0.381	0.324	0.459	0.394	0.327	0.478
C-O	0.116	0.117	0.118	0.116	0.117	0.117
Pt_2-O	0.196	0.186	0.437	0.197	0.187	0.429
Pt_3-O	0.195	0.396	0.620	0.196	0.388	0.621
O-C	0.495	0.204	0.117	0.510	0.210	0.117

3.9.7. Transition state geometries for CO(g) adsorption on sites vicinal of an O* atom on Pt_{201} clusters (reverse of Step 7, Scheme 2). Figure A.6 shows the calculated transition state structures for CO(g) adsorption at Pt sites vicinal to O* atoms on the surface of a Pt_{201} cluster.

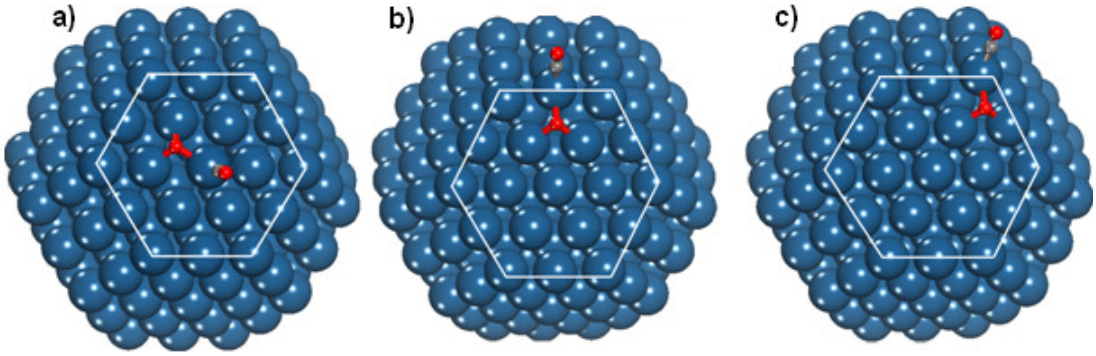

Figure A.6a-A.6c. Transition state geometries for CO(g) adsorption vicinal of O*. The CO adsorbed on a Pt site of type 4 (a), 2 (b), or 1 (c), which will react with a vicinal O* atom located at site of type V (a), IV (b), or II (c), respectively, on the surface of a Pt_{201} cluster.

3.9.8. Estimation of the maximum CO yields from CH_4-O_2 mixtures on bare Pt clusters. Mole balances of CH_4 and CO in a plug-flow reactor, assuming that all CH_4 convert to CO and H_2 and all the H_2 undergo sequential oxidation to H_2O:

$$\frac{d(F_{CH_4})}{dW} = r_{CH_4,2} = -k_{[*-*]}K_{CH_4}\frac{F_{CH_4}}{F_T}P_T \tag{A.18}$$

$$\frac{d(F_{CO})}{dW} = r_{CO} - r_{CH_4,2} = -k_{CO\,ads}\frac{F_{CO}}{F_T}P_T + k_{[*-*]}K_{CH_4}\frac{F_{CH_4}}{F_T}P_T \tag{A.19}$$

$$\begin{aligned}\frac{d(F_{O_2})}{dW} &= r_{O_2} = 0.5r_{CO} + 0.5r_{CH_4,2} + 0.5r_{H_2} \\ \frac{d(F_{O_2})}{dW} &= -0.5k_{CO\,ads}\frac{F_{CO}}{F_T}P_T - 1.5k_{[*-*]}K_{CH_4}\frac{F_{CH_4}}{F_T}P_T\end{aligned} \tag{A.20}$$

W is the number of exposed Pt surface atoms; F_{CH_4}, F_{CO}, and F_{O_2} are the molar flow rates of CH_4, CO, and O_2 and F_T is the total flow rate, respectively. The rate and equilibrium constants are defined in Scheme 2. The overall CH_4 and CO conversion rates on Pt clusters uncovered of O* atoms are limited by the O_2 dissociation step and therefore proportional to O_2 pressure:

$$r_{O_2} = k_{O*}K_{O_2}(O_2) = 0.5r_{CO} + 0.5r_{CH_4,2} + 0.5r_{H_2} \tag{A.21}$$

Differential equations (Eqs. A.18-20) together with the algebraic equation Eq. (A.21) are used to model the reactor using the following parameters of $K_{O_2}k_{O*}$ [22] as a function of the k_{CO}/k_{CH4} ratio (also related to O* selectivity via the reaction stoichoimetry):

$$k_{O*}K_{O_2} = 5600\,kPa^{-1}s^{-1} \tag{A.22}$$

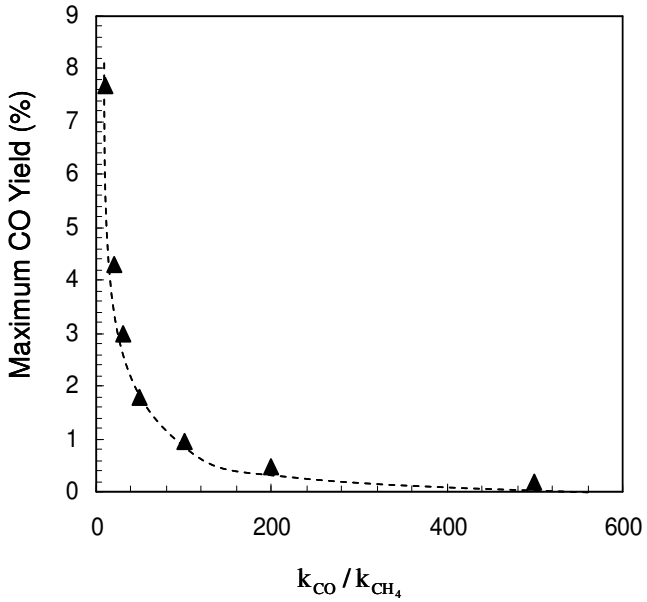

Figure A.7. Maximum CO yields as a function of the rate constant ratio for CO to CH_4 oxidation in CH_4-O_2 reactions, calculated from a model of variable flow isothermal-isobaric plug flow reactor.

Chapter 4:
Elementary Steps, the Role of Chemisorbed Oxygen, and the Effects of Cluster Size in Catalytic CH_4-O_2 Reactions on Palladium

Abstract

Kinetic and isotopic data and effects of cluster size are used to probe elementary steps and their kinetic relevance in CH_4-O_2 reactions on Pd clusters that retain a metallic bulk during catalysis. CO_2 and H_2O were the only products formed, except when O_2 was nearly depleted and trace CO amounts formed. $^{13}CH_4$-^{12}CO-O_2 reactions showed CO reacts with chemisorbed oxygen (O*) much faster than CH_4 with reactive collision probability ratios for CO and CH_4 proportional to O_2/CO ratios via a constant exceeding 500; thus, even if CO desorbed before forming CO_2, it would oxidize via reactions with O* at any reactor residence time required for detectable CH_4 conversion, making direct partial oxidation impractical as a molecular route to H_2-CO mixtures on Pd. CH_4–O_2 turnover rates and effective first-order rate constants initially decreased and then reached constant values as O_2 pressure and O* coverage increased, as a result of a transition in the surface species involved in kinetically-relevant C-H bond activation steps from O*-* to O*-O* site pairs (*, vacancy site). On O*-O* site pairs, C-H bonds are cleaved via H-abstraction mediated by O*, with radical-like CH_3 fragments at transition states weakly stabilized by the vicinal O*. These reactions show large activation barriers (158 kJ mol^{-1}) but involve high entropy transition states that lead to larger pre-exponential factors (1.48×10^9 kPa^{-1} s^{-1}) than for tighter transition states involved in C-H bond activation by *-* site pairs for CH_4 reactions with H_2O or CO_2 (barriers: 82.5 kJ mol^{-1} and pre-exponential factors: 3.5×10^5 kPa^{-1} s^{-1}). CH_3 fragments are effectively stabilized by interactions with vacancy sites on O*-* site pairs, which lead to higher turnover rates as vacancies become available with decreasing O_2 pressure. CH_4-O_2 turnover rates and C-H bond activation rate constants on O*-O* site pairs decreased with decreasing Pd cluster size, because coordinatively unsaturated exposed atoms on small clusters bind O* more strongly and decrease its reactivity for H-abstraction. The stronger O* binding on small Pd clusters also causes the kinetic involvement of O*-* sites to become evident at lower O_2 pressures than on larger clusters. These effects of metal-oxygen bond strength on O* reactivity also lead to the smaller turnover rates observed on Pd clusters compared with Pt clusters of similar size. These effects of cluster size and metal identity and their O* binding energy are the root cause for reactivity differences and appear to be general for reactions involving vacancies in kinetically-relevant steps, as is the case for CH_4, C_2H_6, NO, and CH_3OCH_3 oxidation on O*-covered surfaces and for hydrogenation of organosulfur compounds on surfaces nearly saturated with chemisorbed sulfur.

4.1. Introduction

Small Pd clusters dispersed on high surface area substrates are useful as CH_4 combustion catalysts in power generation and exhaust gas treatment.[1,2,3,4] Similar catalysts also promote CH_4-O_2 reactions at substoichoimetric ratios ($O_2/CH_4 < 2$) to form CO and H_2 via mildly exothermic routes. The latter reactions produce synthesis gas or H_2 via less endothermic routes than CH_4-H_2O/CO_2 reforming (ΔH^o_{298}=206 kJ mol^{-1} (H_2O),

247 kJ mol^{-1} (CO_2))[5,6] and lessen heat transfer requirements and catalyst deactivation. Autothermal reformers use O_2 in flame combustion of CH_4 in CH_4-H_2O-O_2 mixtures at the reactor inlet to provide the heat required for subsequent reforming reactions.[7] These autothermal routes lead to sharp temperature profiles along the catalyst bed, which would be absent if direct catalytic partial oxidation occurred at the molecular scale or within thermal conduction distances in monoliths or packed bed reactors.

The reactions that form CO_2-H_2O[8,9,10] and CO-H_2[6,11,12,13] from CH_4-O_2 reactants on Pd have been previously examined, but the required active sites, the detailed sequence of the elementary steps and their kinetic relevance, and even whether H_2 and CO can form directly as primary products remain issues of active debate and considerable controversy. These issues reflect, at least in part, the presence of ubiquitous temperature and concentration gradients within catalyst pellets and beds as a result of the fast nature of these reactions, the typical high conversions that prevail, and the highly exothermic nature of combustion reactions (ΔH^{o}_{298}=-802 kJ mol^{-1}). The chemical transformations between Pd and PdO bulk chemical states also complicate the mechanistic interpretation of concentration and temperature effects on rate data in terms of elementary steps and their kinetic relevance. These metal-oxide transformations occur in response to changes in oxygen chemical potential and temperature[14,15,16] as O_2 is depleted along the reactor or within porous catalyst pellets. These changes in chemical state can occur concurrently with structural transformations that alter the shape of such clusters and the intimacy of their contact with supports, which alter, in turn, the coverage and reactivity of chemisorbed oxygen atoms, as shown when Pd foils interconvert between metal and oxide states.[17]

Here, we provide evidence for the chemical origins of the rate and selectivity observed in CH_4-O_2 reactions on Pd clusters by measuring the rate of chemical events in the absence of transport corruptions in a range of oxygen chemical potentials that maintains the bulk of Pd clusters (4.5-22.3 nm) in their metallic state. Our recent studies in CH_4–O_2 on Pt[18,19] and CH_4-H_2O/CO_2[20,21,22,23,24,25,26] reactions on several metals (Rh,[20] Pt,[21] Ir,[23,24] Ni,[25] Ru,[22] and Pd[26]) have probed the elementary steps and site requirements for these reactions. CH_4-H_2O/CO_2 turnover rates on Pd clusters are limited by C-H bond activation steps on *-* site-pairs,[26] as also found on other metals,[20,21,22,23,25] but rate constants are significantly larger than on other metal and cause C-H bond dissociation to become reversible. Fast C-H bond activation on Pd also leads to kinetically-detectable coverages by C* and H* intermediates, which inhibit reforming reactions.[26] In CH_4–O_2 mixtures, O*-* and O*-O* site pairs on Pt cluster surfaces activate C-H bonds with different activation enthalpies and entropies, kinetic dependencies, and effects of cluster size effects than the *-* site pairs that activate CH_4 in reactions with H_2O/CO_2.[18] These concepts are extended here to Pd clusters, for which elementary steps and their kinetic relevance for CH_4-O_2 reactions and the selectivity of chemisorbed oxygen in reactions with CH_4 and CO remain uncertain.

We address the catalytic consequences of using O_2 as the oxidant and the role of chemisorbed oxygen (O*) in CH_4–O_2 reactions on Pd clusters that retain their metallic bulk by measuring reaction rates and selectivities under conditions of strict kinetic control without transport artifacts. The chemical equilibrium between O* species and O_2(g) was confirmed by $^{16}O_2$-$^{18}O_2$ isotopic exchange rates. In a parallel study, we address the behavior of CH_4-O_2 reactions on PdO clusters[27] and the dynamics of Pd-PdO phase

transitions.[28] Kinetic and isotopic studies are used to determine the role of O* in the kinetically-relevant elementary steps for CH_4-O_2 reactions and to establish that CO does not form at detectable levels during these reactions on Pd clusters. $^{13}CH_4$-CO-O_2 reactions showed that even if CO* desorbed unreacted, it would react with O* at any residence time required for detectable CH_4 conversion, indicating that direct partial oxidation is not feasible on Pd clusters and that CO (and H_2) form exclusively via sequential reforming reactions. The proposed sequence of elementary steps is consistent with rate data and kinetic isotope effects and with steps that mediate CH_4-H_2O/CO_2 reactions on Group VIII metals[20,21,22,23,25] and CH_4-O_2 reactions on Pt.[18,19] Kinetically-relevant C-H bond activation steps occur on O*-O* site pairs at O* saturated surfaces and on O*-* site pairs as O* coverages decrease below saturation. Rate constants for C-H bond activation increased with increasing Pd cluster size, as a result of a concomitant decrease in O* binding energy. These kinetically-relevant steps and active site structures were similar to those proposed for Pt; the rate constants were, however, smaller on Pd than Pt, because O* binding is stronger on Pd than Pt clusters of similar size.

4.2. Experimental Methods

4.2.1. Synthesis of dispersed Pd clusters on high surface area oxide supports. γ–Al_2O_3 (Sasol North America Inc., Lot#C1643, 193 $m^2\ g^{-1}$, 0.57 cc g^{-1} pore volume) and SiO_2 (Davison Chemical, Grade 923, CAS no. 112926-00-8, 280 $m^2\ g^{-1}$) supports were treated in flowing dry air (Praxair, zero grade, 0.083 K s^{-1}, 60 $cm^3\ g^{-1}$) at 923 K-1073 K for 5 h before impregnation with aqueous $Pd(NO_3)_2$ solutions (Aldrich, 99.999 % purity, 10 % wt. $Pd(NO_3)_2$ in 10 % wt. HNO_3) to obtain samples containing 0.2 % wt. Pd. Impregnated samples were treated in stagnant ambient air at 383 K for 8 h and then in flowing dry air (Praxair, zero grade, 60 $cm^3\ g^{-1}$) by heating to 623 K at 0.033 K s^{-1} (3 h hold) and then to 923 K-1073 K at 0.083 K s^{-1} (5 h hold) and cooling to ambient temperature. A Portion of the catalysts was then treated in flowing H_2-Ar mixture (10 % H_2/Ar, 0.083 K s^{-1}, 60 $cm^3\ g^{-1}$, Praxair certified standard) at a temperature between 923 K and 1023 K for 3 h, cooled to 673 K, and then treated in He (Praxair UHP grade, 60 $cm^3\ g^{-1}$) at 673 K before cooling to ambient temperature. O_2/He mixtures (0.5 % O_2/He, Praxair certified standard, 60 $cm^3\ g^{-1}$) were introduced to the samples at ambient temperature for at least 2 h before exposure to ambient air. The fraction of exposed Pd atoms was determined by volumetric O_2 chemisorption experiments carried out on a Quantachrome Autosorb-1 unit at 313 K. The number of exposed Pd atoms was determined from extrapolation of O_2 adsorption isotherm to zero pressure with the assumptions that the atomic ratio of oxygen-to-exposed Pd equals one and Pd clusters are in hemispherical shapes with a metal density of bulk Pd (12.0 g cm^{-3}).[29]

4.2.2. Measurements of CH_4-O_2 turnover rates and O_2 selectivities. Steady-state CH_4 conversion turnover rates were measured at 873 K-973 K in a tubular flow reactor (quartz; 8.1 mm inner diameter) with plug flow hydrodynamics. Catalysts were diluted with inert SiO_2 (Davison Chemical, Chromatographic Silica Media, CAS no. 112926-00-8, 280 $m^2\ g^{-1}$) at a diluent-to-catalyst mass ratio of 50-200, pelletized, and sieved to retain 106-250 m aggregates. These particles were then mixed with quartz (Fluka, acid purified, product number 84880, 106-250 m diameters) at a diluent-to-Pd/Al_2O_3 catalyst mass ratio in the range of 150-450.

Catalyst samples were heated to reaction temperatures in a flowing H_2-He mixture (5 kPa H_2 in He, Praxair, UHP grade, 0.083 K s^{-1}, 1.67 cm^3 s^{-1}) and then treated in He (Praxair UHP grade, 1.67 cm^3 s^{-1}) for ~0.2 h. Reactant mixtures consisted of 25 % CH_4/He (Matheson, Certified Plus Grade), 1 % CO/He (Praxair, Certified Standard), O_2 (Praxair, UHP) or 5 % O_2/He (Praxair, Certified Standard), and He (Praxair, UHP grade) were metered using electronic mass flow controllers (Porter 201). H_2O (doubly-distilled and deionized) or D_2O (Aldrich, 99.9 % D) were introduced using a syringe (Hamilton, #1005, 5000 L) at a rate controlled by a syringe pump (Cole Parmer, Model 60061) into a heated line (423 K) swept by gaseous reactants. Reactant and product concentrations were measured using gas chromatograph (Agilent 3000A Micro GC) equipped with modules that contain Poraplot Q or Mol Sieve 5A columns and thermal conductivity detectors. The reactor was operated in a differential mode, where CH_4 conversions were maintained below 4 % and for kinetic measurements in Section 3.5, below 0.5 %. CH_4 turnover rates were determined from effluent CO and CO_2 concentrations and O_2 chemisorption uptakes, the latter of which provide the total number of exposed Pd atoms available for chemical turnovers.

Reactions of $^{16}O_2$-$^{18}O_2$, CH_4-$^{16}O_2$-$^{18}O_2$, $^{13}CH_4$-^{12}CO-O_2, CD_4-O_2, $^{13}CH_4$-$^{12}CO_2$-O_2, CD_4-H_2O-O_2, and CH_4-D_2O-O_2 mixtures were carried out in the reactor described above by incorporating isotopic compounds (2 % $^{18}O_2$/He (Icon, 98 % ^{18}O), $^{13}CH_4$ (Isotec, 99 % ^{13}C), or CD_4 (Isotec, 99 % D)) into the feed mixtures. The isotopic composition of each chemical species in inlet and outlet streams was measured by mass spectrometry (Agilent 6890 and 5973 N). $CaSO_4$ (Drierite®) was used to remove water isotopologues before analysis.

4.3. Results and Discussion

4.3.1. Effects of intrapellet and bed dilution on CH_4 conversion turnover rates. Reactions of CH_4 with O_2 on supported Pd clusters form CO_2 and H_2O almost exclusively at all conditions leading to detectable outlet O_2 concentrations (Section 3.2). Sequential reactions of CH_4 with CO_2 and H_2O combustion products form CO (and H_2) after O_2 depletion. Prevalent exothermic combustion reactions cause severe temperature and concentration gradients within individual catalyst pellets and across the reactor bed in the absence of extensive dilution at the bed and pellet scales, which allows rates to be measured under conditions of strict kinetic control.[30,31] Measured CH_4 combustion turnover rates (Table 1, per exposed Pd atom; 973 K) on 0.2 % wt. Pd/Al_2O_3 (21.3 nm mean Pd cluster diameter) were identical within the experimental errors for intrapellet and bed diluent-to-catalyst mass ratios above 50 (SiO_2:catalyst) and 150 (quartz:catalyst), respectively. These data confirm that these dilution levels make local temperatures and concentrations at the catalyst sites identical to those in the extrapellet fluid phase; therefore, rates reported herein reflect the intrinsic chemical reaction rates devoid of transport artifacts. In the next sections, we examine the dependence of reactive CH_4 collision probabilities on O_2 pressures and the relative rates of CO and CH_4 reactions with chemisorbed O* intermediates.

4.3.2. Oxygen selectivity in reactions with CO and CH_4 on Pd clusters. CH_4 conversion turnover rates and CO selectivities were measured on Pd/Al_2O_3 (0.2 % wt., 21.3 nm mean cluster diameter) at 873 and 973 K during initial contact with CH_4-O_2

reactants (at times of 0-7.2 ks) (Figure 1). Reactive CH_4 collision probabilities (also denoted as first-order rate constants $\{ r_{CH_4}(CH_4)^{-1} \}$) depend on O_2 pressures (Figures 1a and 1c); these trends are interpreted mechanistically in Sections 3.4 and 3.5. The effects of O_2 pressure on rate constants and their temporal evolution are similar on Pd clusters of different size (4.5-22.3 nm), in spite of the much larger rate constants measured on the larger clusters (to be discussed in Section 3.7). CO selectivities, reported as $CO/(CO+CO_2)$ ratios in products, reached values as high as 0.9 after O_2 was depleted, but trace CO levels (< 60 Pa CO) were detected only for outlet O_2 pressures below 0.01 kPa at 873 K (< 22 Pa CO for < 0.04 kPa O_2 at 973 K) (Figures 1b and 1d).

The maximum CO (or H_2) yields attainable from CH_4–O_2 mixture (defined as the ratio of CO outlet to CH_4 inlet molar concentrations and expressed in percentage, $\%Y_{CO}$) are determined by the reactivities of CO and CH_4 with O_2-derived chemisorbed species. The relative reactivities are given, in turn, by the ratio of reactive collision probabilities of CO and CH_4, which is defined here as the O* selectivity:

$$O^* \text{selectivity} = \frac{r_{CO}(CO)^{-1}}{r_{CH_4}(CH_4)^{-1}} \quad (1)$$

This value reflects the relative reactivity of O* atoms with CO(g), if formed via CO* desorption before subsequent oxidation, to form CO_2 during the timescale of a CH_4 turnover.

O* selectivities were measured using $^{13}CH_4$-^{12}CO-O_2 reactants on 0.2 % wt. Pd/Al_2O_3 (21.3 nm mean Pd cluster diameter) at conditions that led to complete O_2 conversion (Figure 2; 973 K, 4.85 kPa $^{13}CH_4$, 0.81 kPa ^{12}CO, 0.081-0.36 kPa O_2). O* selectivities were much larger than unity and increased with increasing inlet O_2/CO ratios, indicating that ^{12}CO scavenges O* much more effectively than CH_4. The increase in O* selectivities with O_2/CO ratios reflects a preference for ^{12}CO over $^{13}CH_4$ oxidation in regions near the reactor inlet, where O_2 pressures are higher, and indicates that detectable CO concentrations are unlikely to be observed when O_2 is present at any point along a reactor. After O_2 depletion, $^{13}CH_4$ reacts with residual $^{12}CO_2$ (and with H_2O formed in CH_4-O_2 reactions) to form isotopically mixed CO molecules via reforming routes involving C-H bond activation on exposed Pd site pairs (step 2.1, Scheme 1). These reactive collision probabilities of CH_4 (with O*) also include contributions from $^{13}CH_4$ reactions with O* species derived from $^{12}CO_2$ formed via ^{12}CO oxidation. Even with these additional contributions, $^{13}CH_4$ reactive collision probabilities (0.9-1.3 mol O_2 (g-atom $Pd_{surface}$-kPa-s)$^{-1}$) were much smaller than for ^{12}CO (32-1650 mol O_2 (g-atom $Pd_{surface}$-kPa-s)$^{-1}$) at all O_2/CO ratios (0.064-2.6; Figure 2).

Next, we examine the mechanistic basis for the observed effects of O_2/CO ratios on O* selectivities (Figure 2), which determine O* coverages via kinetic coupling between O* removal by reactions with CO (r_{CO}) and CH_4 (r_{CH_4}) and O* formation from O_2 dissociation (r_{O_2}). For O* species at pseudo-steady-state:

$$r_{O_2} = \nu_{CO} r_{CO} + \nu_{CH_4} r_{CH_4} \quad (2)$$

ν_{CO} and ν_{CH_4} are the respective O_2 stoichoimetric coefficients ($\nu_{CO} = 0.5$ and $\nu_{CH_4} = 1.5$ for CH_4 conversion to CO and H_2O and $\nu_{CH_4} = 2.0$ for CH_4 combustion).

The large selectivity ratios observed (> 35 for $O_2/CO > 0.064$, Figure 2) indicate that r_{CO} is much larger than r_{CH_4}, a conclusion that together with rate and equilibrium constants in Scheme 1 gives O* coverages as a function of O_2/CO ratio (derivation in Supplementary Information, Section 1):

$$\frac{(O^*)}{(*)} \sim \frac{2k_{1bf}K_{O_2}}{k_{CO,f}K_{CO}}\frac{(O_2)}{(CO)} \quad (3)$$

K_{O_2} and K_{CO} are the equilibrium constants for adsorption of O_2 ($k_{1af}(k_{1ar})^{-1}$, step 1.1) and CO (reverse of step 8) and k_{1bf} and $k_{CO,f}$ are the rate constants for O_2 dissociation (step 1.2) and CO oxidation (step 4), respectively, as defined in Scheme 1. This equation, taken together with C-H bond dissociation steps that occur preferentially on *-* site pairs (step 2.1, Scheme 1)[26] present at low O* coverages,[18] leads to a linear dependence of O* selectivities on O_2/CO ratios:

$$O^* \text{selectivity} = 2\upsilon_{O^*}\frac{k_{1bf}K_{O_2}}{k_{[*-*]}}\frac{(O_2)}{(CO)} \quad (4)$$

where υ_{O^*} is the ratio of stoichoimetric coefficients for O_2 reactions with CO and CH_4.[32] Equation 4 accurately describes all data in Figure 2 ($2\upsilon_{O^*}k_{1bf}K_{O_2}(k_{[*-*]})^{-1} = 503$). We infer that O* species, present at low coverages during catalysis, are not involved in the kinetically-relevant C-H bond activation step, but act instead only to remove its products in subsequent steps, as also found for CH_4 oxidation on Pt clusters.[18] If O* species were used in C-H bond activation steps, ^{12}CO and $^{13}CH_4$ would compete for vicinal O* atoms, and O* selectivities would be independent of O* coverages or O_2/CO ratios and given by the ratio of rate constants for CO oxidation and C-H bond activation on O*-* site pairs ($\upsilon_{O^*}k_{CO,f}K_{CO}(k_{[O^*-*]})^{-1}$, derivation in Supplementary Information, Section 2). The linear dependence of O* selectivities on O_2/CO ratios (Figure 2) indicates that any CO that desorbs unreacted from partial oxidation stoichiometric mixtures ($O_2/CH_4 \sim 1$) would rapidly react at the high O* coverages and O_2/CO ratios prevalent near the reactor inlet, which favor CO oxidation over C-H bond activation steps.

These measured O* selectivities allow estimates of maximum CO yields ($\%Y_{CO}$) by using mole balances in plug-flow reactor models for CO (y_{CO}) and CH_4 (y_{CH_4}) mole fractions and assuming that all CH_4 turnovers lead to CO desorption before oxidation to CO_2 (derivation in Supplementary Information, Section 3):

$$\%Y_{CO} = \left(\frac{y_{CO}}{y_{CH_4,0}}\right)_{max} \times 100\% = \frac{1}{\alpha - 1}\left(\exp\left(-\frac{1}{\alpha-1}\ln(\alpha)\right) - \exp\left(-\frac{1}{1-\left(\frac{1}{\alpha}\right)}\ln(\alpha)\right)\right) \quad (5)$$

$$\alpha = \left(\frac{k_{CO,f}K_{CO}}{k_{[*-*]}}\right) \quad (6)$$

These equations give 0.1-2.7 % maximum CO yields for the range of O* selectivities measured in our experiments (36-1300[33]; Figure 2).

Higher CO yields from CH_4-O_2 reactants would require CH_4 oxidation rates faster than CO oxidation, which becomes possible only at very low O* coverages. These O*

coverages are, however, impractical for the reaction stoichiometries (O_2/CH_4 = 0.5) required for practical CH_4 conversions. The much higher reactivity of CO compared with CH_4 (Figure 2), as also found for Pt[18] and Rh[34] catalysts, at all practical O* coverages and O_2/CO ratios renders CO formation via direct partial oxidation pathways infeasible. The O* selectivities towards CO would be even higher with CH_4-O_2 reactants, because CH_4 is a less reactive scavenger and leads to higher O* coverages than in the presence of CO. These conclusions are consistent with the absence of detectable CO levels all O_2 pressures above 0.04 kPa in the reactor effluent (Figures 1b and 1d).

4.3.3. Chemical state of Pd clusters during catalytic CH_4-O_2 reactions. We probe next surface O* coverages on Pd clusters during CH_4–O_2 reactions and confirm that the bulk chemical state of Pd clusters remains in the metallic state throughout the rate measurements reported herein. During catalysis, surfaces of Pd clusters may not be equilibrated with O_2(g) because kinetic coupling between O_2 activation and its reactions with CH_4-derived intermediates can decrease O* coverages below those in equilibrium with O_2(g). Scavenging of O* by CH_4[18] or C_2H_6[35] reactants indeed prevents equilibration of O_2 dissociation-recombination steps on Pt.

The rate of $^{16}O^{18}O$ isotopologue formation from $^{16}O_2$-$^{18}O_2$ mixtures in the presence and absence of CH_4 can be used to determine the reversibility of the O_2 dissociation-recombination steps (step 1, Scheme 1) and whether O* coverages are equilibrated with the prevalent O_2 pressures during catalysis. The ratio of $^{16}O^{18}O$ isotopologue formation rates with CH_4-$^{16}O_2$-$^{18}O_2$ and $^{16}O_2$-$^{18}O_2$ mixtures (denoted as η) would be unity for equilibrated O_2 dissociation, but much smaller than unity for irreversible steps.[36] $^{16}O^{18}O$ formation rates were measured on Pd/Al_2O_3 (0.2 % wt. Pd, 21.3 nm mean Pd cluster diameter) with and without CH_4 at O_2 pressures used here for CH_4-O_2 reactions (< 1.6 kPa; 873 K, Figure 3). These formation rates were the same with CH_4-$^{16}O_2$-$^{18}O_2$ and $^{16}O_2$-$^{18}O_2$ mixtures within experimental accuracy at all O_2 pressure (η=1.01-1.09; Figure 3), indicating that O* is in equilibrium with O_2(g) during CH_4-O_2 reactions, because CH_4 chemical conversion, which consumes O*, is much slower than O* recombination (2.5 mol CH_4 (g-atom $Pd_{surface}$-s)$^{-1}$ vs. 23-39 mol $^{16}O^{18}O$ (g-atom $Pd_{surface}$-s)$^{-1}$, 873 K).

We conclude that oxygen chemical potentials at Pd cluster surfaces during catalysis are equal to those in O_2(g) for all conditions used to measured the rate data reported in Sections 3.4-3.7 (873 K, < 6 kPa CH_4, < 1.6 kPa O_2). Therefore, equilibrium O_2 uptakes on Pd clusters (in the absence of CH_4) rigorously reflect the O* coverages during CH_4-O_2 reactions. These uptakes were measured at 873 K and 1-30 kPa O_2 on 2 % wt. Pd/Al_2O_3 (5.9 nm mean Pd cluster diameter). Bulk oxidation of small Pd clusters has been shown to occur at lower oxygen chemical potentials than the large clusters used in the rate measurements reported herein (21.3 nm mean Pd cluster diameter).[28] The smaller Pd clusters (5.9 nm mean diameter) give constant oxygen uptakes, expressed in (O/Pd) atomic ratios, of 0.18 at O_2 pressures below 7.5 kPa (see Figure S-1 for the O_2 uptake as a function of O_2 pressure in the Supplementary Information Section 4). These ratios resemble those expected for saturation surface O* coverages (the expected O/Pd ratio is 0.17 for 5.9 nm hemispherical Pd clusters), as they correspond to an oxygen-to-exposed Pd ratio of 1.06. Above 7.5 kPa, the (O/Pd) ratios increased gradually from 0.18 and reached 0.98 at 25 kPa O_2. This increase corresponds to the formation of bulk PdO. These results confirm that small Pd clusters (5.9 nm), in spite of their stronger thermodynamic

tendency for bulk oxidation,[28] retain their metallic bulk at temperatures (> 873 K) and O_2 pressures (< 1.6 kPa) used here. Larger metallic Pd clusters are expected to convert to PdO at even higher O_2 pressures; thus, Pd clusters of all diameters used in the rate measurements herein must also be in the metallic phase.[27]

Bulk oxidation of Pd clusters occurs at higher O_2 pressures and forms Pd^{2+}-O^{2-} surface sites that are more effective than sites on O* covered Pd clusters for C-H bond activation.[27] The Pd-PdO phase transition and its kinetic consequences in CH_4–O_2 reactions are addressed in a parallel study at thermodynamic and chemical equilibrium, where oxygen atoms at surfaces and in the bulk of Pd clusters are chemically equilibrated with O_2(g).[28] Here, we specifically address the elementary steps and their kinetic relevance for CH_4 oxidation over O* covered metallic Pd clusters by keeping oxygen chemical potentials below those required for bulk oxidation (< 7.5 kPa at 873 K). We show that the reactive CH_4 collision probabilities depend on O* coverages in the same manner on Pd and Pt clusters, suggesting that identical kinetically-relevant steps and surface site structures are involved and that they evolve with O* coverages in a similar manner.

4.3.4. Reactive CH_4 collision probabilities on Pd metal clusters. CH_4 conversion turnover rates were measured during initial contact (0-7.2 ks) of Pd/Al_2O_3 (0.2 % wt., 21.3 nm mean cluster diameter) with CH_4-O_2 reactants by varying O_2 pressures at a constant CH_4 pressure (4.85 kPa). Reactive CH_4 collision probabilities are shown in Figures 1a and 1c as a function of O_2 pressures at 873 K and 973 K, respectively. The reactive CH_4 collision probabilities were constant at high O_2 pressures (>1.1 kPa and >1.3 kPa for 873 K and 973 K, respectively) but increased as O_2 pressure decreased, as also observed on Pt clusters.[19] These trends were interpreted from kinetic and isotopic data and density functional theory calculations on Pt clusters in terms of a transition in the identity of the kinetically-relevant step and of the most abundant surface intermediate with changes in O* coverages.[19] Specifically, kinetically-relevant C-H bond activation steps occur on O*-O* site pairs at high O* coverages, but benefit from access to vacant sites in O*-* site pairs as O* coverages decrease with decreasing O_2 pressures. The vacant sites can interact with the C-atom in CH_3 groups and stabilize C-H bond activation transition states, causing the observed increase in reactivity on Pd clusters as O_2 pressure decreases, as also found on Pt clusters.[19]

Reactive CH_4 collision probabilities did not depend on O_2 pressure above 1.1-1.3 kPa O_2 (Figures 1a and 1c), because kinetically-relevant C-H bond activation step must use O*-O* site pairs on O*-saturated cluster surfaces, a conclusion confirmed by rate dependencies, normal C-H/C-D kinetic isotope effects, and high C-H bond activation barriers and pre-exponential factors prevalent for O* assisted C-H bond activation steps, as discussed in Section 3.5. As vacant sites emerge with decreasing O_2 pressures, the first-order C-H bond activation rate constants increased and reached values larger than for similar steps on *-* site pairs,[37] which limit rates for CH_4-H_2O/CO_2 mixtures[26] (step 2.1, Scheme 1; Table 2). On Pt clusters, O* atoms vicinal to exposed metal atoms activate C-H bonds during CH_4-O_2[18] and CH_3OCH_3-O_2[38] reactions much more efficiently than exposed metal surfaces at high O* coverages. O* abstracts H-atoms from CH_4 while exposed metal atoms stabilize CH_3 fragments via concerted oxidative addition into the C-H bond.[19] These O*-* site pairs are also more reactive than O*-O* site pairs on both Pd and Pt[19,35] surfaces because CH_3 fragments interact with open sites (*) more strongly than

with O* and stabilize the required transition states. Taken together, the trends of first-order rate constants with O_2 pressures in Figure 1 suggest that O*-* site pairs assist C-H bond activation much more effectively than the *-* or O*-O* site pairs prevalent in the absence of O_2 (in CH_4-H_2O/CO_2 mixtures) or at high O_2 pressures, respectively.

At very low O_2 pressures, O_2 activation becomes the kinetically-relevant step on Pt clusters (8.5 nm mean cluster diameter, $O_2/CH_4 < 0.08$,[39] 873 K).[18] In this regime, turnover rates become proportional to O_2 pressure and independent of CH_4 pressure and CH_4/CD_4 isotope effects are not detected. On Pd, this kinetic regime was detected only at high temperatures (973 K) and very low O_2 pressures (<0.2 kPa; Figure 1c). The difference between Pd and Pt reflects stronger O*-Pd bonds than O*-Pt bonds (382 kJ mol^{-1} vs. 354 kJ mol^{-1} DFT values of an isolated O* atom on Pd(111) and Pt(111) surfaces[40]), making bare surfaces essentially inaccessible before O_2 depletion and the regime that O_2 dissociation controls rates nearly undetected on Pd clusters.

The reactive CH_4 collision probabilities did not change with time on stream at extended times (similar at 32.4-38.0 ks and 77.4-82.8 ks; Figures 1a and 1c), but the rate constants and the transition O_2 pressure between regimes were smaller than those measured during initial contact to CH_4-O_2 reactants (0-7.2 ks). These changes appear to reflect the densification of O* monolayers, as proposed on Pd(100),[41,42] and the formation of more stable structures, within which oxygen vacancies (*) are less likely to exist. Thus, turnover rates and rate constants become smaller after densification and lower O_2 pressures are required for vacancies to form in concentrations for O*-* sites to contribute to C-H bond activation rates (<0.2 kPa and <0.3 kPa for 873 K and 973 K, respectively). These "deactivation" processes do not reflect the coalescence of Pd clusters, because larger clusters would have led to lower O* binding energies and higher reactivity (Section 3.7) and to a transition between regimes to occur at higher O_2 pressures.

4.3.5. Rate equations and their mechanistic interpretations for CH_4-O_2 reactions on oxygen-saturated Pd cluster surfaces. Next, we report kinetic effects of reactant and product concentrations and CH_4/CD_4 kinetic isotope effects at reaction times (> 80 ks) and conditions that led to stable rates and to first-order rate constants independent of O_2 pressure on Pd/Al_2O_3 (0.2 % wt., 21.3 nm mean Pd cluster diameter) at low CH_4 conversions (<0.5 %; H_2O and CO_2 <0.05 kPa at 873 K). CH_4 turnover rates (r_{CH_4}) increase linearly with CH_4 pressure (1.8-5 kPa) but did not depend on O_2 pressure (0.4-1.6 kPa; Figures 4a and 4b) according to the equation:

$$r_{CH_4} = k_{app,1}(CH_4)^1(O_2)^0 \qquad (7)$$

in which $k_{app,1}$ is an effective rate constant. This equation describes the rate data on Pd clusters with mean cluster diameters between 4.5-22.3 nm.

These rate data (Figure 4) are consistent with the sequence of elementary steps shown in Scheme 1. In this mechanistic proposal, O_2 dissociates to form O* species (steps 1.1 and 1.2, Scheme 1) and the resulting O*-O* site pairs activate C-H bonds in CH_4 (step 2.3) to form CH_3O* and OH*. CH_3O* undergoes sequential H-abstraction and O* insertion (step 3) steps to form CO (step 8) or CO_2 (steps 4 and 7). OH* recombination forms H_2O (steps 5 and 6) and CO readsorption (reverse of step 8) and oxidation to CO_2 (steps 4 and 7) completed a catalytic turnover. O_2 dissociation steps (steps 1.1 and 1.2, Scheme 1) are quasi-equilibrated, as shown by isotopic oxygen exchange probe reactions (Section 3.3).

CH_4/CD_4 kinetic isotope effects, measured on the Pd/Al_2O_3 catalyst (0.2 % wt., 21.3 nm mean Pd cluster diameters) with CH_4-O_2 and CD_4-O_2 mixtures, are 2.01 at 873 K; these values confirm that C-H bond activation is a kinetically-relevant step; the linear dependence of rates on CH_4 pressure indicates that C-H bond activation occurs on surfaces with active site structures and concentrations that do not depend on the CH_4 or O_2 pressure. This requires that cluster surfaces be either uncovered or saturated by species derived from CH_4 or O_2 (CH_x* and O*, respectively).

Kinetic studies[26] with CH_4-H_2O/CO_2 reactants showed that C* intermediates are present in kinetically-detectable coverages on Pd clusters, because of strong Pd-C bonds, but such species do not influence CH_4-O_2 reactions, because O_2 is a more effective oxidant than H_2O and CO_2, confirmed from larger CH_4 oxidation rates during reactions with O_2 than with H_2O and CO_2 (Table 2). Pd cluster surfaces partially covered with C* from C-H bond activation steps would have led to different $^{16}O^{18}O$ formation rates with CH_4-$^{16}O_2$-$^{18}O_2$ and $^{16}O_2$-$^{18}O_2$ mixtures, instead of the equal rates measured (Figure 3). Reactive CH_4 collision probabilities and their activation barriers and pre-exponential factors for CH_4 activation on uncovered Pd clusters (step 2.1, Scheme 1) have been previously established using CH_4-H_2O/CO_2 mixtures ($k_{[*-*]}$ ~ 4.0 mol CH_4 (g-atom $Pd_{surface}$ kPa s)$^{-1}$ at 873 K; activation barrier 82.5 kJ mol^{-1}; pre-exponential factor 3.5×10^5 kPa^{-1} s^{-1}; 12.5 nm Pd cluster diameter).[26,37] These values were unlike those measured in CH_4-O_2 reactions (0.53 mol CH_4 (g-atom $Pd_{surface}$ kPa s)$^{-1}$ at 873 K; activation barrier 158 kJ mol^{-1}; pre-exponential factor 1.48×10^9 kPa^{-1} s^{-1}; 21.3 nm mean Pd clusters), derived from regression fitting of the temperature dependence rate constant data in Figure 5. We conclude that Pd cluster surfaces were not uncovered but instead saturated with O* atoms, a conclusion consistent with the ratio of oxygen-to-exposed Pd atom ($O^*/Pd_{surface}$) of near unity (1.06) over the O_2 pressure range (0.5-6.0 kPa, Section 3.3), which determines the oxygen chemical potentials at Pd surfaces, used for rate measurements (see Figure S-1 of the Supplementary Information, Section 4). The apparent rate constant in Equation 7, $k_{app,1}$, thus reflects the elementary rate constant for C-H bond activation on O*-O* site pairs ($k_{[O^*-O^*]}$, step 2.3).

The activation energy (158 kJ mol^{-1}) and pre-exponential factor (1.48×10^9 kPa^{-1} s^{-1}) for C-H bond activation on O*-O* site pairs on Pd/Al_2O_3 (0.2 % wt., 21.3 nm clusters; Figure 5) are similar to those on Pt clusters (155 kJ mol^{-1} and 2.1×10^9 kPa^{-1} s^{-1}, 8.5 nm clusters).[19] These activation barriers are similar to DFT-derived barriers on Pt(111) (149 kJ mol^{-1})[19] and Pd(111) (145 kJ mol^{-1})[43] covered with O* and on O* covered cubo-octahedral Pt clusters (149 kJ mol^{-1}; 201 Pt atoms).[19] C-H bond activation on O*-O* site pairs involves H-atom abstraction by one O* to form a $[CH_3\bullet\text{--}O^*\text{--}OH^*]^{\ddagger}$ transition state,[19,43] in which the O-H* bond is nearly formed and the $CH_3\bullet$ radical-like species interacts weakly with a vicinal O*, as proposed also for C-H bond activation on V-oxide.[44,45] These unstable CH_3 species lead to transition state energies much higher than on O*-* pairs, where CH_3 species interact strongly with * at the transition state.[19] Weakly-held $CH_3\bullet$ species retain most of the translational entropy of the CH_4 reactants. As a result, activation entropies are much less negative when O*-O* (-15.0 J (mol-K)$^{-1}$ and -12.2 J (mol-K)$^{-1}$ for Pd and Pt,[19] respectively) instead of O*-* pairs (-99.0 J (mol-K)$^{-1}$)[19] are used for C-H bond activation; their values are also much smaller (in negative values) than estimates by assuming the loss of one translational mode upon formation of

the transition state from the gas phase CH_4 reactant in the framework of transition state theory (-98 J (mol-K)$^{-1}$).

4.3.6. CO_2 and H_2O effects on CH_4-O_2 reaction rates. Next, we consider the influences of excess CO_2 and H_2O products on CH_4 conversion turnover rates and their mechanistic implications. The kinetic consequences of excess H_2O and CO_2 were measured by adding H_2O and $^{12}CO_2$ to CH_4-O_2 (or $^{13}CH_4$-O_2) reactants. $^{13}CH_4$ turnover rates were not affected by $^{12}CO_2$ (6-12.5 kPa, Figure 6) because CO_2-derived intermediates (CO_2* and CO*) were present at negligible coverages during steady-state catalysis. CH_4 turnover rates decreased markedly when H_2O was added (1-10 kPa). Assumptions of competitive OH* adsorption via quasi-equilibrated H_2O adsorption-desorption steps (steps 5 and 6, Scheme 1), together with irreversible C-H bond activation on O*-O* site pairs and quasi-equilibrated O* adsorption-desorption steps, lead to the rate equation below (derivation in Supplementary Information Section 5):

$$r_{CH_4} = \frac{k_{[O^*\text{-}O^*]}(CH_4)K_{O_2}(O_2)}{\left(\sqrt{K_{O_2}(O_2)} + \sqrt{\frac{(H_2O)\sqrt{K_{O_2}(O_2)}}{K_{H_2O}K_{OH^*}}}\right)^2} \quad (8)$$

This equation is used to describe the rate data in CH_4-O_2-H_2O mixtures (Figure 6) by linear regression analysis with minimization of residuals. Turnover rates decreased more strongly than the trend predicted from Equation 8, as also plotted in Figure 6. Upon H_2O removal, the initial turnover rates were recovered in part. This strong effects of H_2O, together with rates unable to fully recovered upon H_2O removal, led us to conclude that the marked decrease in rates in the presence of H_2O cannot be solely caused by the reversible binding of OH* on Pd and their titration of O* atoms from Pd cluster surfaces. These effects of H_2O might suggest a structural transformation of Pd to a more stable and less reactive surface in the presence of H_2O. Turnover rates in excess H_2O remain proportional to CH_4 pressures (Figure 4a; > 5 kPa H_2O) and unaffected by O_2 pressures (Figure 4b). These kinetic dependencies indicate that O_2 and H_2O concentrations do not affect surface structures and thus do not influence the reactive CH_4 collision probabilities in the presence of excess H_2O (> 4 kPa).

The involvement of OH* (or OD*) species in the kinetically-relevant C-H bond dissociation step and the reversibility of this step can be probed in CH_4-O_2-D_2O mixtures where OH* (or OD*) species are prevalent on Pd cluster surfaces. CH_3D must form via the microscopic reverse of the C-H bond activation steps (step 2.3, Scheme 1). The reversibility of this step is expressed in term of the ratio of CH_xD_{4-x} formation to forward CH_4 conversion rates; these ratios were measured with CH_4-O_2-D_2O and CD_4-O_2-H_2O mixtures on 0.2 % wt. Pd/Al_2O_3 (21.3 nm mean Pd cluster diameter) at 873 K, as shown in Figure 7 as a function of D_2O or H_2O inlet pressures (2-8 kPa). CH_3D (or CD_3H) isotopologues were the primary exchange product detected (> 0.99 of all the CH_xD_{4-x}, x=1-4) in CH_4-D_2O-O_2 (or CD_4-H_2O-O_2) mixtures, indicating that initial C-H bond activation is a reversible step in the presence of excess D_2O (or H_2O); the formation of these isotopologues infers the recombination of C-H (or C-D) bond dissociation products with OD* (or OH*) intermediates and confirms that the initial C-H bond activation step involves O* and forms OD* (or OH*) species.

The ratio of CH_3D formation to forward CH_4 conversion rates in CH_4-D_2O-O_2 (or CD_4-H_2O-O_2) mixtures reflects the relative rates of CH_3* (or CD_3*) and OD* (or OH*)

recombination and forward CH_4 chemical turnover. These ratios were found to be 0.1 and 0.77 in CH_4-D_2O-O_2 and CD_4-H_2O-O_2 mixtures, respectively, and remain unchanged with D_2O (or H_2O) pressures (2-8 kPa), apparently because Pd surface structures and OD* (or OH*) coverages do not vary with the D_2O (or H_2O) pressures, consistent with CH_4 turnover rates remain essentially unaffected by D_2O (or H_2O) pressure at excess D_2O (or H_2O) (> 4 kPa, Figure 6).

4.3.7. Effects of Pd cluster size and oxygen binding strength on the rates of C-H bond activation assisted by oxygen atom site pairs. Metal atoms exposed at cluster surfaces increase in average coordination with increasing cluster size[46] and cause chemisorbed species to be more weakly-bound. For CH_4-O_2 reactions on O*-covered surfaces, these weakly-bound O* atoms would give higher turnover rates on larger clusters, a trend that we confirm from rate data on Pd clusters with 4.5-22.3 nm diameter in this section.

Rate constants for C-H bond activation on O*-O* site pairs ($k_{[O^*-O^*]}$) were measured during the early stages of reactions (0-7.2 ks) on Pd clusters (4.5-22.3 nm; 0.2 % wt. Pd/Al_2O_3 catalysts) at 873 K (Figure 8). C-H bond activation rate constants increased markedly with increasing Pd cluster diameter (Figure 8), as also observed for CH_4-O_2[19] and C_2H_6-O_2[35] reactions on O* saturated Pt clusters. These trends reflect strong effects of oxygen binding energy on its reactivity for kinetically-relevant H-abstraction steps and to a lesser extent its ability to weakly stabilize radical-like CH_3 fragments at the H-abstraction transition state (step 2.3, Scheme 1). On model Pt clusters, DFT-derived activation barriers for C-H bond dissociation on O*-O* site pairs decrease with decreasing O* binding energy and with increasing stability of OH*, which reflects, in turn, the O* basicity and the ability for O* to form stronger OH bonds at the transition states.

These effects of O* binding energy also cause differences in C-H bond activation reactivity between Pt and Pd atoms for a given cluster size and average coordination. DFT-derived heats of atomic O* adsorption are 382 kJ mol^{-1} and 354 kJ mol^{-1} for isolated O* chemisorbed on the fcc sites of Pd(111) and Pt(111) surfaces, respectively.[40] The weakly-bound O* on Pt are more effective for C-H bond activation than on Pd atoms and lead to higher turnover rates for Pt when compared at the same cluster size and average coordination (Figure 8).

When C-H bond activation occurs on O*-* site pairs, O* binding energy influences not only O* reactivity but the number of vacancies in O* monolayers; as a result, cluster size influences both turnover rates and the oxygen chemical potential at which O*-* sites become kinetically-visible and the transition between kinetic regimes occurs. Figure 9 shows first-order rate constants (for 0-7.2 ks time on stream) as a function of O_2 pressure on samples with Pd clusters of 4.8 nm and 21.3 nm mean diameters (0.2 % wt. Pd/Al_2O_3; 873 K). The reactivity of smaller clusters is lower throughout this O_2 pressure range (0.3-1.6 kPa) although large and small clusters exhibit similar O_2 kinetic responses. The shift from O*-O* to O*-* as C-H bond activation sites, indicated by an increase in rate constants with decreasing O_2 pressure, occurs, however, at a lower O_2 pressure on small Pd clusters (~0.7 kPa on 4.8 nm; ~1.2 kPa on 21.3 nm). The stronger O* binding on small clusters leads to smaller vacancy densities than on larger clusters at each O_2 pressure; as a result contributions from the more reactive O*-* site pairs become kinetically-visible only at lower O_2 pressures. These effects of cluster size

on the involvement and reactivity of O*-* site pairs in C-H bond activation are similar to those observed for CH_4[19] and C_2H_6[35] oxidation on Pt and CH_3OCH_3 oxidation on Pt, Pd, and Rh.[47] The effects of surface coordination and cluster size on the binding energy of chemisorbed species and on the availability of vacancies are also evident from the lower reactivity of small clusters observed for NO oxidation on Pd,[36] for which rates are limited by O_2 activation on O*-* site pairs, and thiophene hydrodesulfurization on Ru[48] and Pt[49] clusters, for which rates depend on the availability of vacancies on cluster surfaces nearly saturated with chemisorbed sulfur atoms.

4.4. Conclusions

Elementary steps and their kinetic relevance during CH_4 reactions with O_2 on metallic Pd clusters were established based on kinetic and isotopic studies under conditions of strict kinetic control, attained by removal of temperature and concentration gradients within pellets and the catalyst bed by extensive site dilutions. H_2O and CO_2 were formed nearly exclusively at all non-zero O_2/CH_4 ratios, because reactive collision probabilities for CO oxidation are much larger than for CH_4 oxidation. This difference in reactivity between CO and CH_4 limits the maximum attainable CO yields from direct CH_4 and O_2 reactions at any practical extent of CH_4 conversion.

Reactive CH_4 collision probabilities (also the first-order rate constants) decrease and then reach constant values with increasing oxygen coverages. This trend reflects a transition in the kinetically-relevant step from C-H bond activation on O*-* sites to less reactive O*-O* sites. The relative abundance of oxygen atoms and oxygen vacancies, distribution of O*-* and O*-O* pairs on Pd cluster surfaces, and thermodynamic tendency of bulk Pd oxidation during CH_4-O_2 reactions are set by the prevalent O_2 pressures because O* atoms and O_2(g) are chemically equilibrated. C-H bond activation step on O*-O* site pairs exhibits high barriers (158 kJ mol^{-1}) and unusually high pre-exponential factors (1.48×10^9 kPa^{-1} s^{-1}) that are larger than estimates derived from a transition state theory formalism assuming the loss of a translational degree of freedom in CH_4(g). These kinetic parameters are common features for C-H bond activation on O* saturated metal surfaces, which proceeds via a loosely bound methyl radical-like transition state. In contrast, oxygen vacancies in O*-* site pairs stabilize the methyl group at the transition state, decreasing the barriers and, in turn, leading to more effective C-H bond activation on O*-* than O*-O* pairs.

Larger clusters with weakly bound O* are more effective for C-H bond activation than smaller clusters. The transition of kinetically-relevant step from C-H bond activation on O*-* to O*-O* site pairs occurs at higher O_2 pressures on the larger Pd clusters because oxygen vacancies and O*-* pairs are more abundant than smaller clusters. Similar effects of O* binding strength are also observed among different metals. Stronger O* binding on Pd than Pt atoms of the same coordination leads to less effective C-H bond activation on O*-O* pairs. These effects of O* binding strength on rates appear to be general for oxidation reactions that involve either the O* (CH_4 oxidation on Pd; CH_4, C_2H_6, and CH_3OCH_3 oxidation on Pt) or the oxygen vacancies (NO oxidation on Pt and Pd) in the kinetically-relevant steps.

4.5. References

[1] Ciuparu, D.; Lyubovsky, M.R.; Altman, E.; Pfefferle, L.D.; Datye, A. *Catal. Rev. Sci. & Engr.* **2002**, *44*, 593.

[2] Chin, Y-H.; Resasco, D.E. Catalytic Oxidation of methane on supported palladium under lean conditions: Kinetics, structure and properties. In Catalysis; Spivey, J.J., Eds.; The Royal Society of Chemistry, Thomas Graham House, Science Park, Cambridge, UK, 1999, Vol. 14, 1-39.

[3] Centi, G. *J. Mol. Catal. A, Chem.* **2001**, *173*, 287.

[4] Gelin P.; Primet, M. *Appl. Catal. B-Environ.* **2002**, *29*, 1.

[5] Bhattacharya, A.K.; Breach, J.A.; Chand, S.; Ghorai, D.K.; Hartridge, A.; Keary, J.; Mallick, K. K. *Appl. Catal. A: Gen.*, **1992**, *80*, L1.

[6] van Looij, F.; Stobbe, E.R.; Geus, J.W. *Catal. Lett.* **1988**, *50*, 59.

[7] Armor, J.N. *Appl. Catal. A-Gen.* **1999**, *176*, 159.

[8] Ribeiro, F.H.; Chow. M.; Dallabetta, R. A. *J. Catal.* **1994**, *146*, 537.

[9] McCarty, J.G. *Catal. Today* **1995**, *26*, 283.

[10] Hurtado, P.; Ordonez, S.; Sastre, H.; Diez, F.V. *Appl Catal. B-Environ.* **2004**, *51*, 229.

[11] Kimmerle, B.; Baiker, A.; Grunwaldt, J. D. *Phys. Chem. Chem. Phys.* **2010**, *12*, 2288.

[12] Matsumoto, H. *J. Phys. Chem.* **1994**, *98*, 5180.

[13] Matsumota, H.; Tanade, S. *J. Chem. Soc., Faraday Trans.* **1994**, *90*, 3001.

[14] Datye, A.K.; Bravo, J.; Nelson, T.R.; Atanasova, P.; Lyubovsky, M.; Pfefferle, L. *Appl. Catal. A-Gen.* **2000**, *198*, 179.

[15] Farrauto, R.J.; Hobson, M.C.; Kennelly, T.; Waterman, E.M. *Appl. Catal. A-Gen.* **1992**, *81*, 227.

[16] Farrauto, R.J.; Lampert, J.K.; Hobson, M.C.; Waterman, E.M. *Appl. Catal. B-Environ.* **1995**, *6*, 263.

[17] Zhu, G.; Han, H.; Zemlyanov, D. Y.; Ribeiro, F. H. *J. Phys. Chem. B,* **2005**, *109*, 2331.

[18] Chin, Y-H.; Buda, C.; Neurock, M.; Iglesia, E. *J. Catal.* Submitted.

[19] Chin, Y-H.; Buda, C.; Neurock, M.; Iglesia, E. *J. Am. Chem. Soc*. submitted.

[20] Wei, J.M.; Iglesia, E. *J.Catal.* **2004**, *225*, 116.

[21] Wei, J. M.; Iglesia, E. *J. Phys. Chem. B* **2004**, *108*, 4094.

[22] Wei, J. M.; Iglesia, E. *J. Phys. Chem. B* **2004**, *108*, 7253.

[23] Wei, J.; Iglesia, E. *Phys. Chem. Chem. Phys.* **2004**, *6*, 3754.

[24] Wei, J.; Iglesia, E., *Angew. Chem. Int. Ed.* **2004**, *43*, 3685.

[25] Wei, J.; Iglesia, E., *J. Catal.* **2004**, *224*, 370.

[26] Yamaguchi, A; Iglesia, E., *J. Catal.* **2010***, 274*, 52.

[27] Chin, Y-H.; Iglesia, E. unpublished results.

[28] Chin, Y-H.; García-Diéguez M.; Iglesia, E. in preparation.

[29] David, R. L. *Handbook of Chemistry and Physics*, 87th ed.; CRC Press: Boca Raton, FL 2006.

[30] Koros R. M.; Nowak, E.J. *Chemical Engr. Sci.* **1967**, *22*, 470.

[31] Madon R.; Boudart, M. *Ind. Eng. Chem. Fundam.* **1982**, *21*, 438.

[32] In $^{13}CH_4$-CO-O_2 mixtures and under the complete O_2 depletion, CH_4 can convert to CO_2 and CO with different reaction stoichoimetries of O* atoms.

[33] The calculations assume that both CO and CH_4 oxidation reactions follow the first-order reaction kinetics.
[34] Donazzi, A.; Beretta, A.; Groppi, G.; Forzatti, P. *J. Catal.* **2008**, *255*, 241.
[35] García-Diéguez, M.; Chin Y-H.; Iglesia, E. *J. Catal.* in preparation.
[36] Weiss B. M.; Iglesia, E. *J. Catal.* **2010**, *272*, 74.
[37] Elementary rate constants for C-H bond activation on *-* site pairs (step 2.1, Scheme 1) on the 21.3 nm Pd clusters are expected to be lower than the reported values on smaller Pd clusters in ref. 26 because the metal sites with larger coordination are less effective for C-H bond activation (see ref. 26, 20-23, 25).
[38] Ishikawa,A.; Neurock, M.; Iglesia, E. *J. Amer. Chem. Soc.* **2007**, *129*, 13201.
[39] On Pt clusters, this kinetic regime is defined by the O_2/CH_4 ratio because the O_2/CH_4 ratio determines the surface O* coverage via kinetic coupling of C-H and O=O activation steps.
[40] van Santen, R.A.; Neurock, M. Molecular Heterogeneous Catalysis: a Conceptual and Computational Approach, Weinheim, Cambridge: Wiley-VCH, 2006, p. 107.
[41] Zheng, G.; Altman, E.I. *Surf. Sci.* **2002**, *504*, 253.
[42] Simmons, G.W.; Wang,Y-N.; Marcos, J.; Klier, K. *J. Phys. Chem.* **1991**, *95*, 4522.
[43] Buda, C.; Neurock M., unpublished results.
[44] Dai, G-L.; Liu, Z-P.; Wang, W-N.; Lu, J.; Fan, K-N. *J. Phys. Chem. C* **2008**, *112*, 3719.
[45] Rozanska, X.; Fortrie, R.; Sauer, J. *J. Phys. Chem. C* **2007**, *111*, 6041.
[46] van Hardeveld, R.; Hartog, F. *Surf. Sci.* **1969**, *15*, 189.
[47] Ishikawa, A.; Iglesia, E. *J. Catal.* **2007**, *252*, 49.
[48] Wang, H.; Iglesia, E. *J. Catal.* **2010**, *273*, 245.
[49] Wang, H.; Iglesia, E. *Chem. Cat. Chem.* submitted.

4.6. Figures

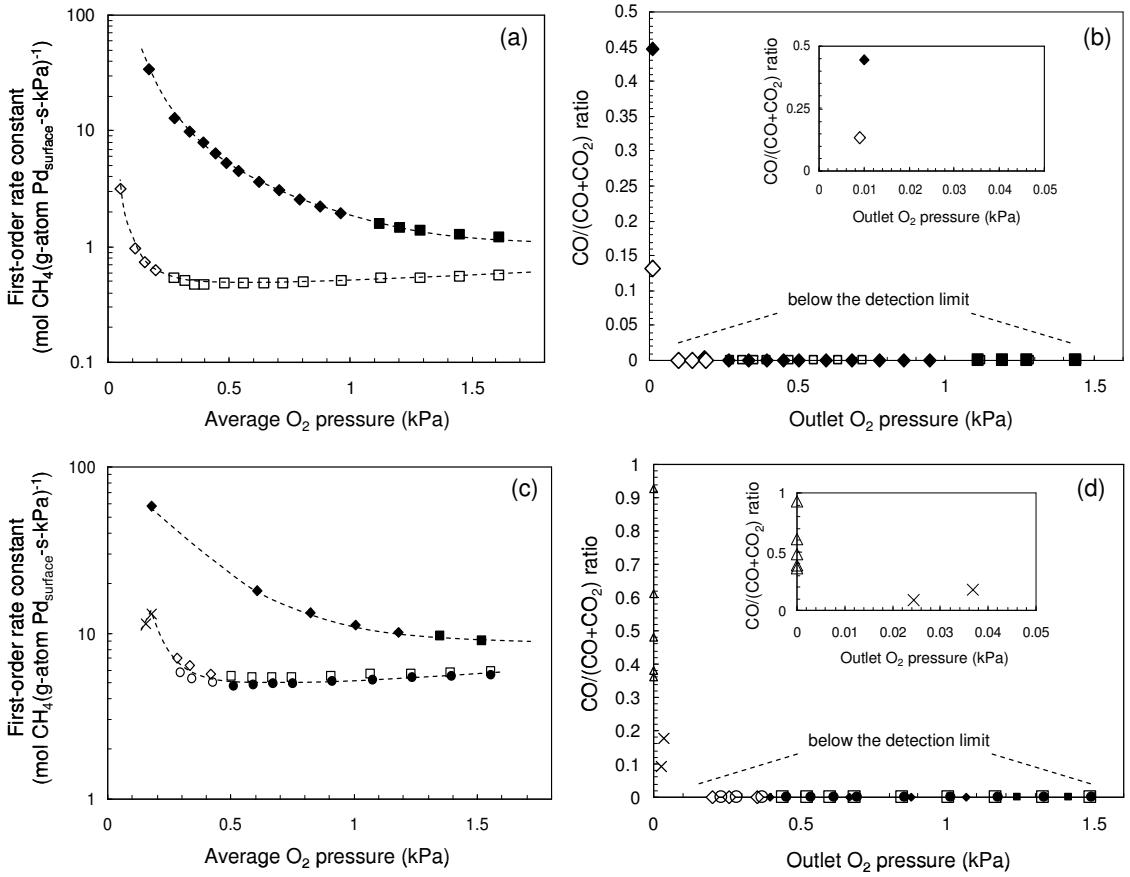

Figure 1a. O_2 pressure dependence of first-order rate constants ($r_{CH_4}(CH_4)^{-1}$, also the reactive CH_4 collision probabilities) during CH_4-O_2 reactions at 873 K and time-on-stream intervals of 0-7.2 ks (♦,■) and 59.4-63 ks (◊,□) on a 0.2 % wt. Pd/Al_2O_3 catalyst (21.3 nm mean Pd cluster diameter). Two distinct kinetic regimes are observed, where the rate constants are inversely proportional to (♦,◊) and independent of (■,□) O_2 pressure, respectively.

Figure 1b. Effects of outlet O_2 pressure on fractional CO contents, $CO/(CO+CO_2)$, during CH_4-O_2 reactions at 873 K and time-on-stream intervals of 0-7.2 ks (♦,■) and 59.4-63 ks (◊,□) on a 0.2 % wt. Pd/Al_2O_3 catalyst (21.3 nm mean Pd cluster diameter). Inset: region of low outlet O_2 pressure 0-0.05 kPa.

Figure 1c. O_2 pressure dependence of first-order rate constants ($r_{CH_4}(CH_4)^{-1}$, also the reactive CH_4 collision probabilities) during CH_4-O_2 reactions at 973 K and time-on-stream intervals of 0-7.2 ks (♦,■), 32.4-38.0 ks (◊,□), and 77.4-82.8 ks (×,○,) on 0.2 % wt. Pd/Al_2O_3 catalyst (21.3 nm mean Pd cluster diameter). Three distinct kinetic regimes

are observed, where the rate constants are proportional to (×), inversely proportional to (♦,◊,○) and independent of (■,□,) O_2 pressure.

Figure 1d. Effects of outlet O_2 pressure on fractional CO contents, $CO/(CO+CO_2)$, during CH_4-O_2 reactions at 973 K and time-on-stream intervals of 0-7.2 ks (♦,■), 32.4-38.0 ks (◊,□), and 77.4-82.8 ks (×,○,) on 0.2 % wt. Pd/Al_2O_3 catalyst (21.3 nm mean Pd cluster diameter). Additional data on the fractional CO contents after O_2 depletion (Δ) are also included here. Inset: region of low outlet O_2 pressure 0-0.05 kPa.

(4.85 kPa CH_4, 1.57×10^9 cm^3 (s mol $Pd_{surface})^{-1}$, 200 SiO_2/catalyst intraparticle dilution ratio, 450 quartz/catalyst bed dilution ratio)

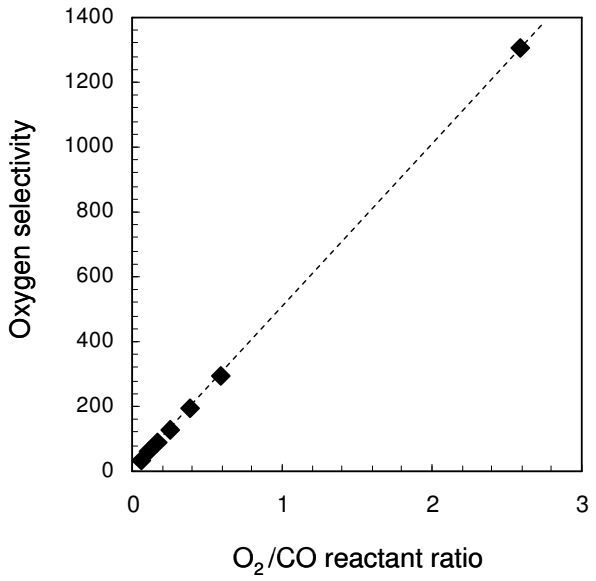

Figure 2. O_2/CO reactant ratio effects on oxygen selectivity, defined as the ratio of first-order rate constants (also the reactive collision probabilities) for CO and CH_4 oxidation (Equation 1), during $^{13}CH_4$-^{12}CO-O_2 reactions on a 0.2 % wt. Pd/Al_2O_3 (21.3 nm mean Pd cluster diameter) catalyst at 973 K.

(4.85 kPa $^{13}CH_4$, 0.81 kPa ^{12}CO, 0.081-0.36 kPa O_2, 1.57×10^9 cm^3 (s mol $Pd_{surface}$)$^{-1}$, 200 SiO_2/catalyst intraparticle dilution ratio, 450 quartz/catalyst bed dilution ratio)

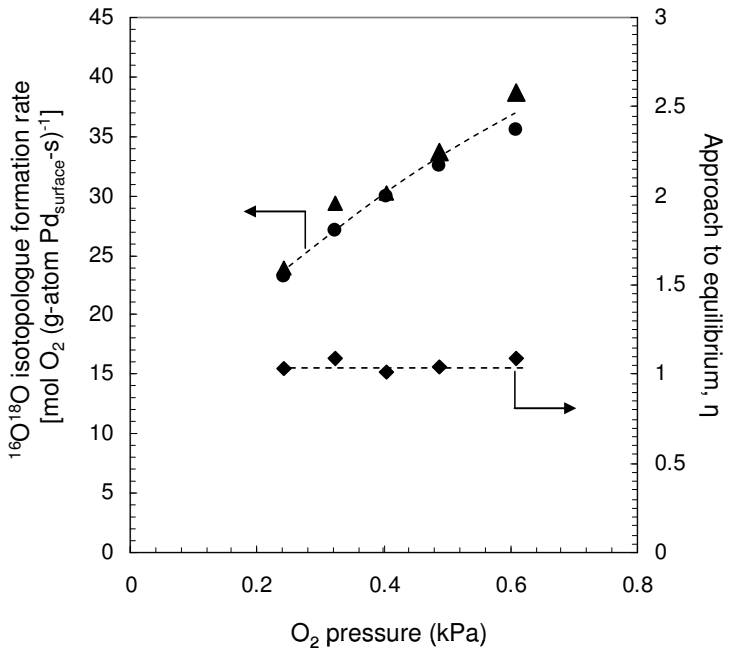

Figure 3. $^{16}O^{18}O$ isotopologue formation rates measured in $^{16}O_2$-$^{18}O_2$ ( ) and CH_4-$^{16}O_2$-$^{18}O_2$ (▲) mixtures and the approach to equilibrium values η (♦), which are the ratios of $^{16}O^{18}O$ isotopologue formation rates in CH_4-$^{16}O_2$-$^{18}O_2$ and $^{16}O_2$-$^{18}O_2$ mixtures, on a 0.2 % wt. Pd/Al_2O_3 (21.3 nm mean Pd cluster diameter) catalyst at 873 K.

(▲: 4.86 kPa CH_4, 1.57×10^9 cm^3 (s mol $Pd_{surface}$)$^{-1}$, 200 SiO_2/catalyst intraparticle dilution ratio, 350 quartz/catalyst bed dilution ratio)

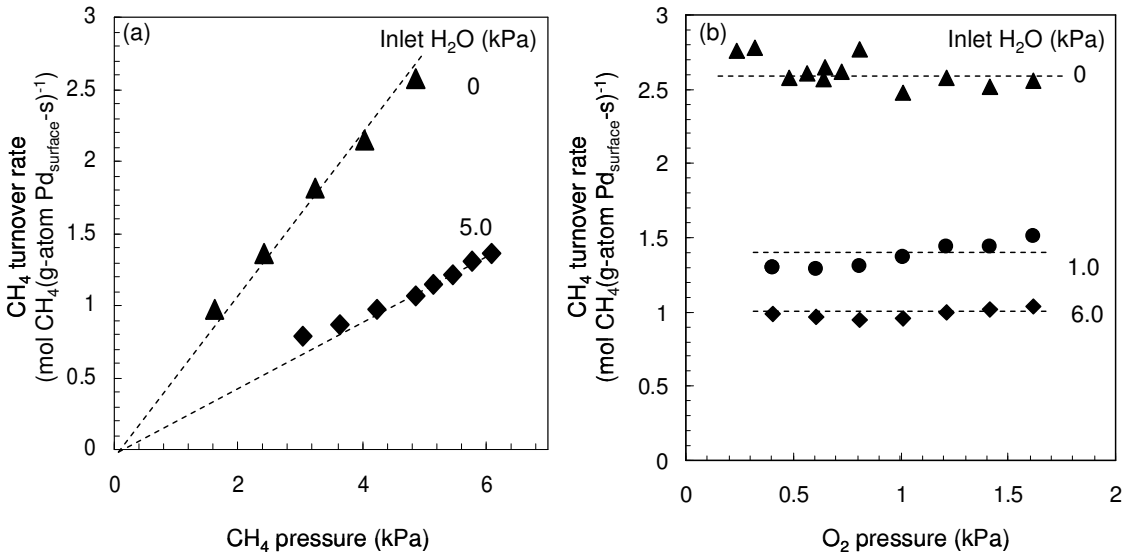

Figure 4a. Effects of CH_4 pressure on CH_4 turnover rates during CH_4-O_2 (▲; 0.48 kPa O_2) and CH_4-O_2-H_2O (♦; 0.48 kPa O_2 and 5.0 kPa H_2O) reactions at 873 K on a 0.2 % wt. Pd/Al_2O_3 (21.3 nm mean Pd cluster diameter) catalyst.

Figure 4b. Effects of O_2 pressure on CH_4 turnover rates during CH_4-O_2 reactions at 873 K on a 0.2 % wt. Pd/Al_2O_3 (21.3 nm mean Pd cluster diameter) catalyst with CH_4-O_2-H_2O mixtures (4.86 kPa CH_4; ▲: 0 kPa H_2O; ●: 1.0 kPa H_2O; ♦: 6.0 kPa H_2O).

(1.57×10^9 cm^3 (s mol $Pd_{surface}$)$^{-1}$, 200 SiO_2/catalyst intraparticle dilution ratio, 450 quartz/catalyst interparticle dilution ratio)

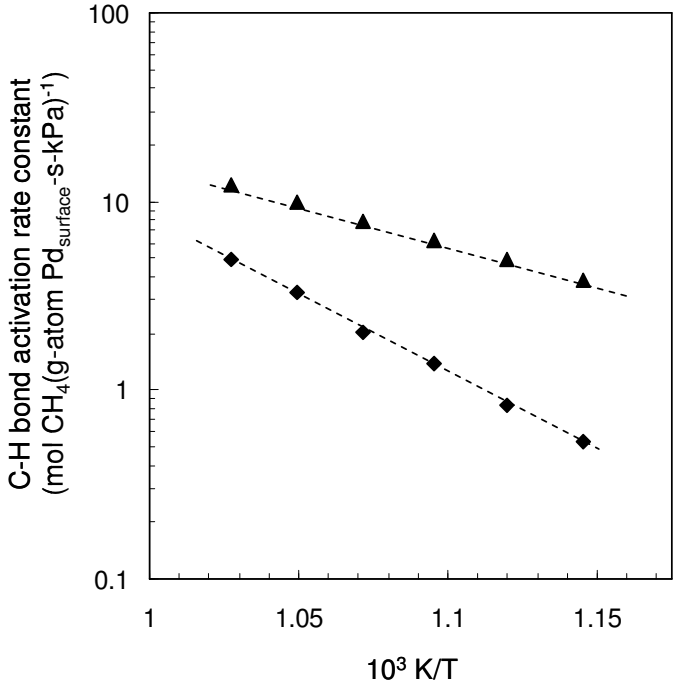

Figure 5. Arrhenius plot of C-H bond activation rate constants in CH_4-O_2 mixtures on Pd clusters (♦, 21.3 nm mean diameter; 0.2 % wt. Pd/Al_2O_3) and C-H bond activation rate constants on *-* site pairs on Pd clusters (▲, 12.5 nm mean diameter, CH_4-CO_2/H_2O mixtures, from ref. [26]).

(9.4×10^8 cm^3 (s mol $Pd_{surface}$)$^{-1}$, 200 SiO_2/catalyst intraparticle dilution ratio, 280 quartz/catalyst interparticle dilution ratio; see ref. [1] for reaction conditions in CH_4-CO_2/H_2O mixtures)

[1] Yamaguchi, A; Iglesia, E., *J. Catal.* **2010***, 274*, 52.

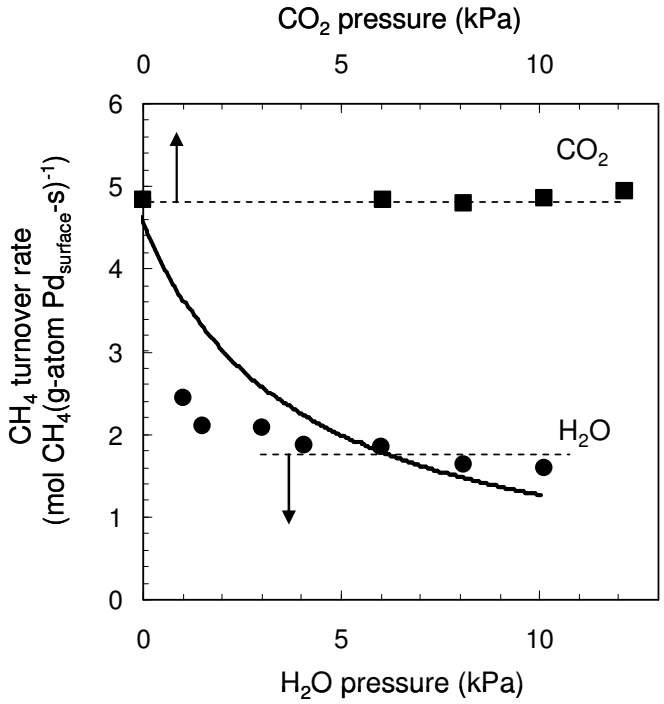

Figure 6. H_2O (●) and CO_2 (■) pressure effects on CH_4 turnover rates during CH_4-O_2-H_2O (●) or $^{13}CH_4$-O_2-CO_2 (■) reactions on a 0.2 % wt. Pd/Al_2O_3 (21.3 nm mean Pd cluster diameter) catalyst at 873 K. The solid line describes the fit from linear regression of rate data with a rate equation (Equation 8) derived from assumptions of equilibrated H_2O and O_2 adsorption-desorption steps and irreversible C-H bond activation on O*-O* pairs.

(CH_4-O_2-H_2O (●): 0.4 kPa O_2, 4.9 kPa CH_4; $^{13}CH_4$-O_2-CO_2 (■): 1.6 kPa O_2, 4.9 kPa CH_4; 1.57×10^9 cm^3 (s mol $Pd_{surface}$)$^{-1}$, 200 SiO_2/catalyst intraparticle dilution ratio, 450 quartz/catalyst interparticle dilution ratio)

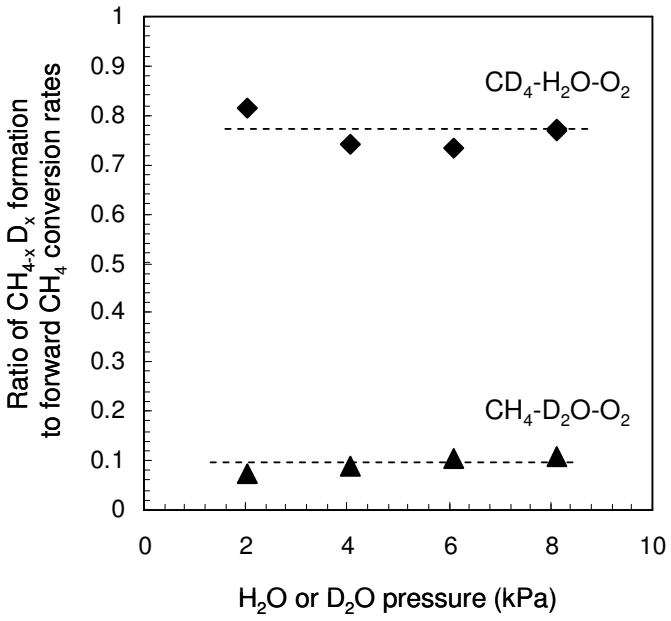

Figure 7. Ratio of CH_xD_{4-x} formation to forward CH_4 conversion rates in CH_4-D_2O-O_2 (▲) or CD_4-H_2O-O_2 (♦) mixtures at 873 K on a 0.2 % wt. Pd/Al_2O_3 (21.3 nm mean Pd cluster diameter) catalyst.

(4.9 kPa CH_4 or CD_4, 1.6 kPa O_2, 2.35×10^8 cm^3 (s mol $Pd_{surface}$)$^{-1}$, 50 SiO_2/catalyst intraparticle dilution ratio, 350 quartz/catalyst interparticle dilution ratio).

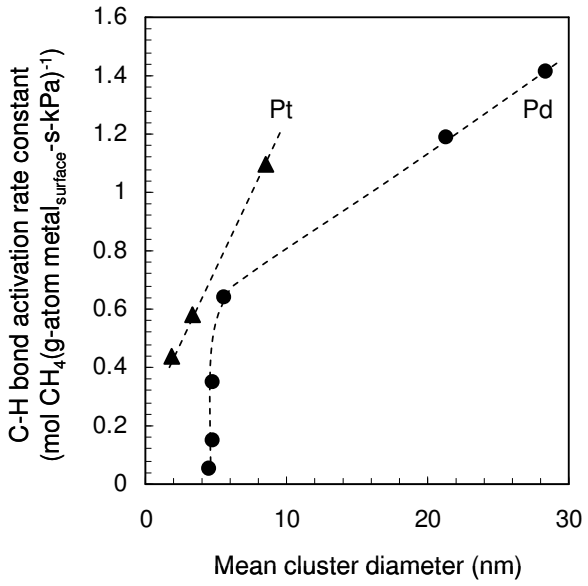

Figure 8. Cluster size dependence of initial rate constants for C-H bond activation on O*-O* site pairs on Pd (●) and Pt clusters (▲; from ref. [2]) at 873 K.

(●: 0.2 % wt. Pd/Al_2O_3, 1.57×10^9 cm^3 (s mol $Pd_{surface}$)$^{-1}$, 200 SiO_2/catalyst intraparticle dilution ratio, 450 quartz/catalyst interparticle dilution ratio, measured within 7.2 ks after exposure to CH_4-O_2 feed mixtures; ▲: see ref. [2] for specific reaction conditions for CH_4-O_2 reactions on 0.2 % wt. Pt/Al_2O_3 catalysts).

[2] Chin, Y-H.; Buda, C.; Neurock, M.; Iglesia, E. *J. Am. Chem. Soc*. submitted.

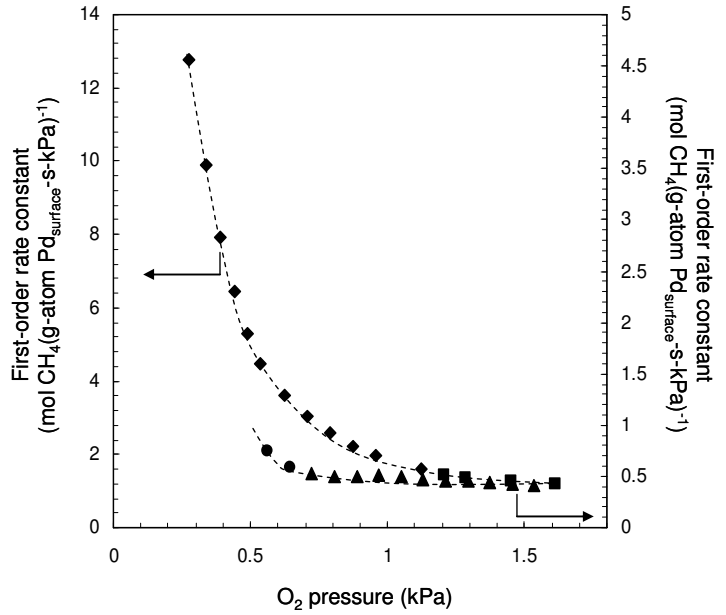

Figure 9. O_2 pressure effects on first-order rate constants ($r_{CH_4}(CH_4)^{-1}$) during CH_4-O_2 reactions on 0.2 % wt. Pd/Al_2O_3 catalysts (4.8 nm (,▲) and 21.3 nm (♦,■) mean Pd cluster diameters) at 873 K. Rate constants are inversely proportional to (♦,) and independent of (■,▲) O_2 pressure.

(0-7.2 ks, 4.85 kPa CH_4, 1.31-1.57×10^9 cm^3 (mol $Pd_{surface}$-s)$^{-1}$, 200 SiO_2/catalyst intraparticle dilution ratio, 450 quartz/catalyst interparticle dilution ratio).

4.7. Schemes

Scheme 1. A proposed sequence of elementary reaction steps for CH_4-O_2 reactions on supported Pd clusters.

	Elementary Step	Rate/ Equilibrium Constant
Step 1.1	$O_2(g) + * \rightleftharpoons O_2*$	k_{1af}, k_{1ar}
Step 1.2	$O_2* + * \rightleftharpoons 2O*$	k_{1bf}, k_{1br}
Step 2.1	$CH_4 + * + * \rightarrow CH_3* + H*$	$k_{[*-*]}$
Step 2.2	$CH_4 + O* + * \rightarrow CH_3* + OH*$	$k_{[O*-*]}$
Step 2.3	$CH_4 + O* + O* \rightarrow CH_3O* + OH*$	$k_{[O*-O*]}$
Step 3	$C* + O* \rightleftharpoons CO* + *$	k_{3f}, k_{3r}
Step 4	$CO* + O* \rightleftharpoons CO_2* + *$	$k_{CO,f}, k_{CO,r}$
Step 5	$2OH* \Rightleftharpoons H_2O* + O*$	K_{OH*}
Step 6	$H_2O* \Rightleftharpoons H_2O + *$	K_{H_2O}
Step 7	$CO_2* \Rightleftharpoons CO_2 + *$	K_{CO_2}
Step 8	$CO* \Rightleftharpoons CO + *$	$1/K_{CO}$

* denotes a surface Pd atom; $\rightarrow$, $\rightleftharpoons$, and $\Rightleftharpoons$ denote irreversible, reversible, and quasi-equilibrated steps, respectively; k_{if} and k_{ir} are the forward and reversed rate coefficients, respectively, and K_i are the equilibrium constants for the various steps (i denotes the individual steps 1.1 to 8).

4.8. Tables

Table 1. Intrapellet and bed dilution effects on CH_4 combustion turnover rates on a 0.2 % wt. Pd/Al_2O_3 (21.3 nm mean Pd cluster diameter) catalyst at 973 K.

Catalyst mass (mg)	Intrapellet dilution ratio[a] (SiO_2:catalyst)	Bed dilution ratio[a] (Quartz:catalyst)	Turnover rate[b] (mol CH_4(g-atom $Pd_{surface}$-s)$^{-1}$)
2.0	50	150	37
1.0	50	280	35
2.5	200	280	41

[a] mass ratio of diluent-to-Pd/Al_2O_3 catalyst. [b] 4.86 kPa CH_4, 1.54 kPa O_2, 2.08 cm^3 s^{-1}, time-on-stream = 3.6 ks.

Table 2. Reactive CH_4 collision probabilities ($r_{CH_4}(CH_4)^{-1}$, also the first-order rate constants) in CH_4-O_2 mixtures and C-H bond activation rate constants on metal atom site pairs (measured in CH_4-CO_2 or CH_4-H_2O mixtures) on Pd clusters at 873 K and 973 K.

Reaction mixture	Mean Pd cluster size (nm)	First-order rate constant (mol CH_4 (g-atom $Pd_{surface}$-s-kPa)$^{-1}$) 873 K	973 K
CH_4-O_2	21.3	34.6[a]	58.2[a]
CH_4-CO_2	12.5	4.0[b]	12.2[b]
CH_4-H_2O	12.5	4.3[b]	12.9[b]

[a] 0.2 % wt. Pd/Al_2O_3, 0.17 kPa O_2, 2.083 cm^3 s^{-1}, time-on-stream = 3.6 ks. [b] 1.6 % wt. Pd/ZrO_2 from ref.[3], see note in ref. [4] for the effects of cluster size.

[3] Yamaguchi, A; Iglesia, E., *J. Catal.* **2010***, 274*, 52.

[4] Elementary rate constants for C-H bond activation on *-* site pairs (step 2.1, Scheme 1) on the 21.3 nm Pd clusters are expected to be lower than the reported values on smaller Pd clusters in ref. [3] because the metal sites with larger coordination are less effective for C-H bond activation.

4.9. Supporting Information

4.9.1. Derivation of O*-to-* ratio in $^{13}CH_4$-^{12}CO-O_2 mixtures. Substituting elementary rate and equilibrium constants from Scheme 1 into the following equation (also Equation 2):

$$r_{O_2} = \nu_{CO} r_{CO} + \nu_{CH_4} r_{CH_4} \tag{S.1}$$

where ν_{CO} and ν_{CH_4} are stoichoimetric coefficients for CO and CH_4 reactions with O_2. Together with the much larger reactivities for CO than CH_4 ($r_{CO} >> r_{CH_4}$), Equation S.1 is simplified to:

$$2k_{1bf} K_{O_2} (O_2)(*)^2 - k_{CO,f} K_{CO} (CO)(O*)(*) \sim 0 \tag{S.2}$$

which can be rearrange to give

$$\frac{(O*)}{(*)} \sim \frac{2k_{1bf} K_{O_2}}{k_{CO,f}} \frac{(O_2)}{(CO)} \tag{S.3}$$

which is Equation 3. The definition of the thermodynamic and rate constants is provided in Scheme 1.

4.9.2. Derivation of O* selectivities in $^{13}CH_4$-^{12}CO-O_2 mixtures assuming that C-H bond activation occurs on O*-* site pairs. Assuming that C-H bond activation occurs predominantly on O*-* site pairs (with the elementary rate constant $k_{[O*-*]}$, step 2.2, Scheme 1), the rates of CH_4 conversion (r_{CH_4}) are:

$$r_{CH_4} = k_{[O*-*]} (CH_4)(O*) \frac{(*)}{L} \tag{S.4}$$

where L denotes the total number of sites on Pd surfaces. Substituting Equation S.4 into the O* selectivity expression (Equation 1) leads to the expression:

$$O* \text{selectivity} = \frac{r_{CO} (CO)^{-1}}{r_{CH_4} (CH_4)^{-1}} = \upsilon_{O*} \frac{k_{CO,f} K_{CO} (O*)(*)}{k_{[O*-*]} (O*)(*)} = \upsilon_{O*} \frac{k_{CO,f} K_{CO}}{k_{[O*-*]}} \tag{S.5}$$

where υ_{O*} is the ratio of stoichoimetric coefficients for O_2 reactions with CO and CH_4.

4.9.3. Estimation of maximum CO yields from oxygen selectivity values using mole balances in plug-flow reactors. Assumptions of exclusive CO formation from CH_4 conversions and first-order dependence for CH_4 and CO oxidation lead to mole balances for CO and CH_4 in plug-flow reactor models:

$$\frac{d(y_{CH_4})}{d\tau} = r_{CH_4} = -k_{[*-*]} (CH_4) \tag{S.6}$$

$$\frac{d(y_{CO})}{d\tau} = r_{CO} = -k_{CO,f} K_{CO} (CO) + k_{[*-*]} (CH_4) \tag{S.7}$$

where y_{CH_4} and y_{CO} are the mole fractions of CH_4 and CO, respectively, τ is the molar ratio of exposed Pd atoms to total inlet molar rates, and rate and equilibrium constants are defined in Scheme 1. The CO yield at a given value of τ is given by:

$$\frac{y_{CO}}{y_{CH_4,0}} = \frac{k_{[*-*]}}{k_{CO,f} K_{CO} - k_{[*-*]}} \left(\exp(-k_{[*-*]} \tau) - \exp(-k_{CO,f} K_{CO} \tau) \right) \tag{S.8}$$

The maximum CO yield { $\left(y_{CO} / y_{CH_4,0} \right)_{max}$ } is then given by solving Equation (S.8) for the τ at the maximum CO yield, τ_{max}:

$$\tau_{max} = \frac{1}{k_{CO,f}K_{CO} - k_{[*-*]}} \ln\left(\frac{k_{CO,f}K_{CO}}{k_{[*-*]}}\right) \quad \text{(S.9)}$$

and substituting into Equation (S.8) to give the maximum attainable CO yield:

$$\left(\frac{y_{CO}}{y_{CH_4,0}}\right)_{max} = \frac{1}{\alpha - 1}\left(\exp\left(-\frac{1}{\alpha - 1}\ln(\alpha)\right) - \exp\left(-\frac{1}{1-\left(\frac{1}{\alpha}\right)}\ln(\alpha)\right)\right) \quad \text{(S.10)}$$

where α is given by

$$\alpha = \left(\frac{k_{CO,f}K_{CO}}{k_{[*-*]}}\right) \quad \text{(S.11)}$$

Equation (S.10) gives maximum CO yields of 0.08-2.7 % for the range of measured O* selectivities in Figure 2 (36-1300).

4.9.4. Equilibrium oxygen contents of Pd clusters (5.9 nm mean Pd cluster diameter) at 873 K. Figure S-1 shows the equilibrium oxygen contents of Pd clusters (2 % wt. Pd/Al_2O_3) at 873 K over a range of O_2 pressures (1-30 kPa). At O_2 pressures below 7.5 kPa, the O* contents, expressed as oxygen-to-Pd atomic ratios, remain relatively constant at 0.18 but increase markedly above 7.5 kPa O_2. The increase indicates O* dissolution into the bulk of the Pd clusters and the formation of PdO above 30 kPa O_2 pressures, reaching an oxygen-to-Pd atomic ratio of 0.98 at 25 kPa O_2.

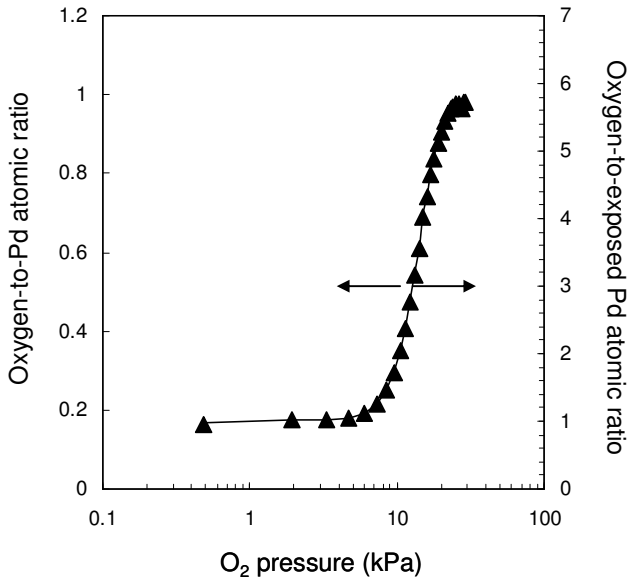

Figure S-1. Equilibrium oxygen contents, expressed as oxygen-to-Pd atomic ratios and oxygen-to-exposed Pd atomic ratios, on 5.9 nm Pd clusters (2 % wt. Pd/Al_2O_3) at 873 K.

4.9.5. Derivation of rate expression for C-H bond activation on O*-O* site pairs on Pd cluster surfaces nearly saturated with OH* species. Kinetically-relevant C-H bond activation steps on O*-O* site pairs, quasi-equilibrated O_2 and H_2O adsorption-desorption steps, together with pseudo steady-state assumptions of reactive intermediates in Scheme 1, lead to a CH_4 conversion rate equation:

$$r_{CH_4} = \frac{k_{[O^*\text{-}O^*]}(CH_4)K_{O_2}(O_2)}{\left(1 + \sqrt{K_{O_2}(O_2)} + \sqrt{\frac{(H_2O)\sqrt{K_{O_2}(O_2)}}{K_{H_2O}K_{OH^*}}}\right)^2} \qquad \begin{matrix} \downarrow & \downarrow & \downarrow \\ * & O^* & OH^* \end{matrix} \tag{S.12}$$

The rate and equilibrium constants are defined in Scheme 1. Each of the terms in the denominator denotes the relative abundance of *, O*, or OH* species, respectively, relative to the * species. When OH* and O* are the most abundant surface intermediates, rate equation (S.12) is simplified:

$$r_{CH_4} = \frac{k_{[O^*\text{-}O^*]}(CH_4)K_{O_2}(O_2)}{\left(\sqrt{K_{O_2}(O_2)} + \sqrt{\frac{(H_2O)\sqrt{K_{O_2}(O_2)}}{K_{H_2O}K_{OH^*}}}\right)^2} \tag{S.13}$$

which is also Equation 8.

Chapter 5:
Catalytic Consequences of Phase Transition between Metal and Oxide: Methane Activation on Pd, Oxygen Covered Pd, and PdO Clusters and Surfaces

Abstract

Kinetic, isotopic, and density functional theory calculations are used to probe the mechanism and structural requirements for CH_4 conversions on Pd clusters of different chemical states and surface site structures. Initial activation of C-H bond in CH_4 is the kinetically-relevant step on Pd, oxygen saturated Pd, or PdO cluster surfaces, but occurs via mechanistically different routes of oxidative addition, oxidative addition and H abstraction, or H abstraction on metal atom (*-*), oxygen atom (O*-O*), or metal atom-lattice oxygen (Pd_{ox}-O_{ox}) site pairs, respectively. Activation enthalpy and entropy requirements for the formation of the C-H bond activated complexes on these surfaces differ markedly and depend on both the availabilities of surface Pd atoms for stabilization of CH_3 fragments and O atoms for H abstraction at the transition states. On oxygen covered Pd metal clusters, C-H bond activation proceeds via a route that exhibits high activation enthalpy and entropy; the transition state is highly mobile with CH_3 fragments remain largely unbound in a radical-like structure. On stable PdO surfaces, which terminate with lattice oxygen atoms (O_{ox}), Pd^{2+} (denotes as Pd_{ox}) atoms are inherently exposed between the rows of lattice oxygen atoms. The Pd_{ox} atoms provide landing sites for CH_3 fragments and aid with the C-H bond activation via oxidative insertion of the Pd atoms into the C-H bond, as also found for C-H bond activation on metal atom site pairs. In oxidative insertion steps on uncovered Pd metal and PdO surfaces, strong Pd-C (or Pd_{ox}-C) and Pd-H (or Pd_{ox}-H) interactions result in tight transition states with activation enthalpies significantly lower than those of O*-O* pairs. Metal-lattice (Pd_{ox}-O_{ox}) oxygen site pairs that are prevalent on PdO surfaces dissociate the C-H bond more effectively than the *-* sites, because the O_{ox} atoms of the Pd_{ox}-O_{ox} pairs assist with the H abstraction step during the oxidative insertion of Pd_{ox} into the C-H bond. Interpretation of measured and theoretically determined free energy differences among the various C-H bond activation transition state complexes indicate that both catalytic functions of metal and oxygen influence the C-H bond activation paths and the tightness of the transition states, and in turn, the required activation enthalpy and entropy. These thermodynamic properties of the transition states compensate with each other, but the significant extent of CH_3 stabilization on PdO cluster surfaces leads to much larger CH_4 conversion rates on oxide than on metal and oxygen covered metal clusters.

5.1. Introduction

Phase transitions (metal-oxide, metal-sulfide, and metal-nitride) of bulk catalyst structures during catalysis occur in response to changing chemical potentials and temperatures of the contacting fluid phase; the bulk phase transitions lead to commensurate changes in active site structures and their chemical states, leading to marked reactivity changes in methane oxidation,[1] hydrodesulfurization,[2,3] and Fischer-Tropsch[4] reactions. Pd-PdO interconversions, which occur during CH_4 oxidation reactions, have remained as one of the most studied phase transfer phenomena in

catalysis. PdO decomposition has led to a curious decrease in rates with increasing temperature while the reverse step of Pd oxidation has led instead to an increase in rates with decreasing temperature.[5] These unusual rate dependencies on temperatures cause the apparent activation barriers for CH_4 combustion reactions to exhibit negative values.[5] Much effort has been spent to correlate the bulk chemical states and the surface catalytic reactivities; yet details in the active site structures on metal and oxide surfaces and their kinetic requirements for CH_4 oxidation have not been unequivocally resolved. The Pd-to-PdO phase transition has been shown to cause the prevalent hysteresis in CH_4 oxidation rates with temperatures,[6,7] which has further complicated the interpretations of phase transition and the catalytic consequences. Specific answers to the questions of how do bulk phase transition and structural changes alter the surface site structures, kinetically-relevant steps, and the associated kinetic requirements are required to rigorously compare the reactivities of metal and oxide clusters and to draw an unequivocal conclusion on which chemical state is more effective for CH_4 oxidation reactions.

We have recently established elementary reaction steps and their kinetic relevance for CH_4 oxidation on metallic Pd[8] and Pt[9] cluster surfaces covered with chemisorbed oxygen atoms to different extents. Our studies have shown that the identities of the kinetically-relevant step and surface sites vary with the relative abundance of oxygen atoms and oxygen vacancies on metal cluster surfaces. Here, we report distinct kinetically-relevant C-H bond activation paths and their kinetic requirements on uncovered Pd metal, O* saturated Pd metal, and Pd oxide surfaces, using a combined kinetic and density functional theory studies. Activation enthalpies and entropies required for the formation of transition state complexes differ markedly among the C-H bond activation path, depending on the involvements of oxygen atoms and Pd sites. C-H bond activation may proceed via an oxidative insertion step, a combined oxidative insertion and H abstraction step, or a H abstraction step on uncovered Pd metal, O* saturated Pd metal, or Pd oxide surfaces, respectively. When oxygen atoms are involved in assisting the C-H bond activation step, their reactivity is correlated with the oxygen basicity, also their affinity towards H atoms. As Pd sites prevail as Pd or Pd^{2+} on Pd metal or PdO surfaces, respectively, these Pd sites assist the C-H bond activation steps that involve an oxidative insertion of the Pd into the C-H bond. Details of the various C-H bond activation paths and characterizations of their transition state properties afford a rigorous comparison of CH_4 oxidation reactivities among metal, O* saturated metal, and oxide surfaces. Details on Pd-PdO interconversions during CH_4 turnovers have also been examined under conditions of strict thermodynamic and oxygen chemical equilibrium,[10] where transports of oxygen atoms between the gas phase and the bulk of Pd clusters are unimportant; these results are reported elsewhere.

5.2. Methods

5.2.1. Catalyst synthesis. 0.2 % wt. Pd/Al_2O_3 catalysts were prepared by incipient wetness impregnation of a Pd precursor solution (Aldrich, 99.999 % purity, 10 % wt. $Pd(NO_3)_2$ in 10 % wt. HNO_3) on γ–Al_2O_3 support (Sasol North America Inc., Lot#C1643, 193 $m^2\ g^{-1}$, 0.57 $cm^3\ g^{-1}$ pore volume), which was heated in flowing dry air at 1073 K (Praxair, zero grade, 0.083 K s^{-1}, 60 $cm^3\ g^{-1}$) for 5 h. The samples were dried in ambient air at 383 K for at least 4 h, and treated in flowing dry air (Praxair, zero grade, 60 $cm^3\ g^{-1}$)

to 623 K (0.033 K s^{-1}) for 3 h and to 1073 K (0.083 K s^{-1}) for 10 h before cooling to ambient temperature. The samples were treated in flowing H_2/He mixture (5 kPa H_2, Praxair, UHP grade H_2 and He, 60 cm^3 g^{-1}) to 1023 K (0.083 K s^{-1}) and hold for 5 h, cooled in He, and in flowing O_2/He (0.5 % O_2/He, Praxair, Certified Standard, 30 cm^3 g^{-1}) for 2 h at ambient temperature. The prepared powders were diluted with SiO_2 (Davison Chemical, Grade 923, CAS no. 112926-00-8, 280 m^2 g^{-1}) supports at a diluent-to-catalyst mass ratio of 200, pelletized, and then sieved to retain 106-250 m aggregates. The fraction of exposed Pd atoms was determined from uptakes of irreversibly chemisorbed O_2 at 313 K using volumetric adsorption measurements (Autosorb-1, Quantachrome) after treating the catalyst sample at 673 K in H_2 (30 cm^3 g^{-1}) for 2 h. The average cluster size was estimated from assuming hemispherical Pd clusters with a bulk Pd metal density of 12.0 g cm^{-3}.[11]

5.2.2. Steady-state catalytic rate measurements. Catalyst aggregates (0.12-0.5 g of the Pd/Al_2O_3 and SiO_2 mixtures) were physically mixed with quartz (Fluka, acid purified, product number 84880, 106-250 m diameters) at a quartz diluent-to-Pd/Al_2O_3 mass ratio in the range of 200-1200. The mixture was supported on a quartz frit inside a tubular packed-bed quartz reactor (inner ID=8.1 mm) with plug flow hydrodynamics. Catalyst temperatures were monitored with a K-type thermocouple, which was contained in a quartz thermowell and placed in the center of the catalyst bed. The sample was treated in H_2/He (5 kPa, 1.67 cm^3 s^{-1}, 0.083 K s^{-1}) to the reaction temperature (800-975 K), and then in flowing He (1.67 cm^3 s^{-1}) at that temperature before introduction to reactant mixtures.

Reactant mixtures were prepared from 25 % CH_4/He (Matheson, Certified Plus grade), O_2 (Praxair, UHP grade) or 5 % O_2/He (Praxair, Certified Standard grade), and He (Praxair, UHP grade) by metering the gas flows using electronic mass flow controllers (Porter 201). The concentrations of CH_4, O_2, and CO_2 in the reactant and product streams were quantified using gas chromatography (Agilent 3000A Micro GC) with modules containing Poraplot Q or Mol Sieve 5A columns and thermal conductivity detectors.

CH_4 turnover rates were calculated from the rates of CO_2 formation normalized by the number of exposed Pd atoms in the catalyst bed. Heat and mass transport corruptions on measured rates within catalyst pellets and the reactor bed were ruled out based on the Koros-Nowak criterion,[12] as reported elsewhere.[8]

5.2.3. Ab initio density functional theory calculations of C-H bond activation in CH_4 on Pd(111), oxygen saturated Pd(111), and PdO(101) surfaces. Geometries and energies of atomic oxygen adsorption on Pd(111) surfaces and of reactant, transition state, and product for C-H bond activation in CH_4 on Pd(111), oxygen saturated Pd(111), and PdO(101) surfaces, were calculated using Perdew Wang 91 (PW91)[13] functional form of the generalized gradient approximation (GGA) implemented in the Vienna Ab-initio Simulation Package (VASP).[14,15,16] A gamma centered Monkhorst-Pack with (3×3×1) subdivisions of the Brillouin zone was used to describe the k-point mesh[17] for Pd(111) and PdO(101) surfaces. Wavefunctions were constructed using a periodic plane wave expansion and a kinetic energy cutoff of 396 eV; ultra-soft Vanderbilt pseudopotentials (US-PP)[18] were used to describe the interactions between core and valence electrons. The threshold of electronic energy relaxations within the self consistent loop was set to 10^{-4} eV, while the forces on each atom were optimized to < 0.5 eV nm^{-1}. A 3×3 unit cell consisting of four Pd atom layers and nine Pd atoms per layer was used to model Pd(111)

surfaces; the Pd surfaces were separated by a 10 Å vacuum slab. The lowest two layers of Pd atoms were kept frozen, while the top two were fully optimized along with all atomic or molecular fragments that interact with the metal surfaces. Geometries and energies for sequential oxygen adsorption on Pd(111) surfaces were optimized for 0.11 to 1 ML oxygen coverages (which correspond to 1 and 9 oxygen atoms, respectively, in a 3×3 unit cell with oxygen atoms adsorbed at fcc sites). All possible atomic configurations at each oxygen coverage were investigated and only the most stable oxygen adsorption configuration was considered as the starting point for the higher coverage.

Activation of the C-H bond in CH_4 was analyzed on the various Pd_{ox}-O_{ox} and O_{ox}-O_{ox} site pairs (O_{ox} and Pd_{ox} denote the lattice O^{2-} and Pd^{2+} atoms, respectively) on PdO(101) surfaces, because this surface termination has one of the lowest surface free energies among the PdO surfaces.[19] A 3×3 PdO unit cell containing nine atomic layers was used with a 10Å vacuum region separating the oxide slabs. Pd and O atoms at the lowest three layers of the PdO(101) systems were kept frozen at their initial lattice position in all calculations, while the remaining layers were fully optimized along with surface atomic or molecular fragments using the convergence criteria described above for Pd(111) systems.

Intermediate images at equal spacing between the reactant and product states were generated and optimized along the reaction coordinate using nudged-elastic band (NEB) approach.[20] Subsequently, the climbing image-nudged elastic band (CI-NEB) method was used to locate the saddle point, which is the transition state of the reaction.[21,22,23]

5.3. Results and Discussion

5.3.1. Kinetically-relevant steps for CH_4-O_2 reactions on Pd and PdO cluster surfaces. Kinetically-relevant steps for CH_4 oxidation are established here over a range of oxygen chemical potentials that led to bulk Pd in either metal or oxide phase at 873 K. Figure 1 shows the O_2 pressure dependence of reactive CH_4 collision probabilities, also the first-order rate constant ($r_{CH_4}(CH_4)^{-1}$), on a 0.2 % wt. Pd/Al_2O_3 catalyst (21.3 nm mean Pd cluster diameter) at low CH_4 conversions (< 1.5 %) and conditions that led to stable rates and selectivities.[24] CO and H_2 were undetected before the near complete O_2 consumption. $^{13}CH_4$-^{12}CO-O_2 reactions gave larger reactive collision probabilities for CO oxidation than for CH_4 oxidation.[8] These results have confirmed the almost exclusive oxygen selectivities towards CO_2 (and H_2O) at all non-zero O_2 pressures, as also found here for CH_4-O_2 reactions on Pd oxide clusters at high O_2 pressures (up to 73 kPa O_2, 873 K).

Reactive CH_4 collision probabilities initially remained at constant values (0.53 mol CH_4 (g-atom $Pd_{surface}$-kPa-s)$^{-1}$, 873 K)) for O_2 pressures up to 1.75 kPa (Figure 1). The constant reactive CH_4 collision probabilities reflect first-order CH_4 and zero-order O_2 dependencies (Figure 2a). These rate dependencies, together with normal C-H/C-D kinetic isotope effects (KIE=2.01, 873 K; Table 1), are consistent with the initial activation of a C-H bond in CH_4 as the kinetically-relevant step. The C-H bond activation step occurs on metallic Pd cluster surfaces saturated with chemisorbed oxygen atoms (O*), confirmed from an O_2 uptake value, expressed as the atomic O-to-exposed Pd ratio, of near unity (1.06; 873 K) within the same oxygen chemical potential range, as reported elsewhere.[8] As O_2 pressure increased above 3 kPa, the reactive CH_4 collision probabilities

increased markedly, reaching a larger value (12.9 mol CH_4 (g-atom $Pd_{surface}$-kPa-s)$^{-1}$, 873 K) and maintaining at that value over a wide range of O_2 pressure (16-73 kPa; Figure 1). This marked increase in reactive CH_4 collision probabilities reflects the bulk oxidation of Pd to PdO structures, the details of which have been reported elsewhere.[10] Upon bulk Pd oxidation, kinetic dependence of CH_4 conversion turnover rates on CH_4 and O_2 pressures (Figure 2b) and C-H/C-D kinetic isotope effects (KIE=1.99, 873 K; Table 1) remained identical to those on O* saturated metallic Pd clusters. These kinetic dependencies led to constant reactive CH_4 collision probabilities on oxygen saturated metal $\{ r_{CH_4}(CH_4)^{-1}\big|_{Pd} \}$ or oxide $\{ r_{CH_4}(CH_4)^{-1}\big|_{PdO} \}$ cluster surfaces:

$$\left.\frac{r_{CH_4}}{(CH_4)}\right|_{Pd\text{ or }PdO} = k_{C-H,Pd\text{ or }PdO}(O_2)^0 \qquad (1)$$

where $k_{C-H,Pd}$ and $k_{C-H,PdO}$ reflect the C-H bond dissociation rate constants on O* covered metallic Pd and PdO cluster surfaces, respectively. The larger C-H bond dissociation rate constants on PdO than on O* covered metallic clusters ($k_{C-H,PdO}$ =12.9 mol CH_4 (g-atom $Pd_{surface}$-kPa-s)$^{-1}$ vs. $k_{C-H,Pd}$ =0.53 mol CH_4 (g-atom $Pd_{surface}$-kPa-s)$^{-1}$ for PdO and Pd, respectively, at 873 K) suggest more effective C-H bond activation steps and a lower activation free energy required for the formation of the C-H bond activation transition state complex on oxide surfaces. The rate constants for C-H bond activation on PdO surfaces were also higher than for similar steps on Pd metal atom (*-*) site pairs, previously determined in CH_4-H_2O/CO_2 mixtures (4.0 and 4.3 mol CH_4 (g-atom $Pd_{surface}$-kPa-s)$^{-1}$ for CO_2 and H_2O, respectively, at 873 K; 12.5 nm Pd clusters).[25] Density functional theory calculations are used next to determine the geometries of reactant, transition, and product states and their energies in these mechanistically distinct C-H bond activation steps occurred over uncovered Pd(111), O* saturated Pd(111), and PdO(101) surfaces.

5.3.2. Kinetically-relevant C-H bond activation steps over Pd metal atom site pairs and O*-O* site pairs on Pd(111) surfaces. Initial C-H bond activation of CH_4 was examined on uncovered and oxygen saturated metallic Pd(111) surfaces. The C-H bond activation over metal atom site pairs occurs via oxidative insertion of Pd atom into the C-H bond, forming a three-centered Pd-C-H transition state (structure **3b**, Figure 3) with an activation barrier of 73 kJ mol^{-1}. The C-H bond is stretched (from 0.109 to 0.155 nm) as the Pd atom interacts with both the C and H bond (bond distances for Pd-C and Pd-H are 0.219 nm and 0.169 nm, respectively, at the transition state), as also found for C-H bond activation over a single metal atom,[26,27] other transition metals (cubo-octahedral Pt clusters,[28] Rh(111),[29] Ir(111)[30]), and organometallic complexes ($Pd(PH_3)_2$[31]).

On Pd surfaces saturated with oxygen atoms, activation of C-H bond must occur at O*-O* sites in the absence of oxygen vacancies (*; also the exposed Pd atoms). The saturation coverage is defined as the coverage at which the differential heat of atomic oxygen adsorption is zero and adsorption of additional O* atoms would lead to energetically unstable structures (enthalpy of O* adsorption, $H_{O^*,\,ads} > 0$ kJ mol^{-1}). The saturation coverage on Pd(111) surfaces was found to contain 6 oxygen atoms in the Pd(111) 3×3 unit cell and each surface Pd atom is connected with two oxygen atoms. On

such surfaces, chemisorbed oxygen atoms prefer to reside at three-fold fcc sites on Pd(111) facets,[32] as they maximize their distance and reduce their lateral repulsive interactions, as also found for atomic oxygen adsorption on Pt(111),[33] Ni(111),[34] and Rh(111)[35] surfaces at high oxygen coverages.

Initial C-H bond activation occurs over oxygen atom pairs (O*-O*) vicinal to each other via an oxygen assisted H abstraction steps (Figure 4) that involve a $(O^*\text{--}\bullet CH_3\text{--}^*OH)^{\ddagger}$ transition state (structure **4b**) with an activation barrier of 145 kJ mol^{-1}. One of the O* atoms interacts with the H atom during the C-H bond activation step, resulting in a nearly formed OH* species and a nearly cleaved C-H bond at the transition state; the O and H bond distance is 0.104 nm (vs. 0.102 nm in the product state) and the C and H bond distance is 0.170 nm at the transition state (vs. 0.109 nm in the reactant state). The leaving CH_3 group is largely unattached to the surfaces and thus takes on significant radical characters, as shown from the large O*--CH_3 distance (0.258 nm) and planar CH_3 geometries that indicate a sp^2-hybridization (structure **4b**). Similar C-H bond activation paths were found for C-H bond activation in CH_4 on O* saturated Pt {(111) surfaces and cubo-octahedral Pt clusters with 201 atoms},[9] and for C-H bond activation of alkanes on V oxide surfaces,[36,37] all of which involve the formation of an unbound radical-like CH_3 fragment and high energy transition states.

The activation barriers ($\Delta E_{C\text{-}H,\,O^*/Pd}$) are interpreted in the framework of Born-Haber thermochemical cycles (Figure 4; Table 2), constructed from the homolytic C-H bond dissociation energy (BDE) of CH_4(g) and interaction energies between the O* atom and gas-phase H radical (ΔE_{O^*-H}) and between the surfaces (with the H adsorbed on one of the O*) and CH_3• radical ($\Delta E_{O^*-CH_3}$), as depicted in Figure 4:

$$\Delta E_{C\text{-}H,\,O^*/Pd} = BDE + \Delta E_{O^*-H} + \Delta E_{O^*\text{-}CH_3} \qquad (2)$$

The interactions of CH_3• with the surfaces are insignificant ($\Delta E_{O^*-CH_3}$ = -6.2 kJ mol^{-1}), thus the C-H bond activation barriers are given solely by the interaction energy between the O* and H radical (ΔE_{O^*-H} = -312.1 kJ mol^{-1}). This energy resembles the energy difference for OH* and O* adsorption on the O* saturated Pd surfaces ($\Delta E_{OH^*-O^*}$ = -321.4 kJ mol^{-1}, Table 2), because the O-H* species at the transition state are essentially formed. It also reflects the affinity of chemisorbed oxygen to H radicals, and thus is a measure of the oxygen basicity.

5.3.3. Kinetically-relevant C-H bond activation steps over Pd_{ox}-O_{ox} site pairs on PdO (101) surfaces. Next, we show that C-H bond activation on PdO surfaces occurs via an energetically favorable route that involves stabilization of CH_3 fragments at the transition state by exposed Pd atoms. Low surface energy PdO surfaces such as (101) and (110) facets contain exposed Pd rows between rows of oxygen atoms (see structures in Supplementary Information). These exposed Pd^{2+} atoms (Pd_{ox}) have remained accessible to CH_4 reactants even in the absence of oxygen vacancies. Together with vicinal lattice oxygen atoms (O_{ox}), they form Pd_{ox}-O_{ox} site pairs that activate C-H bond much more effectively than the O*-O* sites prevalent on oxygen saturated Pd(111) surfaces. We discuss here a representative case of C-H bond activation on these site pairs found on PdO (101) surfaces; specifically, we describe the involvements of exposed Pd atoms in an oxidative insertion step similar to the established mechanism for 1,2 addition on

organometallic complexes[38,39,40] and the formation of a four-center $(H_3C\text{--}Pd_{ox}\text{--}H\text{--}O_{ox})^{‡}$ transition state that is otherwise inaccessible on O* saturated Pd surfaces (Section 3.2).

The structures of reactant, transition state, and product (structures **5a**, **5b**, and **5c**, respectively) for C-H bond activation in CH_4 over Pd_{ox}-O_{ox} site pairs on PdO(101) surfaces are shown in Figure 5. The C-H bond of CH_4 elongates over Pd_{ox}-O_{ox} sites from 0.109 nm to 0.138 nm as CH_4 from the gas phase evolves into the $(H_3C\text{--}Pd_{ox}\text{--}H\text{--}O_{ox})^{‡}$ transition state (structure **5b**). This route is energetically more favorable (activation barrier, $\Delta E_{C\text{-}H,PdO}$ = 62 kJ mol^{-1}) than the same step over the O_{ox}-O_{ox} sites found on the same surfaces (196 kJ mol^{-1}) because concerted Pd_{ox}-C and Pd_{ox}-H interactions during oxidative insertion of Pd_{ox} into the C-H bond lower the transition state energies markedly. Dative-bondings between methane molecule and Pd_{ox} have been investigated from adsorption of small alkanes (C1-C3)[41] and have been estimated to lower the C-H bond activation barriers by at least 100 kJ mol^{-1}.[42] Details of the various interactions at the $(H_3C\text{--}Pd_{ox}\text{--}H\text{--}O_{ox})^{‡}$ transition state are shown in structure **5b** of Figure 5; at the transition state, the O_{ox} interacts with the H weakly (0.128 nm) while the Pd_{ox} atom inserts into the C-H bond in a concerted oxidative insertion step (C-H, Pd-C, and Pd-H bond distances are 0.138, 0.223, and 0.187 nm, respectively) to form the $(H_3C\text{--}Pd_{ox}\text{--}H\text{--}O_{ox})^{‡}$ transition state. The C-H bond activation barriers ($\Delta E_{C\text{-}H,PdO}$), as shown from the transition state energy decomposition analysis using a Born-Haber themochemical cycle (Figure 5), are affected by both the interactions between O_{ox} and H ($\Delta E_{O_{ox}-H}$=-164.1) and between CH_3 and the surfaces ($\Delta E_{Pd_{ox}-CH_3}$ = -238 kJ mol^{-1}), the latter of which reflects predominantly the interaction of CH_3 with the Pd_{ox} and the leaving H atom:

$$\Delta E_{C\text{-}H,PdO} = BDE + \Delta E_{O_{ox}-H} + \Delta E_{Pd_{ox}-CH_3} \quad (3)$$

The interaction energy between the CH_3 group and PdO(101) surface is larger (in absolute value, -238 kJ mol^{-1}) compared with the same interaction in the absence of the leaving H atom, which is coordinating to the O_{ox} site (ΔE_{CH_3} = -125.4 kJ mol^{-1}) (Table 2). This larger value reflects significant C-H interactions, as also inferred from the relatively short C-H bond length of 0.138 nm compared with those on O*-O* and *-* site pairs (0.170 and 0.155 nm, respectively) at the transition state. This significant extent of interaction among the Pd_{ox}, C, and H atoms suggests a tight transition state, consistent with the low activation enthalpy.

5.3.4. Comparison of experimentally and theoretically derived activation free energies for C-H bond activation steps over Pd, O* saturated Pd, and PdO surfaces. In this section, we interpret the measured and calculated activation free energies for the C-H bond activation paths on metal, O* saturated metal, and oxide surfaces in the framework of transition state theory. The activation free energies (ΔG^{+}) contain enthalpy (ΔH^{+}) and entropy (ΔS^{+}) components and reflect the thermodynamic properties of the C-H bond activation transition states relative to CH_4 reactants in the gas phase:

$$k_{C-H} = \kappa \frac{k_B T}{h} \exp\left(-\frac{\Delta G^{+}}{RT}\right) = \exp\left(-\frac{\Delta H^{+}}{RT} + \frac{\Delta S^{+}}{R}\right) \quad (4)$$

where κ, k_B, h, and T are the transmission coefficient, Boltzmann constant, Planck constant, and temperature, respectively. The measured temperature dependence of C-H bond activation rate constants on O*-O* and Pd_{ox}-O_{ox} pairs on metallic Pd and PdO

cluster surfaces (21.3 nm mean Pd cluster diameter), respectively, together with the C-H bond activation rate constants on *-* pairs measured in CH_4-H_2O/CO_2 mixtures (from ref. 25, 12.5 nm mean Pd cluster diameter), are shown in Figure 6. Least squares regression of the rate data gives the enthalpy and entropy components of the free energy change between the transition and reactant states, which are summarized in Table 1 together with the DFT calculated barriers.

C-H bond activation barriers are higher on cluster surfaces of metallic Pd saturated with oxygen (experiment: 158 kJ mol^{-1}, theory: 145 kJ mol^{-1}) than on uncovered Pd metal (experiment: 84 kJ mol^{-1},[25] theory(Pd(111)): 73 kJ mol^{-1}) and PdO (experiment: 61 kJ mol^{-1}, theory(PdO(101)): 62 kJ mol^{-1}). The high activation barriers reflect large enthalpy changes as CH_4 reactants evolve into the $(O^*\text{--}\bullet CH_3\text{--}^*OH)^{\ddagger}$ transition state complexes (structure **4b**), apparently because the CH_3 fragments remain largely unbound at the transition state with an endothermic adsorption energy (on the O* covered surfaces)[43] of +22.4 kJ mol^{-1} (Table 2). In contrast, C-H bond activation barriers are significantly lower on uncovered Pd and PdO cluster surfaces because of the strong interactions between the CH_3 species and the Pd (or Pd_{ox}) atoms, as shown in Figure 5 and Table 2 for the case of PdO, in which the CH_3 adsorption energy (CH_3 group in the transition state geometries, structure **5b**) on Pd_{ox} was found to be -125.4 kJ mol^{-1}. Reactivities of surface oxygen atoms (O* and O_{ox} for Pd and PdO, respectively) towards H abstraction also influence the transition state energies; these reactivities are reflected in their basicity, also the difference in adsorption energy between the OH* and O* species, $\Delta E_{OH^*-O^*}$ (or between the $O_{ox}H$ and O_{ox} species, $\Delta E_{O_{ox}H-O_{ox}}$), for metal and oxide, respectively. This energy is lower for the O_{ox} on PdO(101) surfaces than the O* on Pd surfaces (-298.9 kJ mol^{-1} (PdO) vs. -321.4 kJ mol^{-1} (Pd); Table 2). By inference, lattice oxygen atoms on PdO surfaces are less basic and form weaker bonds with the H than chemisorbed oxygen atoms on Pd metal surfaces at saturation coverage. Thus, the lattice oxygen atoms (O_{ox}) are less reactive than the chemisorbed O* (on metal surfaces) for H abstraction, most likely caused by the strong ionic O_{ox}-Pd_{ox} bonds between the oxygen and neighboring Pd_{ox} atoms that lower their electron density. In spite of the lower oxygen basicity and a less effective H abstraction step, C-H bond activation barriers were much lower on PdO surfaces, because Pd_{ox} of Pd_{ox}-O_{ox} sites binds strongly to both the C and H atoms during the oxidative insertion step in the transition state, $(H_3C\text{--}Pd_{ox}\text{--}H\text{--}O_{ox})^{\ddagger}$. During C-H bond activation, bindings of the O_{ox} atom to the H of C-H bond have withdrawn the electron densities of oxygen and have weakened the O_{ox}-Pd_{ox} bonds, thus the Pd_{ox} atom likely acquires the characters of reduced metallic center, a trend expected from the bond-order bond conservation principle, which requires that the overall binding of the O_{ox} atom to remain constant. As a result, the reduced Pd_{ox} atom is able to form stronger bonds with the C and H during the C-H bond activation steps and lower the activation enthalpy required for transition state formation.

The measured activation entropies (Table 1) reflect the entropy differences between the transition state structures and gas phase CH_4 reactants. Activation entropies (reported and compared herein and after in absolute values) for C-H bond activation were much smaller on O*-O* sites (metal) than Pd_{ox}-O_{ox} sites (oxide) and *-* sites (metal) (15, 92, and 83 J mol^{-1} K^{-1}, respectively) and also smaller than the predicted values based on the loss of a translational degree of freedom in CH_4 as the CH_4 reactant evolves into the transition state (98 J mol^{-1} K^{-1}), consistent with the unbound nature of $CH_3\bullet$ at the

transition state predicted from DFT calculations (Figure 4, structure **4b**). In contrast, activation entropies for C-H bond activation on *-* and Pd_{ox}-O_{ox} pairs were larger than on O*-O* pairs because of the tighter transition states involved in these steps (structures **3b** and **5b**, respectively). Measured and calculated thermodynamic properties of the transition state (Table 1) have both suggested that the large activation entropy for the case of oxide is compensated by the much smaller activation enthalpy as a result of the concerted Pd_{ox}-C and Pd_{ox}-H interactions (Figure 5, structure **5b**), as also the case for uncovered metal surfaces (Figure 3, structure **3b**). The enthalpy stabilization has led to much lower transition state free energies for C-H bond activation on Pd_{ox}-O_{ox} (oxide) than on O*-O* (metal) site pairs and, in turn, much larger rates on oxide than on O* covered metal surfaces (Figure 6).

C-H bond activation on oxide surfaces, which involves the insertion of Pd_{ox} from Pd_{ox}-O_{ox} site pairs into the C-H bond, is mechanistically similar to C-H bond activation on metal atom site pairs on Pd(111) and other closed-packed transition metal surfaces; the latter also involves the formation of a three-center C-Pd-H transition state and concerted M-C and M-H interactions,[44] but without oxygen assisting the H abstraction. The calculated C-H bond activation barriers were lower on Pd_{ox}-O_{ox} than *-* site pairs (62 kJ mol^{-1} vs. 73 kJ mol^{-1}, Table 1), resulted largely from the additional O_{ox}-H interactions. These barriers are consistent with the measured values (61 kJ mol^{-1} vs. 84 kJ mol^{-1} for oxide and uncovered metal surfaces, Table 1) and larger rate constants for C-H bond activation on oxide than on uncovered metal surfaces over the entire temperature range (800-973 K; Figure 6).

The lattice oxygen (O_{ox}) involvement in the H abstraction step during C-H bond activation on Pd_{ox}-O_{ox} site pairs (PdO surfaces) leads to the formation of four-centered $(H_3C\text{--}Pd_{ox}\text{--}H\text{--}O_{ox})^{\ddagger}$ transition states (structure **5b**), which resemble those found for alkane oxidation on oxygen and oxygen vacancy (O*-*) site pairs on metal cluster surfaces.[9] The rate dependencies on reactant pressures, however, differ in spite of the mechanistic similarities. Unlike those on PdO surfaces (Equation 1), first-order rate constants for C-H bond activation on O*-* sites $\{ r_{CH_4}(CH_4)^{-1}\big|_{O^*-^*} \}$ were found to increase proportionally with the reductant-to-oxidant ratio on metal surfaces nearly saturated with chemisorbed oxygen atoms (as shown and derived elsewhere for Pt[9]):

$$\left.\frac{r_{CH_4}}{(CH_4)}\right|_{O^*-^*} = k_{eff,O^*-^*}\frac{(CH_4)}{(O_2)} \tag{5}$$

$$k_{eff,O^*-^*} = \frac{\left(k_{C-H,O^*-^*}\right)^2}{k_{O_2}}\,;\, E_{eff,O^*-^*} = 2E_{C-H,O^*-^*} - E_{O_2} \tag{6}$$

where k_{eff,O^*-^*} and E_{eff,O^*-^*} are the effective rate constant and barrier, respectively; k_{C-H,O^*-^*} and k_{O_2} are the rate constants and E_{C-H,O^*-^*} and E_{O_2} are the barriers for C-H bond activation on O*-* pairs and for O_2 dissociative adsorption, respectively. The dependence of rate constants on reductant-to-oxidant ratios on metal cluster surfaces nearly saturated with O* is resulted from the kinetic requirements of O* removal to create oxygen vacancies as C-H bond activation sites by the kinetic coupling of CH_4 and O_2 activation steps.[9] Relative concentrations of oxygen vacancies and oxygen atoms on such surfaces are proportional to reductant-to-oxidant ratios and the rate constant ratio of C-H

to O_2 activation ($k_{C-H,O^*-*}(k_{O_2})^{-1}$), derived from the assumptions of a pseudo steady state balance of O* and irreversible O_2 dissociation steps.[9] Thus, the effective barriers contain contributions from the activation enthalpy components of both the C-H bond (E_{C-H,O^*-*}) and O_2 dissociation (E_{O_2}) steps (Equation 6). In contrast, Pd_{ox} atoms are inherently exposed on PdO surfaces (see surface structures in Supplementary Information) and participate in the oxidative insertion step without the need of removing the lattice oxygen atoms and the associated energy penalty of generating oxygen vacancy sites.

These combined theoretical and experimental assessments on the thermodynamic properties of transition states show that active site structures and their catalytic functions mediate the C-H bond activation route, leading to characteristically different transition state geometries, activation enthalpies and entropies, manifested on the surfaces of metal, O* covered metal, and oxide clusters during CH_4 oxidation reactions. These detailed descriptions of the transition states properties and their thermodynamic requirements provide the conclusive evidence on why CH_4 activation is more effective on PdO than on Pd clusters.

5.4. Conclusions

Rate measurements in the kinetic control regime and density functional theory calculations led to quantitative description of the kinetic requirements for CH_4 oxidation on Pd metal, oxygen covered Pd metal, and Pd oxide cluster surfaces. Activation of the first C-H bond in CH_4 remains as a kinetically-relevant step on all of the cluster surfaces, but proceeds via mechanistically distinct paths. The free energy required for the formation of C-H bond activated complexes from CH_4 were measured and compared with DFT calculated values and interpreted within the framework of transition state theory. C-H bond activation on O* saturated Pd cluster surfaces occurs via an H abstraction path and involves the formation of a methyl-radical like species and a nearly formed O-H bond at the transition state. The weakly bonded nature of the methyl fragment led to high activation enthalpies, which are compensated by the low entropy losses. Detail analysis of transition state using a Born-Haber thermochemical cycle shows that the C-H bond activation enthalpy is determined largely by oxygen reactivity in the H abstraction step and thus by oxygen affinity to H, which is also the oxygen basicity. In contrast, an oxidative insertion step prevails on uncovered Pd and PdO surfaces because Pd atoms are accessible to CH_4 reactants, even on the PdO surfaces without lattice oxygen vacancies. These Pd atoms bind both C and H atoms in the transition state, thus leading to a tighter transition state with activation enthalpies significantly lower than those on O* saturated Pd cluster surfaces. For the case of PdO, lattice oxygen atoms vicinal to the Pd atoms interact weakly with H at the transition state and assist with the H abstraction step. The lattice oxygen atoms on PdO are less basic and thus less reactive for H abstraction than the chemisorbed oxygen on Pd cluster surfaces, but the involvement of Pd atoms in stabilizing the methyl fragments lowers the activation enthalpy markedly. The enthalpy gains overcome the entropy penalty and lead, in turn, to larger CH_4 oxidation rates on oxide than on metal surfaces. Oxygen basicities and metal accessibilities both dictate the C-H bond activation path and the thermodynamic properties of the transition states during the CH_4 conversions on metal and oxide clusters.

5.5. References

[1] Zhu, G.; Han, J.; Zemlyanov, D.Y.; Ribeiro, F. *J. Phys. Chem. B* **2005**, *109*, 2331.
[2] Wang, H.; Iglesia, E. *J. Catal.* **2010**, *273*, 245.
[3] Hensen, E.J.M.; Vissenberg, M.J.; de Beer, V.H.J.; van Veen, J.A.R.; van Santen, R.A. *J. Catal.* **1996**, *163*, 429.
[4] Hummel, A.A.; Wilson, A.P.; Delgass, W.N. *J. Catal.* **1988**, *113*, 236.
[5] McCarty, J.G. *Catal. Today* **1995**, *26*, 283.
[6] Datye, A.K.; Bravo, J.; Nelson, T.R.; Atanasova, P.; Lyubovsky, M.; Pfefferle, L. *Appl. Catal. A: Gen.* **2000**, *198*, 179.
[7] Farrauto, R.J.; Hobson, M.C.; Kennelly, T.; Waterman, E.M. *Appl. Catal. A-Gen.* **1992**, *81*, 227.
[8] Chin, Y-H.; Iglesia, E. *J. Phys. Chem. C*, submitted.
[9] Chin, Y-H.; Buda, C.; Neurock, M.; Iglesia, E. *J. Amer. Chem. Soc.* submitted.
[10] Chin, Y-H.; García-Diéguez M.; Iglesia, E. in preparation.
[11] David, R. L. *Handbook of Chemistry and Physics*, 87th ed.; CRC Press: Boca Raton, FL 2006.
[12] Koros R. M.; Nowak, E.J. *Chemical Engr. Sci.* **1967**, *22*, 470.
[13] Perdew, J. P.; Chevary, J. A.; Vosko, S. H.; Jackson, K. A.; Pederson, M. R.; Singh, D. J.; Fiolhais, C. *Phys. Rev. B* **1992**, *46*, 6671.
[14] Kresse, G.; Hafner, J. *Phys. Rev. B* **1994**, *49*, 14251.
[15] Kresse, G.; Furthmuller, J. *Comput. Mater. Sci.* **1996**, *6*, 15.
[16] Kresse, G.; Furthmuller, J. *Phys. Rev. B* **1996**, *54*, 11169.
[17] Monkhorst, H. J.; Pack, J. D. *Phys. Rev. B* **1976**, *13*, 5188.
[18] Vanderbilt, D. *Phys. Rev. B* **1990**, *41*, 7892.
[19] Rogal, J.; Reuter, K.; Scheffler, M. *Phys. Rev. B* **2004**, *69*, 075421.
[20] Mills, G.; Jonsson, H.; Schenter, G. K. *Surf. Sci.* **1995**, *324*, 305.
[21] Henkelman, G.; Uberuaga, B. P.; Jonsson, H. *J. Chem. Phys.* **2000**, *113*, 9901.

[22] Henkelman, G.; Jonsson H. *J. Chem. Phys.* **2000**, *113*, 9978.
[23] Sheppard, D.; Terrell, R. Henkelman G. *J. Chem. Phys.* **2008**, *128*, 134106.
[24] Stable CH_4 turnover rates were attained at extended reaction times (> 80 ks) on both the metal and oxide clusters. Refer to ref. [8] for the effects of time-on-stream on first-order rate constants during CH_4 oxidation on Pd metal cluster surfaces.
[25] Yamaguchi, A; Iglesia, E., *J. Catal.* **2010***, 274*, 52.
[26] Diefenbach, A.; de Jong, G. Th.; bickelhaupt, F. M. *J. Chem. Theory Comput.* **2005**, *1*, 286.
[27] Theodoor de Jong, G.; Geerke, D. P.; Diefenbach, A.; Matthias Bickelhaupt, F. *Chem. Phys.* **2005**, *313*, 261.
[28] Chin, Y-H.; Buda, C.; Neurock, M.; Iglesia, E. *J. Catal.* submitted.
[29] Bunnik, B.S.; Kramer, G.J. *J. Catal.* **2006**, *242*, 309.
[30] Henkelman, G.; Jónsson, H. *Phys. Rev. Lett.* **2001**, *86*, 664.
[31] Biswas, B.; Sugimoto, M.; Sakaki, S. *Organometallics*, **2000**, *19*, 3895-3908.
[32] Todorova, M.; Reuter, K.; Scheffler, M. *J. Phys. Chem. B* **2004**, *108*, 14477-14483.
[33] Pang, Q.; Zhang, Y.; Zhang, J-M.; Xu, K-W. *Appl. Surf. Sci.* **2011**, *257*, 3047-3054.

[34] Lazo, C.; Keil, F.J. *Phys. Rev. B* **2009**, *79*, 245418.
[35] Ganduglia-Pirovano, M.V.; Scheffler, M. *Phys. Rev. B* **1999**, *59*, 15533-15543.
[36] Dai, G-L.; Liu, Z-P.; Wang, W-N.; Lu, J.; Fan, K-N. *J. Phys. Chem. C* **2008**, *112*, 3719.
[37] Rozanska, X.; Fortrie, R.; Sauer, J. *J. Phys. Chem. C* **2007**, *111*, 6041.
[38] Cundari, T. R.; Grimes, T. V.; Gunnoe, T. B. *J. Am. Chem.* Soc. **2007**, *129*, 13172.
[39] Cummins, C. C.; Baxter, S. M.; Wolczanski, P. T. *J. Am. Chem.* Soc. **1988**, *110*, 8731.
[40] Cummins, C. C.; Schaller, C. P.; Van Duyne, G. D.; Wolczanski, P. T.; Chan, A. W. E.; Hoffmann, R. *J. Am. Chem.* Soc. **1991**, *113*, 2985.
[41] Weaver, J.F.; Hakanoglu, C.; Hawkins, J.M.; Asthagiri, A. *J. Chem. Phys.* **2010**, *132*, 024709.
[42] Weaver, J.F.; Hinojosa Jr., J.A.; Hakanoglu, C.; Antony, A.; Hawkins, J.M.; Asthagiri, A. *Catal Today* **2011**, *160*, 213-227.
[43] The O* atom interacting with the CH_3 group has promoted from three fold fcc site to the bridge site (at its transition state location) to interact with the CH_3 group in the CH_3 adsorption energy calculations.
[44] van Santen, R.A.; Neurock, M.; Shetty, S.G. *Chem. Rev.* **2010**, *110*, 2005-2048.

5.6. Figures

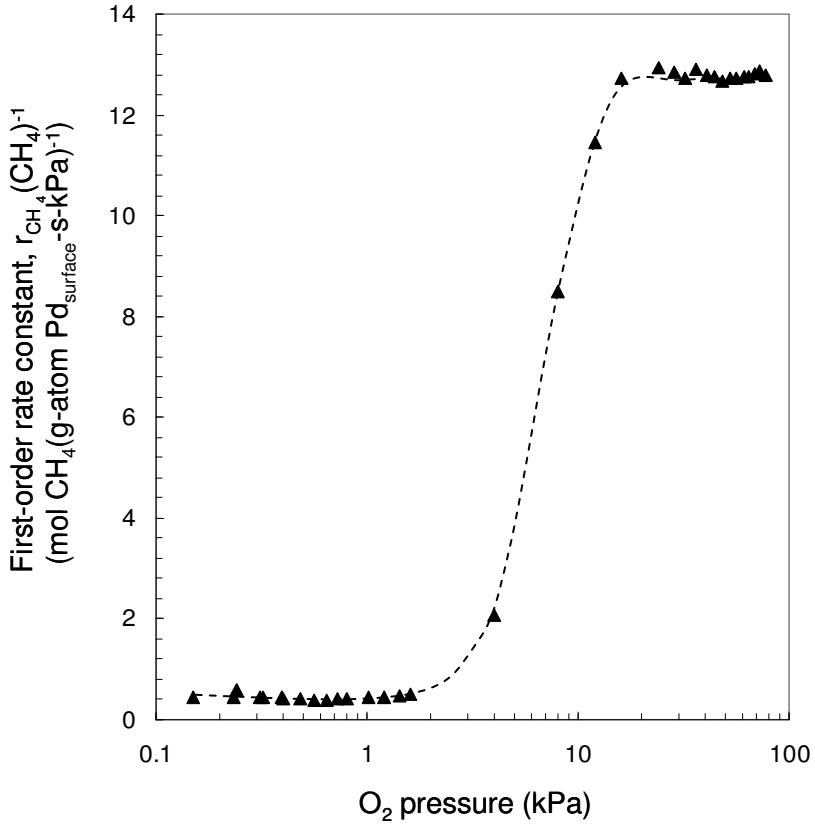

Figure 1. Oxygen pressure dependence of reactive CH_4 collision probabilities, also the first-order rate constants ($r_{CH_4}(CH_4)^{-1}$), on a Pd/Al_2O_3 catalyst (21.3 nm mean Pd cluster diameter) at 873 K.

((0.94-3.92)×10^9 cm^3 (s mol $Pd_{surface}$)$^{-1}$, 200 SiO_2/catalyst intraparticle dilution ratio, 200 and 1200 quartz/catalyst interparticle dilution ratio for O_2 pressures below and above 4 kPa, respectively)

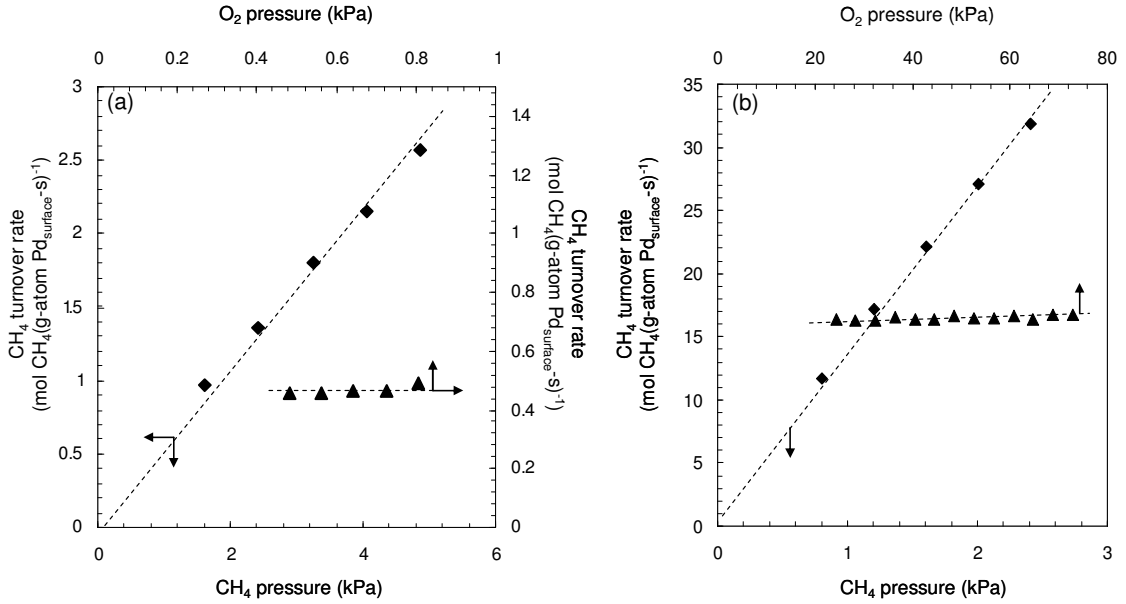

Figure 2a and 2b. Dependence of CH_4 turnover rates on CH_4 (♦) and O_2 (▲) pressures on a 0.2 % wt. Pd/Al_2O_3 catalyst (21.3 nm mean Pd cluster diameter) at 873 K at the oxygen chemical potential range[a] that led to stable bulk metallic Pd (a) or PdO (b) clusters.

([a]oxygen chemical potential is given by the O_2 pressures on metallic Pd cluster surfaces, as shown elsewhere,[1] but by the O_2/CH_4 ratios on PdO cluster surfaces because the O_2 dissociative adsorption steps are quasi-equilibrated on metallic Pd but become irreversible on PdO surfaces at 873 K; $(0.94\text{-}3.92)\times10^9$ cm^3 (s mol $Pd_{surface}$)$^{-1}$, 200 SiO_2/catalyst intraparticle dilution ratio, 200 and 1200 quartz/catalyst interparticle dilution ratio for O_2 pressures below and above 4 kPa, respectively; ♦: 0.48 kPa and 77 kPa O_2 on Pd (a) and PdO (b) clusters, respectively; ▲: 1.0 kPa and 1.2 kPa CH_4 on Pd (a) and PdO (b) clusters, respectively)

[1] Chin, Y-H.; Iglesia, E. *J. Phys. Chem. C*, submitted.

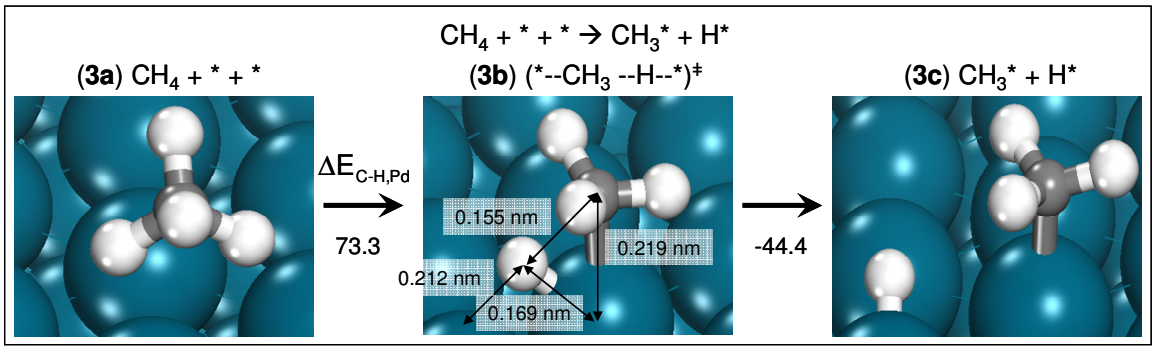

Figure 3. DFT derived structures of reactant (**3a**), transition (**3b**), and product (**3c**) states and energy changes (in kJ mol^{-1}) for C-H bond activation steps on Pd metal atom (*-*) site pairs ($CH_4 + * + * \longrightarrow CH_3 * + H *$) on Pd (111) surfaces.

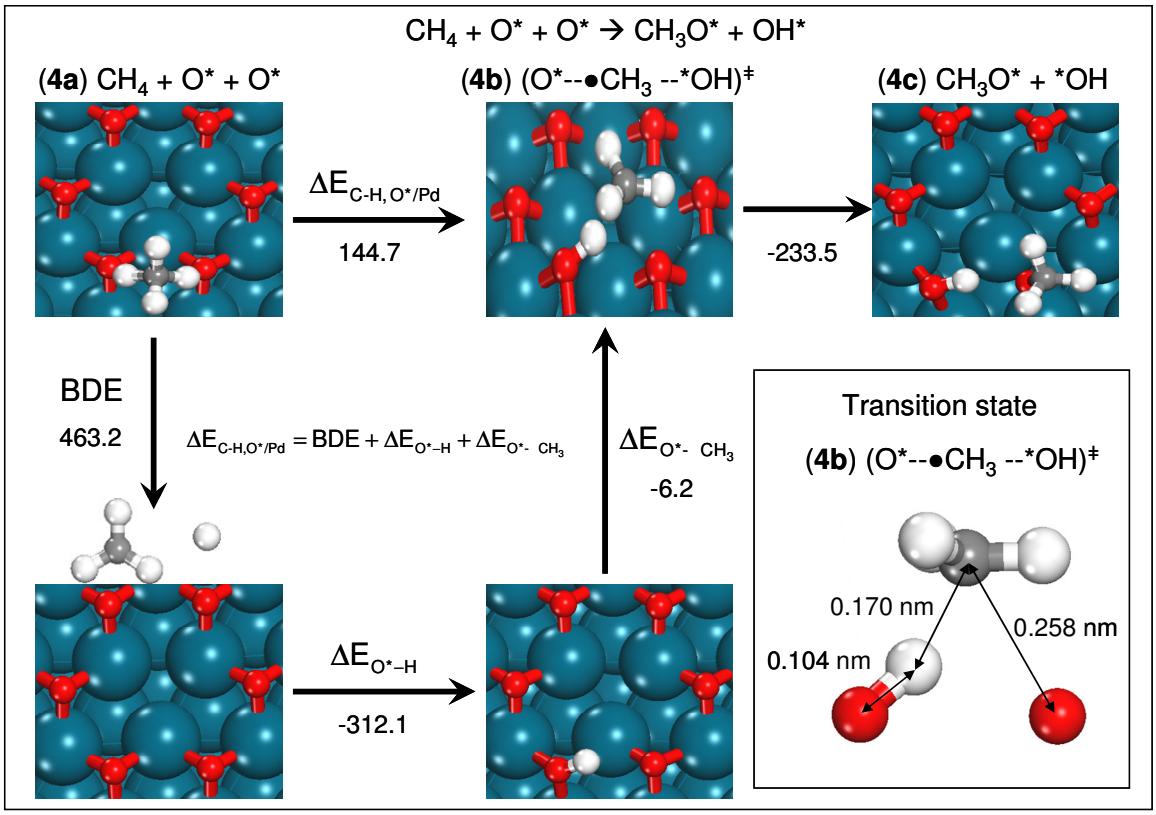

Figure 4. DFT derived structures of reactant (**4a**), transition (**4b**), and product (**4c**) states and energy changes (in kJ mol^{-1}) for C-H bond activation steps over O*-O* site pairs ($CH_4 + O* + O* \longrightarrow CH_3O* + OH*$) on Pd (111) surfaces saturated with chemisorbed oxygen atoms and Born-Haber thermochemical cycle analysis (Equation 2) of the activation enthalpies ($\Delta E_{C\text{-}H,\ O*/Pd}$). Inset: detailed transition state structures, showing only the molecular fragments and active sites involved. Blue: Pd atom, red: O atom, grey: carbon atom, white: H atom.

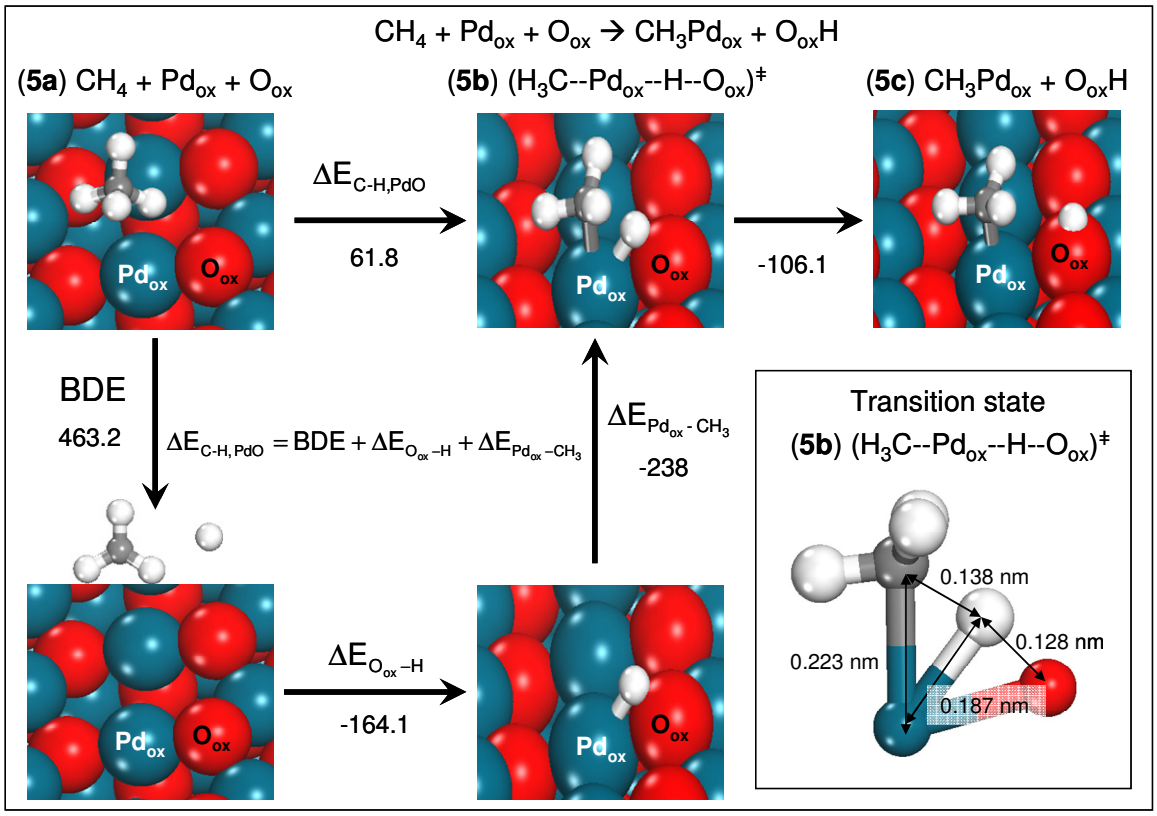

Figure 5. DFT derived structures of reactant (**5a**), transition (**5b**), and product (**5c**) states and energy changes (in kJ mol^{-1}) for C-H bond activation steps over Pd_{ox}-O_{ox} site pairs ($CH_4 + Pd_{ox} + O_{ox} \longrightarrow CH_3Pd_{ox} + O_{ox}H$) on PdO (101) surfaces and Born-Haber thermochemical cycle analysis (Equation 3) of the activation enthalpies ($\Delta E_{C\text{-}H,PdO}$). Inset: transition state structures, showing only the molecular fragments and active sites involved. Blue: Pd atom, red: O atom, grey: carbon atom, white: H atom.

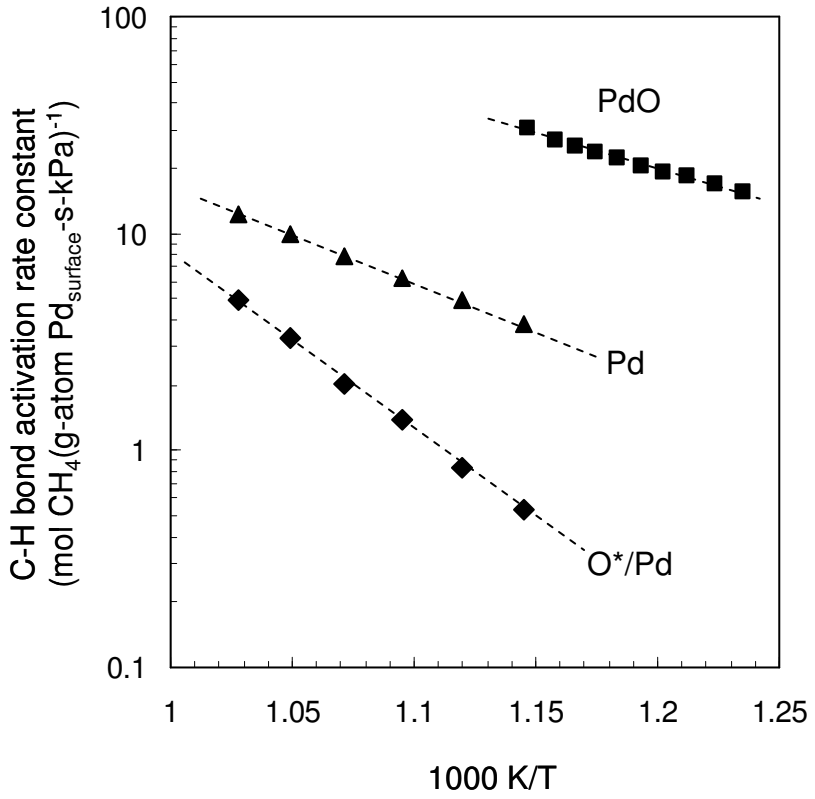

Figure 6. Temperature dependence of initial C-H bond activation rate constants in CH_4 on Pd metal (▲), oxygen saturated Pd metal (♦), and PdO (■) cluster surfaces.

(♦, ■: 21.3 nm nominal mean Pd cluster diameter, 0.2 % wt. Pd/Al_2O_3. PdO (■): 4.85 kPa CH_4, 72 kPa O_2, 3.92×10^9 cm^3 (s mol $Pd_{surface})^{-1}$, 200 SiO_2/catalyst intraparticle dilution ratio, 1200 quartz/catalyst bed dilution ratio; oxygen saturated Pd metal (♦): 4.85 kPa CH_4, 1.2-1.6 kPa O_2, 9.40×10^8 cm^3 (s mol $Pd_{surface})^{-1}$, 200 SiO_2/catalyst intraparticle dilution ratio, 280 quartz/catalyst bed dilution ratio; Pd metal (▲): rate data were taken from ref. [2], which were measured on 12.5 nm mean Pd cluster diameter, 1.6 % wt. Pd/ZrO_2)

[2] Yamaguchi, A; Iglesia, E., *J. Catal.* **2010***, 274*, 52.

5.7. Tables

Table 1. C-H/C-D kinetic isotope effects, measured kinetic parameters, and DFT-calculated energies for the initial C-H bond activation in CH_4 on Pd, O* covered Pd, and PdO.

		C-H/C-D kinetic isotope effects	Activation barrier (kJ mol^{-1})	Pre-exponential factor (experimental) (kPa^{-1} s^{-1})	Activation entropy[e] (J mol^{-1} K^{-1})	Activation barrier (theory) (kJ mol^{-1})
Pd[a]	1.6 % wt. Pd/ZrO_2 (12.5 nm Pd clusters)[d]	1.41 (823K)	84	4×10^5	83	73[f]
O*/Pd[b]	0.2 % wt. Pd/Al_2O_3 (21.3 nm Pd clusters)[d]	2.01 (873 K)	158	1.48×10^9	15	145[g]
PdO[c]	0.2 % wt. Pd/Al_2O_3 (21.3 nm Pd clusters)[d]	1.99 (873 K)	61	1.36×10^5	92	62[h]

[a]from ref. [3], measured in CH_4-CO_2 mixtures. [b]1.2-1.6 kPa O_2. [c]72 kPa O_2. [d]nominal mean cluster diameters, estimated based on Pd in metallic state with assumptions of an oxygen-to-exposed Pd atomic ratio of one and hemispherical Pd cluster shapes. [e]reported in absolute values of the entropy changes required for CH_4(g) to form the C-H bond activated transition state complexes. [f]Pd(111) surfaces. [g]O* saturated Pd(111) surfaces. [h]PdO(111) surfaces.

[3] Yamaguchi, A; Iglesia, E., *J. Catal.* **2010***, 274*, 52.

Table 2. DFT-calculated interaction energies of C-H bond activation transition state complexes and adsorption energies of H radicals on chemisorbed or lattice oxygen atoms at O*/Pd(111) and PdO(101) surfaces.

	Interaction energy ΔE_{O^*-H} [a,b] (kJ mol^{-1})	Interaction energy $\Delta E_{O^*-CH_3}$ [c,b] (kJ mol^{-1})	Interaction energy ΔE_{CH_3} [d,b] (kJ mol^{-1})	Adsorption energy $\Delta E_{OH^*-O^*}$ [e] (kJ mol^{-1})
O*/Pd(111)	-312.1	-6.2	+22.4	-321.4
	Interaction energy $\Delta E_{O_{ox}-H}$ [f,b] (kJ mol^{-1})	Interaction energy $\Delta E_{O_{ox}-CH_3}$ [g,b] (kJ mol^{-1})	Interaction energy ΔE_{CH_3} [d,b] (kJ mol^{-1})	Adsorption energy $\Delta E_{O_{ox}H-O_{ox}}$ [h] (kJ mol^{-1})
PdO(101)	-164.1	-238	-125.4	-298.9

[a]interaction energy between gas-phase H radicals and O* atoms; [b]in the transition state geometries; [c]interaction energy between the CH_3 fragments and surfaces (including the H leaving group binds to the vicinal oxygen); [d]interaction energy between the CH_3 fragments and the surfaces (with H from the cleaved C-H bond removed from the surfaces); [e]difference in OH* and O* adsorption energies. [f]interaction energy between gas-phase H radicals and O_{ox} atoms; [g]interaction energy between the CH_3 fragments and surfaces (including the H leaving group binds to the vicinal lattice oxygen). [h]difference in $O_{ox}H$ and O_{ox} adsorption energies.

5.8. Supplementary Information

Figures S1.a and S1.b show the PdO(101) surfaces at 45^{o} (a) and 60^{o} (b) views. On the surfaces, Pd atoms locate between the rows of lattice oxygen atoms and remain accessible to CH_4.

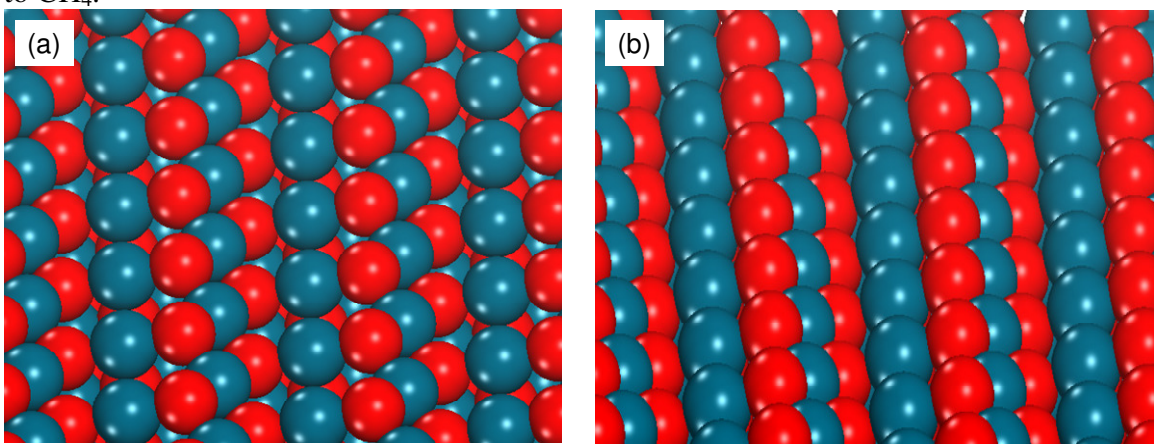

Figure S1.a and S1.b. Surfaces of PdO(101) at 45^{o} (a) and 60^{o} (b) views, where Pd (Pd_{ox}, blue) atoms reside between rows of lattice oxygen atom (O_{ox}, red).

Chapter 6:
Dynamics of Pd Oxidation and PdO Decomposition in Nanometer-sized Clusters and their Catalytic Consequences in Methane Oxidation Reactions

Abstract

Rate measurements in kinetically controlled regime were used together with oxygen uptake and evolution studies to gain insight on the Pd-PdO interconversions and establish the relation between the oxygen contents within Pd clusters and the surface reactivity for C-H bond activation in CH_4. Chemical equilibration among oxygen atoms in the gas phase, in the bulk and on the surfaces of Pd clusters is attained during CH_4-O_2 reactions at high CH_4 pressures (> 1.6 kPa CH_4, 973 K). The oxygen equilibration is confirmed from reversible Pd-PdO interconversions, in which the measured C-H bond activation rate constants on Pd cluster surfaces are independent of the previous Pd chemical state and are a strict function of the oxygen contents in the clusters.

C-H bond activation rate constants, measured under conditions of oxygen equilibration, increase with increasing O_2 pressure. This increase appears to correlate directly to the total number of oxygen atoms within the Pd clusters during Pd oxidation in O_2 (without CH_4); by inference, the oxygen atoms in the absence of CH_4 are also equilibrated with O_2(g) during Pd oxidation. The equilibrium oxygen contents of Pd clusters increase gradually as surface oxygen atoms dissolute into the bulk over a wide range of oxygen chemical potentials. The onset of oxygen dissolution depends strongly on cluster sizes and occurs at lower oxygen chemical potentials for small than large Pd clusters, indicating that the thermodynamic tendencies for bulk oxidation are higher for the small clusters. PdO decomposition follows the reverse path of Pd oxidation only at high CH_4 pressures (>1.6 kPa 973 K). At low CH_4 pressures (0-1.6 kPa; 973 K), this step occurs at much lower O_2 pressures, indicating that the decomposition step at low CH_4 pressures is a kinetically limited step. Pd-PdO phase boundaries, determined based on PdO decomposition during a decrease in O_2 pressure (without CH_4) at constant temperatures, are in agreement with previously reported values, which are consistent among the studies on Pd single crystal surfaces and clusters over a wide range of oxygen chemical potentials (from 1×10^{-10} -100 kPa O_2). These results, some of which have been used to establish the standard thermodynamic data for Pd and O_2 equilibration, have not been shown to occur reversibly. Our study has instead suggested that the PdO decomposition is a kinetically limited step, thus the "thermodynamics" properties of PdO derived from the reported data are likely not of true thermodynamic origin. In contrast, oxygen equilibration is rigorously established here during Pd oxidation based on rate and oxygen content measurements. The oxygen uptake data during Pd oxidation reflect the thermodynamics of Pd clusters at chemical equilibration.

6.1. Introduction

Nanometer-sized Pd clusters undergo metal-to-oxide interconversions during CH_4 oxidation catalysis in response to changes in oxygen chemical potential and temperature in the contacting fluid phase. The bulk Pd and PdO interconversions lead to commensurate changes in active site structures on the cluster surfaces and, in turn, to

changes in the kinetically-relevant step, effective barrier and pre-exponential factor for CH_4 oxidation reactions,[1,2] and to the hysteresis in CH_4 conversion rates observed during Pd oxidation and PdO decomposition.[3,4] Pd-PdO interconversions during catalysis have been analyzed extensively using in-situ (thermogravimetric analyses,[3] Raman,[5] X-ray diffraction,[5] temperature-programmed adsorption-desorption[6]) and ex-situ (transmission electron microscope[7]) methods, but details of the transition and their catalytic effects have not been interpreted rigorously at the atomic scale, even the transition itself has not been shown to occur reversibly at true thermodynamic and chemical equilibrium.

Lack of detailed understanding of phase transition phenomena and their catalytic consequences have rendered the modeling of catalytic combustors and their control difficult, because reactivities and kinetic parameters for CH_4 oxidation on oxide and metal surfaces differ significantly.[1, 8] The study of phase transitions during catalytic turnovers is not a trivial task because it requires an accurate assessment of oxygen chemical potentials at Pd cluster surfaces, which may depend on both the reductant and oxidant pressures,[14] and quantitative measurements of oxygen contents at thermodynamic equilibrium. Rigorous connections of equilibrium oxygen contents at surfaces and in the bulk of the clusters to catalytic reactivities also require that the rate data are obtained in the regime of strict kinetic control and thus, free of heat and mass transport corruptions prevalent in the highly exothermic CH_4 combustion reactions (ΔH^o_{rxn} = -802 kJ (mol CH_4)$^{-1}$).

Herein, CH_4 oxidation rate measurements, carried out in the regime of strict kinetic control, together with volumetric oxygen uptake and evolution measurements, are used to probe the Pd-to-PdO interconversions and their kinetic consequences at oxygen equilibration, in which the oxygen atoms in the gas phase, on the surfaces and in the bulk of Pd clusters are chemically equilibrated. In contrast to previous reports, we found that PdO decomposition, a step that is often used to obtain the thermodynamic parameters for Pd to PdO conversion, is kinetically limited. The reverse step of Pd oxidation is instead shown to occur at thermodynamic equilibrium, and the Pd-PdO interconversions become reversible in the presence of CH_4. The oxygen pressures required for the onset of Pd oxidation are lower for the smaller than larger clusters and, by inference, the oxygen content at each oxygen chemical potential is higher for the smaller clusters during the bulk Pd oxidation to PdO. These results indicate that thermodynamic tendencies for oxidation depend strongly on the relative abundance of surface and bulk Pd atoms; they increase as the cluster size decreases and surface-to-bulk Pd ratio concomitantly increases. The increase in bulk oxygen contents leads to more weakly bound surface oxygen atoms and to exposed Pd atoms, the latter assist with stabilization of the methyl groups in CH_4 at the C-H bond activation transition states, and in turn to more effective C-H bond activation steps. The catalytic effects of Pd-PdO transient are reported here while the measured and DFT calculated kinetic requirements for the C-H bond activation steps in CH_4 over O* saturated Pd and PdO surfaces are provided elsewhere.[8]

6.2. Nonequilibrium thermodynamic treatments of oxygen chemical potentials at Pd cluster surfaces and requirements of oxygen equilibration between the bulk oxygen atoms in Pd clusters and gas phase oxygen during CH_4 oxidation reactions

In this section, we show that oxygen chemical potentials at Pd cluster surfaces during steady-state CH_4 oxidation reactions, which determine the surface coverages of chemisorbed oxygen (O_s*) and thermodynamic tendencies of bulk Pd to undergo oxidation, may not depend solely on O_2 pressures but on both the CH_4 and O_2 pressures and on the kinetic properties of the reactions. We introduce oxygen virtual pressure, $(O_2)_{virtual}$, derived from nonequilibrium thermodynamic treatments of reaction elementary steps, as a rigorous surrogate of the oxygen chemical potentials and then describe the requirements of chemical equilibrium among the oxygen atoms in the gas phase, at the surfaces and in the bulk of the Pd clusters.

Oxygen virtual pressure, $(O_2)_{virtual}$, is defined as the fictitious O_2 pressure that is equilibrated with the chemisorbed oxygen atoms during steady-state catalysis (as depicted in Scheme 1):

$$(O_2)_{virtual} + 2* \longleftrightarrow 2O_s* \tag{1a}$$

$$\frac{(O_s*)}{(*)} = \sqrt{K_{O_2}(O_2)_{virtual}} \tag{1b}$$

where K_{O_2} is the equilibrium constant for the O_2 dissociation step (Equation 1a). The concept of virtual pressures has been previously established in a seminal work on NH_3 decomposition on Fe;[9,10] the theoretical framework of virtual pressures has been shown rigorously by applying the De Donder equation to elementary reaction steps within the catalytic sequence,[11] and its kinetic relevance has been demonstrated for alkane reactions[12,13] and for CH_4 oxidation on Pt clusters.[14] The reactive CH_4 collision probabilities are shown to be a single-valued function of oxygen virtual pressures during CH_4-O_2 reactions on Pt clusters because coverages of reactive $O*_s$ intermediates, which are set by the oxygen virtual pressures (via Equation 1b), dictate the predominant kinetically-relevant step for CH_4 oxidation reactions.[14]

During steady-state CH_4 oxidation reactions, the O_s*-to-* ratios in Equation 1b, the resulting $(O_2)_{virtual}$, and the oxygen chemical potentials on Pd cluster surfaces are given by kinetic coupling of rates that form and remove O_s* atoms (refer to Scheme 1):

$$r_{O_2,f} = r_{O_2,r} + 2r_{CH_4} \tag{2}$$

where $r_{O_2,f}$, $r_{O_2,r}$, r_{CH_4} are the rates of O_2 dissociation, O_s* recombination, and CH_4 conversion. Expressing the rates of O_2 activation in Equation 2 in terms of the elementary O_2 dissociation-recombination steps:

$$O_2 + 2* \rightarrow 2O_s* \qquad\qquad k_{O_2,f}, k_{O_2,r} \tag{3}$$

where $k_{O_2,f}$ and $k_{O_2,r}$ are the forward and reverse rate constants, respectively, leads to:

$$k_{O_2,f}(O_2)(*)^2 = k_{O_2,r}(O_s*)^2 + 2r_{CH_4} \tag{4}$$

Rearranging this equation gives the O_s*-to-* ratio; substitution of this ratio into Equation 1b provides the expression for $(O_2)_{virtual}$, a rigorous description of the oxygen chemical potentials at Pd cluster surfaces. This treatment of oxygen chemical potential requires describing CH_4 conversion rates in terms of elementary rate constants and pressures. We

have derived the $(O_2)_{virtual}$ expression during CH_4-O_2 reactions on oxygen covered metallic Pt clusters and showed that the $(O_2)_{virtual}$ equals to O_2 pressure in the limiting case of equilibrated O_2 dissociative-recombination steps (Equation 3) but becomes lower than the actual O_2 pressure and depends on O_2/CH_4 ratios and CH_4 and O_2 activation rate constants for irreversible O_2 dissociation steps.[14] For the latter case, the $(O_2)_{virtual}$ has become a kinetic property of the reactions. We note that the identity of elementary steps and rate constants for CH_4 and O_2 activation in Equation 4 differ for metal and oxide surfaces.[8] These changes in the elementary steps and kinetic parameters have further complicated the interpretation of O_s*-to-* ratios and $(O_2)_{virtual}$, the thermodynamic tendency of bulk oxidation, and their catalytic consequences during the Pd-PdO interconversions.

$(O_2)_{virtual}$ determines the thermodynamic tendency of bulk Pd oxidation according to the chemical equation:

$$Pd + 0.5(O_2)_{virtual} \longleftrightarrow O_s* + Pd \longleftrightarrow PdO_b \quad (5)$$

Although oxidation of Pd clusters is thermodynamically favorable ($\Delta G_{PdO} < 0$) at low temperatures (< 550 K), it is limited by the dissolution of chemisorbed oxygen (O_s*) from surfaces into the bulk.[15] As a result, the extent of bulk oxidation varies with Pd cluster diameters,[16,17] and metal and oxide may co-exist in metastable states. PdO decomposition may also be a kinetically limited step, most likely by the removal of lattice O_s* from PdO surfaces. Increasing the temperature could overcome the barriers required for O_s* dissolution, but the Pd oxidation step (Equation 5) becomes thermodynamically unfavorable because the negative entropy term ($\Delta S_{PdO}(950K) = -94.1$ J (mol-K)$^{-1}$ [18]) associated predominantly with the loss of O_2(g) entropy dominates the free energy of PdO formation.

These kinetic constraints on surface O_s* equilibration and on O_s* dissolution, together with thermodynamic constraints on the extent of oxidation, have complicated the mechanistic interpretations of Pd-to-PdO interconversions, corrupted the resulting thermodynamic parameters, and in turn, hindered the assessment of their catalytic consequences. A true equilibrium between the bulk of Pd clusters and the contacting O_2(g) in Equation 5 is established when the bulk oxygen contents at any given oxygen chemical potential are independent of the previous chemical states. This criterion, which presents the only rigorous evidence of chemical equilibrium among oxygen atoms in the gas phase, the bulk (O_b), and on the surfaces (O_s*) of Pd clusters, was seldom applied to ensure the complete removal of kinetic restrictions and that the acquired data are of true thermodynamic origin.

Herein, we show that reactive CH_4 collision probabilities, under a set of specific conditions, are independent of CH_4 pressures and thus $(O_2)_{virtual}$ and oxygen chemical potentials are defined entirely by O_2 pressure. We also show that all oxygen atoms (O_2(g), O_b, O_s*) are chemically equilibrated and thermodynamic equilibriums are established above a critical CH_4 pressure (> 1.6 kPa at 973 K) and during Pd oxidation (in O_2 and without CH_4). We then assess the Pd-PdO interconversions and their catalytic consequences under conditions that have led to the oxygen equilibration.

6.3. Experimental methods

6.3.1. Catalyst synthesis. γ–Al_2O_3 (Sasol North America Inc., Lot#C1643, 193 $m^2\ g^{-1}$, 0.57 $cm^3\ g^{-1}$ pore volume) was treated in flowing dry air (Praxair, zero grade, 1.5 $cm^3\ g^{-1}\ s^{-1}$) at 1098 K for 5 h. Pd was deposited on γ–Al_2O_3 supports by incipient wetness impregnation of an aqueous $Pd(NO_3)_2$ (Aldrich, 99.999 % purity, 10 % wt. $Pd(NO_3)_2$ in 10 % wt. HNO_3) solution to give 0.6 % wt. Pd loadings. The sample was treated in ambient air at 383 K for > 8 h, heated (at 0.033 K s^{-1}) to 623 K and held for 3 h and then to 1098 K (at 0.083 K s^{-1}) and held for 5 h in flowing dry air (Praxair, zero grade, 1.5 $cm^3\ g^{-1}\ s^{-1}$) before cooling to ambient temperature. The sample was heated in a 10 kPa H_2/He (Praxair, UHP grade H_2 and He, total flow 1.5 $cm^3\ g^{-1}\ s^{-1}$) mixture to 923 K (at 0.033 K s^{-1}) and held for 3 h, subsequently cooled to ambient temperature in flowing He (Praxair, UHP, 1.5 $cm^3\ g^{-1}\ s^{-1}$) and then exposed to flowing 0.5 kPa O_2/He (Praxair, Certified Standard, 0.5 $cm^3\ g^{-1}\ s^{-1}$) for 2 h before exposure to ambient air. The fractional dispersions were estimated from extrapolation of irreversible oxygen adsorption isotherm at 413 K to zero pressure and cluster sizes were estimated from assumptions of Pd clusters in hemispherical shapes and an O-to-surface Pd atomic ratio of one using the bulk Pd density (12.0 g cm^{-3}).[19]

6.3.2. Oxygen uptake and evolution measurements. The oxygen contents in 0.6 % wt. Pd/Al_2O_3 catalysts were determined during stepwise changes in O_2 pressure by measuring volumetric oxygen uptake and release at 973 K. The apparatus consists of a quartz tube with a fritted sample holder, a thermocouple (K-type) in contact with the outer tube wall, and a stainless steel dosing chamber (10-11 cm^3 (reactor cell) and 11.9 cm^3 (dosing chamber); 5×10^{-4} mol of gas (STP) in the total chamber) with leak rates < 3×10^{-9} mol h^{-1} at ambient temperature and < 6×10^{-9} mol h^{-1} at 973 K. Samples (1 g) were treated at 773 K in flowing 10 % H_2/He (1.33 $cm^3\ s^{-1}$, Praxair UHP grade H_2 and He, 0.033 K s^{-1} heating rate) for 1 h and evacuated for 1 h. Samples were then heated to 973 K (at 0.033 K s^{-1}) under vacuum and held for 8 h before O_2 uptake-release measurements. O_2 uptakes were measured by increasing O_2 pressures from 0.25 kPa to 90 kPa through the introduction of O_2 pulses (Praxair UHP grade; 5-10 μmol O_2 per pulse) at 5.4 ks intervals. The amount of O_2 evolved was measured by decreasing O_2 pressures stepwise from 90 to 0.15 kPa at steps correspond to 5-50 μmol O_2 at 5.4 ks intervals. Pressures were measured with a dual-range absolute pressure transducer (MKS Baratron, type D28B, 0-13.3 kPa and 0-133.3 kPa pressure ranges) with ±0.25 % accuracy.

6.3.3. CH_4 oxidation rate measurements. Turnover rates for CH_4-O_2 reactions were measured in a continuous flow packed-bed tubular reactor (quartz, 8.1 mm inner diameter) with plug-flow hydrodynamics. Pd/Al_2O_3 powders were diluted with SiO_2 (Davison Chemical, Chromatographic Silica Media, CAS no. 112926-00-8, 280 $m^2\ g^{-1}$; treated in flowing dry air, Praxair, 99.99 %, 0.8 $cm^3\ g^{-1}\ s^{-1}$; 0.083 K s^{-1} ramp to 1123 K and hold for 5 h) at an intra-particle SiO_2-to-catalyst dilution ratio (mass basis) of 100 and then pelleted to retain 106-250 m aggregates. These aggregates were mixed with quartz (Fluka, acid purified, product number 84880, 106-250 m diameter) at an inter-particle quartz-to-aggregate dilution ratio (mass basis) of 280. These dilution levels are sufficient to avoid temperature and concentration gradients at the heat loads of these experiments (< 15×10^{-2} W cm^{-3}) for 8 mm tubular reactors used herein.[20]

Reactant mixtures were prepared by electronic metering (Porter 201) of 25 % CH_4/He (Matheson, Certified Plus Grade), O_2 (Praxair, UHP grade) or 5 % O_2/He (Praxair, Certified Standard), and He (Praxair, UHP grade). CO_2, O_2, and CH_4 effluent concentrations were measured by on-line gas chromatography (Agilent 3000A) using Poraplot Q or Mol Sieve 5A columns, each connected to a thermal conductivity detector.

6.4. Results and Discussion

6.4.1. Oxygen uptake and evolution measurements. The oxygen contents in 10.6 nm Pd clusters (0.6 % wt. Pd/Al_2O_3 catalysts), defined as the total O-to-Pd atomic ratio (O_t/Pd, where O_t, the total number of oxygen atoms in Pd clusters, is the sum of surface (O_s*) and bulk (O_b) oxygen atoms, see Scheme 1), at 973 K were measured during sequential steps of O_2 pressure increase (from 1.1 to 91 kPa) and then decrease (from 91-0.25 kPa). Figure 1 shows the total O-to-Pd atomic ratios as a function of O_2 pressure at different times (3.6 ks, 5.4 ks) after the sample was exposed to the O_2 pressure. The time-dependent (0.72-5.4 ks) O_t/Pd ratios upon introducing the sample to a new O_2 pressure set point are provided in Figures A-1 and A-2 in the Appendix at various O_2 pressures (25-90 kPa). O_t/Pd ratios at each O_2 pressure remained essentially unchanged for exposure times larger than 3.6 ks, except at low O_2 pressures (< 0.4 kPa) during the sequential O_2 pressure decrease, for which O_t/Pd ratios decreased with increasing exposure time (Figure A-2 in the Appendix).

The O_t/Pd ratio at zero O_2 pressure { $(O_t/Pd)_{O_2=0}$ }, determined from extrapolation of O_t/Pd values (0.1-0.17) at the low O_2 pressure range of 10 to 25 kPa (Figure 1), was found to be 0.082. This value is similar to the atomic ratio of surface Pd to total Pd (Pd_s/Pd=0.094) within the experimental errors and translates to an O-to-surface Pd atomic ratio (O_t/Pd_s) of near unity (0.87). These results indicate that the bulk of Pd clusters is in the metallic state but surfaces are saturated with chemisorbed oxygen atoms at low O_2 pressures (< 25 kPa). As the O_2 pressure increased (> 25 kPa), O_t/Pd ratios increased gradually from 0.17 to 0.83 with increasing O_2 pressure (31-91 kPa); this increase reflects oxygen dissolution from cluster surfaces into the bulk and the oxidation of bulk Pd to PdO for which a complete Pd oxidation would give a O_t/Pd ratio of unity.

The step-wise O_2 pressure decrease (from 91 kPa to 0.6 kPa) gave constant O_t/Pd ratios of 0.84±0.02 over a wide range of O_2 pressure (91-0.6 kPa). The O_t/Pd ratios did not begin to decrease until the O_2 pressure decreased to values below 0.6 kPa, as shown in Figure 1, an indication that oxygen atoms are being removed from the oxygen rich Pd clusters and that PdO decomposition begins to occur at these low O_2 pressures. The O_t/Pd ratios were much larger during PdO decomposition than Pd oxidation at all O_2 pressures (Figure 1); these trends reflect a hysteresis in oxygen contents (also the Pd chemical states) with O_2 pressure. This hysteresis indicates that at least one of these processes (Pd oxidation and PdO decomposition) occurred at conditions away from equilibrium. Increasing the exposure time from 3.6 to 5.4 ks at each O_2 pressure did not remove the apparent kinetic restrictions, confirmed from oxygen contents during the uptake and evolution measurements were nearly the same and the hysteresis persisted for exposure times larger than 3.6 ks (Figures 1, A-1, and A-2, the latter two are in the Appendix).

Next, we assess the chemical equilibration between oxygen atoms in Pd clusters and O_2(g) during Pd-PdO interconversions in CH_4-O_2 mixtures and compare the O_2

pressure dependencies of CH_4 conversion rate constants and oxygen contents, the latter of which were measured in O_2 (without CH_4). We describe the use of C-H bond activation rate constant as a diagnostic parameter to confirm that the equilibrium is established for the various oxygen atoms, namely $O_2(g)$, O_b, and O_s* (defined in Scheme 1), during Pd oxidation in both CH_4-O_2 and O_2 (without CH_4) mixtures and during PdO decomposition in CH_4-O_2 mixtures at high CH_4 pressures (1.6 kPa). We also show that the oxygen atoms are not equilibrated during PdO decomposition at low (or without) CH_4 pressures.

6.4.2. Assessment of chemical equilibration of oxygen atoms in the gas phase, on the surfaces, and in the bulk of Pd clusters during CH_4 and O_2 reactions. Reactive CH_4 collision probabilities, also the first-order rate constants of CH_4 and defined as turnover rates divided by CH_4 pressure ($r_{CH_4}(CH_4)^{-1}$), were measured in CH_4-O_2 mixtures on Pd clusters (10.6 nm mean cluster diameter, 0.6 % wt. Pd/Al_2O_3 catalyst) during the sequential steps of O_2 pressure increase (Figure 2) and then decrease (Figure 3) in the pressure range of 8-82 kPa at 973 K. Previous kinetic and isotopic studies at a lower temperature (873 K) have shown that the reactive CH_4 collision probabilities at low O_2 pressures (< 1.6 kPa O_2) reflect the initial C-H bond activation rate constants in CH_4 on oxygen atom site pairs (O_s*-O_s*) at metallic Pd cluster surfaces saturated with oxygen atoms.[20] Equal oxygen isotopologue formation rates in CH_4-$^{16}O_2$-$^{18}O_2$ and $^{16}O_2$-$^{18}O_2$ mixtures have confirmed that the oxygen chemical potentials at Pd cluster surfaces are set by O_2 pressures and that O_s and $O_2(g)$ are chemically equilibrated (at 873 K).[20] The bulk of Pd clusters is in the metallic state at these oxygen chemical potentials (< 7.5 kPa O_2) because the atomic oxygen-to-exposed Pd ratio is near unity (O_s/Pd_s=1.06; 873 K).[20] At higher temperatures (973 K), C-H bond activation on O_s*-O_s* site pairs remains as the kinetically-relevant steps at these O_2 pressures, as shown by the rate dependencies of first-order in CH_4 and zero-order in O_2, normal C-H/C-D kinetic isotope effects (1.8), and an atomic oxygen-to-exposed Pd ratio of near unity (O_s/Pd_s=0.87, Section 3.1).

Reactive CH_4 collision probabilities at 973 K increased as the O_2 pressure increased further (8-82 kPa, Figure 2). This trend appears to coincide with the dependence of total oxygen contents in Pd clusters (O_t/Pd, O_t=O_b+O_s, Scheme 1) on O_2 pressure (Figure 1), which were measured in O_2 (without CH_4, Section 3.1), as also plotted in Figure 2. It reflects more reactive surface oxygen atoms (O_s*) towards C-H bond activation (k_{C-H}) as the oxygen contents in Pd clusters increase and O_t-to-Pd atomic ratio approaches unity (to be discussed in Section 4.6), during which Pd clusters undergo bulk oxidation to PdO:

$$\frac{r_{CH_4}}{(CH_4)} = k_{C-H}\left(f\left(\frac{O_t}{Pd}\right)\right) \quad (6)$$

C-H bond activation remains as the kinetically-relevant step on PdO structures but occurs at $Pd^{2+}O^{2-}$ sites, as proposed based on kinetic and isotopic methods at lower temperatures (553 K,[21] 800-875 K[8]), consistent with DFT results for C-H bond activation in CH_4 on PdO(101) surfaces.[8] Rate constants (k_{C-H}) are larger and barriers are lower (experiment: 12.9 vs. 0.53 mol CH_4 (g-atom $Pd_{surface}$-s-kPa)$^{-1}$ at 873 K, 61 vs. 158 kJ mol^{-1} for 21.3 nm PdO and Pd clusters, respectively; theory: 62 vs. 145 kJ mol^{-1} on PdO(101) and O* saturated Pd(111), respectively)[8] for C-H bond activation on $Pd^{2+}O^{2-}$ sites at oxide surfaces than on O_s*-O_s* sites at metal surfaces. Bulk oxidation exposes Pd^{2+} atoms, which interact and stabilize the CH_3 fragments of CH_4 at the transition state during the C-

H bond activation steps[8] in a mechanism similar to those reported for C-H bond activation on oxygen-oxygen vacancy pairs on O* covered Pt clusters;[14] thus, the C-H bond activation barriers are lower and the C-H bond activation rate constants are higher than those on O_s*-O_s* pairs.[8]

CH_4 pressure does not affect the C-H bond activation rate constants at each O_2 pressure during the sequential O_2 pressure increase (Figure 2). By inference, rates of O_s* removal by reactions with CH_4 (r_{CH_4}) are insignificant compared with those of O_s* recombination ($r_{O_2,r}$), because varying the CH_4 rates in scavenging the reactive oxygen atoms does not alter the total oxygen contents and reactivities of surface oxygen atoms (Equation 4, Figure 2). Thus, oxygen activation steps are quasi-equilibrated, surface oxygen atoms are chemically equilibrated with O_2(g), and O_2 virtual pressures (Equation 1b) equal the actual O_2 pressures. These conclusions were unlike those found for CH_4 oxidation reactions on PdO clusters,[22] CH_4[14] or C_2H_6[23] oxidation on Pt cluster surfaces below O* saturation, and CH_4 oxidation on Rh oxides[22] at lower temperatures (873 K) for which C-H bond activation steps appear to be the dominant route for O* removal that scavenges the O* effectively to coverages lower than at chemical equilibrium.

As O_2 pressure decreased step-wise from 91 kPa O_2, C-H bond activation rate constants decreased with decreasing O_2 pressure, as shown in Figure 3. This decrease reflects the PdO decomposition and the formation of less reactive surfaces for C-H bond activation. Unlike the oxidation step (Figure 2), the rate constants and the chemical state of Pd during PdO decomposition depend on the prevalent CH_4 pressure (Figure 3). C-H bond activation rate constants at low CH_4 pressures (0.2 kPa) did not begin to decrease until the O_2 pressure reached values below 60 kPa. At any given O_2 pressure, C-H bond activation rate constants at CH_4 pressures below 1.6 kPa were higher during PdO decomposition (Figure 3) than during Pd oxidation (Figure 2, one of the trends during Pd oxidation is plotted in Figure 3 for comparison), but decreased as CH_4 pressure increased from 0.2 to 1.6 kPa until equal rate constant values were attained in the oxidation and decomposition steps. Above 1.6 kPa CH_4, C-H bond activation rate constants during Pd oxidation and PdO decomposition were essentially identical and became a single-valued function of O_2 pressure (which is also the O_2 virtual pressure), irrespective of the previous O_2 pressure and chemical states of Pd clusters (Figure 3). These conditions, when met, confirm that C-H bond activation rate constants depend strictly on the oxygen contents of Pd clusters. They also confirm that the oxygen contents are a state function of O_2 virtual pressures and thus reflect the equilibrium distribution of oxygen atoms in Pd clusters without the diffusion restrictions of surface oxygen into the bulk. Taken together, we conclude that surface and bulk oxygen atoms during Pd oxidation in CH_4-O_2 mixtures are equilibrated with O_2(g) at all CH_4 (0.2-4.9 kPa) and O_2 (8-92 kPa) pressures, as also the case for PdO decomposition at CH_4 pressures larger than 1.6 kPa. The O_2 pressure dependence of rate constants during Pd oxidation resembles those of equilibrium oxygen uptakes (Figures 1 and 3), suggesting that the C-H bond activation rate constants are directly correlated to the total oxygen contents in Pd clusters (to be discussed in Section 4.6) and that chemical equilibration of oxygen atoms in the gas phase, in the bulk and on the surfaces of Pd clusters is also attained during Pd oxidation in the absence of CH_4.

The difference in C-H bond activation rate constants during Pd oxidation and PdO decomposition transients at low CH_4 pressures (<1.6 kPa) indicates a reactivity hysteresis with O_2 pressure (Figure 3). As CH_4 pressure decreases, the reactivity hysteresis

approaches the trend of O* contents in the absence of CH_4 (Figure 1, Section 3.1), as also plotted in Figure 3 for comparison. These results indicate a deviation of oxygen chemical potentials in the bulk of Pd clusters from values set by the $O_2(g)$ during PdO decomposition in CH_4-O_2 mixtures at low CH_4 pressures (<1.6 kPa) and in O_2 (without CH_4), suggesting that the oxygen atoms in the clusters are not equilibrated with $O_2(g)$. Thus, PdO decomposition is a kinetically limited step, likely caused by the large barriers required for recombinative desorption of lattice oxygen on PdO cluster surfaces, as inferred from the significant heats required for PdO formation ($\Delta H^{o}_{298} = -187 kJ(molO_2)^{-1}$).[24] CH_4 appears to remove the reactivity hysteresis (Figure 3) and promote the PdO reduction; it does not do so by lowering the oxygen chemical potentials because if it did, the C-H bond activation rate constants would be affected by CH_4 pressures during the step-wise O_2 pressure increase (Figure 2). We surmise that CH_4 assists the PdO reduction via its chemical turnovers by providing a route of shuffling the O* on PdO cluster surfaces. CH_4 conversions on PdO surfaces occur via kinetically-relevant C-H bond activation assisted by lattice oxygen atoms that form OH* intermediates, followed by kinetically inconsequential OH* removal (as H_2O) from PdO surfaces.[8] The barriers for removing lattice oxygen atoms (as reaction products) from PdO surfaces during CH_4-O_2 reactions are given by the barriers of the kinetically-relevant C-H bond activation step (experiment: 61 kJ mol^{-1} for 21.3 nm mean Pd cluster diameter; theory: 62 kJ mol^{-1} on Pd(110) surfaces),[8] which are much lower than O* removal via their recombinative desorption.

6.4.3. Thermodynamics of Pd and oxygen. Thermodynamic and chemical equilibrium requires equal oxygen chemical potentials in the gas phase ($_{O_2(g)}$), on Pd cluster surfaces ($_{O_s}$), and in the bulk of Pd clusters ($_{O_b}$):

$$_{O_2(g)} = _{O_s} = _{O_b} \quad (7)$$

Equal oxygen chemical potentials are shown to attain here during Pd oxidation at all O_2 and CH_4 pressures and during PdO decomposition at CH_4 pressures above 1.6 kPa (Section 4.2) at 973 K. We derive next the Pd-PdO phase boundary based on the rate and oxygen content measurements under conditions of equal oxygen chemical potentials that satisfy Equation 7. Figure 4 shows the O_2 pressures (also the oxygen chemical potentials) required for the onset of bulk Pd oxidation (2.2 nm and 10.6 nm mean Pd cluster diameters; 0.6 % wt. Pd/Al_2O_3) as a function of inverse temperature. These O_2 pressures are defined as the O_2 pressures required for increasing the O_t/Pd values above those expected from the O-to-surface Pd atomic ratio (O_t/Pd_s) of unity; these values depend on cluster sizes, the trend of which will be discussed in Section 4.5. The oxygen chemical potentials required for Pd oxidation were also determined from the increase in first-order rate constants in CH_4-O_2 mixtures during the step-wise increase in O_2 pressure (Figure 2). These data and the oxygen pressure required for PdO decomposition, the latter is determined from the decrease in first-order rate constants in CH_4-O_2 mixtures (for CH_4 > 1.6 kPa) with decreasing O_2 pressure (Figure 3), are measured at equilibrium and their values are essentially the same within the experimental errors, as shown in Figure 4a.

Figure 4a also shows the oxygen chemical potential required for PdO decomposition in the same sample of 10.6 nm mean Pd cluster diameter (0.6 % wt. Pd/Al_2O_3), which was measured in O_2 (the absence of CH_4) at 973 K by decreasing the O_2 pressure step-wise (Figure 1). The oxygen chemical potential required for PdO

decomposition in O_2 (without CH_4) is consistent with the Pd-PdO phase boundary derived from linear regression fittings of the reported PdO decomposition data (in the absence of CH_4, and shown in Figure 4b)[3,5,25,26,27,28,29,30,31,32] by least squares minimization. These reported values for PdO decomposition on Pd single crystal surfaces (111),[30,32] supported clusters,[3,5,28,29,25] and bulk structures[26,27,31] are consistent among each others over a wide range of oxygen chemical potentials (10^{-10}-100 kPa, Figure 4b). Some of these values have been used to establish the heats and entropies of PdO formation. However, the PdO decomposition steps in O_2 (or diluted O_2 in inert gases (N_2, He)) and the derived "thermodynamics" in Figure 4b have not been shown to occur reversibly; in other words, these values have not been attained from the reverse step of Pd oxidation. Both oxygen pressure dependencies of oxygen contents and of C-H bond activation rate constants during the Pd-PdO transients have shown that PdO decomposition at low CH_4 pressures (< 1.6 kPa CH_4; 973 K) is a kinetically limited process (Section 4.2). Thus, the Pd-PdO phase boundary, derived from the thermal PdO decomposition (Figure 4b), does not reflect the intrinsic thermodynamics of PdO. We have instead confirmed rigorously, based on rate constant measurements in CH_4-O_2 mixtures and O_2 uptakes in O_2 (without CH_4) (Sections 4.1 and 4.2), that oxidation of Pd clusters occurs at thermodynamic and chemical equilibrium. The phase boundary data derived from Pd oxidation appear to agree with the reported data[3,25,33] (shown in Figure 4a) measured from temperature programmed cooling of metallic Pd clusters in air or in diluted O_2/He mixtures from temperatures above the PdO decomposition temperatures, all of which give O_2 pressures larger than those required for PdO decomposition.

6.4.4. Oxygen dissolution and the gradual increase in bulk oxygen contents of Pd clusters during Pd oxidation at equilibrium. Next, we probe the increase in oxygen contents with increasing oxygen chemical potentials during the Pd cluster oxidation at thermodynamic and chemical equilibrium. Equilibrium oxygen contents (expressed as O_t/Pd, 10.6 nm mean Pd cluster diameters) increased gradually as O_2 pressure increased from 12 kPa to 91 kPa (Figure 1). This increase reflects a gradual phase transition in which bulk oxygen contents increase continuously over a wide range of oxygen chemical potentials. The gradual phase transition contradicts the abrupt phase changes expected from classical thermodynamics on macroscopic phases, which are derived based on the Gibbs phase rule (F=C-P+2) that limits the maximum degrees of freedom (F) for a given number of phases (P) and components (C). We cannot rule out that the gradual increase in oxygen contents was caused by the size variance among the Pd clusters within the sample because cluster sizes have marked effects on oxygen contents and the required O_2 pressures for oxygen dissolution. These effects of cluster size on oxygen contents and bulk oxidation will be discussed in Section 4.5.

Dissolution of one element into another is, by analogy, similar to the mixing of binary elements, which has been treated in alloy systems using the quasi-lattice theory[34] and Monte Carlo methods.[35] The thermodynamic tendencies of oxygen dissolution are defined by the Gibbs energy of dissolution, which are driven by the enthalpy (also related to the internal energy) and entropy of dissolution. We propose a sequence of molecular events occurred during oxygen dissolution and discuss the thermodynamic driving forces that cause the dissolution and the eventual Pd oxidation. The oxygen dissolution in small clusters is, by analogy to solvation of a solute in a solvent, a molecular process with its thermodynamic driving forces influenced largely by the fraction of exposed atoms and

their properties (as shown in Section 4.5). These events are accessible only through statistical mechanics formalism.[36]

Oxygen dissolution begins with migration of surface oxygen (O_s*) atoms into the bulk of the clusters; this step involves breaking of bulk Pd-Pd bonds followed by an expansion of local unit cells to accommodate the oxygen atoms. The solvated oxygen atoms (O_b) form Pd-O-Pd bonds with vicinal Pd atoms. These Pd-O_b-Pd structures, initially present as isolated units in the limit of infinite dilution, are stabilized for a period of time before oxygen atoms migrate from one site to another. In each of the O_b migration step, vacancy sites (□) are created as a result of O_b removal from the sites but annealed by re-forming the Pd-Pd bonds, whereas vicinal Pd-Pd bonds are broken to accommodate the oxygen atoms and form Pd-O_b-Pd structures. The driving force for the oxygen dissolution and migration, by analogy to the solution thermodynamics of polymer,[37 38] is the gain in configurational entropy from their abilities to delocalize within the Pd clusters in a solid-solution-like state upon mixing. Oxygen atoms, as a result of their dissolution from the surfaces, acquire additional degrees of freedom. As the concentrations of bulk oxygen and Pd-O_b-Pd structure increase, Pd clusters expand their volume commensurately to accommodate the oxygens. This volume expansion elongates the Pd-Pd bond distances between two next nearest Pd atoms of 0.275 nm[39] in fcc metallic Pd structures (lattice parameter a=0.38898 nm) to 0.343 nm in PdO (lattice parameters for PdO a=b=0.3043 nm and c=0.5337 nm) and as a result, creates additional surface areas. As oxygen contents approach those of PdO structures, the electronic band structures of metallic clusters gradually transform to acquire p-semiconductor characters of PdO.[40] The electron configurations of Pd atoms change from d^{10} to d^8 and Pd atoms acquire formal charges of +2 (as Pd^{2+}). The Pd oxidation exposes some of the Pd^{2+} on the cluster surfaces, making them accessible to CH_4 for the kinetically-relevant C-H bond activation steps.[8] A rigorous interpretation of Pd-to-PdO interconversions, attained only by treating the system in the framework of statistical mechanics, deserves further investigations but is beyond the scope of this report.

6.4.5. Effects of Pd cluster size on phase transition of Pd to PdO. As the ensemble size becomes smaller and the fraction of exposed atoms concomitantly increases, physical and chemical properties of the clusters may deviate from their macroscopic values. Size confinement effects in small atomic ensembles (< 1000 atoms) have led to reduced latent heat of fusion,[41] suppressed melting temperature,[42,43,44] as well as changes in electronic states,[45] optical properties,[45] and magnetic properties.[46] As the surface-to-volume ratio (also the fractional dispersion) increases, properties of surfaces such as surface free energy begin to influence the overall thermodynamics of the clusters. We explore here the effects of cluster size (inversely correlated to the fractional dispersion) on the thermodynamic tendency of bulk oxidation by measuring the total oxygen contents at thermodynamic and chemical equilibrium. Equilibrium was rigorously shown to establish for the largest Pd clusters examined here (10.6 nm mean diameter, Section 4.2), as also the case for the smaller clusters because transport restrictions of oxygen atoms from surfaces to the bulk are more prevalent on larger clusters. Thus, the measured oxygen contents in Pd clusters reflect the oxygen concentrations chemically equilibrated with O_2(g) and defined by the free energy of oxygen dissolution.

Oxygen uptakes were measured as a function of O_2 pressures (0.16-91 kPa) in a series of 0.6 % wt. Pd/Al_2O_3 catalysts with different mean Pd cluster diameters (1.8-10.6

nm) at 973 K. The oxygen uptakes (O_t/Pd) and bulk oxygen contents (defined here as the atomic ratio of oxygen-to-Pd in the bulk phase, O_b/Pd_b) are shown in Figure A-3 (in the Appendix) and Figure 5, respectively. Oxygen uptakes (O_t/Pd) at low O_2 pressures for each cluster diameter (e.g. 10 to 25 kPa for 10.6 nm clusters, Section 4.1) give an O-to-surface Pd atomic ratio of near unity. As O_2 pressure and oxygen chemical potential increased, the total oxygen contents increased above the surface saturation, suggesting that O_s* atoms dissolute into the bulk of Pd clusters. The oxygen pressures required for the onset of oxygen dissolution were found to depend strongly on cluster sizes, as shown in Figures 6 and A-3 (in the Appendix), and occurred at much lower O_2 pressures for clusters with smaller mean diameters (22.1 kPa and 38.9 kPa for 1.8 nm and 10.6 nm cluster diameters, respectively). On small clusters (1.8 nm), the O_b/Pd_b ratios (and O_t/Pd ratios) increased with increasing O_2 pressure and reached 0.8 (O_t/Pd=0.92) at 41 kPa O_2 (Figure 5). Similar trends were found for large clusters, but the increase in O_b/Pd_b (and O_t/Pd ratios) occurred at larger O_2 pressures (Figure 5). Size-dependent oxygen contents were reported previously based on decomposition of PdO (2-10 nm) supported on α-Al_2O_3 (0001),[47] but those results were likely measured under kinetically restricted conditions (as discussed in Section 4.3).

The strong dependence of equilibrium oxygen contents on cluster sizes (Figures 5 and 6) indicate that thermodynamic tendencies for bulk oxidation are higher on smaller clusters. Small clusters contain a large fraction of coordinatively unsaturated metal atoms that binds adsorbates strongly, as predicted from the bond energy-bond order theory, which assumes that the bond indices are conserved. These effects of coordination on binding strengths were reported on a model cubo-octahedral Pt cluster, in which the DFT calculated oxygen binding strengths (heats of atomic oxygen adsorption as isolated O* species) increase from 96 to 133 kJ mol^{-1} as the average coordination number decreases from 9 to 6.5.[48] This dependence of oxygen binding strengths on coordination numbers leads to more exothermic oxygen adsorption on smaller clusters. Such effects of average surface coordination appear to increase the heats of PdO formation for small clusters than bulk PdO structures, and in turn, increase the thermodynamic driving forces for them to undergo bulk oxidation.

6.4.6. Effects of oxygen contents in Pd clusters on C-H bond activation rate constants of CH_4. Kinetic and isotopic assessments of alkane oxidation on oxygen covered Pt,[14,23, 48] oxygen covered Pd,[8,20] and PdO[8] clusters, together with DFT calculations on Pt (cubo-octahedral clusters with 201 Pt atoms; Pt(111))[14,48] and Pd surfaces (PdO(101) and O* saturated Pd(111)),[8] have brought rigor to the roles of surface oxygen atoms (either as chemisorbed oxygen on metallic cluster surfaces or lattice oxygen on PdO) on C-H bond activation. Here, we describe the effects of total oxygen contents in Pd clusters, which include the surface and bulk oxygen atoms, on the reactivity of cluster surfaces for C-H bond activation. Figure 7 shows C-H bond activation rate constants in CH_4 (k_{C-H}, Equation 6) on Pd clusters (10.6 nm mean cluster diameters, 0.6 % wt. Pd/Al_2O_3 catalysts) at 973 K as a function of total oxygen contents (expressed as oxygen-to-Pd atomic ratios, O_t/Pd, 0.06-0.9) in the Pd clusters. At oxygen-to-Pd atomic ratios below 0.87, oxygen atoms reside predominantly on Pd cluster surfaces as chemisorbed species. These oxygen atoms abstract H from C-H bond, as reported for CH_4 activation on O* saturated Pd cluster surfaces[8,20] and O* covered Pt clusters,[14] as well as CH_3OCH_3[49] and C_2H_6[23] activation on O* covered Pt clusters. C-H

bond activation rate constants remained constant (0.73 mol CH_4 (g-atom $Pd_{surface}$ kPa s)$^{-1}$; 973 K) during initial oxygen dissolution for O_t/Pd ratios up to 0.11, indicating that the initial increase in bulk oxygen contents that results in isolated O_b species within bulk Pd metals does not affect the surface oxygen reactivity towards C-H bond activation. A further oxygen dissolution and increase in oxygen contents (> 0.11 O_t/Pd) lead the C-H bond activation rate constants to increase monotonically over the entire range of oxygen-to-Pd ratios (O_t/Pd=0.11-0.9). This increase reflects a decrease in binding strength of surface oxygen with increasing bulk oxygen contents and, in turn, more effective H abstraction during the C-H bond activation. Weakly bound oxygen atoms have been shown to abstract the H in C-H bond much more effectively than the strongly bound oxygen atoms[14,20,23] because of their higher electron density, which allow them to form stronger O-H bonds with the H and stabilize the transition state energy.[8] The increase in C-H bond activation rate constants with oxygen contents also reflects the creation of more reactive surface sites as oxygen atoms begin to acquire negative charges and oxygen dissolution creates exposed Pd^{2+} atoms that are accessible to the reactants. These Pd^{2+} atoms promote the C-H bond activation by facilitating an oxidative insertion step and interacting strongly with the methyl fragments in CH_4 at the transition state; such interactions stabilize the transition state energies and result in activation barriers significantly lower than the O* saturated surfaces {experiment: 61 kJ mol^{-1} (PdO) vs. 158 kJ mol^{-1} (O* saturated Pd cluster surfaces), 21.3 nm Pd clusters; theory: 62 kJ mol^{-1} PdO(101) vs. 145 kJ mol^{-1} (O* saturated Pd(111))}, as reported in detail elsewhere.[8]

The gradual increase in reactivities infers a gradual surface reconstruction and formation of diverse surface structures in response to changing oxygen chemical potentials; the reactivities of these intermediate structures in C-H bond activation correlate directly to the oxygen contents in the clusters (Figure 7). Previous studies on Pd oxidation have reported diverse surface structures and sub-surface oxide formed on Pd single crystal facets upon exposure to O_2.[50,51,52] These reported structures might not resemble those on Pd clusters, because oxygen uptakes on single crystal surfaces are limited by the ability of the substrates to expand in all three dimensions to accommodate the bulk oxygen atoms. These structural confinements, in large part, lead to formation of oxygen deficient metastable oxides that are different than those found on bulk PdO structures,[50,53] and may also be different than on PdO clusters. The structures of active sites during oxygen dissolution from cluster surfaces into the bulk, the oxygen dissolution, cluster volume expansion, and the reverse of these processes are molecular processes, and as shown here, of significant catalytic consequences. These processes depend on the local properties of the system, and remain as important topics that deserve further examination in the framework of statistical mechanics.

6.5. Conclusion

Pd-PdO interconversions and their catalytic consequences are probed at chemical and thermodynamic equilibrium, confirmed from fully reversible steps between Pd and PdO and from the C-H bond activation rate constants and chemical states of clusters independent of previous history. Oxygen equilibration among the surfaces of Pd, bulk of Pd, and gas phase was attained above a CH_4 pressure in CH_4-O_2 mixtures or during Pd oxidation in the absence of CH_4. In contrast, PdO decomposition, which requires the

removal of oxygen from PdO clusters, is a kinetically-limited step. Equilibrium oxygen contents of Pd clusters increase gradually with increasing oxygen chemical potentials during Pd cluster oxidation; this increase appears to occur at lower oxygen chemicals on small than large clusters, indicating that small clusters exhibit a stronger thermodynamic tendency for oxidation. The C-H bond activation rate constants increase with increasing equilibrium oxygen contents in Pd clusters over the entire range of O-to-Pd ratios during Pd-PdO interconversions because the increase in oxygen contents weakens the binding energy of surface oxygen and exposes Pd atoms, leading to more reactive oxygen for H abstraction and to larger extent of Pd-C interactions at the C-H bond activation transition states.

6.6. References

[1] Zhu, G.; Han, J.; Zemlyanov, D.Y.; Ribeiro, F. H. *J. Phys. Chem. B* **2005**, *109*, 2331.
[2] Lyubovsky, M.; Pfefferle, L. *Catal. Today* **1999**, 47, 29.
[3] McCarty, J. G. *Catal. Today* **1995**, *26*, 283.
[4] Farrauto, R. J.; Hobson, M. C.; Kennelly, T.; Waterman, E.M. *Appl. Catal. A-Gen.* **1992**, *81*, 227.
[5] Baylet, A.; Marécot, P.; Duprez, D.; Castelazzi, P.; Groppi. G.; Forzatti, P. *Phys. Chem. Chem. Phys.* **2011**, *13*, 4607.
[6] Salomonsson, P.; Johannson, S.; Kasemo, B. *Catal. Lett.* **1995**, *33,* 1.
[7] Garbowski, E.; Feumi-Jantou, C.; Mouaddib, N.; Primet, M. *Appl. Catal. A: Gen* **1994**, *109*, 277.
[8] Chin, Y-H.; Buda C.; Neurock, M.; Iglesia, E. *J. Amer. Chem. Soc.* in preparation.
[9] Temkin, M.I. ; Pyzhez, *V. Zhur. Fiz. Xhim.* ***1939*** , *13*, 851
[10] Temkin, M.I.; Pyzhev, V. *Acta Physicochim.* **1940**, *12*, 327.
[11] Boudart, M. *J. Phys. Chem.* **1983**, *87*, 2786.
[12] Iglesia, E.; Baumgartner, J.E.; Price, G.L. *J. Catal.* **1992**, *134*, 549.
[13] Yu, S.Y.; Biscardi, J.A.; E. Iglesia, *J. Phys. Chem. B* **2002**, *106*, 9642.
[14] Chin, Y-H.; Buda C.; Neurock, M.; Iglesia, E. *J. Amer. Chem. Soc.* submitted.
[15] Su, S.C.; Carstens, J.N.; Bell, A.T. *J. Catal.* **1998**, *176*, 125.
[16] Chen, J. J.; Ruckenstein, E. *J. Phys. Chem.* **1981**, *85*, 1606.
[17] Hicks, R. F.; Qi, H.; Young, M. L.; Lee, R. G. *J. Catal.* **1990**, *122*, 295.
[18] Bell, W.E.; Inyard, R.E.; Tagami, M. *J. Phys. Chem.* **1966**, *70*, 3735.
[19] David, R. L. *Handbook of Chemistry and Physics*, 87th ed.; CRC Press: Boca Raton, FL 2006.
[20] Chin, Y-H.; Iglesia, E. *J. Phys. Chem. C* submitted.
[21] Fujimoto, K.; Ribeiro, F. H.; Avalos-Borja, M.; Iglesia, E. *J Catal.* **1998**, *179*, 431.
[22] Chin, Y-H.; García-Diéguez, M.; Iglesia, E. in preparation.
[23] García-Diéguez, M.; Chin Y-H.; Iglesia, E. *J. Catal.* in preparation.
[24] Ho, Y-S.;Wang, C-B.; Yeh, C-T. *J. Mol Catal. A: Chem* **1996**, *112*, 287.
[25] Farrauto, R.J.; Lampert, J.K.; Hobson, M.C.; Waterman, E.M. *Appl. Catal. B: Environ.* **1995**, *6*, 263.
[26] Zhang, H.; Gromek, J.; Fernando, G. W.; Boorse, S.; Marcus, H.L. *J. Phase Equil.* **2002**, *23*, 246.
[27] Bayer, G.; Wiedemann, H. G. *Thermochimica Acta*, **1975**, *11*, 79.
[28] Groppi, G.; Artioli, G.; Cristiani, C.; Lietti, L.; Forzatti, P. *Stud. Surf. & Catal.* **2001**, 345.
[29] Hoost, T.E.; Otto, K. *Appl. Catal.* **1992**, *92*, 39.
[30] Gabasch, H.; Unterberger, W.; Hayek, K.; Klötzer, B.; Kleimenov, E. Teschner, D.; Zafeiratos, S.; Hävecker, M.; Knop-Gericke, A.; Schlögl, R.; Han. J.; Ribeiro, F. H.; Aszalos-Kiss, B.; Curtin, R.; Zemlyanov, D. *Surf. Sci.* **2006**, *600*, 2980.
[31] Dushman, S. In Scientific Foundations of Vacuum Technique; Lafferty, M., Ed.: John Wiley & Sons: 1962; p. 748.
[32] Zheng, G.; Altman, E.I. *Surf. Sci.* **2000**, *462*, 151.

[33] Datye, A. K.; Bravo, J.; Nelson, T.R.; Atanasova, P.; Lyubovsky, M.; Pfefferle, L. *Appl. Catal. A: Gen.* **2000**, *198*, 179.
[34] Novakovic, R.; Zivkovic, D. *J. Mater. Sci.* **2005**, *40*, 2251.
[35] Gironcoli, S. d.; Giannozzi, P. *Phys. Rev. Lett.* **1991**, *66*, 2116.
[36] Ben-Naim, A. Elementary Background. In Solvation Thermodynamics, Plenum Press, New York, 1987, Ch. 1.
[37] Flory, P.J. *J. Chem. Phys.* **1941**, *9*, 660.
[38] Huggins, M.L. *J. Chem. Phys.* **1941**, *9*, 440.
[39] Wyckoff, R.W.G. Crystal Structures, 2nd Ed.; John Wiley and Sons, New York, NY; 1963; Vol. 1, 580.
[40] Pillo, Th.; Zimmermann, R.; Steiner, P.; Hüfner, S. *J. Phys.: Condens. Matter* **1997**, *9*, 3987.
[41] Bachels, T.; Guntherodt, H.J.; Schafer, R. *Phys. Rev. Lett.* **2000**, *85*, 1250.
[42] Li, T.X.,; Ji, Y.L.; Yu, S.W.; Wang, G.H. *Solid State Comm.* **2000**, *116*, 547.
[43] Xie, D; Qi, W.H.; Wang, M.P. *Acta Metallurgica Sinica* **2004**, *40*, 1041.
[44] Cleveland, C.L.; Luedtke, W.D.; Landman, U. *Phys. Rev. B* **1999**, *60*, 5065.
[45] Alivisatos, A.P. Science **1996**, *271*, 933.
[46] Hendriksen, P.V.; Linderoth, S.; Lindgard, P.-A. *Phys. Rev. B* **1993**, *48*, 7259.
[47] Penner, S.; Bera, P.; Pedersen, S.; Ngo, T.; Harris, J.J.W.; Campbell, C.T. *J. Phys. Chem. B* **2006**, *110*, 24577.
[48] Chin, Y-H.; Buda, C; Neurock, M.; Iglesia, E. *J. Catal.* submitted.
[49] Ishikawa, A.; Neurock, M.; Iglesia, E. *J. Amer. Chem. Soc.* **2007**, *129*, 13201.
[50] Klikovits, J.; Napetschnig, E.; Schmid, M.; Seriani, N.; Dubay, O.; Kresse, G.; Varga, P. *Phys. Rev. B* **2007**, *76*, 045405.
[51] Kan, H.H.; Weaver, J.F. *Surf. Sci.* **2009**, *603*, 2671.
[52] Lundgren, E.; Gustafson, J.; Mikkelsen, A.; Andersen, J. N. *Phy. Rev. Lett.* **2004**, *92*, 046101.
[53] Stierle A. *Int. J. Mater. Res.* **2009**, *100*, 1308.

6.7. Figures

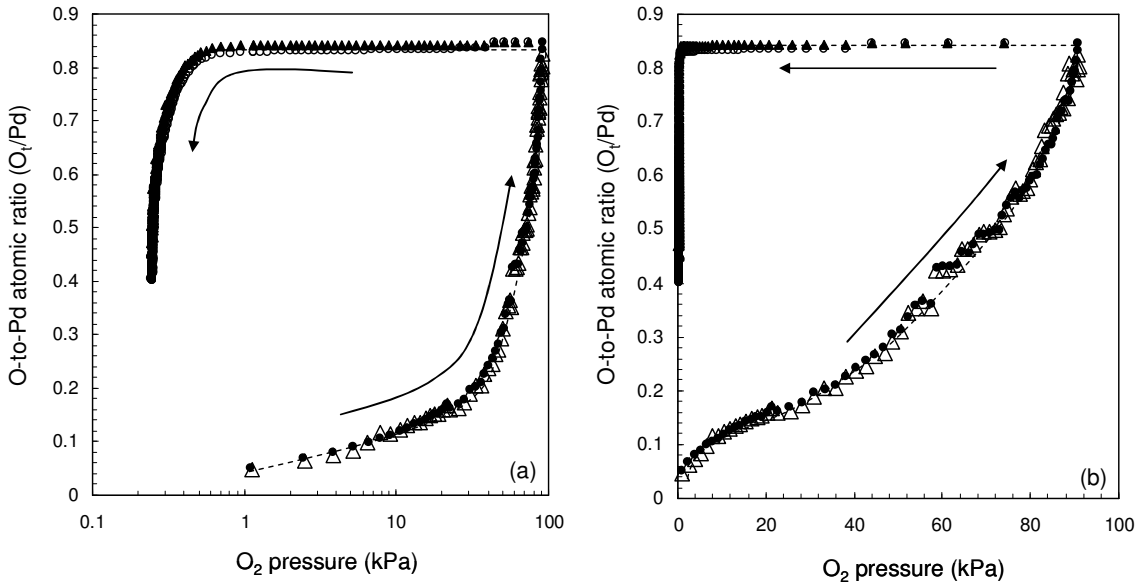

Figure 1a and 1b. Oxygen contents in Pd clusters (0.6 % wt. Pd/Al_2O_3 catalyst, 10.6 nm mean cluster diameter), expressed as the total O-to-Pd atomic ratio (O_t/Pd; $O_t=O_s+O_b$, Scheme 1), as a function of oxygen pressure during the incremental O_2 pressure increase (●, Δ) and decrease (▲,○) after 3.6 ks (●,▲) or 5.4 ks (○,Δ) upon exposure of Pd clusters to each O_2 pressure set point at 973 K. → denotes the step-wise O_2 pressure increase or decrease. Figure 1b: data from Figure 1a, with O_2 pressures plotted on a linear scale.

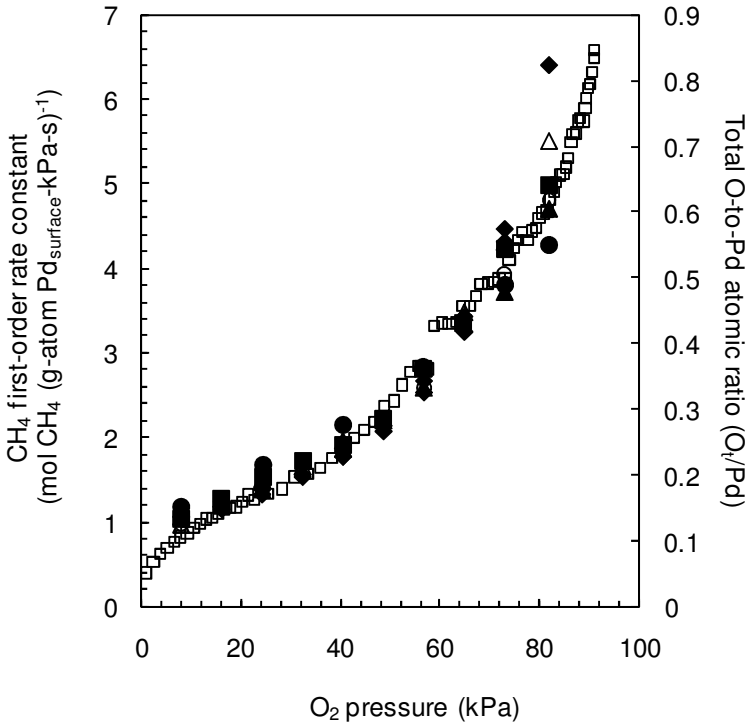

Figure 2. Reactive CH_4 collision probabilities, also the first-order rate constants of CH_4 and defined as turnover rates divided by CH_4 pressure, during the step-wise O_2 pressure increase in CH_4-O_2 mixtures on a 0.6 % wt. Pd/Al_2O_3 catalyst (10.6 nm mean Pd cluster diameter) at 973 K for 0.2 kPa (●), 0.4 kPa (○), 0.7 kPa (▲), 1.6 kPa (■), 2.4 kPa (Δ), and 4.9 kPa (♦) CH_4. O_2 uptakes in O_2 (in the absence of CH_4), denoted here as the total oxygen-to-Pd atomic ratio (O_t/Pd), during the step-wise increase (□) in O_2 pressure from Figure 1 are plotted here for comparison.

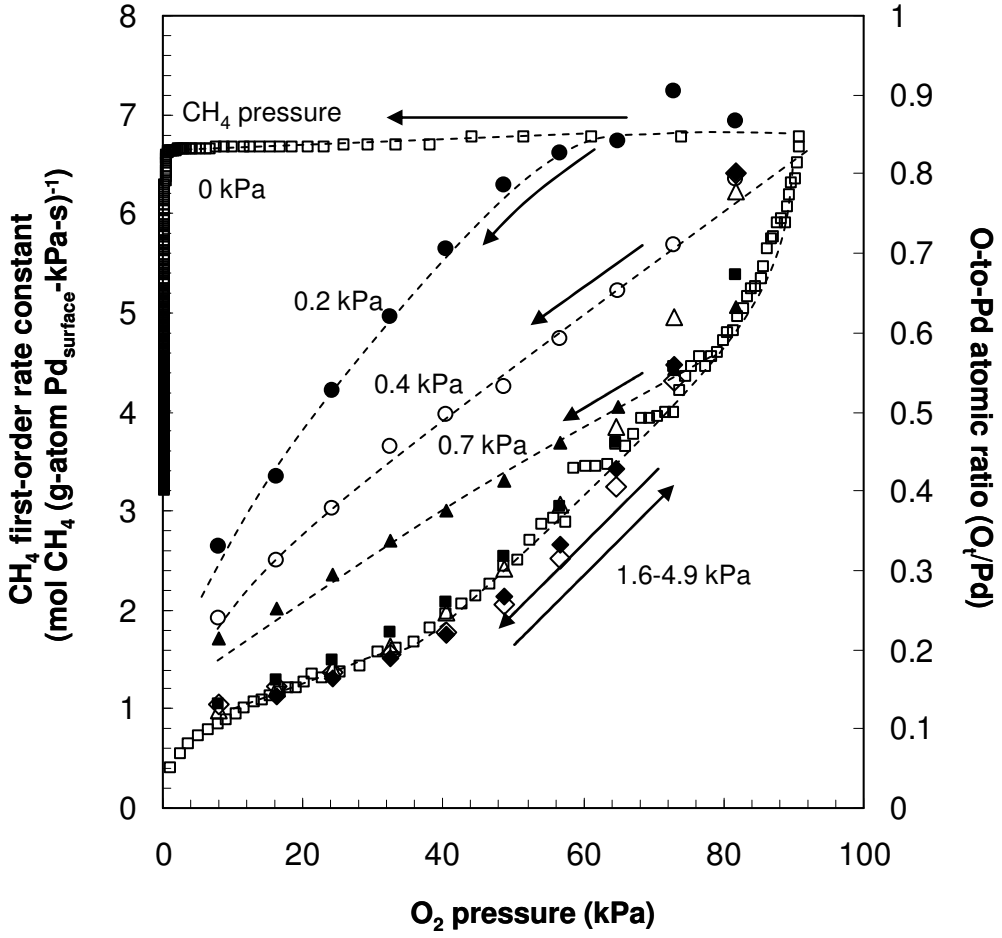

Figure 3. CH_4 first-order rate constants, defined as turnover rates divided by CH_4 pressure, during the step-wise O_2 pressure decrease (from 91 kPa) in CH_4-O_2 mixtures on a 0.6 % wt. Pd/Al_2O_3 catalyst (10.6 nm mean Pd cluster size) at 973 K in 0.2 kPa (●), 0.4 kPa (○), 0.7 kPa (▲), 1.6 kPa (■), 2.4 kPa (Δ), and 4.9 kPa (♦) CH_4. CH_4 first-order rate constants during the step-wise O_2 pressure increase in 4.9 kPa (◊) CH_4 from Figure 2, and the total O-to-Pd atomic ratios (denoted as O_t/Pd) during the O_2 pressure increase and then decrease (□) (in the absence of CH_4) from Figure 1 are plotted here. → denotes the step-wise O_2 pressure increase or decrease.

(4.09×10^8 cm^3 (mol $Pd_{surface}$-s)$^{-1}$, 100 SiO_2/catalyst intraparticle dilution ratio, 1400 quartz/catalyst interparticle dilution ratio)

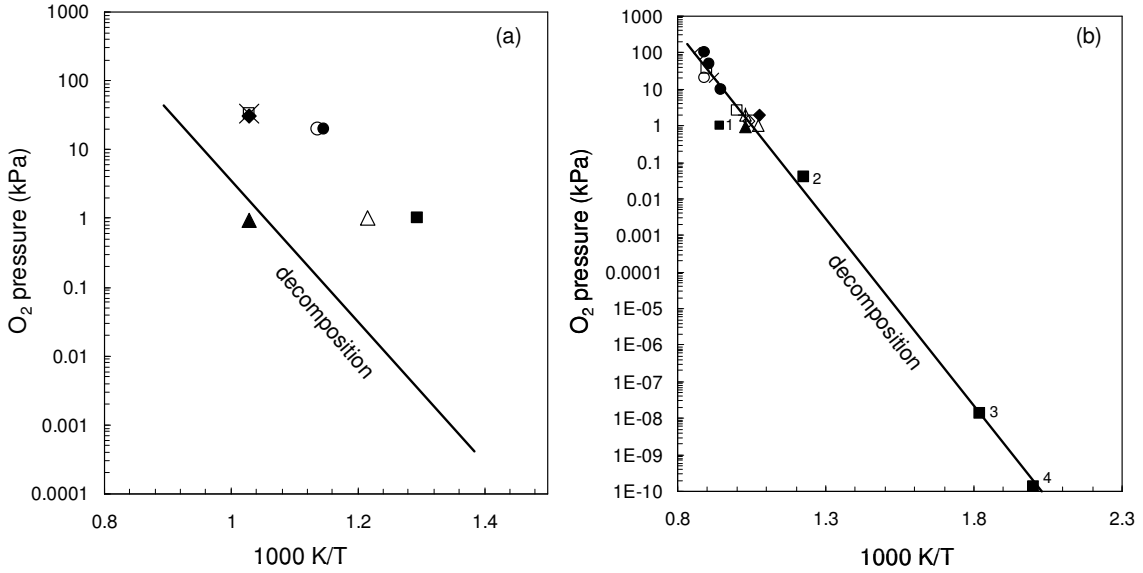

Figure 4a. O_2 pressure required for Pd oxidation determined from O_2 uptake (+: 2.2 nm mean Pd cluster diameter, ♦: 10.6 nm mean Pd cluster diameter) and CH_4-O_2 reactions (×: 10.6 nm mean Pd cluster diameter, 4.85 kPa CH_4) during the step-wise O_2 pressure increase from 1.1 to 91 kPa. Oxygen pressure required for PdO decomposition (10.6 nm mean Pd cluster diameter) determined from O_2 evolution (▲) and CH_4-O_2 (□) reactions (4.85 kPa CH_4) during the step-wise O_2 pressure decrease from 91 kPa to 0.6 kPa. Oxygen pressure required for Pd oxidation determined from cooling of metallic Pd above the PdO decomposition temperature (●,[1] ○,[2] ■,[3] Δ[4]). The linear line shows the Pd-PdO phase boundary determined from least squares regression analysis of the PdO decomposition data reported in the literature (in Figure 4b).

Figure 4b. O_2 pressure required for PdO decomposition determined from decomposition of Pd clusters (10.6 nm mean Pd cluster diameter) during the step-wise O_2 pressure decrease (▲) from 91 kPa to 0.6 kPa and from heating of PdO (reported in the literature; ×,[1] Δ,[3] ■1,[4] ●,[5] ◊,[6] □,[7] ○,[8] ■2,[9] ■3,[10] ■4,[11] +,[12]). The linear line shows the Pd-PdO phase

[1] Farrauto, R.J.; Lampert, J.K.; Hobson, M.C.; Waterman, E.M. *Appl. Catal. B: Environ.* **1995**, *6*, 263.
[2] Datye, A. K.; Bravo, J.; Nelson, T.R.; Atanasova, P.; Lyubovsky, M.; Pfefferle, L. *Appl. Catal. A: Gen.* **2000**, *198*, 179.
[3] McCarty, J. G. *Catal. Today* **1995**, *26*, 283.
[4] Baylet, A.; Marécot, P.; Duprez, D.; Castelazzi, P.; Groppi. G.; Forzatti, P. *Phys. Chem. Chem. Phys.* **2011**, *13*, 4607.

[5] Zhang, H.; Gromek, J.; Fernando, G. W.; Boorse, S.; Marcus, H.L. *J. Phase Equil.* **2002**, *23*, 246.
[6] Bayer, G.; Wiedemann, H. G. *Thermochimica Act*a, **1975**, *11*, 79.

boundary determined from least squares regression analysis of the PdO decomposition data.

---

[7] Groppi, G.; Artioli, G.; Cristiani, C.; Lietti, L.; Forzatti, P. *Stud. Surf. & Catal.* **2001**, 345.

[8] Hoost, T.E.; Otto, K. *Appl. Catal.* **1992**, *92*, 39.

[9] Gabasch, H.; Unterberger, W.; Hayek, K.; Klötzer, B.; Kleimenov, E. Teschner, D.; Zafeiratos, S.; Hävecker, M.; Knop-Gericke, A.; Schlögl, R.; Han. J.; Ribeiro, F. H.; Aszalos-Kiss, B.; Curtin, R.; Zemlyanov, D. *Surf. Sci.* **2006**, *600*, 2980.

[10] Dushman, S. In Scientific Foundations of Vacuum Technique; Lafferty, M., Ed.: John Wiley & Sons: 1962; p. 748.

[11] Zheng, G.; Altman, E.I. *Surf. Sci.* **2000**, *462*, 151.

[12] Bell, W.E.; Inyard, R.E.; Tagami, M. *J. Phys. Chem.* **1966**, *70*, 3735.

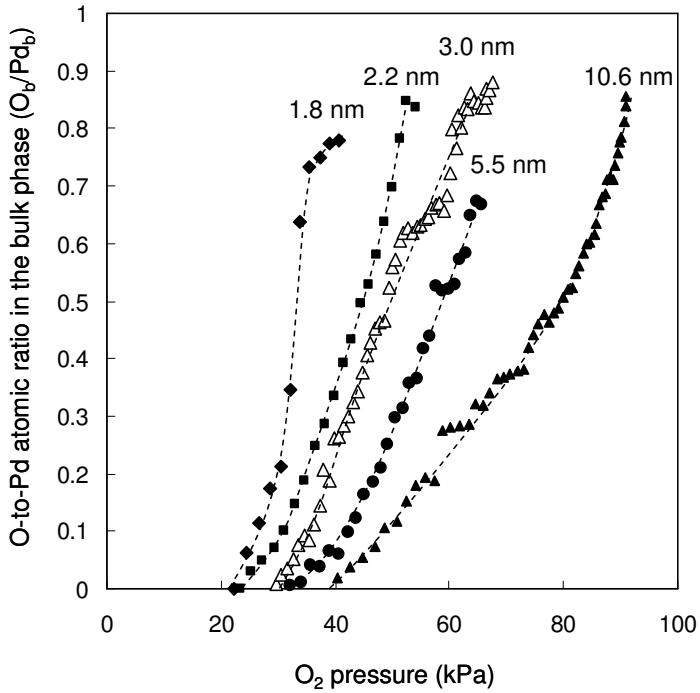

Figure 5. Equilibrium bulk oxygen contents (defined here as the atomic ratio of oxygen-to-Pd in the bulk phase, O_b/Pd_b) in Pd clusters of different mean diameters (1.8 (♦), 2.2 (■), 3.0 (Δ), 5.5 (●), 10.6 (▲) nm, 0.6 % wt. Pd/Al_2O_3 catalysts) at 973 K as a function of O_2 pressures.

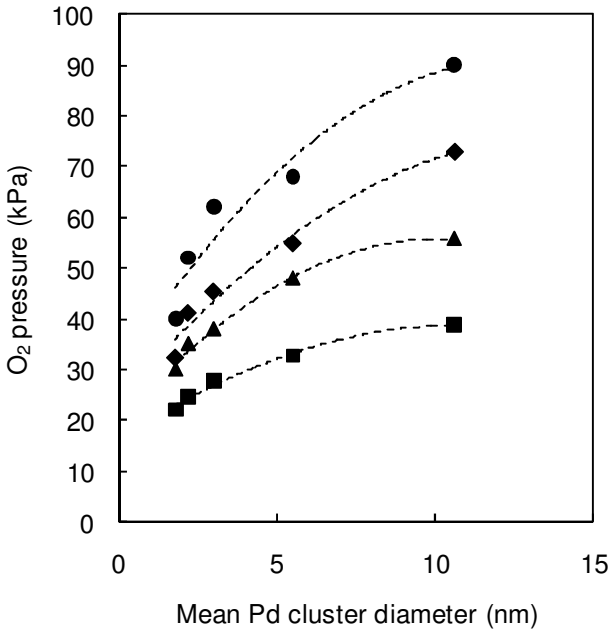

Figure 6. O_2 pressures required for attaining oxygen contents above a monolayer (■) and for attaining equilibrium bulk oxygen contents (atomic ratio of oxygen-to-Pd in the bulk phase, O_b/Pd_b) of 0.2 (▲), 0.6 (♦), and 0.8 (●) in Pd clusters (0.6 % wt. Pd/Al_2O_3 catalysts) as a function of mean Pd cluster diameters (1.8-10.6 nm) at 973 K.

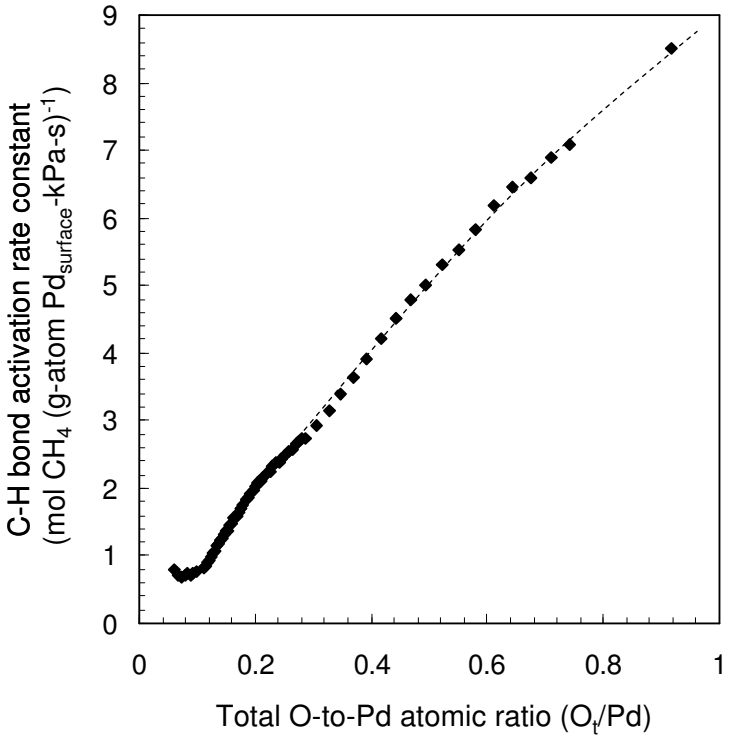

Figure 7. Influence of total O-to-Pd atomic ratio (O_t/Pd; O_t=O_s+O_b, Scheme 1) on C-H bond activation rate constants for CH_4-O_2 reactions on a 0.6 % wt. Pd/Al_2O_3 catalyst (10.6 nm mean Pd cluster size) at 973 K.
(4.09×10^8 cm^3 (mol $Pd_{surface}$-s)$^{-1}$, 100 SiO_2/catalyst intraparticle dilution ratio, 1400 quartz/catalyst interparticle dilution ratio)

6.8. Schemes

Scheme 1. Thermodynamics of oxygen on the surfaces and in the bulk of Pd clusters during CH_4-O_2 catalytic turnovers.

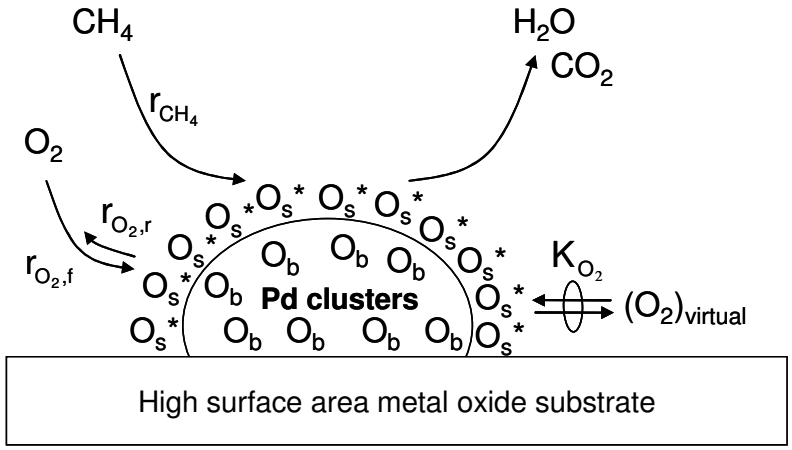

(O_s*: chemisorbed oxygen atom, O_b: bulk oxygen atom, r_{CH_4} : rate of CH_4 conversion, $r_{O_2,f}$: rate of O_2 dissociation, $r_{O_2,r}$: rate of O_s* recombination, $(O_2)_{virtual}$: oxygen virtual pressure defined by Equation 1b, examples of high surface are metal oxide substrate: Al_2O_3, SiO_2)

6.9. Appendix

6.9.1. Time-dependent oxygen contents on 10.6 nm Pd clusters (0.6 % wt. Pd/Al_2O_3 catalyst) at 973 K

Figure A-1 shows the time-dependent oxygen contents, expressed as the atomic O-to-Pd (O_t/Pd, where $O_t=O_s+O_b$, Scheme 1) ratios, in 10.6 nm Pd clusters (0.6 % wt. Pd/Al_2O_3 catalyst) at various O_2 pressures (25-90 kPa) and 973 K during the step-wise increase in O_2 pressure.

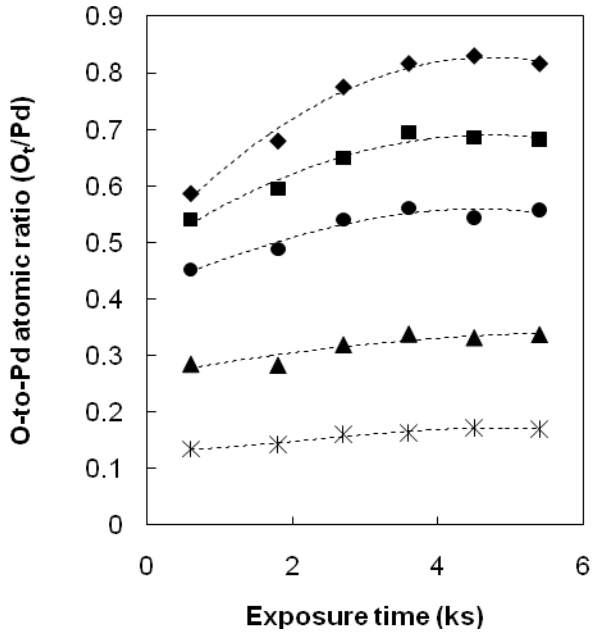

Figure A-1. Oxygen contents in Pd clusters (0.6 % wt. Pd/Al_2O_3 catalyst, 10.6 nm mean Pd cluster diameter), expressed as total O-to-Pd atomic ratio (O_t/Pd), at different exposure times (0.72-5.6 ks) upon introducing the sample to O_2 pressures of 25 kPa (✳), 50 kPa (▲), 75 kPa (●), 85 kPa (■), and 90 kPa (◆) during a step-wise O_2 pressure increase at 973 K.

Figure A-2 shows the time-dependent oxygen contents, expressed as the atomic oxygen-to-Pd ratios (O_t/Pd, where $O_t=O_s+O_b$, Scheme 1), in 10.6 nm Pd clusters (0.6 % wt. Pd/Al_2O_3 catalyst) at various O_2 pressures (0.25-10 kPa) during the step-wise O_2 pressure decrease.

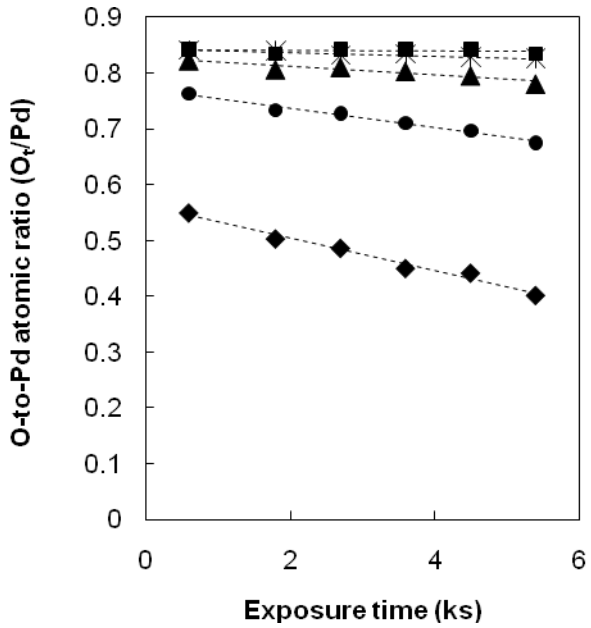

Figure A-2. Oxygen contents in Pd clusters (0.6 % wt. Pd/Al_2O_3 catalyst, 10.6 nm mean Pd cluster diameter), expressed as total O-to-Pd atomic ratios, at different exposure times (0.72-5.6 ks) upon introducing the sample to O_2 pressures of 0.25 kPa (◆), 0.3 kPa (●), 0.4 kPa (▲), 0.8 kPa (✳), and 10 kPa (■) during a step-wise O_2 pressure decrease at 973 K.

6.9.2. Cluster size effects of total oxygen contents in Pd clusters (0.6 % wt. Pd/Al_2O_3 catalyst) during Pd cluster oxidation in O_2 at 973 K

Figure A-3 {(a) and (b)} shows the total O-to-Pd atomic ratios (O_t/Pd; $O_t=O_s+O_b$, Scheme 1) in Pd clusters of different mean cluster diameters (1.8-10.6 nm, 0.6 % wt. Pd/Al_2O_3 catalysts) as a function of O_2 pressures at chemical equilibrium at 973 K.

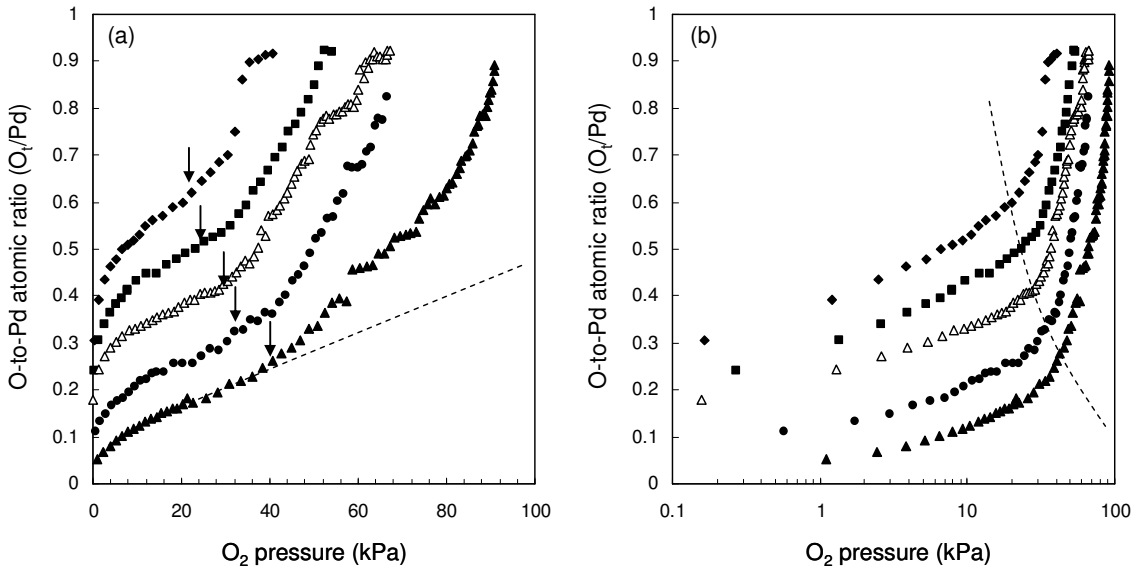

Figure A-3. Total O-to-Pd atomic ratios (O_t/Pd) in a series of 0.6 % wt. Pd/Al_2O_3 catalysts of different mean Pd cluster diameters (1.8 (♦), 2.2 (■), 3.0 (Δ), 5.5 (●), 10.6 (▲) nm) as a function of O_2 pressures in the linear (a) and log scales (b) at 973 K and equilibrium. The arrows in (a) and the dotted line in (b) indicate the onset of oxygen dissolution from cluster surfaces into the bulk.